Development of Graphene Atomic Mirrors for Neutral Helium Microscopy

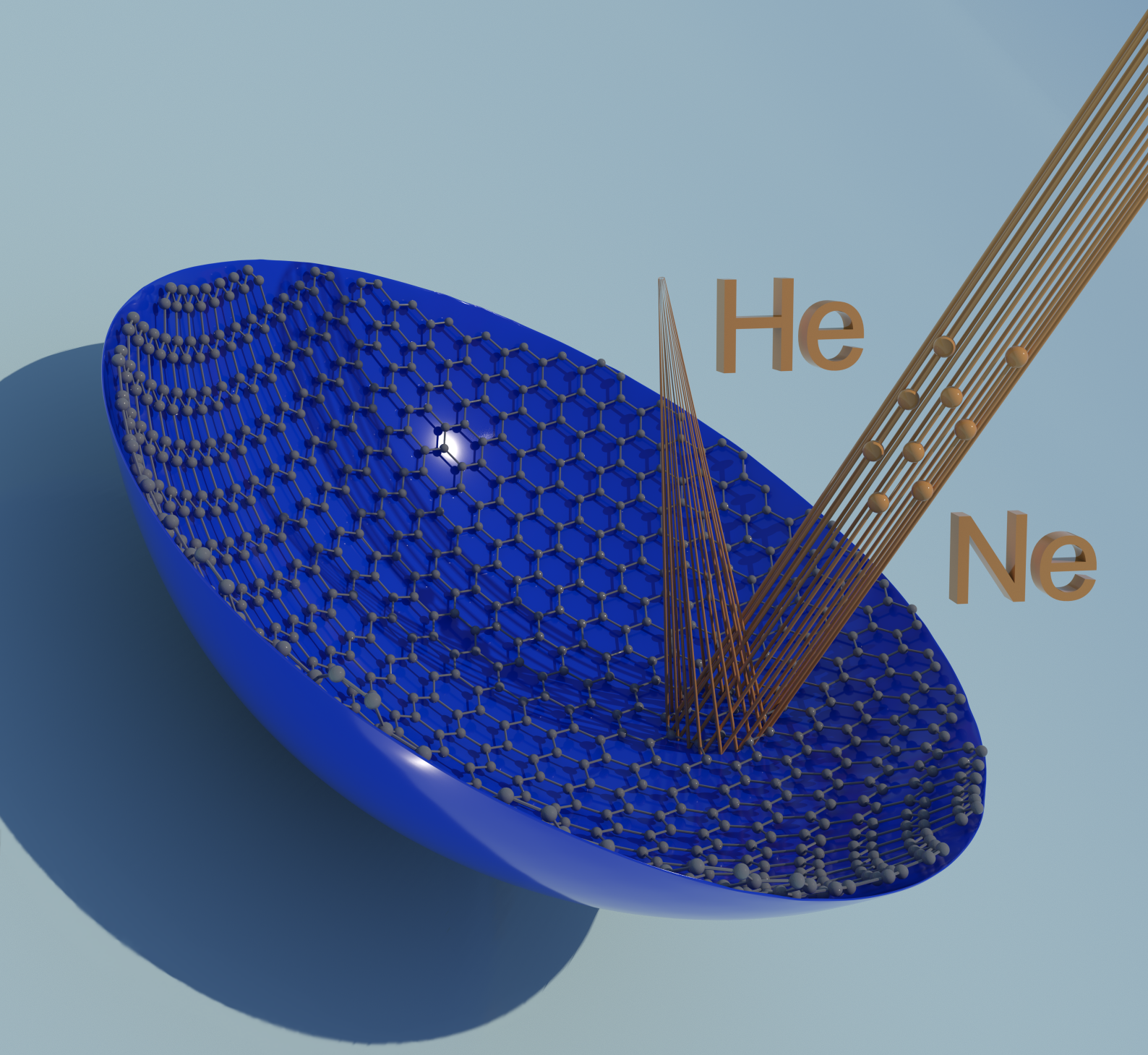

PhD Thesis 2017

Gloria Anemone

Development of Graphene Atomic Mirrors for Neutral Helium Microscopy

By

GLORIA ANEMONE

Departamento de Física de la Materia Condensada
Facultad de Ciencias
UNIVERSIDAD AUTÓNOMA DE MADRID

A dissertation submitted to the University of Madrid in accordance with the requirements of the degree of DOCTOR OF PHILOSOPHY in Condensed Matter Physics and Nanotechnology.

2017

Supervisor: PROF. DANIEL FARÍAS

Alla mia famiglia
della quale fa parte Luis

Agradecimientos

Al fin ha llegado el momento de rellenar la última hoja de esta tesis, y me gustaría hacerlo agradeciendo todos aquellos que me han ayudado durante estos años y han hecho posible que llegara hasta aquí.

En primer lugar me gustaría agradecer a mi director de tesis, Daniel Farías, por haberme dado la oportunidad de trabajar en este proyecto tan interesante y por haberme guiado durante estos cuatro años a evolucionar científicamente, corrigiendo sí los errores pero siempre dando espacio a todas las ideas que han podido surgir a lo largo de este trabajo. Siempre disponible a ayudarme con cualquier duda tuviese.

Gracias a todas las personas con la que he tenido la oportunidad de colaborar. Me gustaría agradecer a Carlos Prieto por su ayuda, sus explicaciones y por haberme dado siempre completa disponibilidad de su equipo cuando lo necesitaba. Agradezco también a Alicia de Andrés, Esteban Climent-Pascual y Felix Jiménez-Villacorta del Instituto de Materiales de Madrid por las medidas Raman y AFM y por toda la ayuda ofrecida. I would also like to thanks J.R. Manson and W. Hayes for all the constructive scientific discussions and for their help with Ne calculations.

Un gracias muy grande va a mi compañero de trabajo Amjad Al Taleb, por haberme enseñado a utilizar los equipos y repararlos, por estar allí siempre que le he necesitado y también a aprender a afrontar con una sonrisa todos los problemas que podían surgir en el laboratorio. No puedo expresar con palabras la deuda que tengo contigo.

Un gracias también a todos aquellos que están o han pasado por el laboratorio de Superficies. Gracias a Miguel Ángel, José Luis, Jesús Álvarez, Fernando, Paolo, Cristina y Davide. Un gracias también a los que fueron mis compañeros de tesis en los primeros años Luigi y Flavio, gracias por vuestro apoyo y amistad. Gracias a Nacho por las agradables charlas. A lo que han sido mis compañeros en los días pasados en materiales durante estos años, Leo y David, gracias por la ayuda y las muchas risas.

Gracias a todo el personal técnico, Andrés Buendía, Santiago Márquez, José María Pérez, José María Castilla y José Luis Romera, que me han permitido salir adelante cuando surgían problemas con los equipos. A Elsa Fuentes y Luisa Carpallo les quiero dar las gracias también por su ayuda con la parte burocrática-administrativa.

A mis amigos madrileños, por haberme hecho sentir como en casa desde el minuto uno. En especial a Davo, Juan, Rami y Jorge por haberme animado en los momentos de bajón y por haber hecho que estos cuatro años fueran súper divertidos. Mención especial para Crisis, gracias por todo y sobre todo gracias por todo el apoyo que me has dado en estos últimos meses.

Grazie ai miei amici dell'Aquila: Robby, Cesare, Daniela, Cialó, Galera, Silvia, Marco e Alessio è sempre una grande gioia rivedervi quando torno o meglio quando torniamo tutti. Rivedersi tutti, magari al Boss, non ha prezzo! La distanza non puo niente contro di noi. Ad Alessia Bill in particolare vorrei ringriazzarla per tutte le telefonate e il supporto dato in tutti questi anni. Ad Alessia e Alessandra, grazie per stare li quando torno e per essere venute a farmi visita piú volte e supportarmi in questi ultimi mesi. Grazie anche a Laura che anche se lontana so che é sempre li disposta ad aiutarmi.

Gracias también a la familia de Luis para haberme acogido y animado en estos años aquí. Muchisimas gracias de todo corazón a María Jesús, Julia, Inés, Clara, Cristina y Rèmi por todo. No hubiera podido tener más suerte!

A tutta la mia famiglia, cugini e zii per tutto l'affetto che mi dimostrate ogni volta che torno. Un grazie speciale va ai miei genitori. Sicuramente non sarei arrivata fin qui senza il vostro sforzo e il vostro aiuto. Grazie a mio padre per avermi trasmesso la curiosità nello scoprire cose nuove e il gusto nel risolvere problmi nuovi. A mia madre per il costante supporto e incoraggiamento. Lo ammeto, grazie anche per farmi tenere sempre il congelatore pieno, di notevole aiuto durante la scrittura della tesi. Al mio tatuoozzo, grazie per avermi aiutato con la copertina e per stare sempre lí quando ne ho bisogno. Mi piacerebbe tenervi più vicini tutti!

Infine un ringraziamento speciale a Luis, per tutti gli anni che abbiamo passato insieme y por estar allí siempre por mí. Sobre todo gracias por el ayuda preciosa, el apoyo que me has dado en estos últimos meses y bueno, sí, por haberme aguantado! Semplicemente non saprei che fare senza di lui.

Abstract

This thesis investigates the design of atomic mirrors that can handle the focusing of neutral ground-state He atoms. The atomic mirror is a fundamental element in the development of a scanning neutral helium microscope (NEMI), which uses a focused beam of helium atoms to image the surface of a sample.

The first part of this work describes in details two new methods developed to grow graphene on sapphire samples in UHV, using Cu as catalyst. A systematic structural and dynamical characterization of this system has been performed, using HAS, AFM, Raman and optical transmission. The HAS measurements represents the first experimental determination of the ordered structure formed by graphene on sapphire as well as of the dispersion of the flexural mode (ZA). High reflectivity (6.5%) together with well-ordered domains (lateral scale of microns) and stability at ambient conditions, make this system an excellent candidate to be used as atomic mirror. In fact, although the study has been performed on flat surfaces its extension to curved sapphire could be possible.

One of the options studied to build a curved atomic mirror has been the use of flexible thin crystals that can be electrostatically bent. For this purpose, the He reflectivity of Cu(111), Ni(111) and Ru(0001) crystals of thickness between 50 and 150 μm as well as Ru(0001) and Ni(111) thin films on mica substrates has been investigated. Remarkable results have been obtained for thin Cu(111) (100 μm) crystals, that reveals a very high specular reflectivity (20%) and high crystallinity (long-range order larger than 200 nm). Furthermore, the crystal has been bent by an electrostatic field and He atoms has been focused, reaching an absolute specular intensity two orders of magnitude larger than previously reported.

The second line explores a pioneering path to produce atomic mirrors by coating curved substrates. Graphene-terminated Ru has been grown on curved fused silica and curved sapphire substrates. Laser polishing technique has been applied to fused silica lenses, ensuring an improvement of the surface quality of the metal coating on the substrate, which leads to a high specular reflectivity and the first observation of He diffraction peaks from thin films grown on curved amorphous substrates. Best result has been obtained for graphene-terminated Ru(0001) on curved sapphire, for which the surface quality is comparable with the one measured for flat graphene grown on Ru(0001) single crystal samples.

Finally, the work is completed with a systematic investigation of elastic and inelastic Ne scattering from graphene on Ru(0001) and from Ru(0001) surface to assess the possibility of employing Ne as probe in neutral microscopy, due to its high sensitivity

to surface details. The HAS measurements taken in the classical regime have been compared with theoretical calculation using the smooth surface model. This comparison shows a good agreement between the multi phonon characteristic predicted and detected.

Resumen

En esta tesis se ha investigado el diseño de espejos atómicos capaces de enfocar átomos de helio en estado fundamental. Estos espejos representan un elemento fundamental en el desarrollo de un nuevo tipo de microscopio de átomos neutros (NEMI) que emplea un haz de átomos de helio para obtener imágenes de la superficie de una determinada muestra.

La primera parte de este trabajo describe en detalle dos novedosos métodos desarrollados para depositar grafeno sobre sustratos de zafiro en condiciones de ultra alto vacío, usando para ello cobre como catalizador. Se aporta también una caracterización sistematica de la estructura y de la dinámica de este sistema (grafeno – zafiro), usando para ello HAS, AFM, Raman y transmisión óptica. A partir de las medidas HAS se ha obtenido la primera determinación experimental de la estructura ordenada formada por el grafeno sobre zafiro, así como la dispersión del modo fonónico llamado flexural mode (ZA). Su alta reflectividad (6,5%) junto a los dominios ordenados (del orden de micrones) y la estabilidad en condiciones ambientales hacen de este sistema un candidato excelente para ser usado como espejo atómico. De hecho, a pesar de que el estudio se ha limitado a muestras planas los resultados pueden ser extrapolados sin problemas a muestras con zafiro curvo.

Una de las dos opciones estudiadas para construir un espejo atómico curvo ha sido el uso de cristales delgados flexibles que puedan ser doblados mediante la aplicación de un campo electrostático. Para ello se ha investigado el grado de reflectividad de cristales de Cu(111), Ni(111) y Ru(0001) con espesores de entre 50 y 150 μm, así como de películas delgadas de Ru(0001) y Ni(111) sobre sustratos de mica. Se han obtenido resultados notables para el caso de los cristales delgados de Cu(111) (100 μm), que han revelado una muy alta reflectividad especular (20%) y una alta cristalinidad (del orden de los 200 nm). Más aún, los cristales han sido efectivamente curvados a través de un campo electrostático, lo que ha permitido enfocar átomos de helio y alcanzar una intensidad especular absoluta hasta dos órdenes de magnitud mayores que las reportadas previamente.

La segunda opción explora una vía pionera en la producción de espejos atómicos a través del recubrimiento de superficies curvas. Se han depositado películas delgadas de Ru sobre sustratos curvos de vidrio y zafiro, a continuación estas películas se han pasivado mediante la deposición de una monocapa de grafeno. Se han aplicado técnicas de pulido láser a los sustratos de vidrio usados, lo que asegura una mejora en la calidad de la superficie del recubrimiento metálico, lo que a su vez conlleva una reflexión especular

más alta. Esto ha permitido observar picos de difracción de helio sobre películas delgadas depositadas en sustratos amorfos. El mejor resultado se ha obtenido para el Ru(0001) pasivado con grafeno y depositado sobre zafiro curvo, para el que la calidad de la superficie es comparable con la medida para grafeno plano depositado sobre un monocristal de Ru(0001).

Por último, el trabajo se ha completado con un investigación sistemática de la dispersión elástica e inelástica de Ne en muestras de grafeno sobre Ru(0001) y Ru(0001) para evaluar la posibilidad de emplear haces de Ne como sonda en microscopios neutros, dada su alta sensibilidad a las irregularidades de la superficie. Las medidas de HAS para régimen clásico del sistema se han comparado con los cálculos teóricos elaborados usando el modelo de superficie lisa (smooth Surface model). Esta comparación muestra un buen ajuste entre las características multi-fonón esperadas y detectadas.

Table of Contents

Introduction

Thermal energy neutral Helium atoms probe the outermost surface layer of any material in an inert, completely nondestructive manner [1]. Due to the low energies used (usually less than 100 meV), the interaction occurs through the electron density distribution of the topmost surface atoms. Thus, He atoms are ideally suited to investigate all kinds of materials, including insulating and/or fragile surfaces, biological samples or polymeric nanostructures, without damaging them. Recent developments in the field of neutral beams manipulation have led to a renewed interest in the use of a helium atom beam to image surfaces in real space. One of the crucial challenges for the construction of high-resolution He-microscopes is the development of optical elements that can handle the focussing of neutral He atoms.

In order to solve this problem, two main paths have been pursued in the last decade: diffractive optical elements using Fresnel zone plates [2–4], and reflective elements using curved mirrors [5, 6]. By using Fresnel zone plates, the helium beam has been focused below one micron [3]. However, a major problem with Fresnel zone plates is that they suffer from chromatic aberrations, in addition to the low intensity of the focused beam (ca. 5-10% of the incident beam). Chromatic aberration is an issue for He-microscopy, because the He beam, generated by a supersonic expansion, will always have a given velocity distribution [7, 8]. The use of curved mirror surfaces could solve these limitations. Besides being inherently achromatic, mirrors can focus an incident beam with a diameter of several millimetres, leading to higher focused beam intensities.

Creating surfaces that are both curved and smooth at the atomic scale is a major challenge. Due to the high sensitivity of He atoms to surface defects, their density must be very low [9]. This requires the design of a new method to build atomic mirror. Two lines of research have been pursued in this thesis to achieve this goal.

The first line is focused on the use of flexible thin crystals that can be electrostatically bent. A good candidate to be used as a mirror is a thin semiconductor crystal, like Si(111), since their surfaces can be manufactured with larger terraces and smaller density of defects than metal surfaces. This approach has been followed in the past,

using electrostatically bent thin Si(111) crystals as mirrors. However, two main problems persist when semiconductor crystals are used: the poor flexibility and the large surface corrugation compared to metal crystals. The former is essential to bend the crystal electrostatically, whereas the latter imposes a limitation to the intensity of the specular peak. In effect, highly-corrugated surfaces lead to the appearance of many diffraction channels, causing a loss in intensity of the specular peak [1]. As a consequence, the absolute specular reflectivity for Si(111) is with ca.1% considerably smaller than the high reflectivity measured for metal surfaces (from 15% to 40%) [10, 11].

Until now, technical restrictions limited the thickness of the metal crystals used. However, nowadays commercial crystals of about 50 μm are available for many metals. This characteristic allows the manipulation of metallic surfaces and the possibility of a controlled bending of the metal itself. But so far no investigations have been reported on the surface quality and the long-range order of these thin crystals, which are determinant factors of the quality of the reflected He beam. In this work, the reflectivity to incoming He atoms of Cu(111), Ni(111) and Ru(0001) crystals of thickness between 50 μm and 150 μm as well as of Ru(0001) and Ni(111) films deposited on Mica substrate has been studied.

The second possibility explores a pioneering path to produce atomic mirror coatings on curved substrates. Recently, graphene on epitaxial Ru(0001) thin films on c-axis sapphire (Al_2O_3) has been demonstrated to have a very high He reflectivity (23%), together with ambient-stable behaviour [12]. Thus, Gr/Ru(0001)/Al_2O_3 appears as a promising system as mirror for He atoms. In this work, the option of growing graphene layer directly on sapphire substrate has also been explored, studying its structural and dynamic property. A new preparation method had to be previously developed, using Cu as catalyst, to produce high quality graphene on sapphire samples. However, its extension to curved substrates is not trivial, due to the difficulties to find commercial curved sapphire. For this reason, in this work also an alternative path has been followed using fused silica lenses as curved substrates. While some research has been carried out on thin films on fused silica substrates, no single study exists about the synthesis of graphene on macroscopically curved surfaces and its use as atomic mirror.

Here, curved atom mirrors have been achieved by coating both sapphire and fused silica plano-concave lenses with graphene-terminated Ru(0001) thin films. The recently developed laser polishing technique has been applied to fused silica lenses to reduce the surface roughness. The high reflectivity obtained together with the observation of He diffraction peaks, shown by both crystals, is a remarkable result, especially if the

amorphous nature of the fused silica lenses is taken into account.

Furthermore, a systematic investigation of Ne scattering from Gr/Ru(0001) and on Ru(0001) surface has been conducted to assess the possibility of employing Ne as probe in neutral microscopy, due to its high sensitivity to surface details.

The overall structure of the thesis take the form of seven chapters:

Chapter 1 provides a general overview of He atom scattering and the state of the art in the field of neutral miscroscopy. The chapter ends with a brief review of the graphene structure grown on transition metallic substrates.

Chapter 2 presents a description of the experimental techniques used in this work.

Chapter 3 is dedicated to the mirror simulations implemented in this thesis to evaluate the position of the focus for a reflected beam by an off-axis parabolic mirror.

Chapter 4 describes the two new methods developed to produce high-quality, transparent graphene on sapphire samples, using Cu as catalyst. Comprehensive structural and dynamical characterization of this system has been accomplished with HAS experiments and complemented with AFM, Raman spectroscopy and UV-VIS transmission spectroscopy.

Chapter 5 is divided in two main parts. The first part deals with He measurements on flat flexible thin crystal mirrors of Cu(111), Ni(111), Ru(0001) and Ru(0001) on mica with a thickness between 50 and 150 μm. Moreover, it has been demonstrated that graphene can be grown on thin Ni(111) crystals. The second part demonstrates the possibility to focus a beam of He by applying an electrostatic potential to the thin Cu(111) crystal.

Chapter 6 presents macroscopically curved mirrors and it is divided in two main parts. The first part deals with the He diffraction from graphene-terminated Ru on both sapphire and fused silica flat substrates. The second part describes the extension to the curved substrates and of use these system as atomic mirrors.

Chapter 7 is focused on the possibility to use Ne atoms as probe for neutral microscopy. An extensive and systematic studies of Ne on clean Ru(0001) and on Gr/Ru(0001) is given in quantum and classical regime. Finally the experimental results taken in classical regime are compared with theoretical calculations, using the smooth surface model.

Finally, general conclusions ends this thesis.

CHAPTER 1

THEORETICAL FOUNDATIONS

This chapter is divided in three main sections. In the first one a description of basic concepts of Helium Atoms Scattering (HAS) is given. The second section provides an overview of Scanning Neutral Microscope and a brief description of the NEMI microscope, where the atomic mirror will be implemented. Finally, the third section explains the main properties of graphene with special focus on the interaction with metal substrates.

1.1 Helium Atom Scattering

Helium Atom Scattering (HAS) is a well-established technique, due to its power as sensitive surface probe. Structural and dynamical properties of materials can be studied by measuring the He diffracted beam from a given surface sample. The energy of the probing atoms in the helium beam is usually less than 150 meV. This value is several orders of magnitude smaller than typical electron energies used in microscopy, hence allowing to classify this technique as non-penetrating and non-destructive.

A graphical representation of the different processes between helium and electron scattering is shown in Fig. 1.1. While the use of electron scattering implies the penetration of the incident beam inside the sample, the turning point of the helium atoms is 3-4 Ångstrom above the surface. This means that the sample will not be damaged, even for very fragile ones, and since the beam is composed by neutral atoms, no distortion will be present due to charging effects.

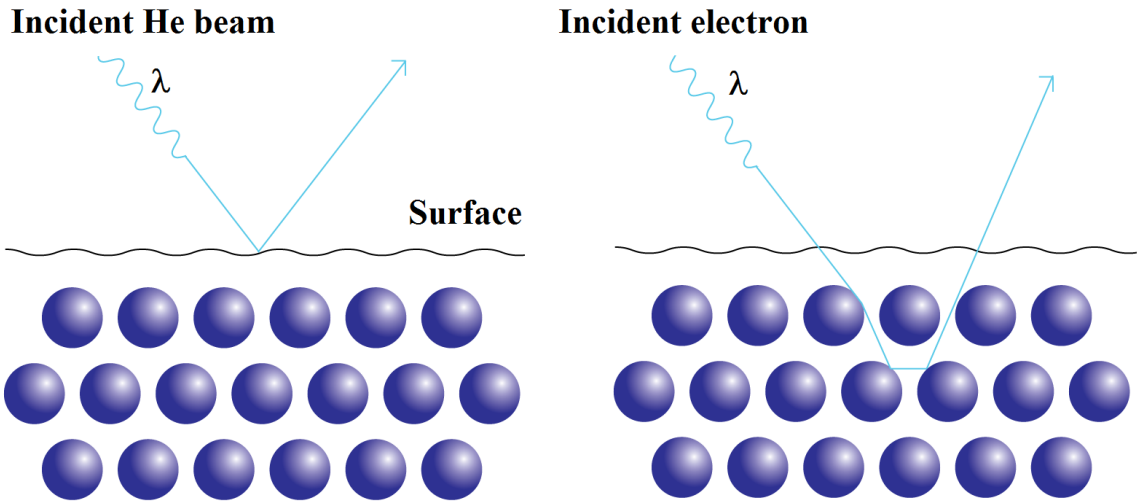

Figure 1.1: Schematic draw showing the different interaction mechanism of He atoms and electrons with the crystal. Thanks to the low incident energies (~ 20-150 meV) of the He atoms the interaction is restricted to the outermost surface layer, undergoing only a single scattering process. Whereas the electrons undergo multiple scattering involving several layer of the crystal.

1.1.1 Beam generation

The monochromaticity of the atomic beam plays a key role in diffraction experiments for structural investigations as well as surface lattice dynamic experiments. This condition

was achieved by supersonic beam technique that provides low energy spread ΔE of only a few percent of the incident energy [13]. The supersonic molecular beam is formed when a high pressure gas (typically $P_0 \approx 70$ bar) expands adiabatically in a region of low pressure P_B through a small aperture of diameter d (typically 10-20 μm) called *nozzle*. The *free-jet expansion* process is schematized in Fig. 1.2 [14].

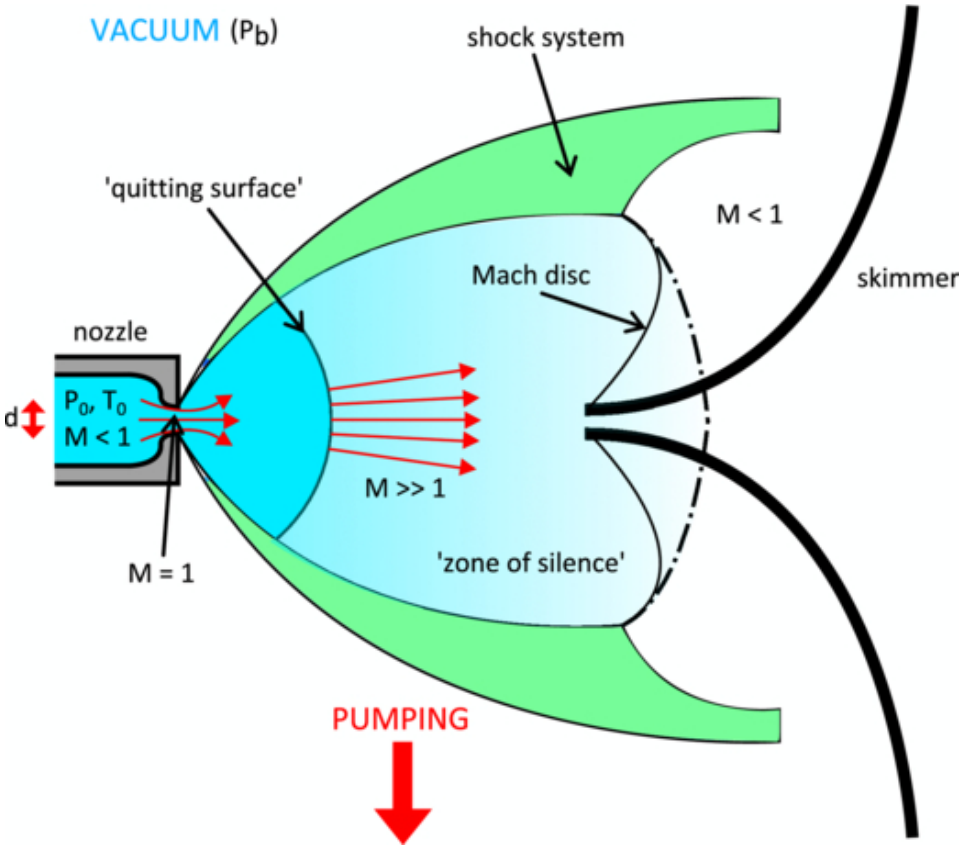

Figure 1.2: Schematic sketch of the free jet expansion [14].

If $P_0 \gg P_B$, the gas is accelerated from the so-called *stagnation state* (P_0; T_0) until it reaches the speed of sound (Mach No. M = 1) at the narrowest point of the nozzle and it expands increasing its velocity and decreasing the density. Gas particles reach supersonic velocities in the expansion when the ratio P_0/P_b exceeds a certain critical value $G = \left(\frac{\gamma+1}{2}\right)^{\frac{\gamma}{\gamma+1}}$, where $\gamma = \frac{C_p}{C_V}$ is the ratio of the specific heat by constant pressure and volume. This ratio γ is 1.66 for an ideal monoatomic gas [15]. At a certain distance away from the nozzle, the flow changes from continuous flow to atomic free flow without further inter-atomic collisions. Furthermore, since the atoms move faster than the speed of sound, there is a region of space known as a *zone of silence*, in which the atoms are

independent of the boundary conditions. The zone of silence is surrounded by a non-isentropic region of high density where the gas readjusts to boundary conditions. This region ends in the so-called Mach 1 disk, located at a distance X_M given by

$$X_M = \frac{2}{3} d \left(\frac{P_0}{P_B} \right)^{\frac{1}{2}} \tag{1.1}$$

where d is the nozzle diameter [16].

The central part of the beam is extracted a few millimeters away from the nozzle by means of a conical *skimmer*. The pressure in the following chambers is low enough to ensure a large free mean path and to avoid significant attenuation by collisions with the background gas. Thus, the characteristics of the central part of the beam can be approximated by vacuum isentropic expansion with negligible viscosity and heat conduction. Since the system can be considered adiabatic, in agreement with the first law of thermodynamics, the total energy of the gas has to be conserved. It possible, then, to write the following equation:

$$H_0(P_0, T_0) + \frac{1}{2} m v_0^2 = H_f(P_f, T_f) + \frac{1}{2} m v_f^2 \tag{1.2}$$

where the terms on the left side of the equation are the sum of the enthalpy and the kinetic energy of the atoms collected in stagnation stage, while the terms on the right side are the corresponding enthalpy and kinetic energy of the gas in the final stage, that is, when the gas is in the atomic flow region.

For a monoatomic ideal gas, the enthalpy in the source reservoir is given by

$$\begin{aligned} H_0(P_0, T_0) &= c_p T_0 \\ &= \frac{\gamma}{\gamma - 1} k_B T_0 \\ &= \frac{5}{2} k_B T_0 \end{aligned} \tag{1.3}$$

Likewise, the enthalpy in the final stage is given by

$$H_0(P_f, T_f) = \frac{5}{2} k_B T_f \tag{1.4}$$

The average kinetic energy of the particles before the expansion can be neglected since their mean velocity is zero, leaving the Eq.1.2 as

$$\frac{5}{2} k_B T_0 = \frac{5}{2} k_B T_f + \frac{1}{2} m v_f^2 \tag{1.5}$$

When the gas has fully expanded into the vacuum it is possible to assume the enthalpy vanishingly small. Thus, the final mean velocity of the atoms in the beam, known as *terminal velocity*, can be expressed as a function of nozzle temperature:

$$v_f = \sqrt{\frac{5k_B T_0}{m}} \tag{1.6}$$

The beam velocity dispersion $\Delta v/v_f$ is characterized by the so-called *speed ratio* $S = \sqrt{mv_f^2/2k_B T_0}$. The Full Width High Maximum (FWHM) of the velocity distribution (Δv) centered in v_f is related to S by $\Delta v/v_f \sim 1.65/S$, that it is usually $< 1\%$ for He atoms [17]. Furthermore, thanks to Eq.1.5 it is possible to estimate the beam energy by knowing the nozzle temperature. In the case of He gas, as $E_i = \frac{5}{2}K_B T$, for nozzle temperatures between 100 and 700 K, the beam energies are in the range of 20-150 meV.

1.1.2 Atomic beam–surface interaction

At large separations the interaction between thermal energy He atoms (20-150 meV) and surface is described by an attractive potential due to the Van der Waals force. Since it decays as z^{-3}, where z is the distance between the He atom and the surface, these force present a long range.

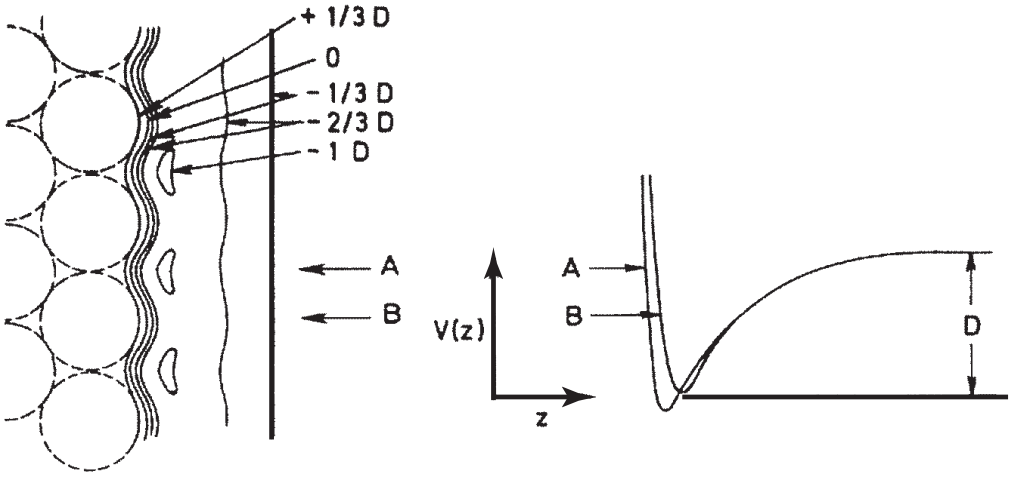

Figure 1.3: Left: Schematic sketch of the equipotential lines as function of the well depth D in for the interation of an atom with ordered surface. Right: the potential as a function of z (normal to the surface) for two different positions A and B is illustrated. Adapted by Ref. [19].

Closer to the surface the He atoms experiment a repulsive interaction due to the the overlap between the electronic cloud of the He atoms with the valence electrons of the surface (Pauli exclusion). These repulsive part has short range. The shape of the potential depends on the incident angle and the position of the He particle with respect to the surface. A qualitative sketch of the atom-solid potential can be achieved by summing over the binary interaction potential between the incoming atom and individual atoms of the surface (Fig. 1.3) [1, 9, 18]. In a classical approach, the turning point of an He atom is further away from the surface if it hits just above one atom than if it hits between several atoms. This implies a periodic modulation of the repulsive part of the potential, which is described by the corrugation function $\zeta(\mathbf{R})$, where $\mathbf{R}$ is the two-dimensional vector in the surface plane. In a first approximation, $\zeta(\mathbf{R})$ is equivalent to a contour of constant electron surface charge density $\rho(r)$, which is proportional to the particle energy $E(r)$ [20],

$$E(r) = \alpha\rho(r) \tag{1.7}$$

In this approach, the turning point lies about 2-3 Å from the surface atom cores. Therefore, the topography of the surface atoms can be obtained by relating the experimental corrugation to the calculated surface charge-density profiles [1].

1.1.3 Kinematics of helium atom scattering

Before discussing the kinematics of the atoms impinging on a periodic surface, a brief introduction on the surface geometry is required. The periodic surface can be described by the Brevais lattice as a superimposition of the unit vector, $\mathbf{a}_1$ and $\mathbf{a}_2$, of the primitive cell:

$$\mathbf{R} = p\mathbf{a}_1 + q\mathbf{a}_2 \tag{1.8}$$

where p and q are integer numbers. The reciprocal lattice will be defined by generating its two reciprocal primitive vectors, $\mathbf{b}_1$ and $\mathbf{b}_2$:

$$\mathbf{G} = n\mathbf{b}_1 + m\mathbf{b}_2 \tag{1.9}$$

The reciprocal lattice vectors $\mathbf{b}_1$ and $\mathbf{b}_2$ are related to the unit cell vectors $\mathbf{a}_1$ and $\mathbf{a}_2$ by the following relation:

$$\mathbf{a}_i \cdot \mathbf{b}_j = 2\pi\delta ij \tag{1.10}$$

with i,j = 1,2. This equation implies that $\mathbf{b}_1$ and $\mathbf{b}_2$ are normal to $\mathbf{a}_1$ and $\mathbf{a}_2$, respectively. Thus the lengths of $\mathbf{b}_1$ and $\mathbf{b}_2$ are determined by

$$|\mathbf{b}_1| = \frac{2\pi}{a_1 \sin\beta} \qquad |\mathbf{b}_2| = \frac{2\pi}{a_2 \sin\beta} \tag{1.11}$$

where β is the angle between $\mathbf{a}_1$ and $\mathbf{a}_2$.

Elastic scattering

Consider a beam of the He atoms with mass m and incident energy E_i impinging on a crystalline surface. Given the wave nature of the helium atom beam it is possible to define its wavelength λ according to the De Broglie relation:

$$\lambda = \frac{h}{\sqrt{p}} = \frac{h}{\sqrt{2mE_i}} \tag{1.12}$$

The wave vector $\mathbf{k}_i$ of the incident atoms relates to the wavelength λ by,

$$|\mathbf{k}_i| = \frac{2\pi}{\lambda} \tag{1.13}$$

So that, the expression for the incident energy will be

$$E_i = \frac{\hbar^2 k_i^2}{2m} \tag{1.14}$$

For in-plane scattering $\mathbf{k}_i$ can be separated into parallel and perpendicular components to the surface sample, as shown in Fig. 1.4,

$$\mathbf{k}_i \equiv (\mathbf{K}_i, k_{iz}) = (k_i \sin\theta_i, -k_i \cos\theta_i) \tag{1.15}$$

For any periodic surface the elastic scattering process for helium atom is ruled by the conservation of the energy and of the parallel component of the momentum to the surface plane (Bragg law). Thus

$$\Delta E = E_{f,nm} - E_i = \frac{\hbar^2}{2m}(k_{f,nm}^2 - k_i^2) = 0 \qquad \textbf{Conservation of energy} \tag{1.16}$$

$$\mathbf{K_i} + \mathbf{G}_{nm} = \mathbf{K}_{f,nm} \qquad \textbf{Bragg law} \tag{1.17}$$

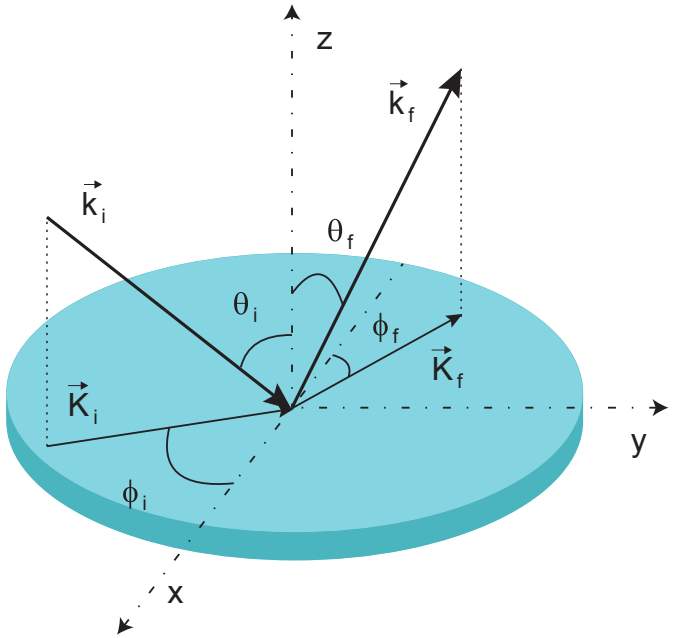

Figure 1.4: Schematic draw showing the scattering geometry conditions. The initial $\mathbf{k}_i$ and final $\mathbf{k}_f$ wavevectors form an angle θ_i and θ_f with the normal to the surface. The vector components $\mathbf{K}_i$ and $\mathbf{K}_f$ parallel to the surface form an angle ϕ_i and ϕ_f with respect to the x-axis.

where $n, m \epsilon Z$ and $\mathbf{K}_{f,nm}$ is the wave vector of the outgoing atoms which have been scattered to the (nm) diffraction peak. Eq. 1.16 limits the number of reciprocal lattice vectors for which diffraction can occur to the finite set $\{\mathbf{G}\}$ for which

$$k_{fz,nm}^2 = k_i^2 - (\mathbf{K}_i + \mathbf{G}_{nm})^2 > 0 \tag{1.18}$$

This conditions (1.16 and 1.17) can be graphically represented with the Ewald construction, as shown in Fig. 1.5. From these equations it is possible to extract the angular positions of the diffracted peaks, that provides information about the size of the unit cell and its orientation.

For one dimensional lattice the Bragg condition can be rewritten as

$$\Delta K = k_i(\sin\theta_f - \sin\theta_i) = \frac{2\pi}{a} n \tag{1.19}$$

where a is the constant lattice and n is the diffraction order.

For two dimensional lattice with unit vectors $\mathbf{a}_1$ and $\mathbf{a}_2$ comprising the angle β, two angles have to be define in order to specify the scattering direction: $in-plane$ angle

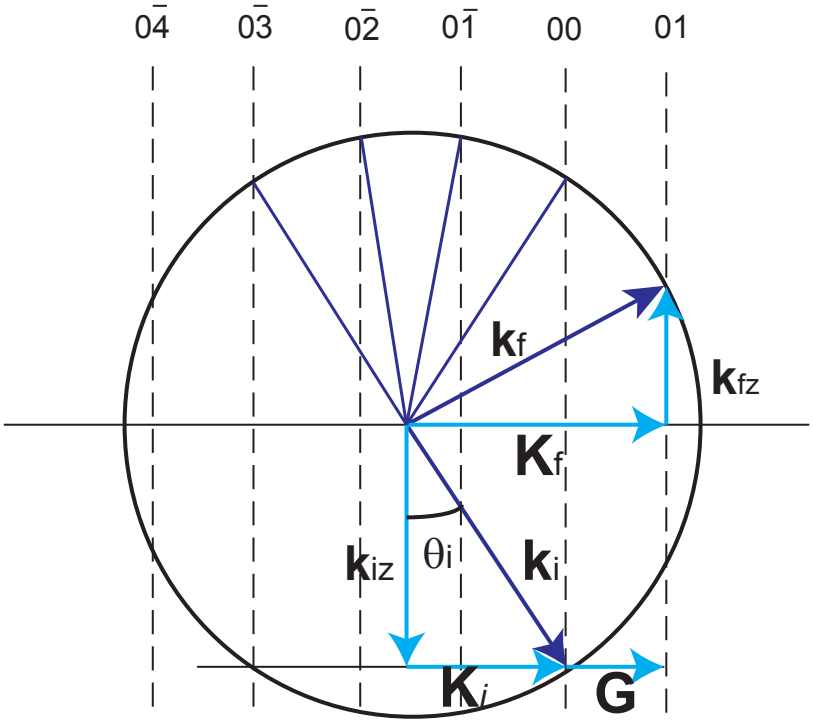

Figure 1.5: The Ewald construction for diffraction from surface in the one dimensional case.

Θ_{nm} and $out-of-plane$ angle Φ_{nm} for the (nm) diffraction channel

$$\sin\Theta_{nm} \equiv \frac{k_{fx,nm}}{|\mathbf{K}_f|} \tag{1.20}$$

$$\sin\Phi_{nm} \equiv \frac{k_{fy,nm}}{|\mathbf{K}_f|} \tag{1.21}$$

According to these definitions Θ_{nm} and Φ_{nm} can be calculated from the following formulae:

$$\sin\Phi_{nm} = \lambda_i\Big[-\frac{n}{a_1}(\sin\gamma+\cos\gamma\cot\beta)+\frac{m}{a_2}\frac{\cos\gamma}{\sin\beta}\Big] \tag{1.22}$$

$$\sin\Theta_{nm} = \frac{1}{\cos\Phi_{nm}}\Big[\sin\Theta_i+\lambda_i\frac{n}{a_1}(\cos\gamma-\sin\gamma\cot\beta)+\lambda_i\frac{m}{a_2}\frac{\sin\gamma}{\sin\beta}\Big] \tag{1.23}$$

where γ is the angle between $\mathbf{K}_i$ and $\mathbf{a}_1$, Θ_i the incident angle and β is the angle between the real space lattice vectors. When $\Phi_f = 0°$ in-plane angular distribution will bee recorded, otherwise out-of-plane diffraction will take place.

Inelastic scattering

The particles impinging the surface can exchange energy with the crystal though inelastic scattering processes, in which they can either create or annihilate surface phonons. This interaction may be single phonon, in which the particles are acting in the quantum regime, or multiphonon, in which several energy transfers are involved. In the single phonon case a new factor must be added to the parallel momentum conservation law in order to include the phonon waver vector, $\mathbf{Q}$:

$$\Delta\mathbf{K} = k_f \sin\theta_f - k_i \sin\theta_i = \mathbf{G} + \mathbf{Q} \tag{1.24}$$

Likewise, the conservation energy law must also be modified so that the exchanged energy between the impinging particle and the surface is considered:

$$E_f - E_i = \pm\hbar w(\mathbf{Q}) \tag{1.25}$$

where E_i and E_f are, respectively, the initial and final energy of He atom and $\hbar w(\mathbf{Q})$ is the energy of the phonon. If the exchange energy is positive the phonon suffers an annihilation phonon, whereas if it is negative the phonon is created.

The combination between Eq. 1.25 and Eq. 1.24 provides the kinematic conditions for inelastic atom-surface scattering and is called scan curve[21].

$$\frac{\hbar w(\mathbf{Q})}{E_i} = \frac{(\sin\theta_i + \Delta K/k_i)^2}{\sin^3\theta_f} - 1 \tag{1.26}$$

By using this curve, it can be calculated the range of energies and wave vectors cinematically allowed in TOF experiments for given incident energies E_i and angles θ_i.

Figure 1.6 represents typically scan curves in a He scattering experiment for our experimental set-up ($\theta_i + \theta_f$ = 105.4°) taken for two different incident energies E_i = 15 and 25 meV and several angles $\Delta\theta_i$ = -30° to 30° relative to the specular position. The sine curves (solid lines) represent the Rayleigh phonon mode. The intersections between the scan curve with the phonon mode dispersion curve gives the points in which single phonon events are expected to arise. When $\Delta K > 0$ the dispersion is called forward directed, whereas for $\Delta K < 0$ is called backward directed [22].

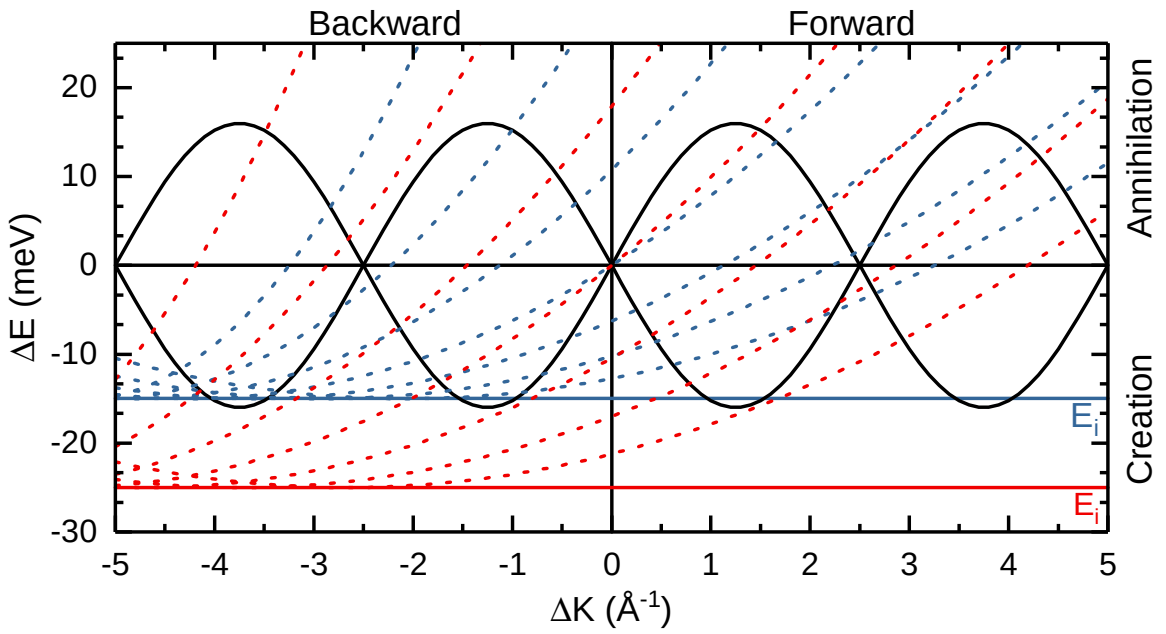

Figure 1.6: Typical scan curves are represented as dashed lines for a fixed source-detector angle system (θ_{SD} = 105.4°) of He scattering with incident energy E_i = 15 and 25 meV (blue and red, respectively). The Rayleigh modes are schematically represented by sine (solid line) functions. (Figure by courtesy of A. Al Taleb.)

1.1.4 The Debye–Waller factor

In first approximation, the thermal attenuation of the He atoms scattered by a solid surface can be described by the Debye−Waller model. The intensity $I(T_S)$ of a diffraction peak for a crystal at a given temperature T_S is related to its value I_0 from a lattice at rest by the following relation:

$$I(T_S) = I_0 e^{-2W(T_S)} \tag{1.27}$$

where $e^{-2W(T_S)}$ is the Debye−Waller factor and its exponent can be written as:

$$2W(T_S) = \langle (\vec{u} \cdot \Delta\vec{k})^2 \rangle_{T_S} \tag{1.28}$$

with $\vec{u}$ the displacement of a lattice atom out of its equilibrium position, $\Delta\vec{k}$ the total momentum transfer in the scattering process and the outer brackets refer to a thermal average[1]. Eq. 1.28 can be decomposed into two contributions: perpendicular Δk_z and parallel ΔK components of momentum transfer:

$$2W = \Delta k_z^2 \langle u_z^2 \rangle + \Delta K^2 \langle u^2 \rangle. \tag{1.29}$$

where $\langle u_z^2 \rangle$ and $\langle u^2 \rangle$ is the average displacement of a crystal atom, respectively, perpendicular and parallel to the surface. ΔK is given by the equation

$$\Delta K = k_i(\sin\theta_f - \sin\theta_i) \tag{1.30}$$

For the specular channel ($\theta_i = \theta_f$) the momentum transfer ΔK parallel to the surface is zero. Thus the Eq. 1.29 can be write as:

$$2W = \Delta k_z^2 \langle u_z^2 \rangle \tag{1.31}$$

For a harmonic lattice (i.e. the Model of Debye for solid) it possible to use the following relation:

$$\frac{1}{2} M w_D^2 \langle u^2 \rangle = \frac{3}{2} K_B T_S \tag{1.32}$$

where w_D is the Debye frequency. Defining the Debye temperature in terms of w_D: $\Theta_D = \hbar w_D / K_B$, the Debye–Waller factor can be expressed as:

$$2W = \frac{3\hbar^2 \Delta k_z^2 T_s}{M K_B \Theta_D} \tag{1.33}$$

To evaluate the effect of the attractive well near the surface in the scattering process of thermal atoms from surfaces, the so-called Beeby correction has to be taken into account. This correction requires that Δk_z must have an additional contribution due to a one-dimensional potential wall with depth D. Thus the He atoms hit the repulsive wall with a perpendicular momentum transfer which differ from the corresponding values at large separation, Δk_z, according to

$$\Delta k_z^{'2} = \Delta k_z^2 + \frac{2mD}{\hbar^2} \tag{1.34}$$

where m is the particle mass [1, 9, 23]. Placing this term in Eq. 1.33, we find

$$2W = \frac{3(\hbar^2 \Delta k_z^2 + 8mD) T_s}{M K_B \Theta_D} \tag{1.35}$$

For the specular beam, the Debye-Waller factor can be simplified as a function of the incident beam energy E_i and the angle of incidence θ_i

$$2W = \frac{24m(E_i \cos^2\theta_i + D) T_s}{M K_B \Theta_D} \tag{1.36}$$

This equation states that the specular intensity is higher for grazing incidence, low surface temperature and low incidence energy, in agreement with experiments. Eq. 1.36 does not have a correct dependence with the moment and the temperature simultaneously. A complete treatment of thermal attenuation in realistic cases also requires a detailed study of multiphonon processes. However, Debye-Waller model describes many experiments, with an acceptable degree of precision.

1.2 NEutral MIcroscopy (NEMI)

1.2.1 Background

Since the invention of the primitive microscopes in the daybreak of the European renaissance [24], the scientists were moved from the impetus to observe objects and features smaller and smaller in order to answer fundamental questions in natural science. To achieve this, three main types of microscope have been developed or improved in the last century: optical microscopes, based on electromagnetic waves; scanning probe microscopes, such as atomic force microscopes (AFM) and scanning tunneling microscopes (STM), in which a solid probe scans the sample surface; and matter wave microscopes, such as scanning electron microscope (SEM) or scanning helium ion microscope (SHIM), which use particles as probe. The incoming of these new microscopic techniques was stimulated by the need to overcome the resolution limit imposed by the Abbe criterion [25]. This formula states that the resolution limit of a given microscope is

$$d = \frac{\lambda}{2n \sin \alpha} \tag{1.37}$$

where λ is the light wavelength and n is the refractive index of the medium and α the aperture angle. As a consequences of this relation, the resolution improve with decreasing wavelengths. Thus, this criterion fixes the resolution limit for visible light under ideal conditions in the range about 200 nm. However, in the real case it is hard to achieve resolutions of less than 1 micron.

An outstanding improvement was given by the development of a super-resolved fluorescence microscopy [26], enabling a resolution of 20 nm by means of using visible light in combination with fluorescence [27–29]. Eric Betzig, Stefan W. Hell and William E. Moerner were awarded the Nobel Prize in Chemistry 2014 for overcoming the Abbe limit [30].

The second type of microscope, Scanning Probe Microscopy (SPM) overcomes Abbe limit by using entirely a different concept to image the surface. STM was the first

technique of this kind invented (Binning $at\ al.$ 1982)[31]. The surface can be imaged with atomic resolution using a tunneling current between the probe tip and the surface sample. For this reason both tip and sample have to be good conductors. On the contrary, AFM can also be used on insulator substrates. It uses the inter-atomic forces between the surface and the tip to map the surface sample. The major drawback for AFM is, probably, the difficulty to image high aspect ratio structures and low speed while scanning soft or rough surfaces.

Another group of microscopes is the matter wave microscope, which uses the dual nature of the wave-particle. The wavelength of a massive particle is determined by the de Broglie relationship

$$\lambda = \frac{h}{p} \tag{1.38}$$

that associates the momentum of the particle with its wavelength [32]. Therefore, bearing in mind the Abbe criterion (Eq. 1.38), a particle with high momentum can furnish high resolution if used as probe in a microscope. The first particle used as probe beam to image a surface was the electron (1932 Knoll and Rusk). The resolution of the recent SEM or TEM can achieve sub-Ångstrom resolution and the measurements can be very fast and more suitable for high aspect ratio structure. However, to reach such a high resolution, a high momentum is required, which means high energy incident beams ($E = p^2/2m$) typically in the range of 0.1-500 keV. This implies that the beam penetrates into the material (50-100 nm), possibly damaging it. Furthermore the sample used in these microscopes must be an electric conductor, so in order to study an insulator sample a coating of a conductive material, usually gold, is required.

In addition, scanning helium ion microscopy (SHIM) offers an alternative method to the inspection of the surface sample, using charged particles of He as a probe beam. With the low wavelength of the helium ions and the possibility to focus the beam through electric fields, this technique can achieve high resolutions. Nevertheless, high energy beams are required, so, as in the case of SEM, it can damage the surface.

All this microscopic techniques remain extremely important tools in most of the natural sciences. However, it does not exist any technique that could image insulator, fragile and with a high aspect ratio samples. Neutral microscope (NEMI) could be able to overcome all this boundaries and revolutionize the nano-metrology field.

1.2.2 Previous work on helium atoms focusing

Helium neutral microscopy is strictly surface sensitive, which means that there is no penetration in the bulk, thanks to the very low energy of the probing atoms. The energy of the incident helium beam associated with a wavelength of 1 Å is of about 20 meV. Several order of magnitude lower than the electron energies of the SEM technique for a comparable de Broglie wavelength. As detailed in the precedent section, helium atoms are scattered at about 3-4 Å from the surface, thus no sample damage is possible even for fragile or biological samples. In addition, no distortion effect caused by charging effects can happen. However, focusing a beam of neutral atoms is a big challenge given its very low polarizability and lack of spin, so no electric or magnetic field can be used to manipulate the atoms. Furthermore, as the beam does not penetrates solid matter, the use of lenses has to be discarded too.

The method pursued in the last decade to manipulate neutral atomic beam has been the use optical element in diffraction, using Fresnel zone plates, or in reflection, using atomic mirrors.

The diffraction of atoms from nanostructured transmission grating was seen for the first time by Keith et al. in 1988 [33] and shortly after, in 1991, Carnal et al. [34] demonstrated for the first time the possibility to focus neutral atoms with a zone plate element from 210 μm to 18 μm.

In 1999 R. Doak et al. [35] improved the spot size, reaching less than 2 μm thanks to the use of a so called microskimmer, which improved the spatial resolution and He intensity.

The He beam focused via a zone plate was subsequently used by B. Holst at al. in 2008 [2] as probe in a neutral microscope, obtaining the first microscopy image in transmission mode recorded with neutral helium atoms. The resolution was around 1.5 μm. On the other hand, the first image in reflection mode was recorded by P. Witham and E. Sanchez in 2011 [36] with a neutral microscope that used as focusing element an optic analogous to the pin hole. Also in this case the resolution achieved was of about 1.5 μm. After one year both groups improved their techniques: Holst at al. [3] achieved submicron focusing with zone plate and P. Witham and E. Sanchez obtained images with a spatial resolution of 350 nm [37]. An alternative method to the zone plate was given from S. Eder et al. [4] using a photon-sieve structure as optical element reaching a spot size of less than 4 μm.

W. Allison and coworkers [14] presented in 2012 a compact model of scanning He microscope (SHeM), and in 2016 they recorded the first contrast image by using a range of mechanisms that included chemical contrast from metal-semiconductor interface [38].

Even though these results are really promising and demonstrate the power of this new technique, an alternative focusing element has to be considered if nanometer resolution has to be achieved. Fresnel zone plates suffer chromatic aberration, which sets an intrinsic limit to the spatial resolution, in addition to the low intensity of the focused beam.

In principle, these disadvantages can be overcome by the use of atomic mirror as focusing element of the helium beam. So far, few experiments that implement this optical element to focus neutral helium atoms have been reported. The possibility to focus a neutral beam using a bent crystal mirror was presented by R. Doak at al. in 1992 [13], reducing the FWHM of the reflected beam from 0.4° to 0.12°. In 1997 B. Holst achieved the first two-dimensional focusing by reflection from electrostatically bent H-passivated 50-μm Si(111) crystal [5]. The spot size of the focused beam was about (250±50) μm. Improvements using this kind of reflective mirror allowed the achievement of circular spots of about 26±8 μm ×31±4μm [6].

1.2.3 NEMI scheme

The Neutral Helium Scattering Microscope, Nemi for short, is a new neutral matter-wave microscope that employs ground-state helium-4 as probe. This prototype was built at the UiB (detailed in the Ph.D thesis of S. Eder [39]) and improved during NEMI project.

The current set-up uses as optical element a Fresnel zone plate. However, atomic mirror can be placed instead of this zone plate, in order to obtain the maximum intensity and the smallest focus. A schematic design of the new microscope is shown in Fig. 1.7. The neutral He beam expands adiabatically across the nozzle and it is extracted a few millimeters away from the nozzle by a conical skimmer. With the right gas pressure, temperature, nozzle diameter and nozzle-skimmer distance the so called free-jet expansion is ensured, as well as the monochromaticity of the He beam. After passing through the skimmer the beam is collimated by an aperture, until it reaches the curved atomic mirror, where the beam is focused and directed onto the surface sample to analyze. Finally the diffracted beam, once ionized, is extracted to a channeltron counter via a mass-spectrometer.

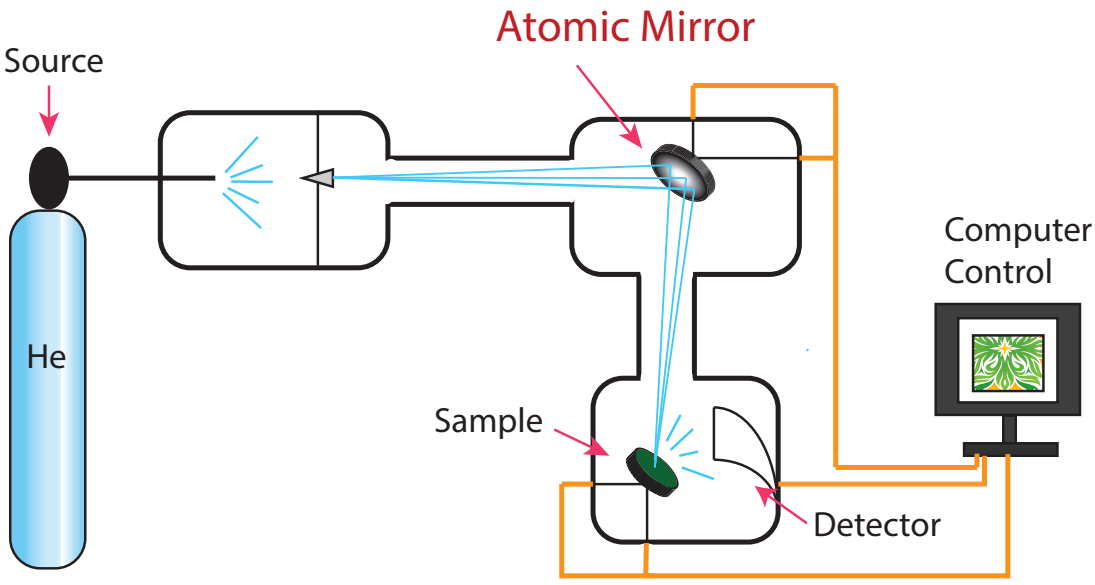

Figure 1.7: Sketch design of scanning neutral microscopy using an atomic mirror as focusing element.

1.3 Graphene

Since it was discovered in 2004 by Geim, Novoselov and co-workers [40], graphene has earned a lot of interest across academia and industry, due to its unique physical and chemical properties [41].

1.3.1 Structure and phonon dispersion of graphene

Graphene is a single atomic layer (2D materials) of sp^2 hybridized carbon arranged in a honeycomb network. In the ground state carbon presents two electrons in the 2s shell and two in the 2p shell.

Thanks to the hybridization sp^2 (2s, $2p_x$, $2p_y$ orbitals), the formation of a strong σ covalent bond between the three neighbouring carbon atoms is possible. The C-C distance is 1.42 Å. This bound, besides making the graphene the strongest material known, also makes it very stable under ambient conditions [43–45].

The remaining unhybridised $2p_z$ orbital results perpendicular and mirror symmetric to the graphene plane and leads to the formation of weaker π bonds [46], responsible for the semi-metallic band structure. These bands confer the graphene its unique electronic

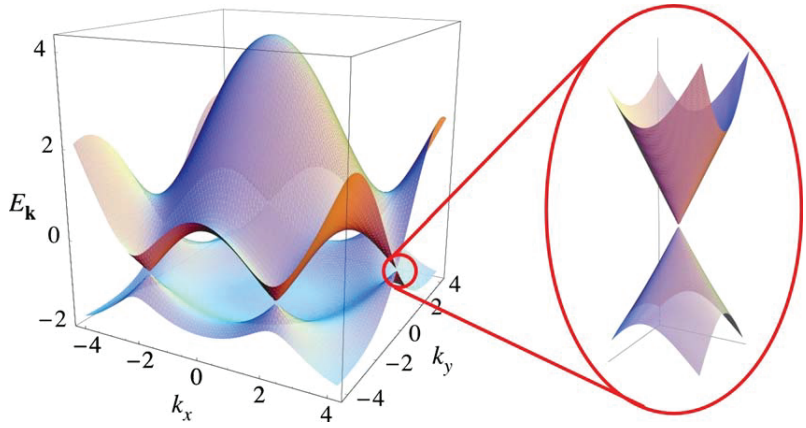

Figure 1.8: Three dimensional plot of electronic band structure for the uppermost occupied and the lowermost empty bands, π and π^* , respectively. Adapted from [42].

properties, thanks to the half-filled band that allow free-moving electrons. As shown in Fig. 1.8, the occupied valence band π and the empty conduction band π^* touch each other at K and K' points of the Brillouin zone (called Dirac point). This means that graphene is semiconductor material with zero energy gap [47, 48].

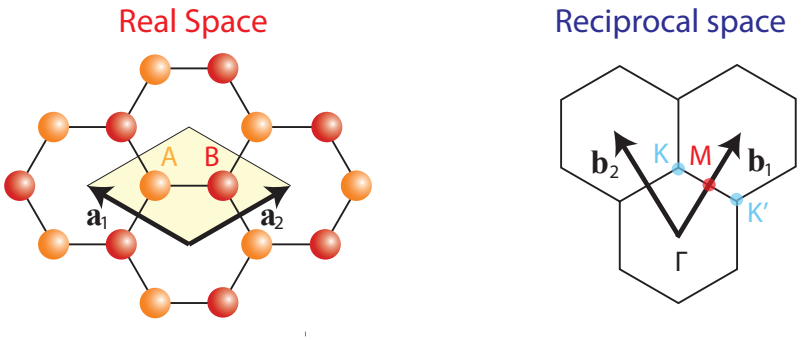

Figure 1.9: Honeycomb lattice of graphene in the real space (left side). Reciprocal space (right side).

In Fig. 1.9 are shown both the lattice in the real and reciprocal space. The primitive

vector can be defined as follows:

$$\mathbf{a}_1 = \frac{a}{2}(\sqrt{3},1); \qquad \mathbf{a}_2 = \frac{a}{2}(-\sqrt{3},1) \tag{1.39}$$

where a is the graphene lattice constant and have a value of $|\mathbf{a}_1| = |\mathbf{a}_1| = a = 2.46$ Å. These vector span the Bravais lattice by the position vector $\mathbf{R}$:

$$\mathbf{R} = n_1\mathbf{a}_1 + n_s\mathbf{a}_2 \tag{1.40}$$

Then the reciprocal lattice vector can be generated by the two primitive vectors, obtaining the following relations:

$$\mathbf{b}_1 = \frac{2\pi}{a}(\frac{1}{\sqrt{3}},1); \qquad \mathbf{b}_2 = \frac{2\pi}{a}(-\frac{1}{\sqrt{3}},1) \tag{1.41}$$

and they have to satisfy

$$\mathbf{a}_{ij} = 2\pi\delta_{ij} \qquad (i,j = 1,2); \tag{1.42}$$

where δ_{ij} is the Kronecker delta.

In the first Brillouin zone the three points, K', K and M, mentioned before, are marked (right side of Fig. 1.9).

Since graphene primitive cell has N = 2 carbon atoms, six phonon branches exist: three acoustic branches (A) and 3N-3 = 3 optic (O) branches. Depending on their polarization, the phonon branches are separated between out-of-plane (called flexural modes, Z), if the vibration is perpendicular to the graphene plane, and in-plane mode, where the vibration is parallel. Both acoustic and optic branches have an out-of-plane mode and two in-plane modes. In-plane modes are classified in longitudinal (L) and transversal (T) modes, also depending on their vibration direction with respect to the carbon bonds: parallel for L and perpendicular for T. [50–52].

Figure 1.10 shows the theoretical phonon dispersion curve for graphene monolayer using DFT calculation [49]. Along the two high symmetry directions $\overline{\Gamma M}$ $\overline{\Gamma K}$ all the phonon modes LO, TO, ZO, LA, TA, and ZA are allowed. The two main experimental techniques usually used to measure these dispersion curves are high-resolution electron loss spectroscopy (HREELS) and inelastic helium atom scattering (HAS). As we will see in Chapter 4, from the studies of phonon dispersion curves, the strength of the Gr-substrate interaction can be deduced. In fact, the ZA mode, also called *flexural mode*, contains informations about the bending rigidity and the Gr-substrate coupling strength.

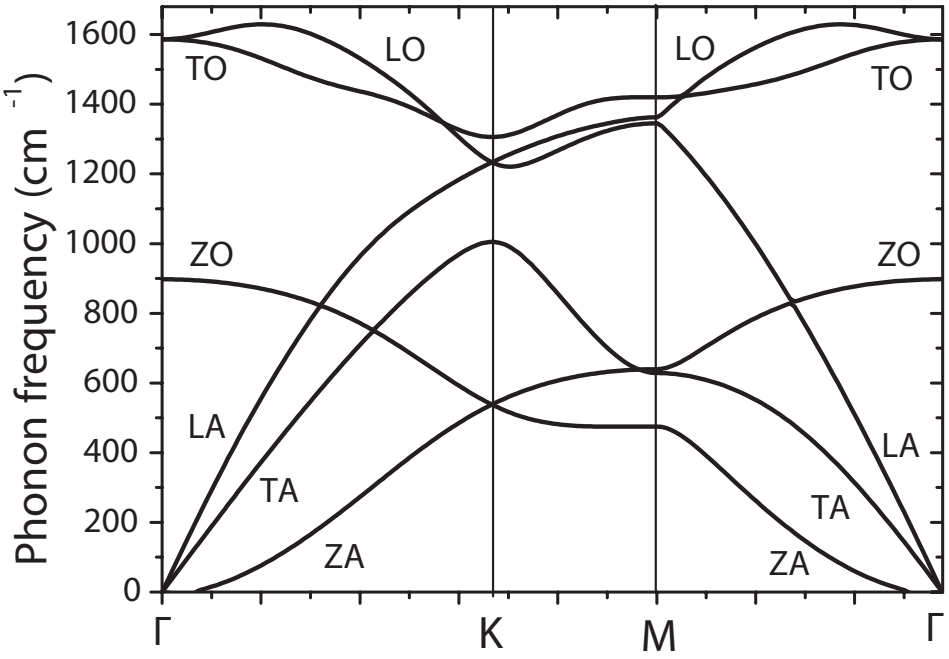

Figure 1.10: Phonon dispersion calculation of monolayer graphene adapted by [49]

In order to analyze Gr, Raman spectroscopy is the main candidate, since it is traditionally one of the most widely used spectroscopy technique in the analysis and characterization of carbon materials, distinguishing its crystalline, nanocrystalline and amorphous phase [53–55]. The spectra of these materials present common characteristics in the range of 800 cm^{-1} and 2000 cm^{-1}: the G and D peaks, which appears at around 1560 and 1360, respectively [55]. In the case of Gr also the second order of the D peak, labelled 2D peak, is detected at ~ 2700 cm^{-1}, using a single laser line of 2.41 eV (see Fig. 1.11).

The G band arises from the doubly degenerate (TO and LO) phonon mode at the Brillouin zone center $\overline{\Gamma}$ and it is the only band coming from a normal first order Raman scattering process in Gr. In fact, the D and 2D-bands come out from a second-order process near the $\overline{K}$ point, that involves one TO phonon and one defect for the D-band or two TO phonons for the 2D band. G and 2D peaks are always recorded, while D peak needs defects to be active.

Due to its sensitivity of Gr defects, Raman spectroscopy is a standard tool to study

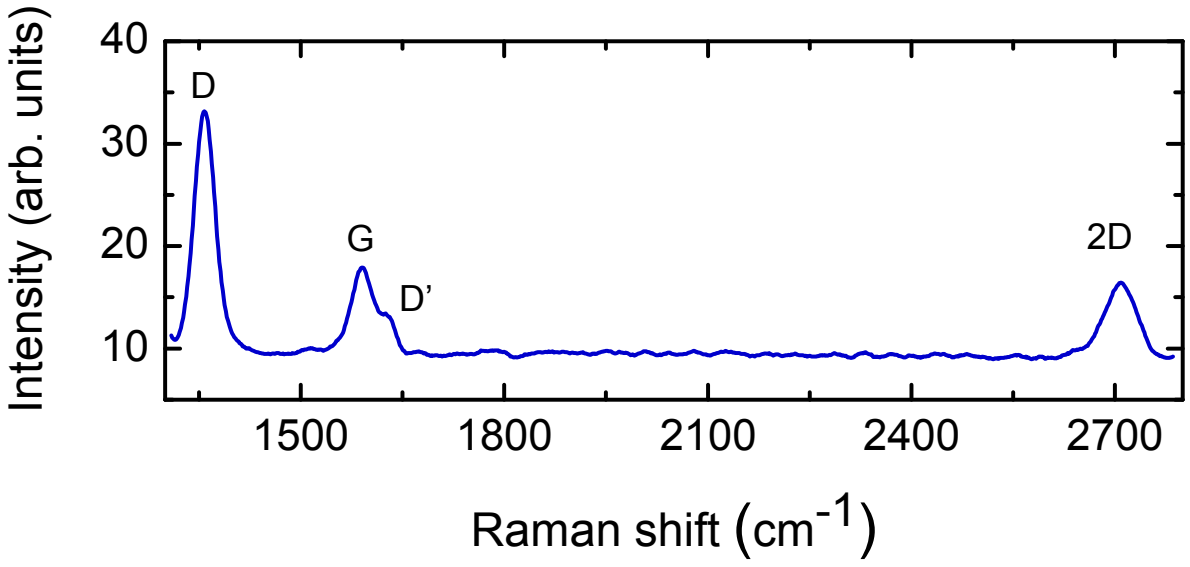

Figure 1.11: Raman spectra recorded for Gr on sapphire. The characteristic peaks of Gr D, G, D' and 2D are indicated.

the quality of Gr layers. Defects in a 2D lattice can be zero dimensional (0D) or one dimensional (1D), and they are usually quantified by measuring the distance, L_D, between 0D pointlike defects or by measuring the size grain, L_a in the case of 1D defects. In Chapter 4 the equation used to evaluate each value would be explained with more detail. Both parameters strictly depend on the D to G peak intensity ratio, usually denoted as I_D/I_G. In addition, the 2D to G peak intensity ratio, I_{2D}/I_G, is related to the quality of the Gr domains, that is, the regularity of the carbon network. The value of this ratio is an indicator of the number of layer too. For multilayer Gr the intensity ratio I_{2D}/I_G is around 0.6, lower than the single layer case in which the ratio is almost 2.

Furthermore, the FWHM of the peaks provides information about the structural disorder. Specially, the change in shape and in width of the 2D peak can be used to evaluate the number of Gr layers, along with its frequency shift. A typical 2D band at room temperature presents a single Lorentzian peak with a FWHM of 24 cm^{-1} [50, 56]. By contrast, a convolution of few Lorentzian peaks is necessary to fit the 2D peak when two or more layer are presented.

However, in systems with a strong Gr-metal interaction, such as Gr/Ru(0001) or Gr/Ni(111) the Raman signal is suppressed. In this cases, phonon dispersion curve are fundamental to study the Gr-metal dynamics.

1.3.2 Graphene on transition metals

Graphene has been grown onto a large number of transition metals, such as Ru(0001) [57–61], Ni(111) [11, 62, 63] Cu(111) [64–67], Ir(111)[68–70], Pt(111)[71–74], Pd(111)[75], Rh(111) [71] and Co(0001)[76]. Different properties arise from all this systems depending on the interaction between Gr and the metal substrate.

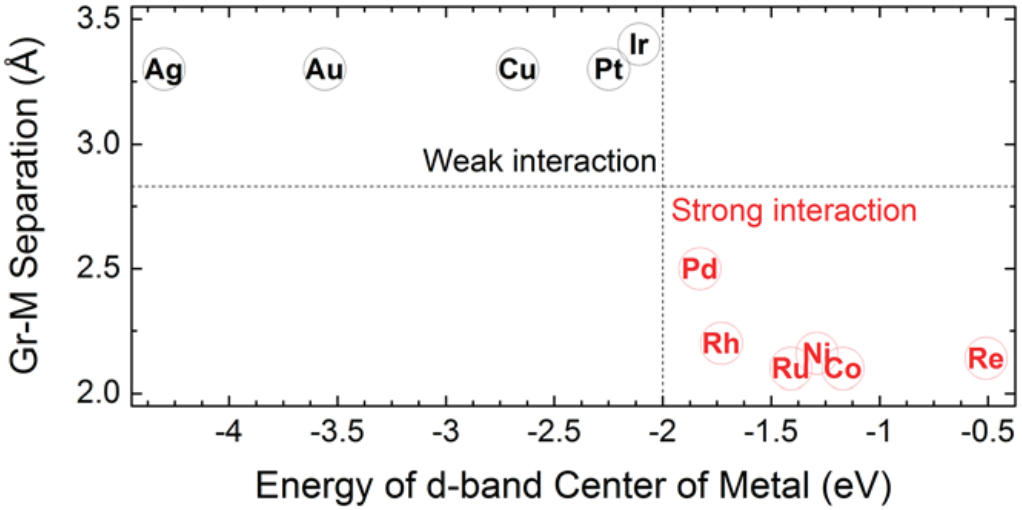

Figure 1.12: Gr-metal separation as function of the d-band center of the substrate metal. Adapted from [77]

.

The different structural properties between Gr and metal interfaces can best be treated under two headings: lattice mismatch and strength of Gr-metal interaction. Lattice mismatch arises from the superposition of two lattice with different periodicities. Thus, different behaviors of the Gr layer appear depending on the lattice constants of the metal surface. When Gr is grown on Ni(111) or Co(0001) a mismatch less than 2% is found between Gr and substrate lattice constants. The Gr layer slightly stretching or quenching the C-C bonds forms a (1×1) structures aligned with the (1×1) substrate unit cell. However, if Gr is grown on Ru(0001), Rh(111), Ir(111) or Pt(111), the mismatch with underling metal is about 10%. In this case, the superimposition of the two lattices generates a new periodicity called moiré pattern. This superstructure can arise also for relative rotation of the two lattices. In the case of Ru, Rh and Ir, for example, it is

possible to reach the optimum conditions to growth one domain Gr, so that this is aligned with the principal symmetry direction of the underlying metal. In contrast, for metals like Cu and Pt, different rotational domains are detected [77–79].

Regarding the interaction between Gr and the metallic substrate, it possible to classify it into weak and strong interactions. If Gr is grown onto Cu, Pt or Ir, the iteration with the metal substrate is weak and the Gr preserves the main properties of free-standing Gr. As it will be shown in Chapter 4, also a weak interaction is recorded from Gr on sapphire substrate. As general rule for weak interaction, the separation between Gr and metal is about 3.3 Å, very closed to the value obtained for the inter-planar separation in HOPG, 3.35 Å. Nevertheless, when the Gr is grown on Ru, Pd, Rh, Ni or Co a strong interaction is observed and a smaller value of 2.2 Å is found for the separation between Gr and substrate. A visual image of this difference in Gr-metal distance and interactions is represented in Fig. 1.12, where Gr-metal separation is shown as function of the d-band center to Fermy energy of a given metal [77, 80].

CHAPTER 2

EXPERIMENTAL DETAILS

This chapter deals with the description of sample preparation and the experimental techniques used to investigate and characterize the surfaces described in this thesis. In the first section the sputtering deposition technique employed to grow thin films and the experimental set up are described. The second part describes in details the two HAS apparatus (TEAMS and ERASMO) used in this work to study the structural and dynamical surface properties. Likewise, a brief description of AFM and Raman set up used to characterized graphene on sapphire system is done.

2.1 Sample preparation: sputtering deposition

Thin films have been deposited by means of DC magnetron sputtering, which is a special branch of the various PVD (Physical Vapour Deposition) processes. The main advantage with respect to simple DC sputtering is the lower voltage used, thanks to the higher efficiency of the initial ionization. In addition, the deposition rate is increased and lower operating pressure is needed in order to generate the plasma.

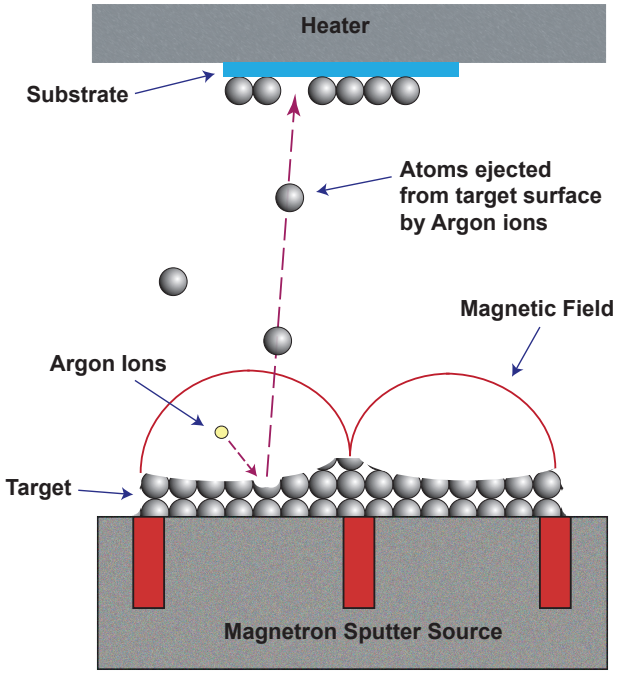

Figure 2.1: Sputtering process scheme. Atoms form the target are knocked out by Argon ions and deposit on the substrate.

2.1.1 Sputtering phenomena

Sputtering is a process in which a removal of surface atoms of a determined target is provoked through the impact of incident ions (usually Ar^+) confined in a plasma (Fig. 2.1). This atoms emission can be used to grow thin films on a desired substrate. Ar gas is ionized by applying an electric potential difference between the target (cathode) and the substrate (anode) to be coated. The atoms are ejected from the target by the mechanical action of the impinging ions; after that they are accelerated to the anode, where the substrate is placed, thanks to the presence of the electrostatic field. The sputtering is, then, a consequence of momentum transfer from Ar^+ ions to the target atoms through

a collision cascade in the region closest to the target surface. In order to be able to execute proper sputtering process, the incident ion mass must be large enough so that the momentum transfer to the targets atom can be efficient. Likewise, the use of a noble gas is essential unless reactive sputtering is desired. During the collision with the target, secondary electrons are also emitted and the ionization of other atoms gas is achieved.

2.1.2 Magnetron guns

By using magnets behind the cathode, a magnetic field is added to the system. This configuration constrain secondary electrons to move close to the target, thus facilitating higher ionization. Given that more ions means more ejected atoms from the target, this helps to increase the efficiency of the sputtering process.

The geometric configuration of the magnetron sputtering source used in the experiments performed in this thesis has two circular and concentric permanent magnets, that force the electrons to follow a helical path. The cathode is surrounded by a shield that works as anode in order to avoid the lateral sputtering. The substrate to be coated is fixed approximately 15 cm away from the target.

2.1.3 Experimental apparatus

In this thesis, the metal thin film deposition was performed in the experimental sputtering set-up shown in Fig. 2.2 belonging to Sputtering Lab at the Instituto de Ciencia de Materiales de Madrid (ICMM). The set-up includes a PLS 500 Pfeiffer high vacuum system. The base pressure of $\sim 10^{-7}$ mbar is ensured by a TMH 520 turbomolecular pump. Between the vacuum chamber and the turbomolecular pump a throttle valve is placed to reduce the pumping rate during sputtering. The main component of the set-up is a Thin Film Consulting Gmbh planar magnetron, which can be either used in DC or RF for conductive or high resistive materials, respectively. Circular Ru targets (2" diameter) are clamped to the water-cooled electrodes. Argon (99.999%) was used as the sputter gas and introduced into the chamber by means of UFC 1200A mass flow controllers (MFCs) from UNIT Instruments [81, 82].

Thanks to a pre-chamber, the sample-holder can be introduced in the sputtering chamber through a load-lock without breaking the main vacuum chamber. A vacuum of $\sim 10^{-3}$ mbar is ensured for this secondary chamber by a mechanical pump. This quick loading of the sample is possible only when the deposition takes place at room temperature. A 1.6" substrate heater can be mounted into the main chamber, allowing

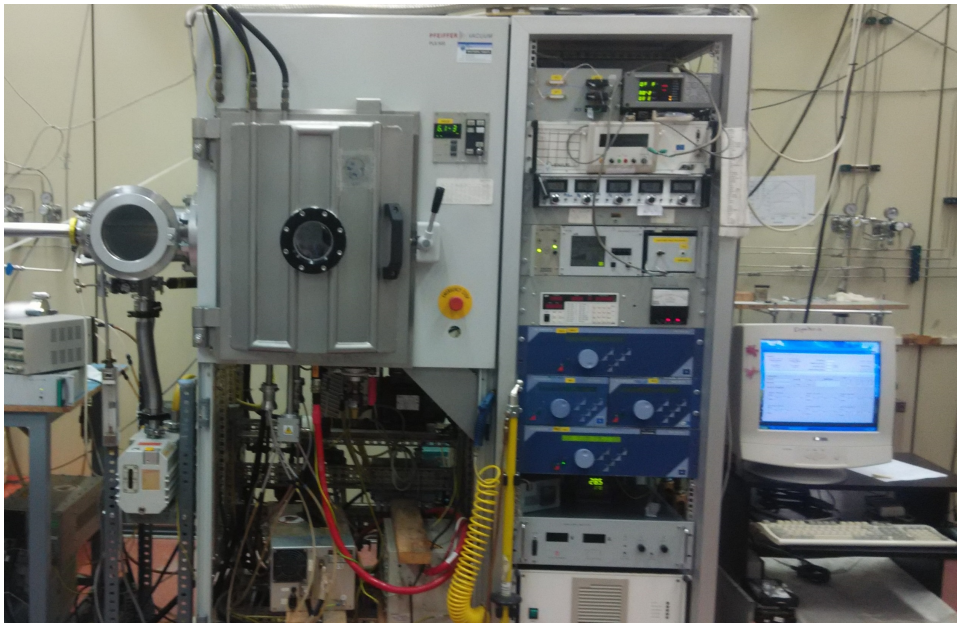

Figure 2.2: Picture of the Sputtering Apparatus at the Instituto de Ciencia de Materiales de Madrid (ICMM).

the heating of the substrate from room temperature up to 800°C, as shown in Fig. 2.3a. An example of Ar plasma generated in a sputtering process from a Ru circular target is shown in Fig. 2.3b.

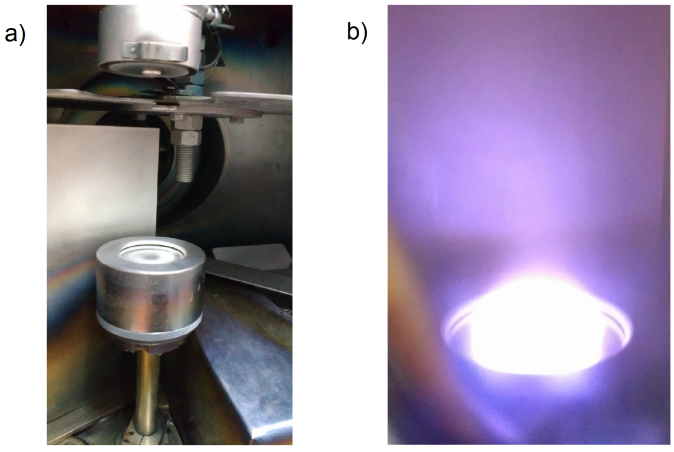

Figure 2.3: (a) Picture of the inside of the vacuum chamber, where the magnetron with Ru target and the substrate heater, with attached the substrate, are placed. (b) Plasma from a circular Ru target under Ar ion bombardment.

2.2 Sample analysis

2.2.1 HAS set-up: TEAMS

Diffraction experiments were performed on the TEAMS (Thermal Energy Atomic and Molecular Scattering) apparatus (Fig. 2.4) belonging to LASUAM (Laboratorio de Superficies de la Universidad Autónoma de Madrid). The system was donated by the Freie Universitat Berlin and moved to LASUAM by D. Farías in 2004. It was assembled and put into operation by P. Nieto during his PhD work [83].

As presented in Fig. 2.5 it is possible to divide the set-up in two main parts: (1) the source chamber where the incident He beam is collimated and monochromatized, in which we can find nozzle and chopper; and (2) the main chamber, where the scattering process takes place, in which we can find manipulator, sample and detector.

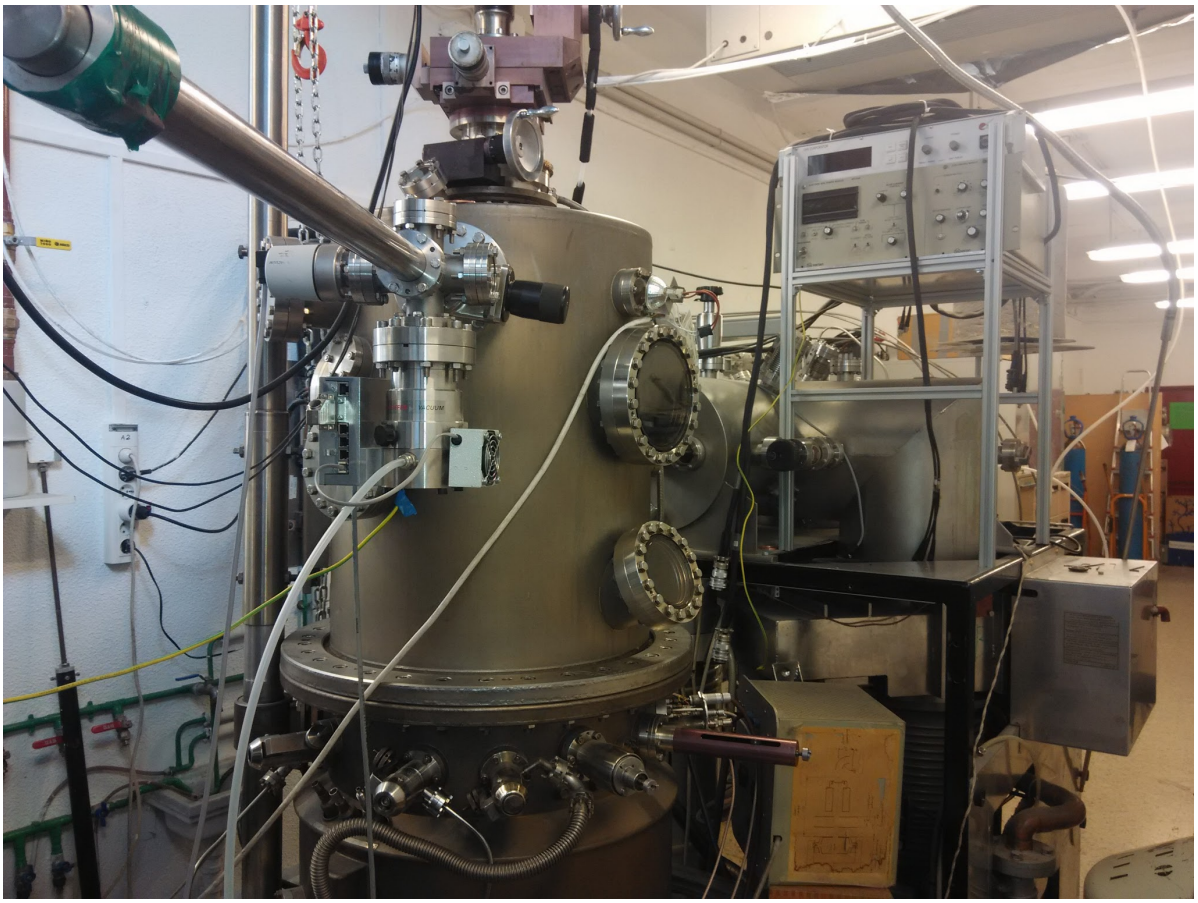

Figure 2.4: Picture of the Helium Atom scattering apparatus (TEAMS).

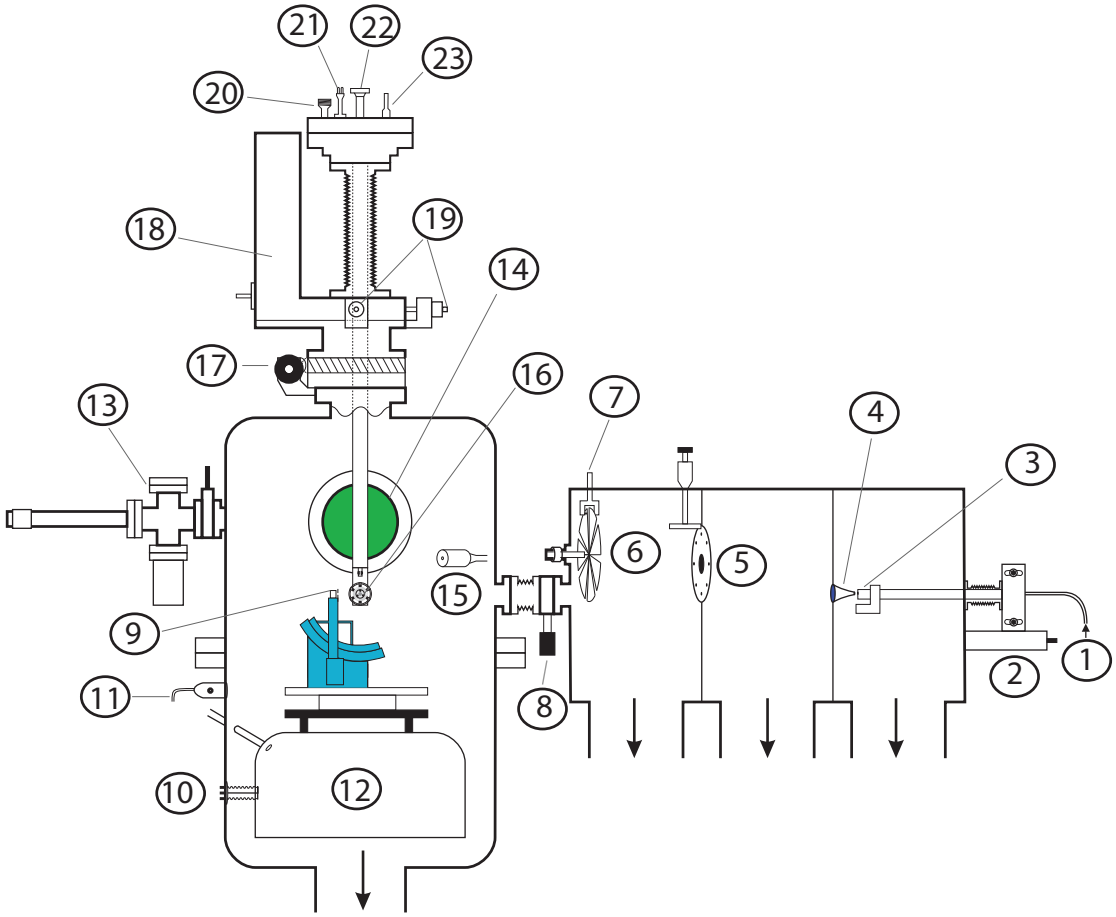

Figure 2.5: Schematic of the Helium atom scattering apparatus (TEAMS). Recreated from [83].

The Source Chamber

The source chamber is a three-staged differentially pumped vacuum system, i.e it consists of three connected vacuum chambers operating at different pressures. The first two chambers are connected to 4600 l/s liquid nitrogen baffled oil diffusion pumps while the third is connected to a 350 l/s turbomolecular pump. The beam is generated by a free expansion of helium gas passing through a 10 μm aperture (nozzle), located in the first part of the system. High pumping rate is mandatory in this first stage in order to avoid the high background pressure produced by the helium expansion and to ensure a pressure of $\sim 10^{-3}$ mbar. At this stage the beam energy can be changed by regulating the nozzle temperature. Low nozzle temperatures can be achieved by the use of two copper

Table 2.1: Legend to Fig. 2.5.

Beam chamber	
1	High pressure He inlet
2	XYZ Adjustment of the nozzle source
3	Nozzle
4	Skimmer
5	Rotary disk with diaphragm of different sizes
6	Chopper
7	LED-Photodiode for reference signal from Chopper
8	Valve
Main chamber	
9	Detector Goniometer
10	Titanium sublimation pump
11	Dosage valves
12	Liquid Nitrogen trap
13	Load-Lock chamber
14	LEED
15	Ion gun
16	Sampleholder
17	Manipulator's rotary feedthrough
18	Z movement motor
19	X-Y adjustment of the manipulator
20	Multipin feedthrough
21	Thermocouple feedthrough
22	Cryostat inlet
23	Cryostat outlet

blocks that can be cooled down to 100 K with liquid nitrogen; high temperatures, up to 700 K, can be achieved by resistibly heating the nozzle. After passing through the skimmer, the beam enters in the second stage chamber, with a pressure of $\sim 10^{-6}$ mbar, and it is collimated by a diaphragm whose diameter can be varied with a rotary disk with apertures of different diameters (400-3000 μm). In the last stage, with a pressure of $\sim 10^{-8}$ mbar, the beam is chopped by a rotary blade moved through a magnetically coupled feedthrough, while a LED-Photodiode couple records beam phase and frequency, hence allowing phase sensitive detection whit a lock-in amplifier.

Table 2.2: Dimensions of the scattering apparatus TEAMS

Nozzle aperture diameter (d)	10 μm
Skimmer aperture diameter (δ_s)	0.5 mm
Diaphragms diameters (δ_a)	400, 750, 1200, 2000, 3000 μm
Detector aperture (δ_d)	1 mm
Nozzle-Skimmer distance	~10 mm
Skimmer-Diaphragms distance (D_a)	383 mm
Skimmer-Sample distance (D_s)	1173 mm
Sample-Detector distance (D_d)	55 mm

The Main Chamber

The sample is located in the main chamber, where the scattering process takes place. The base pressure is kept at 8 $\times 10^{-10}$ mbar, thanks to the turbomolecular pump (500 l/s). A lower pressure can be reached filling a liquid nitrogen tramp combined with the use of a supplementary titanium sublimation pump. The manipulator has three translational (X, Y and Z) and two rotational (θ_i, the angle of incidence, and ϕ, the azimuthal angle) degrees of freedom. Therefore, the sample can be placed in the position for maximum intensity diffraction, as well as any other relevant positions desired. The sample can be mounted on the manipulator through a load-lock, thus avoiding the need to bake the chamber each time after mounting a new sample. The manipulator and the sample-holder are cooled down at 80 K by using liquid nitrogen. The sample can also be heated up by electronic bombardment, which enables higher temperatures than a resistive heater. The sample temperature was measured with a type-C thermocouple spot-welded to the sample holder.

The scattered He atoms are detected by the quadrupole mass spectrometer (Mod. Balzers QMG 511) mounted on a two-axis goniometer. This configuration allows the measurement of the intensity of the incident and of the reflected beam for a spherical sector of 200° in the incident plane and 15° out-of-plane. In this way absolute diffraction intensities can be determined. Two stepper motors, with a minimum step of 0.02° for in-plane and out-of-plane rotation enables the detector movement. The minimum step A circular slit of 1.0 mm in diameter and located 55 mm away from the sample is the entry for the quadrupole ionization chamber. The angle subtended by the aperture is 1.04°.

Angular Broadening

In order to understand the shape and width of the specular peaks and their correlations with the quality of the samples' surface, several factor must be taken into account. On an ideal experiment in which the particles are represented by a plane wave scattered on a perfect crystal surface, the momentum of the particle is completely determined and, consequently, the angular width of the peaks will be zero. However, due to the finite distance between source and detector, it is more appropriate to represent the particle as a spherical wave packet, which leads to a not perfectly determined momentum and broadening of the peaks. The broadening of the angular distributions of an atomic beam rises from three principal contributions: instrumental limitations, due to the finite aperture diameters of both source and detector; the non-ideal beam monochromaticity, that causes the energy spread; and the imperfection of the crystals surfaces, as random terrace disposition and finite domain size. To investigate the quality of the surface and to estimate the average domain size it is important to know the total angular broadening intrinsic to the instrument. The total angular broadening $\Delta\theta_f$ will be:

$$\Delta\theta_f \simeq \sqrt{(\Delta_\theta\theta_f)^2 + (\Delta_{E_i}\theta_f)^2} \tag{2.1}$$

where $\Delta_\theta\theta_f$ is the geometrical contribution, due to the finite dimensionality of the beam and detector and $\Delta_{E_i}\theta_f$ is the contribution of the energy spread [7].

The geometrical contribution $\Delta_\theta\theta_f$ is composed of four terms which take into account the contribution of the source dimension, of the aperture, of the spot size and of the detector opening, respectively:

$$(\Delta_\theta\theta_f)^2 \simeq \left(\frac{\cos\theta_i}{\cos\theta_f}\frac{\delta_s}{D_s}\right)^2 + \left(\frac{\cos\theta_i}{\cos\theta_f}\frac{\delta_a}{D_a}\right)^2 + \left(\frac{\cos\theta_i}{\cos\theta_f}\frac{D_s}{D_d}\frac{\delta_a}{D_a}\right)^2 + \left(\frac{\delta_d}{D_d}\right)^2 \tag{2.2}$$

By using the third term of this formula it is possible to estimate the spot size at the sample for the different diaphragm apertures of the TEAMS apparatus, as it is shown in Tab. 2.3.

Furthermore, the contribution due to the energy spread of the source $\Delta_{E_i}\theta_f$ can be expressed as:

$$\Delta_{E_i}\theta_f = \frac{|\sin\theta_i - \sin\theta_f|\sqrt{\frac{(\Delta E_i)^2}{E_i^2}}}{\cos\theta_f} \tag{2.3}$$

Table 2.3: The estimated spot size at the sample

Diaphragms diameter (mm)	Spot size (mm)
0.4	1.2
0.75	2.3
1.2	3.7
2.0	6.1
3.0	9.2

where $\overline{(\Delta E_i)}$ is the mean-square energy spread in the beam [7]. For the specular peak ($\theta_i = \theta_f$) this term is zero, so it does not affect the broadness of the specular peaks. Thus using Eq. 2.2 it is possible to give an estimation of the width of the direct beam and of the specular peak due to geometrical factors. In Fig. 2.6 it is shown how the $\Delta_\theta \theta_f$ changes when the diaphragm aperture varies and its comparison with the experimental width of the direct beam.

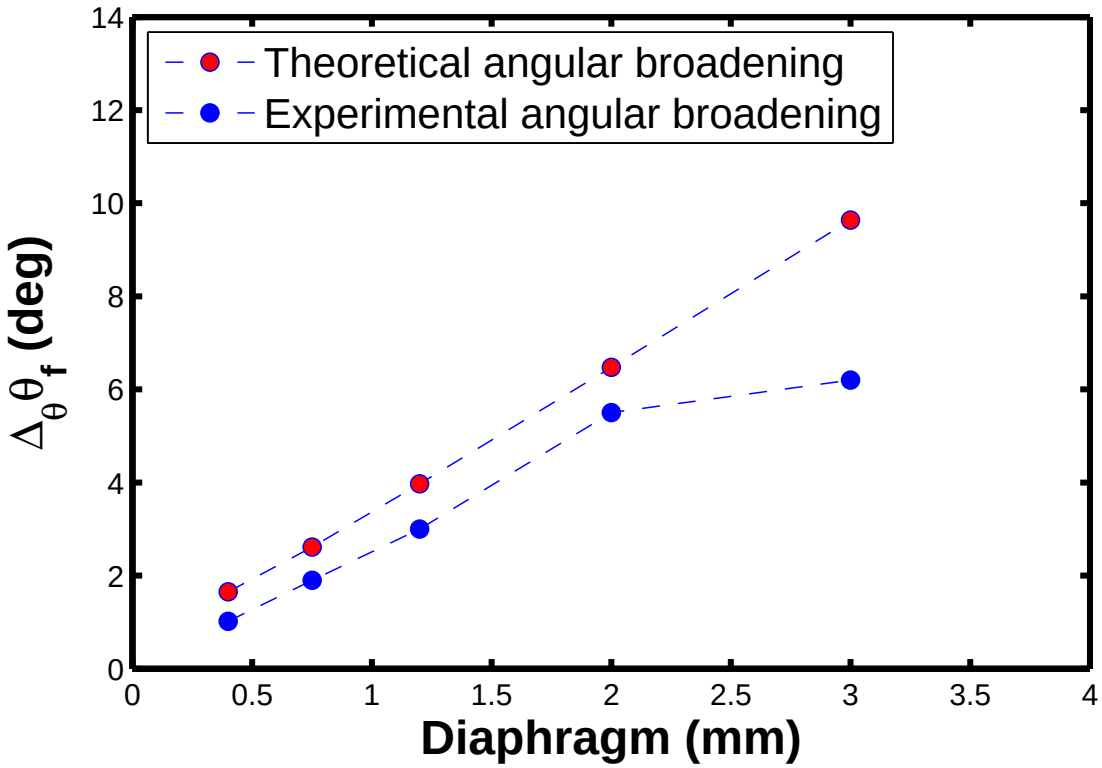

Figure 2.6: Theoretical angular broadening versus experimental angular broadening for different apertures of the diaphragm.

Once an estimation of the angular broadening is given, it is possible to evaluate the energy spread by taking Eqs. 2.1 and 2.3, and replacing $\Delta\theta_f$ with the experimental FWHM of the diffraction peak and estimating $\Delta_\theta\theta_f$ from Eq.2.2. The resulting energy spread, $\frac{\overline{(\Delta E_i)}}{E_i}$ ranges from about 5% for E_i = 64 meV to 14% for E_i = 150 meV.

Transfer width

The purely instrumental broadening of diffraction peaks can be formally correlated with the lateral dimension length, known as *transfer width* w. This parameter represents the minimum lateral dimension over which the surface must be perfectly crystalline in order to have diffraction peaks whose widths are limited only by the instrumental resolution. An estimation of this length can be obtained by taking into account the angular spread of a beam emitted at an angle θ_f by a great number of coherent sources arranged along an interval w, that lead to the follow expression:

$$w \simeq \frac{\lambda_i}{\Delta\theta_f \cos\theta_f} \tag{2.4}$$

where λ_i is the de Broglie wavelength of the incident beam [7].

Once the instrumental contribution has been isolated, it is possible to deduce the angular broadening due to the surface. In fact, if the surface is not well ordered over dimensions smaller than the transfer width, an additional broadening $\Delta\theta_{incoh}$ due to the incoherent scattering produced by finite domains size, has to be taken into account. In such cases the total broadening is given by:

$$\Delta\theta^2_{exp} = \Delta\theta^2_f + \Delta\theta^2_{incoh} \tag{2.5}$$

Lapujoulade *et al* [84] showed that the angular broadening measured for the specular beam can be approximated as

$$\Delta\theta_{incoh} = \frac{5.564}{l_c |k_i| \cos\theta_i} \tag{2.6}$$

where k_i is the wavevector of the incoming He beam and l_c is the *coherence length*, that can be associated with a length at the surface in which the incident beam is scattered coherently. The scattering incoherence arises from the finite size of this coherent scattering regions. The smaller these zones are, the more the peak angular broadening

becomes. Therefore from Eqs. 2.5 and 2.6 it is possible to deduce an estimation (lower limit) for the average domain size:

$$l_c = \frac{5.564}{\left(\Delta\theta^2_{exp} - \Delta\theta^2_f\right)|k_i|\cos\theta_i} \tag{2.7}$$

2.2.2 HAS set-up: ERASMO

Part of the experiments presented in this work were carried out with the experimental Helium Atom Scattering and Time of Flight (HAS-TOF) ERASMO UHV apparatus, shown schematically in Fig. 2.7. A more detailed description of this set-up can be found in the PhD dissertations of D. Barredo and A. Al Taleb [85, 86].

The set-up consists of three main independents chambers, separated each other by UHV valves:

- nozzle and chopper chamber;
- target chamber;
- detector chamber.

In a similar manner to the foregoing for TEAMS apparatus, the atomic beam is generated by the adiabatic expansion of a high pressure gas from a nozzle situated in the first chamber, called beam source. In this stage the working regime pressure ($\sim 10^{-4}$ mbar) is ensured by an oil diffusion pump with flow capacity of 8000 l/s combined with a roots pump. After passing through the skimmer, the beam is chopped in other chamber which has a typical base pressure of $\sim 10^{-6}$ mbar, obtained by a 3000 l/s oil diffusion pump. The rotating disk chopper is essential for the time of flight experiment in case of inelastic measurements. Further collimation of the beam is achieved by a diaphragm whose diameter can be varied (0.5-2 mm). Between the chopper chamber and the main one, an additional pumping stage is employed in order to preserve the pressure gradient between the two chambers.

In the main chamber, where the scattering takes place, a base pressure of $\sim 10^{-11}$ mbar is reached thanks to a turbomolecular pump (520 l/s) and a rotatory pump. The sample is mounted in a manipulator with six degrees of freedom (three translational and three rotational) that permits to find the best diffraction condition point. In order to record angular distributions of the scattered beam, the manipulator is rotated around the normal to the plane defined by the incident and the outgoing beams, by means of a

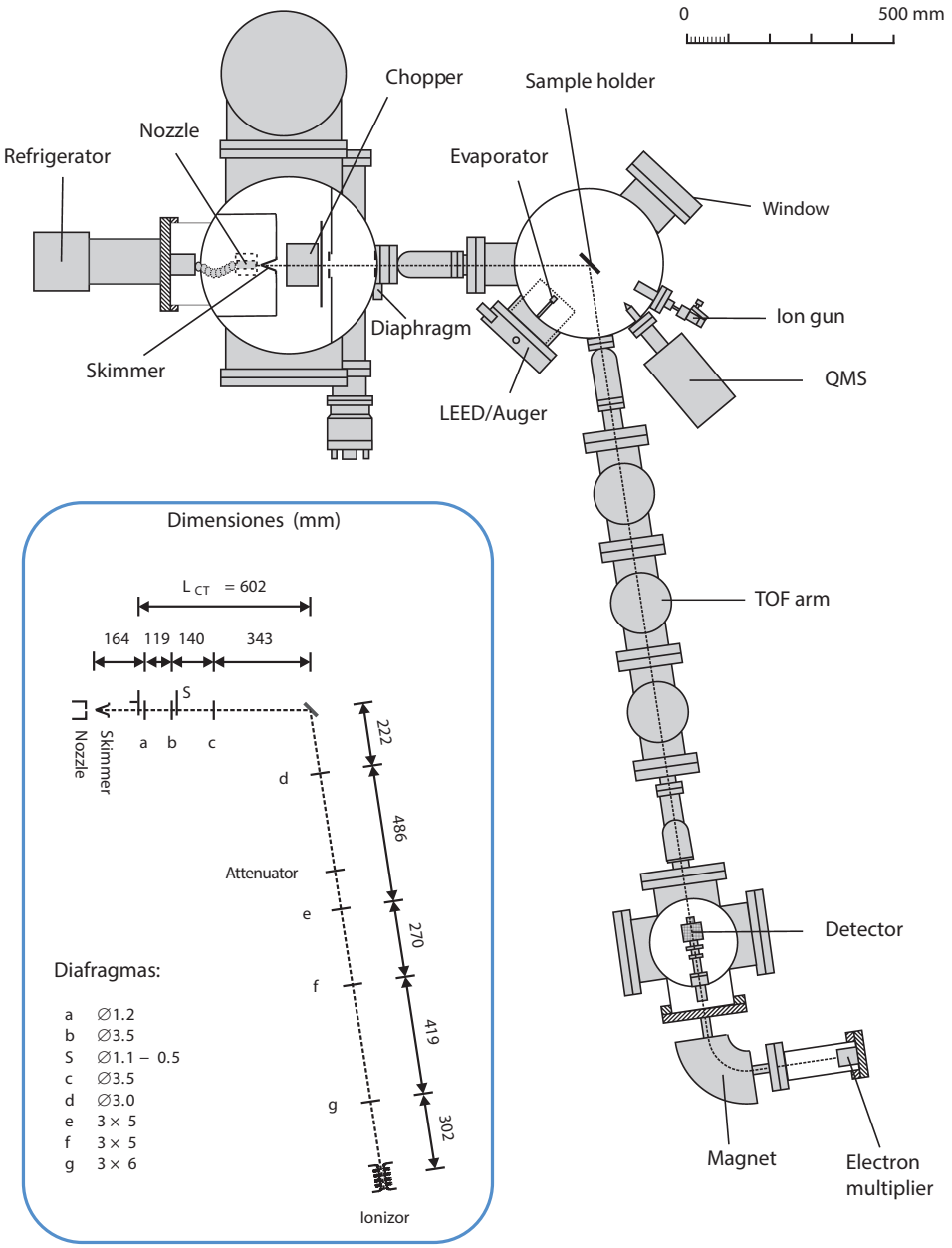

Figure 2.7: Schematic of ERASMO apparatus. Adapted from the Ref. [85].

stepper motor controlled by a computer. The minimum step of the motor is of 0.045°. The sample can be cooled down to 90 K using liquid nitrogen, and heated up to 1800 K by electron bombardment. Moreover, a LEED system, an ion gun and three different dosage valves were employed to clean and characterize the sample. The last stage of the system

is composed by the time of flight arm, known as *drift tube* and the detector chamber. The drift tube is divided into three differential pumping stages, each one equipped with turbomolecular, diffusion and rotatory pump.

The structure of the final stage has two main advantages. In the first place it improves the pulses beam separation for inelastic scattering measurements. In second place the signal-noise ratio is increased thanks to the reduction of background gas. Finally, the beam arrives to the detector chamber. The detection takes places through the following processes: first, the reflected beam passes through an UHV chamber where an ionizer, an extractor and focusing optics are installed. Then, it is accelerated to a deflection magnetic system, which guides it into a SEM (Secondary Electron Multiply) detector.

TOF analysis

To deduce the energy and momentum exchanged in the inelastic interaction, the intensity of the elastic and inelastic scattering is recorded as function of the time needed to travel from chopper to detector. The energy exchange is defined as $\Delta E = E_f - E_i$, where the final and initial energy, E_f and E_i respectively, are given by

$$E_f = \frac{m}{2}\left(\frac{L_{TD}}{t^i_{TD}}\right)^2 \tag{2.8}$$

$$E_i = \frac{m}{2}\left(\frac{L_{CD}}{t^e_{CD}}\right)^2 \tag{2.9}$$

where L_{TD} is the distance target-detector, t^i_{TD} is the inelastic time of flight between target and detector, $L_{CD} = L_{CT} + L_{TD}$ is the chopper-detector distance and t^e_{CD} is the elastic time of flight between chopper and detector.

We can write $t^i_{TD} = t^i_{CD} - t^i_{CT} = t^i_{CD} - t^e_{CT}$

knowing that $t^e_{CT} = t^e_{CD} - t^e_{TD} = t^e_{CD} - t^e_{CD}\left(\frac{L_{TD}}{L_{CD}}\right)$

Thus, t^i_{TD} can be rewritten as

$$t^i_{TD} = t^i_{CD} - \left(t^e_{CD} - t^e_{CD}\left(\frac{L_{TD}}{L_{CD}}\right)\right)$$

In order to evaluate t^e_{CD} the Eq. 2.9 is used, as E_i is fixed in the experiment.

Hence we have all the parameters to calculate ΔE, that is:

$$\Delta E = \frac{m}{2}\left\{\left(\frac{L_{TD}}{t^i_{CD} - \left(t^e_{CD}\left(1 - \frac{L_{TD}}{L_{CD}}\right)\right)}\right)^2 - \left(\frac{L_{CD}}{t^e_{CD}}\right)^2\right\} \tag{2.10}$$

To transform the TOF spectra into energy transfer scale domain, the Jacobian has to be included in the transformation. Thus, the peak intensity will be:

$$I_{\Delta E}(\Delta E) = I_t(t_{TD})\left|\frac{dt}{dE}\right| = I_t(t_{TD})\frac{(t^i_{TD})^3}{m(L_{TD})^2} \tag{2.11}$$

The energy measurement resolution depends on the phonon energy, since the Jacobian is non linear. For phonon creation events, that is when the exchange energy is negative, the peaks become broader and lower, whereas for annihilation events the peaks appear narrower and higher.

2.2.3 Raman

Given its requirements to perform successful analysis, Raman spectroscopy is an extremely useful characterization technique: it is a non destructive method, the sample does not require any previous preparation process and it can be used regardless of the sample phase (solid, liquid or gas). As the name suggests, Raman spectroscopy is based on the use of Raman effect. Most of the photons impinging a surface are elastically dispersed, trough Rayleigh dispersion, without any change on the photon's wavelength. The remaining photons are, though, dispersed in an inelastic way in which the reflected wavelength varies with respect to the incident one. This behaviour is due to the interaction of the incident beam with the atoms composing the sample, and the resulting difference between both frequencies (incident and dispersed) equals the frequency of the normal vibration modes. If the difference is negative, the photon has lost energy during the process, which is then called Stokes dispersion; if, on the other hand, the difference is positive, the photon has gained energy during the process and it is called anti-Stokes dispersion.

Raman spectra were recorded with Raman set-up belonging to Optical Spectroscopies Lab at the Instituto de Ciencia de Materiales de Madrid (ICMM). Micro-Raman experiments were performed at room temperature using the 488 nm line of an Ar^+ laser (incident power around 8 mW) with an Olympus microscope (×100 objective) of very high numerical aperture, NA=0.95 and a "super-notch-plus" filter from Kaiser. The

scattered light was analysed with a Jobin-Yvon HR-460 monochromator coupled to a Peltier cooled Synapse CCD. Raman spatial resolution is estimated to be around 0.8 μm. Raman images of different sizes (20 × 10 μm^2 and 10 × 10 μm^2) and 1 μm steps as well as individual spectra were obtained. Optical images of the same areas were also collected [87].

2.2.4 Atomic Force Microscopy

Atomic Force Microscopy (AFM) is based on the interaction between the mass of the atoms forming the probe and the sample. The probe point is usually shaped as a pyramid and mounted on a cantiliever; in this way any interaction between the probe and the surface implies subtle variations of the cantilever position. This cantilever is continuously supervised by a laser beam, so the interactions between the probe and the surface provoke differences in the reflected beam, which can be detected immediately via photodiodes. Based on these principles there are several measurement techniques, such as contact mode, where the repulsion force between the probe and the sample is constant; or dynamic mode, in which the cantilever vibrates at its resonance frequency.

AFM images were recorded with AFM set-up belonging to Sputtering Lab at the Instituto de Ciencia de Materiales de Madrid (ICMM). AFM characterization was carried out in the tapping mode using a microscope head and software from Nanotec. Commercial PPP-NCH-w tips, with resonance frequency of about 270 kHz and spring constant around 34 Nm^{-1} (between 10 and 100 Nm^{-1}), adequate for dynamic mode, were utilized to collect topographic images, as well as amplitude and phase mappings. Several areas in different regions were checked (for every sample).

CHAPTER 3

Mirror Simulations and Experimental Tests

The first step to design a curved substrate for neutral microscopy is to get a realistic estimation of the focusing properties of parabolic mirrors. For this purpose a numerical ray tracing method has been developed. This program does not intend to be an exhaustive study of exact ray-trace beam for an off-axis paraboloid surface. Our aim is to report a simple numerical approach to evaluate the position of the focus of an incident beam reflected by an off-axis parabolic mirror. Specifically, we are interested in achieving two main goals: to derive as change the position of the focal point as a function of the surface curvature in the case of flexible mirror and to obtain the parametric values that a fixed mirror must have to focus in a given position. Finally, an estimation of the minimum focal spot of the reflected beam for a parabolic mirror at off-normal incidence is given.

3.1 Mirror deflection approximation

First at all, 2D simulations in the plane defined by the main axes of the mirror and the incident beam were performed. Exact rays were numerically traced in order to obtain the focal point of the mirror using Snell's law. The resulting algorithm was coded in Matlab.

For the algorithm creation it was assumed that the off-axis concave mirror is at a fixed position in space and that the incident beam is rotated with respect to the mirror by an angle θ_i, as shown in Fig. 3.1.

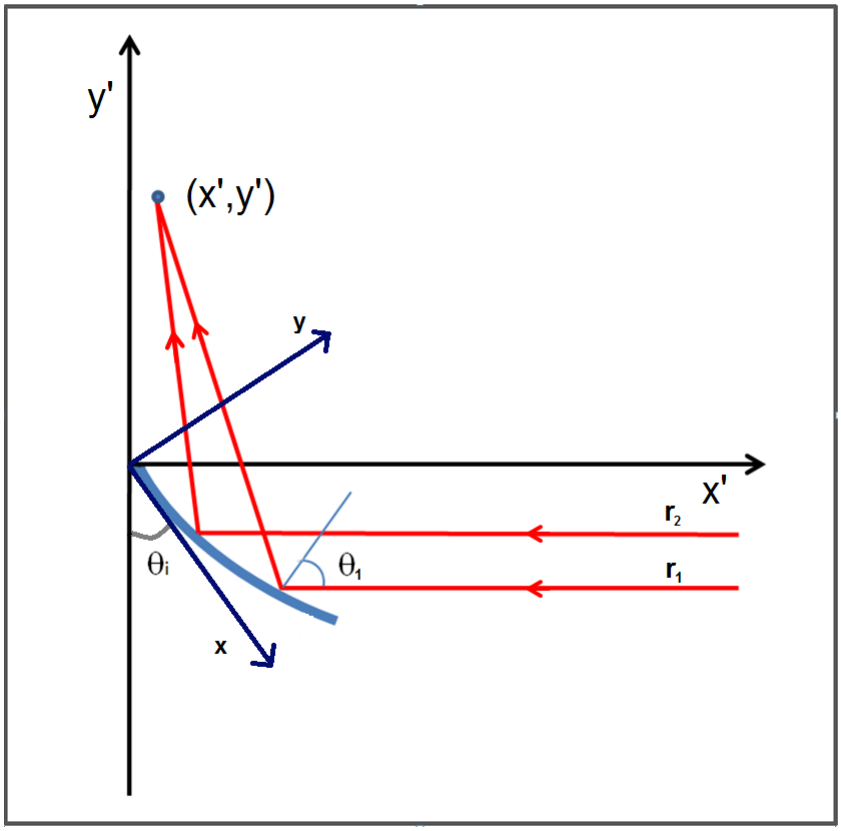

Figure 3.1: Schematic diagram of our experimental setup.

The parametrization of the surface can be changed according to the type of mirror to be used. In the experimental set-up built to test the program, a flexible flat mirror is placed onto a piezoelectric bender actuator, forming a single unit. This unit is fixed in one end, leaving the other to move freely. When a voltage is applied, the mirror-actuator unit is bended, resulting in a concave mirror. This system can be modelled as a cantilever plate with an external vertical load at the free end. (Fig. 3.2).

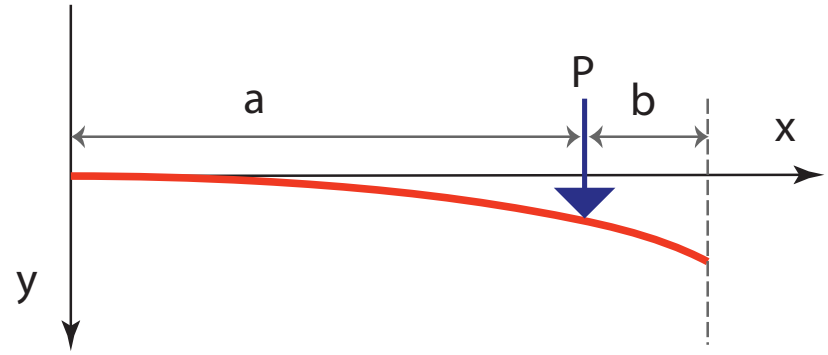

Figure 3.2: Cantilever beam loaded with an external vertical load at the free end.

Given the model used for the mirror surface, the plate deflection formulae are [88]:

$$\begin{cases} y(x) = -\frac{Px^2}{6EI}(3a - x) & for \quad x \leq a \\ y(x) = -\frac{Pa^2}{6EI}(3x - a) & for \quad x \geq a \end{cases}$$

where E is the elastic or Young's modulus, I is the moment of inertia of the beam cross section and P is the load applied at the free end. For convenience in calculations, it is also introduced the load parameter K, defined as follows:

$$K = \frac{P}{6EI} \tag{3.1}$$

Using this K parameter, it is possible to obtain a more general view of the results, since cantilever plates with different combinations of E, I and P may yield the same value of K and, consequently, present the same behavior. Taking into account the definitions of K, Eq. **??** can be rewritten as

$$y(x) = -Kx^2(3a - x) \tag{3.2}$$

where K is found experimentally.

To retrieve the curved mirror focal point, an incident light beam was modelled as two single rays separated by the distance Δx. Those rays can be described through the following equations:

$$r_1 = ax + d \tag{3.3}$$

$$r_2 = ax + b \tag{3.4}$$

Since it is assumed that the incident rays are both parallel to each other, the slope shall be the same for both and it can be obtained from θ_i angle.

By using Eqs. 3.2, 3.3 and 3.4 the incident points in the mirror for both rays can be calculated: (x_1, y_1) for the first ray and (x_2, y_2) for the second. The derivative of Eq. 3.2 evaluated at (x_1, y_1) and (x_2, y_2) yields the slope of the tangent line to the mirror for those points. Once the tangent is available, it is possible to calculate the normal line to the mirror surface for each point, as it is shown in Fig. 3.1.

With all those data available, the reflected rays are then calculated by means of Snell's law:

$$n_{1i} sin(\theta_{1i}) = n_{1f} sin(\theta_{1f}) \tag{3.5}$$

In the case under study, since the surface is an ideal mirror, the incident ray and the refracted ray make the same angle with the normal to the surface at the point of reflection.

$$\theta_{1i} = \theta_{1f} \tag{3.6}$$

As the final step, the focal point can be found in the intersection of the two reflected rays.

To compare the simulated with the experimental data, a rotation around the origin by the θ_i angle has to be performed, since the reference frame is not the same for both situations. The relationship between both reference frames is given in the following equations:

$$\begin{cases} x\prime = x\cos\theta_i - y\sin\theta_i \\ \\ y\prime = x\sin\theta_i + y\cos\theta_i \end{cases}$$

3.2 Experimental set–up

In order to verify the simulation an experimental set up has been built in ambient conditions reproducing the exact geometry used in the calculations. To simulate the rays

described in the previous section, a laser has been used, since its coherence makes it very close to the ideal case. Regarding the mirror and the deformable surface, a thin crystal Ni(111) with a thickness of 100 μm has been attached to a piezoelectric bender actuator (PL140.10), as shown in Fig. 3.3. This piezoelectric piece, thanks to an operating voltage range that goes from 0 to 60 V (±30 V), allows a displacement up to ±1 mm. In this way, by changing the voltage applied to the piezoelectric, the shape of the mirror can be modified by bending it and therefore the focal point can be shifted.

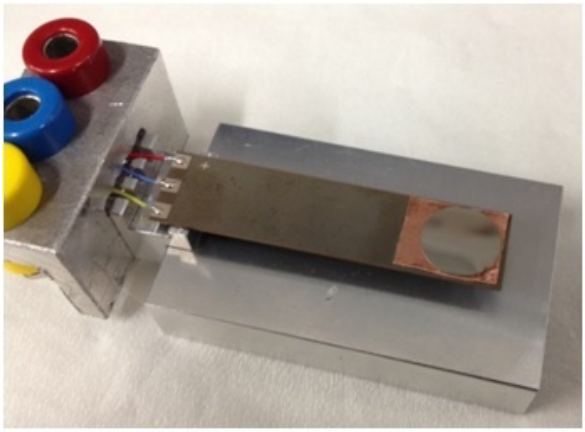

Figure 3.3: Piezoelectric bender actuator.

3.3 Comparison of experimental results with numerical simulations

Figure 3.4a shows the comparison between the numerical simulation performed with an incident angle of 30° and the experimental results obtained at the same conditions. By increasing the voltage, the position of the focus is shifted at the lowest value for both x and y coordinates. The experimental results are in good agreement with the calculations, thus verifying the validity of the used algorithm. As proof of the robustness of the numerical simulation, the focal point position for different incident angles has been recorded. As we can see in Fig. 3.4b and c, the theoretical curve fits very well the experimental results for incident angles of 50° and 60° as well.

Interestingly enough, the thin mirror crystal follows very well the shape of the actuator, and the deformation results to be temporary. When the voltage set to zero, the thin crystal recovers its original flat shape.

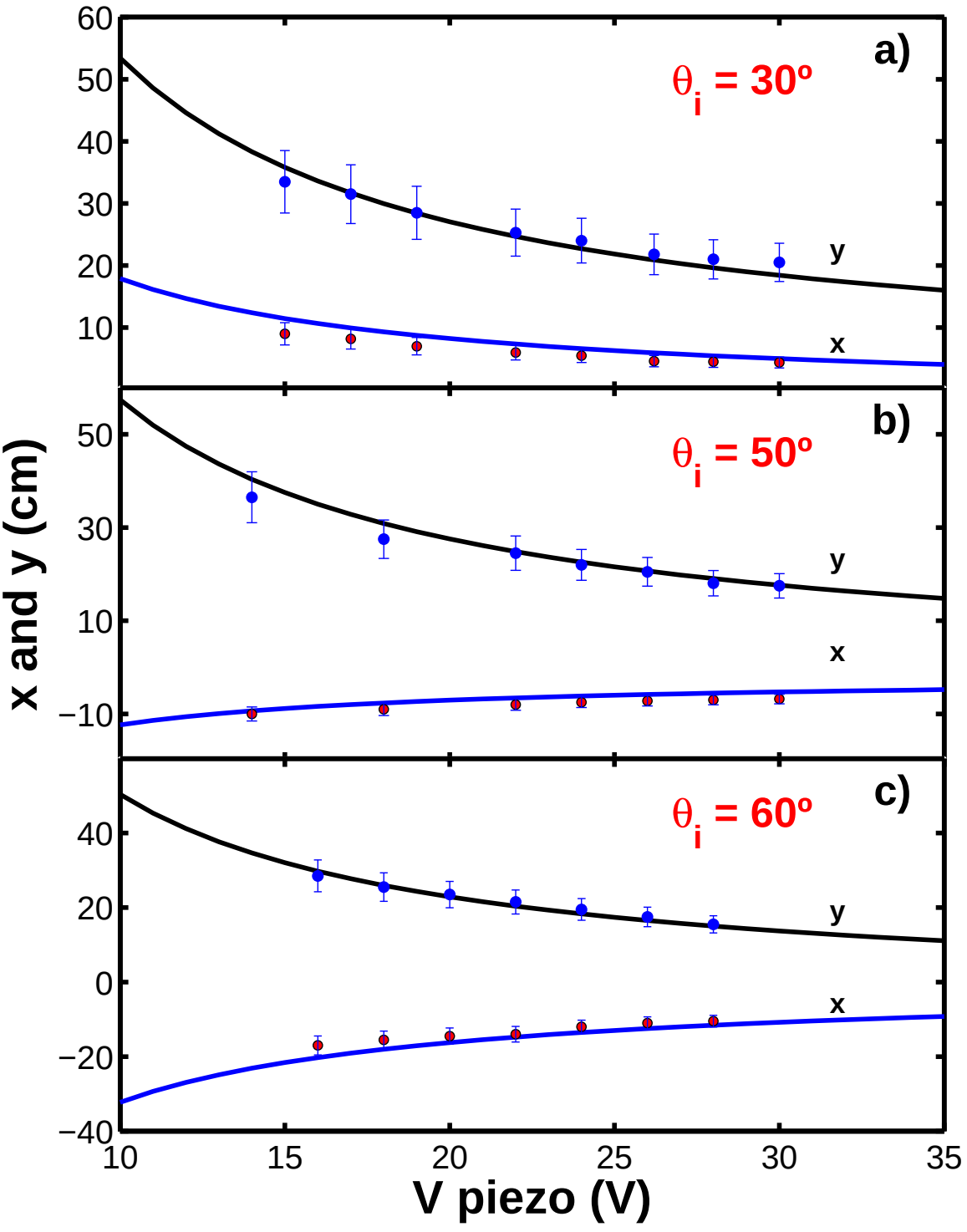

Figure 3.4: Comparison between experimental data (circles) and theoretical calculation (continuous line) of the focal position as function of the voltage applied at the piezoelectric. Three different incident angles were used: θ_i = 30° (a), θ_i = 50° (b), θ_i = 60° (c).

3.4 Parabolic mirror design

The ideal mirror surface to obtain the narrowest focus spot in a three dimensional space is an ellipsoidal surface. However, getting a sample with a good surface quality and this geometry is not trivial. This is why a parabolic profile was the selected geometry for the surface, which in addition helps to limit possible aberrations in the reflection. It is necessary to estimate the dimensions and the parameters that the parabolic mirror should have in order to place its focal point at the detector, located in both TEAMS and ERASMO apparatuses.

In the case of TEAMS set up the distance between the target and the detector is about 5 cm. It was found through the simulations that, in order to focus the He beam at 5 cm from the mirror vertex, the parabolic shape must be $y = 0.018 \cdot x^2$. Due to the off-axis incidence, the focal point of the mirror doesn't match the focus of the parabolic surface. Thus, in order to design a mirror with the focal point 5 cm away from the parabola vertex, it was necessary to calculate the focus of the parabola. For the parabola mentioned above this is 13.9 cm. Thanks to simulations it was observed that the point of incidence is not a critical factor for the focal point position, thereby allowing the selection of the mirror size according to the geometry imposed by the HAS experimental set-up.

On the other hand, for ERASMO set up the geometry is different. It has a fixed detector at 1698 mm and a piezotable at 535 mm away from the mirror. The piezotable has been mounted in order to measure micron and submicron spot sizes. Thus, in this case the focal point has to be placed in the piezotable position. Using the simulation program results that the mirror should have a focal length of about 83.3 cm.

It is worth mentioning that in the cases in which a parabolic shape was not commercially available, a spherical shape was used instead. The difference in the shape of both geometries is of the order of 10^{-14} mm for a beam spot size of 0.5 mm centered with the principal axis of the mirror and a focal length of about 83.3 cm.

3.5 Minimum focal spot

The next step was to extend the code in order to estimate the minimum focal spot of the reflected beam for a parabolic mirror at off-normal incidence. Due to the coma aberration that parabolic mirror suffers when the incident rays are off-axis, the rays will not be perfectly focused to a point. The geometry used was the one corresponding to the HAS experimental set-up. Most focusing measurements of He-atoms impinging on

the parabolic mirror have been recorded with the HAS machine in which the detector is located 5 cm away from the mirror position. Therefore, the simulations were carried out with parameters optimized to have the minimal spot size at that distance. For an incident beam size of 0.5 mm, a point of incidence taken 0.1 mm away from the parabolic centre and an incident angle of 50°, the minimal (ideal) focal spot was estimated in 60 nm. Furthermore, it was seen that the focal spot remains below 100 nm if the incident angle is in the range of 30°-70°.

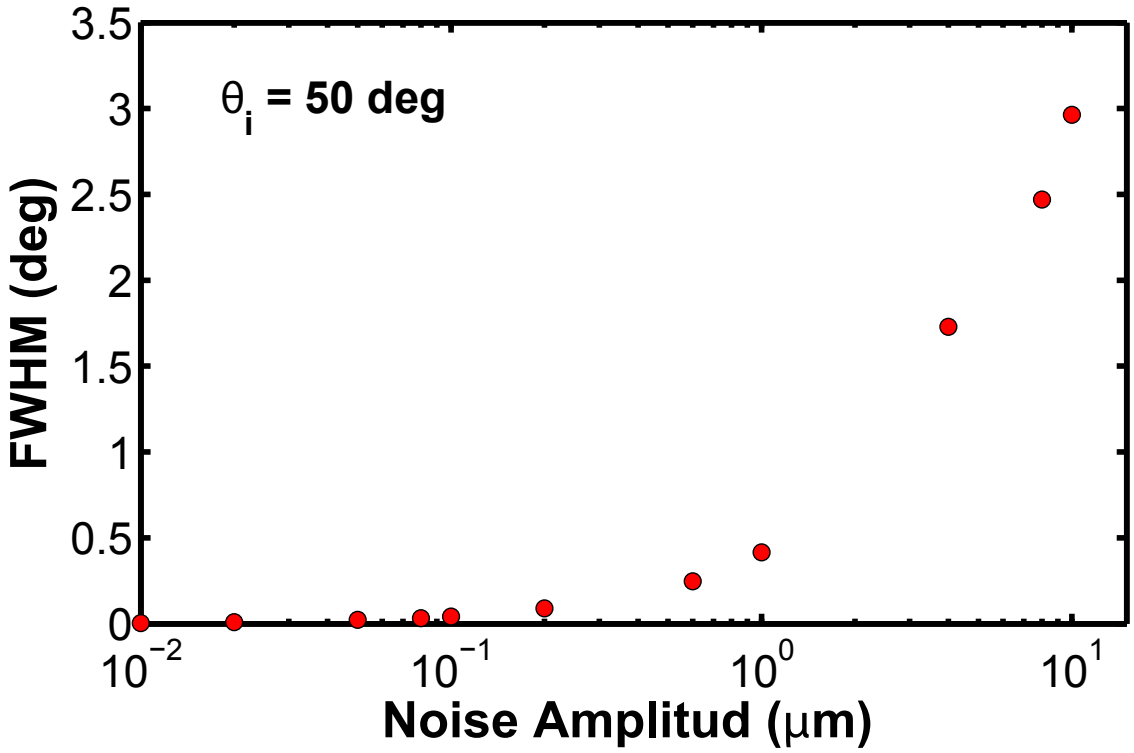

Figure 3.5: Simulation of specular scattering from a perfect parabolic mirror, including "noise". The inset shows the mirror profile used in the simulations. The figure shows the dependence of the width of the specular peak as a function of the noise amplitude.

In order to evaluate the influence of surface waviness and defects on focusing, it has been performed optical ray tracing simulations adding "noise" to a flat, parabolic mirror surface. The "noise" has been modelled by a long wavelength and small amplitude corrugation, which has been added to the mirror surface. The wavelength used was of the order of 1 mm, i.e. shorter than the mirror diameter (10 mm) but much larger than the transfer width of the HAS system (200 nm). Several simulations at different wavelengths have been run, including values close to 0.1 mm, and obtained essentially

the same results. The results obtained for a mirror with focal distance f = 13.9 cm are shown in Fig. 3.5. The influence of the "noise" on the spot size begins to be significant for amplitudes above 100 nm. This value is too large and therefore, unrealistic in well-prepared graphene-covered mirror surfaces. These results motivated new simulations, aimed to establish the theoretical limit of focusing using a real mirror.

The results are summarized in Fig. 3.6. As we can see, sub micron (i.e. below 1000 nm) focusing can be achieved even for noise amplitudes of 0.8 nm. This is a large value compared to typical corrugation amplitudes found in He-graphene systems, which lie in the range of 1-2 Å, i.e. 0.1-0.2 nm.

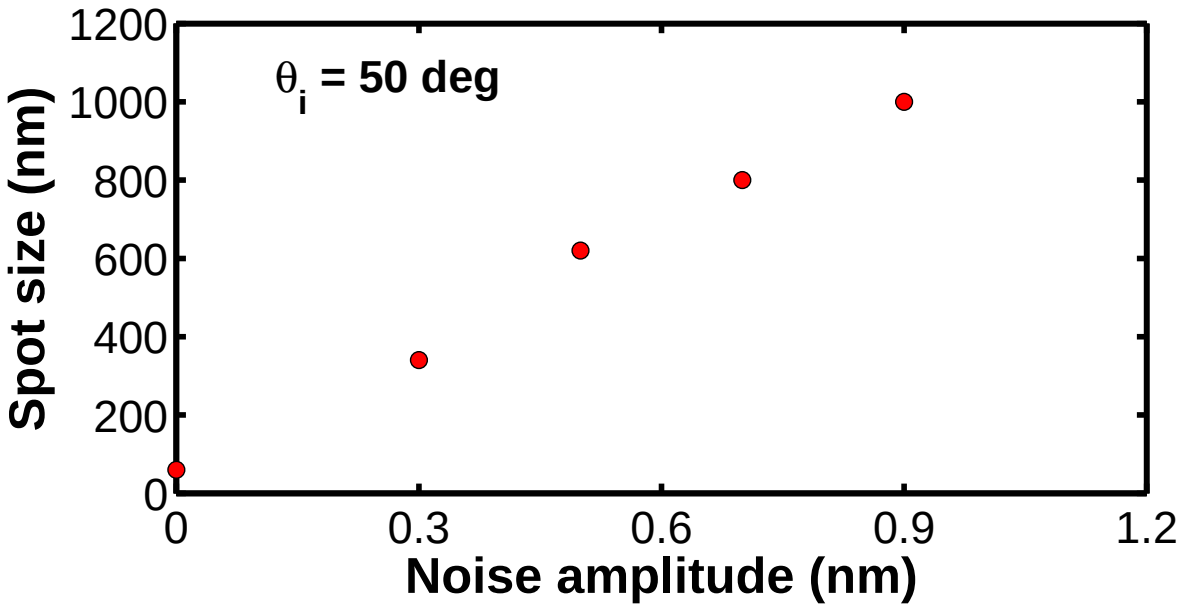

Figure 3.6: Dependence of the width of the specular peak as a function of added noise in the limit of small noise amplitude. The zero noise limit corresponds to a spot size of 60 nm.

Our simulations suggest that with such corrugation amplitudes, even spot sizes of 200-300nm could be obtained. This justifies our further work to improve focusing using parabolic mirrors, which are both much easier to prepare and commercially available.

It is important to bear in mind that this is a 2D simulation. The first goal is to focus in the set-up detectors, which are able to scan in just one direction. This is why the best conditions to have a minimum focal spot in the scan direction were studied. However, the 3D situation is more complex. It is known that symmetric surfaces, such as paraboloidal mirrors, can suffer astigmatism aberration if the incident rays are off-axis, as it happens in the analysed case. This means that in the direction perpendicular to the scan plane,

the rays have a different focal point. The use of ellipsoidal mirrors, that avoids this problem, should be the next choice once sub micron focussing has been achieved.

CHAPTER 4

GRAPHENE ON SAPPHIRE

In this chapter, two new methods are reported to produce high–quality, transparent graphene on sapphire samples, using Cu as a catalyst. He–diffraction, Atomic Force Microscopy (AFM), Raman spectroscopy and optical transmission have been used to assess the quality of graphene in metal free areas and to characterize its structural and dynamical properties. We used helium atom scattering as sensitive probe of the crystallinity of graphene on sapphire. The observation of high reflectivity (6.5%) combined with narrow specular peak and clear diffraction peaks demonstrates the presence of flat and homogeneous graphene domains over lateral scales of microns, consistent with AFM results. Surprisingly, growing graphene on sapphire improves the quality of the He–diffraction spectra. These properties, together with graphene stability at ambient conditions, suggest that this system may be an excellent candidate to be used as a focussing mirror in scanning He atom microscopy. The uniformity of the graphene layer has also been investigated by Raman mapping. Judging by the ratio of the 2D to G peaks, the quality of the graphene is not degraded by Cu removal. Graphene/sapphire system can play an important role in the development of the He-microscopy optics due to its possible use as mirror for neutral atoms. Moreover, the high transparency (90%) measured in the visible range makes this system suitable for many applications that require the hybrid properties commonly associated with metals (conductivity) and insulators (transparency). Finally, our study shows that He–diffraction and Raman provide crucial information on quite different and complementary aspects of the same samples.

4.1 Introduction

The special interest of the study presented in this chapter lays in the fact that the growth of graphene (Gr) on α–Al_2O_3(0001) (c-plane sapphire) allows us to investigate the structure and the dynamical properties of the Gr on insulator substrates. To this respect, the interaction of He atoms with Gr/sapphire system recovers particularly interest in order to be employed as an atomic mirror. Focusing atoms with de Broglie wavelengths of the order of an Angstrom imposes tight conditions on the mirror surface termination. In particular, the large cross-section of the defects experienced by thermal energy atoms requires a surface with the following properties: high crystallinity, homogeneity over lateral scales of microns and low reactivity to possible contaminants [1, 9]. The Gr/sapphire surface gathers all these properties. For this reason, it can be an excellent candidate to be used as a high-reflectivity mirror for He atoms. In future research, the atomic beam might be focused to the desired focal point growing the Gr on a curved sapphire substrate.

Furthermore, the growth of Gr on transparent insulators is readily applicable to a broad range of applications such as light emitting diodes [89] and transparent conductors [90]. This effort is motivated by the fact that these materials require scarce metals (like in indium tin oxide, ITO), perform poorly on flexible substrates and require expensive vacuum deposition techniques [91, 92]. Reducing the cost of transparent conductors, moving away from elements that are expensive and/or in short supply, is crucial for the future [93–95]. Gr/sapphire samples may provide a possible alternative to these materials for many applications. However, most of the available methods for controlled and scalable preparation of Gr on metallic substrates cannot be easily extended to grow Gr on sapphire. Thus, most of the methods reported have not produced Gr layers of quality comparable to that obtained for instance on Cu [64, 96–99]. Typically, the Raman D-peak (related to the presence of defects) is larger than the G-peak, indicating small grain size ($\sim$ 15nm). For Gr on sapphire, a few methods have been reported in which the Raman D-peak was significantly reduced; these methods are either based on the high- temperature (1500 – 1600°C) decomposition of the precursor gas without using metal catalyst [100, 101] or by direct CVD growth on dielectric surfaces by simultaneously dewetting the Cu film [102]. Even though some of these samples exhibit excellent performances, like a room-temperature Hall mobility of 2.000 $cm^2/V{\cdot}s$ [100], it is interesting to explore alternative ways of producing similar samples.

In this chapter, new methods to produce high quality, transparent Gr/sapphire sam-

ples in UHV are reported. The starting point is a high-quality Gr layer prepared by CVD using Cu as a catalyst [66] by Dr. H Yu. in the group of Prof. A. Wodtke at the Max Plank Institute for Biophysical Chemistry in Göttingen. The samples are then transferred to UHV, where Gr on sapphire are prepared following two different methods. The first method consists in heating the sample to 1150 K in order to evaporate the Cu film. The second method is an improvement of the first one and included heating in Ethylene while the sample is heated. This last method is named in this thesis as *modified method*. The samples have been characterized by Helium Atom Scattering (HAS), Inelastic Helium Atom Scattering (IHAS), Atomic Force Microscopy (AFM), UV-VIS transmission spectroscopy and Raman spectroscopy.

In addition to the novelty of the preparation method, a comprehensive structural characterization of the Gr/Sapphire system has been performed combining surface science measurements, that require UHV conditions, and a set of other techniques, such as Raman and AFM, for the characterization of the Gr. In fact, our study shows that HAS and Raman provide complementary information on the sample$'$s quality, and that a wrong conclusion might be drawn if just one of these techniques is applied.

Finally, our approach presents several advantages with respect to previous reported methods, like a high transparency (80% - 90%) in the visible range, the use of a moderate preparation temperature ($\sim 900^{\circ}$C). and a short preparation time, that ranges from 30 minutes (with the first method) to 2 hours and half (with the modified method).

4.2 Experimental details

4.2.1 Sample preparation

The starting point is a high-quality Gr layer prepared by CVD on Cu(111) grown on α-Al_2O_3(0001) (c-plane sapphire). The growth of Cu film on c-plane sapphire was achieved by using electron beam evaporation method, as reported in our previous study [66], except for the total thickness (1000 nm) and growth rate (0.3 nm/s). Different initial thicknesses of Cu(111) films have been used for Gr growth in order to improve the quality of Gr layer and the elimination of Cu without Gr film deterioration. We have tested several sample with HAS technique before to find the optimal parameters of growing. Best results have been obtained with a 1000 nm thick Cu film. The samples were prepared by CVD in Göttingen [66] and then transported to Madrid to complete the preparation in UHV chamber with base pressure in the low 10^{-10} mbar range; typically,

the samples were exposed to ambient conditions for one week before being introduced into the UHV scattering chamber for He diffraction. Once in UHV, the samples were annealed at 800 K with 2×10^{-7} mbar of C_2H_4. This treatment leads to a significant improvement in surface quality, as indicated by the increase of the He–specular intensity [67]. Gr on sapphire has been obtained *in situ* by evaporation of the Cu film in UHV, heating the samples at 1150 K for 30 min. The sample temperature was measured with a type-C thermocouple spot-welded to the sample holder. The sample preparation steps are schematically illustrated in Fig. 4.1. A better quality of the Gr on sapphire has been achieved with the modified method. In this method, during the Cu evaporation the heating of the sample takes place in a partial pressure of 3×10^{-6} mbar of C_2H_4, keeping the surface temperature at 1150 K. In order to achieve the evaporation of the copper in all the sample (1×1 cm^2) a longer time with respect to the first method is required.

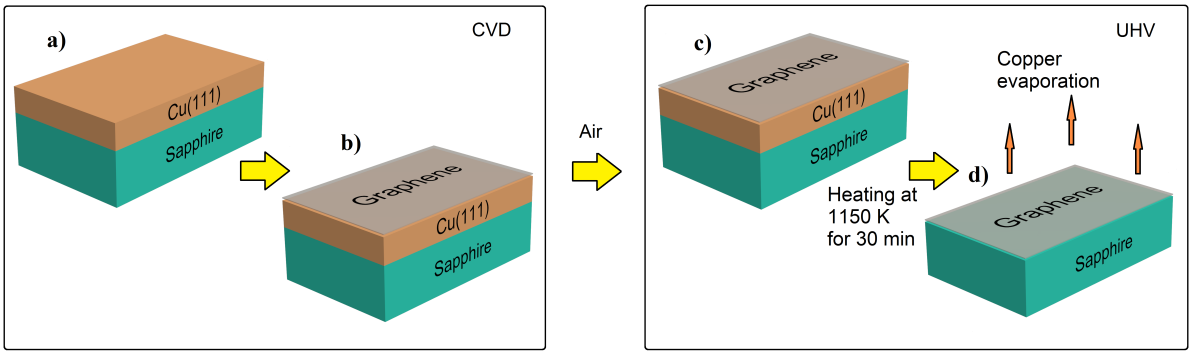

Figure 4.1: Schematic procedure for the Gr growth on sapphire. a) Copper is deposited on c-plane (0001) sapphire by electron beam evaporation. b) Gr growth on Copper by CVD. c) After air exposition, the sample was introduced into the He-scattering UHV chamber. d) After heating up in UHV, Cu evaporates, leaving a Gr layer deposited on the sapphire substrate.

4.3 Helium Atom Scattering

The He diffraction experiment was carried out using the high resolution He atom scattering time-of-flight (HAS-TOF) spectrometer (ERASMO apparatus) and TEAMS systems, which enables the measurement of absolute diffraction reflectivity. Both described in detail in the chapter. Diffraction spectra have been recorded for the spectra before (Gr/Cu/Al_2O_3 sample) and after Cu evaporation (Gr/Al_2O_3 system). Moreover, with one of the samples of Gr/Cu/Al_2O_3 we have investigated all the layers that compose it, that

is Gr/Cu/Al_2O_3, Cu/Al_2O_3 and clean Al_2O_3. These steps are important in order to investigate accurately the effects of the layers underneath Gr or its structural property. The angular distributions presented in this work were measured after aligning the sample along the $\overline{\Gamma M}$ direction of the dominant Gr orientation (80%), which corresponds to the [$\bar{2}$11] direction of the Cu(111) underneath. The remaining 20% of the sample is covered by domains rotated 30° with respect to the [$\bar{2}$11] direction [67]. In the following, after discussing the shapes of specular peaks we analyze the structures corresponding to the measured diffraction peaks.

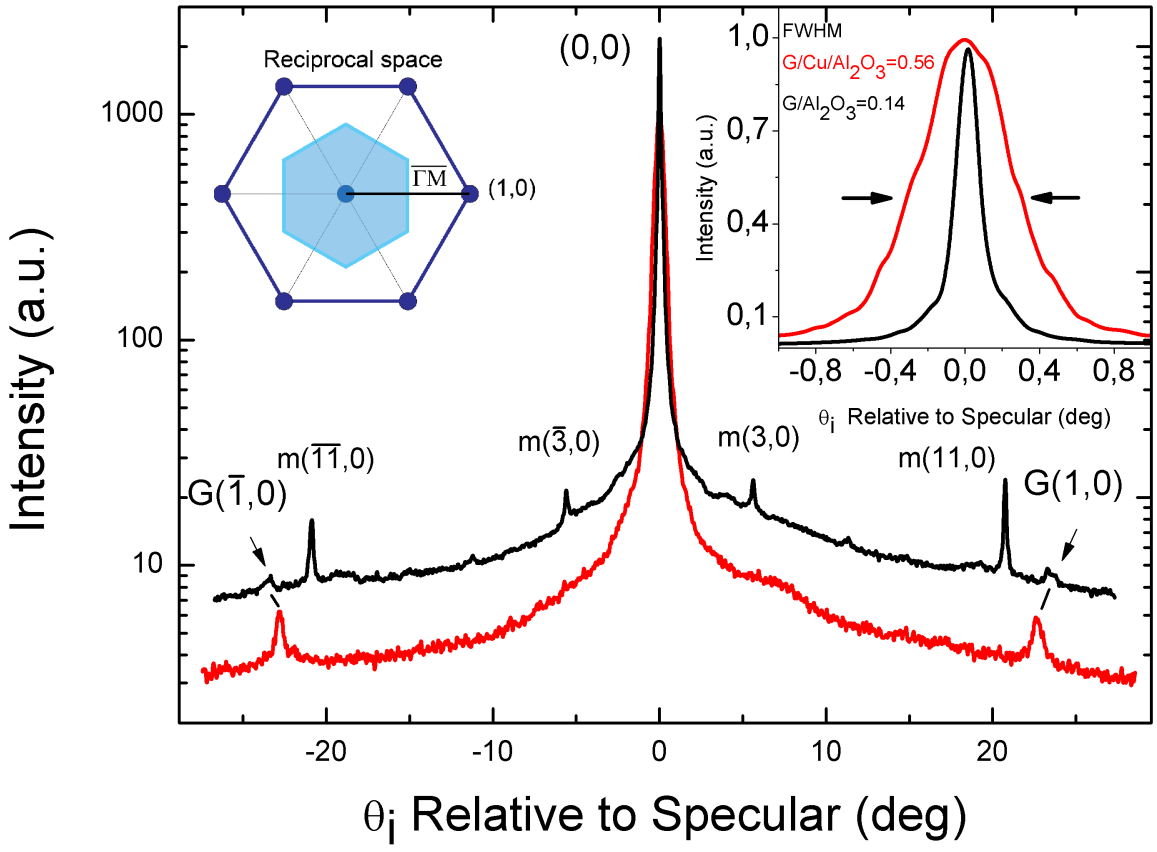

Figure 4.2: Angular distributions of He atoms scattered from Gr/Cu/Al_2O_3 (red spectrum) and Gr/Al_2O_3 (black spectrum) along $\overline{\Gamma M}$. The inset on the right side shows a detailed view of the profile of the specular peaks. The sample temperature is 90 K, and the He-incident energy is E_i = 19.8 meV (the small shift in the position of first order peaks is a result of quite small differences in the He beam energy). The diffraction peaks of the moiré superstructure are labelled as m(n,0).

Figure 4.2 shows a comparison of angular distributions of He atoms scattered from Gr/Cu/Al_2O_3 (red) and Gr/Al_2O_3 (black). The high specular reflectivity, the presence of

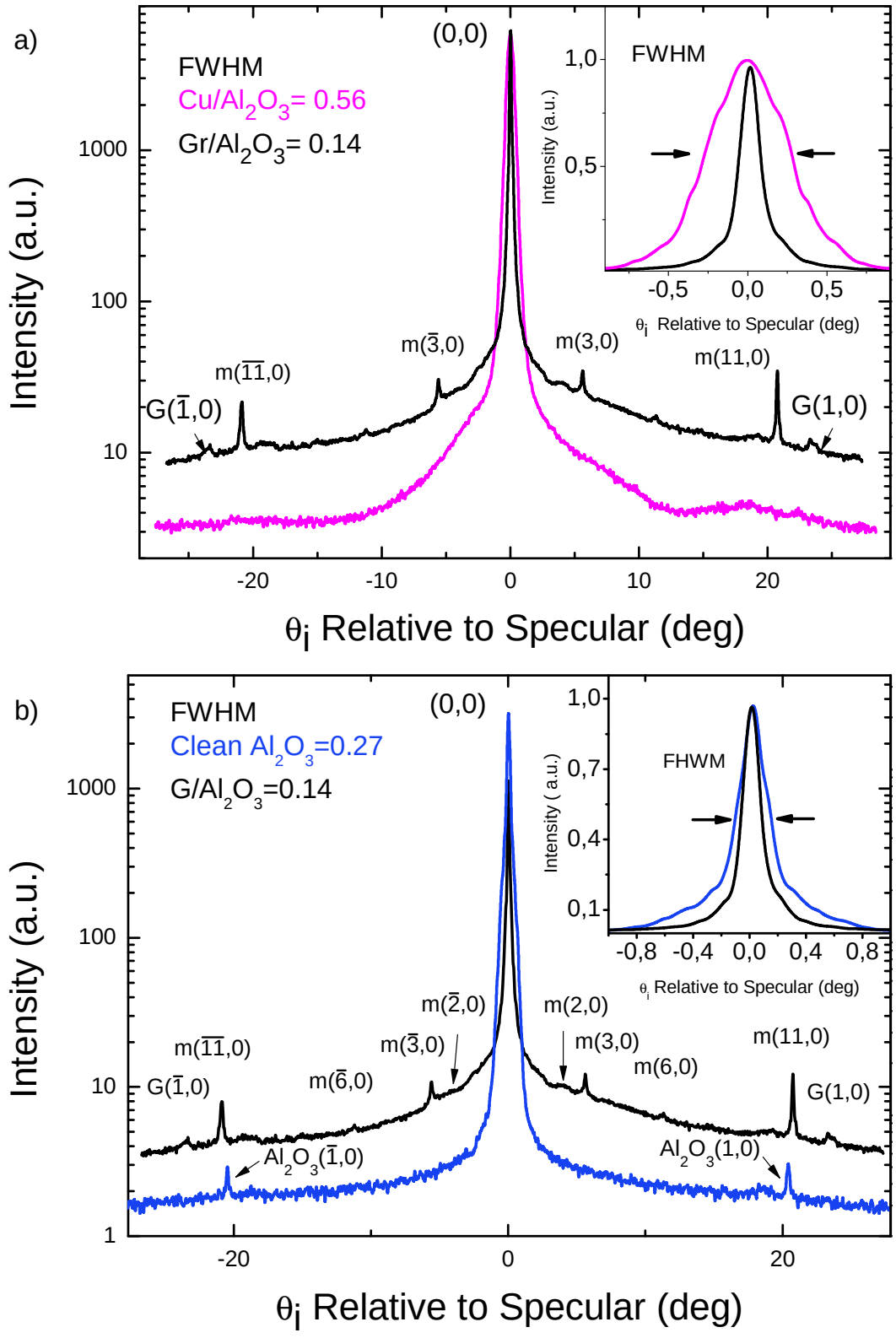

Figure 4.3: (a) Comparison of He diffraction spectra from Gr/Al_2O_3 (black) and Cu/Al_2O_3 (red). (b) Comparison of He diffraction spectra from Gr/Al_2O_3 (black) and clean Al_2O_3 (blue). The sample temperature is 90 K, and the He-incident energy is E_i = 19.8 meV.

diffraction peaks and the existence of moiré (in the case of Gr/Al_2O_3) demonstrate the existence of a well-ordered Gr layer, with a low density of defects, over areas of the order of the beam size (ca. 1 mm). However, the width of the specular peak of Gr/Al_2O_3 FWHM = 0.14°, which corresponds roughly to the angular resolution of the HAS machine, is lower than that of Gr/Cu/Al_2O_3 FWHM = 0.56°. The width of the specular peak depends on the quality of the surface and gives information about the domain size w through the relationship FWHM $\sim 1/w$ [7]. Therefore, the above comparison can lead to the counterintuitive interpretation that the Gr layer exhibits larger domains after the copper removal. However, this is not the case, as we find by comparing the surfaces of Al_2O_3 and Cu/Al_2O_3. The latter has been obtained by removing the Gr layer in Gr/Cu/Al_2O_3 through Ar^+ sputtering, followed by annealing at 940 K. The corresponding angular distributions are shown in Fig. 4.3a. Further heating at 1150 K for 30 min led to obtaining the clean Al_2O_3 surface. The corresponding peak widths are FWHM = 0.56° and 0.27° for Cu/Al_2O_3 and Al_2O_3, respectively. This clearly shows that the FWHM of the Gr covered surface is determined mainly by the substrate underneath. The width of the specular peaks of Gr/Cu/Al_2O_3 and Cu/Al_2O_3 are almost identical. A possible explanation is that the Cu film is terminated by a wavy surface, which may induce an additional broadening of the specular peak.

On the other hand, a comparison of HAS angular distributions from Al_2O_3 and Gr/Al_2O_3 (Fig. 4.3b) shows a decrease of the FWHM by 50% in the Gr covered surface, which points to the formation of larger domains. The inset in Fig. 4.3b shows the normalized specular peaks in a linear scale, where a quasi–triangular background appears around the specular peaks and is especially pronounced in the Al_2O_3 spectrum. Previous HAS studies have shown that the presence of a triangular background in the vicinity of the specular peak is the signature of a random distribution of defects [103]. Similar conclusions have been obtained in a more recent study reported by Manson et al. [104]. Therefore, we conclude that scattering from point defects dominates in both surfaces, although to a lesser degree in the Gr covered surface. These observations suggest that the Gr layer covers like a carpet the rough and flat sapphire substrate, hiding a portion of the single defects and softening the roughness of the step edges. Even though the Gr layer certainly contains many defects, our data suggest that the Gr/Al_2O_3 layer exhibits a reduced number of defects, leading to an average domain size larger than that of clean Al_2O_3. Since the FWHM observed for Gr/Al_2O_3 is limited by the resolution of our system, we can conclude that the average domain size is at least one order of magnitude larger than the transfer width of our system (200 nm). The coherence length

for the Al_2O_3 surface, which is of the same order of the size [84] of the terraces is ~ 40 nm. The measured absolute reflectivity of He atoms from Gr/Al_2O_3 is 5% at the incident conditions used in Fig. 4.3b. This high reflectivity combined with the narrow specular peak observed suggests that these samples are excellent candidates to be employed as a focussing mirror in scanning He-microscopy [5, 6, 10].

The different diffraction peaks in the angular distributions of Fig. 4.4b correspond to the periodicities of the Gr, sapphire and multiple moiré superstructures resulting from the mismatch of the two surfaces. The lattice constant of Gr on sapphire has been determined from the positions of its first order diffraction peaks indicated as G(0,1) and G($\bar{1}$,0) in Fig. 4.2 and Fig. 4.3, using the in-plane Bragg diffraction condition for a hexagonal two-dimensional structure. The derived value $a = (2.44 \pm 0.02)$Å is identical to the one reported for Gr/Cu(111) [67], and agrees well with 2.4612Å, the periodicity of a single carbon layer in graphite [105]. The low intensity of the first order diffraction peaks points to a low corrugation of the Gr/Al_2O_3 surface. Well-resolved and intense first order diffraction peaks are present in the blue spectrum in Fig.4.3b of the Al_2O_3 substrate, denoted by Al_2O_3(10) and $Al_2O_3(\bar{1}0)$, appear at the positions expected for the shortest hexagonal lattice length of sapphire (Al-Al distance), $a = 2.74$Å. As far as we know, this is the first He–diffraction spectrum reported from a clean sapphire surface.

The He–diffraction spectrum measured from the Gr/Al_2O_3 surface exhibits a more complex structure, due to the moiré reconstruction. The (10) diffraction peak of the atomic lattice of Gr (denoted by Gr(1,0)) is observed at 23° away from the specular peak (0,0). However, the existence of other diffraction peaks, due to the moiré superstructure, is clearly detected along the whole diffraction pattern. The angular position of the diffraction peaks from the Gr moiré lattice are in good agreement with expected values for an hexagonal structure with a periodicity of $\sim$30Å. In particular, the third, the sixth and the eleventh order diffraction of the moiré pattern (labelled m(3,0), m(6,0) and m(11,0)) are clearly observed in the the black spectrum in Fig. 4.3b. A comparison of the angular positions of diffraction peaks of Gr/Al_2O_3 and clean Al_2O_3 surfaces shows that the high-intensity sharp peak m(11,0) matches exactly the position of the peak (1,0) of sapphire. Thus, we can conclude that the moiré pattern corresponds to a (11×11) periodicity aligned with the (1×1) sapphire unit cell. This is schematically shown in Fig. 4.4b.

The moiré structure has been investigated by varying the azimuthal orientation of the sample. Fig. 4.4a shows several He–diffraction angular distributions. Each spectrum has been recorded after a small azimuthal rotation of the sample with respect to an axis

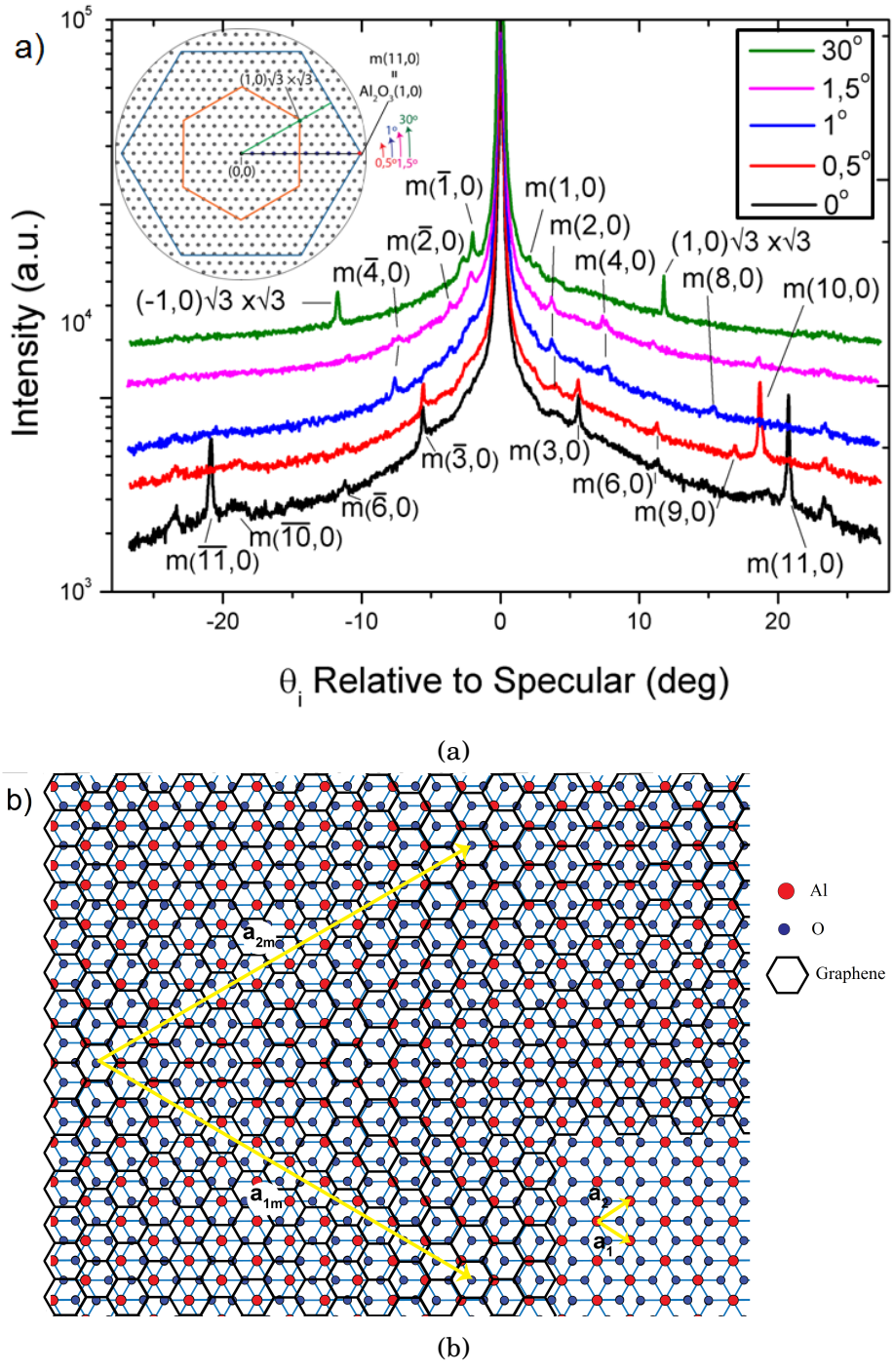

Figure 4.4: (a) Angular distribution of He scattering from Gr/Al_2O_3 as a function of azimuthal rotation. The inset shows the directions on the moiré reciprocal lattice and the first order diffraction of the sapphire (blue hexagon) and ($\sqrt{3} \times \sqrt{3}$)R30°(red hexagon) structures. (b) Proposed model for the moiré (11×11) structure, which is obtained by superimposing (12×12) Gr honeycombs on top of (11×11) sapphire unit cells. The primitive vectors of the moiré ($\mathbf{a}_{1m}$ and $\mathbf{a}_{2m}$) and sapphire unit cells ($\mathbf{a}_1$ and $\mathbf{a}_2$) are also shown.

lying in the incident plane. The black curve is the same as that shown in Fig. 4.3b and is denoted as 0°. Rotating the sample we can see how different peaks from the moiré pattern are detected. In the red curve, rotated by 0.5°, the peak m(11,0) disappears, whereas the m(9,0) and the m(10,0) diffraction peaks are clearly resolved. With a further rotation of 0.5° (denoted as 1°, blue curve), the measured spectrum exhibits weaker but still clear peaks for different order of diffraction (m(8,0), m(4,0) and m(2,0)). For a rotation of 1.5° (magenta curve) the peaks m(4,0) and m(2,0) are still observed, but the m(8,0) peak is not present. The green curve has been recorded for an azimuthal rotation of ∼30°. The position of the detected diffraction peaks fits the diffraction pattern produced by a Gr layer rotated by 30° with respect to the (1×1) sapphire unit cell, which corresponds to a $(\sqrt{3} \times \sqrt{3})$R30° structure. The presence of shadows of the m(1,0) and m(2,0) peaks in this spectrum is due to small misalignment of the tilt angle which appears for different azimuthal orientations.

The diffraction patterns from the moiré superstructure indicate that the Gr/sapphire system keeps the same domains ratio (80% along the main direction, and 20% rotated 30° with respect to this direction) present in the starting system, Gr/Cu/Al_2O_3. We have also recorded He–diffraction spectra for intermediate azimuthal rotations, and no evidence of additional periodicities has been detected. It is interesting to compare our data with the results reported by Hwang et al. [100]. These authors have grown Gr on c-plane (0001) sapphire directly (without using a metal catalysis) and concluded, based on detailed spatial electron diffraction measurements and DFT calculations, that Gr on sapphire grows forming a single dominant crystal orientation for around 80% of the material. In their work, however, the orientation is determined at an early stage of the nucleation during the growth process, and therefore multiple rotational domains with respect to the substrate is obtained. The preparation method described in our current work, on the other hand, could in principle lead to the formation of only one rotational domain if the starting point, i.e. Gr/Cu/Al_2O_3, was formed by only one domain.

Hwang et al. also performed DFT calculations (including the van der Waals interaction) for commensurate cells with orientations of 0°, 11° and 22° with respect to the sapphire [100]. From the similarity of the binding energy obtained for all three commensurate cells it has been concluded that the dispersion interaction depends weakly on the orientation of the Gr layer on the sapphire surface. The unit cells rotated by 11° and 22° with respect to the sapphire correspond actually to moiré patterns with a periodicity smaller than (11×11), and are therefore not consistent with our HAS data. However, our data provide evidence for the presence of the cell with orientation of 0°,

which corresponds to the above mentioned $(\sqrt{3} \times \sqrt{3})$R30° structure.

4.4 Phonon dispersion

In order to study the surface dynamics of Gr/Al_2O_3, time-of-flight (TOF) measurements have been carried out in ERASMO system. The experimental technique used for this measurement is described in section 2.2.2. Several series of TOF spectra have been

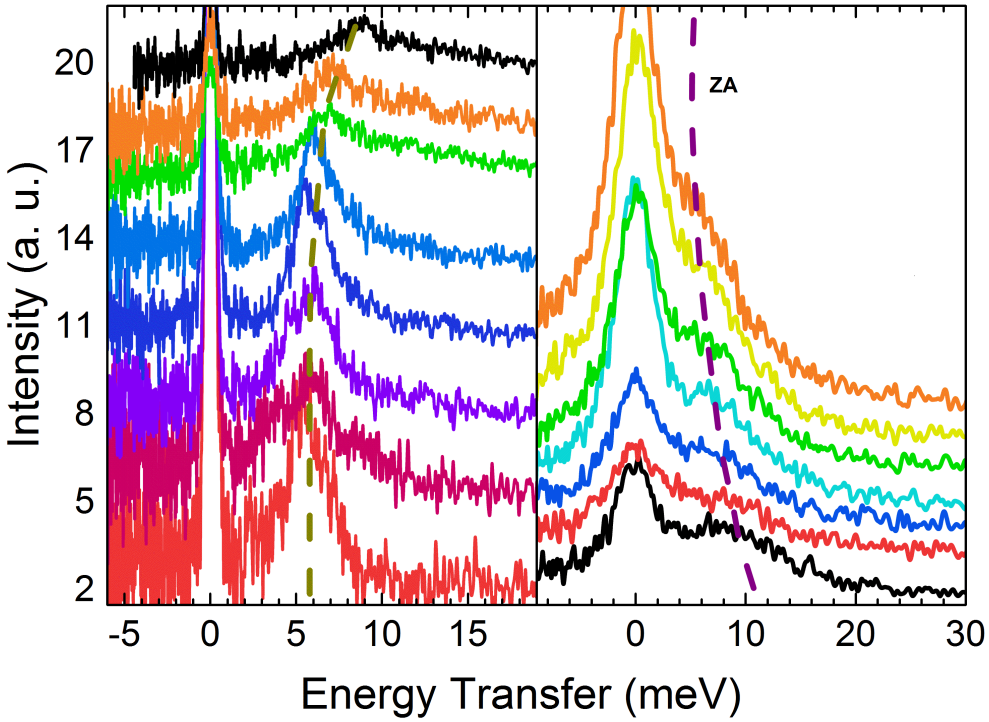

Figure 4.5: Time-of-flight spectra of He scattered from Gr/Al_2O_3 for two different incident energies E_i = 21.5 meV (left) and E_i = 67.5 meV (right). Dashed lines show the ZA mode.

taken under different incident conditions, so as to get the phonon dispersion curves. Figure 4.5 shows a representative series of TOF data, taken by changing the incident angle for two different incident energies, E_i = 21.5 meV (left) and E_i = 67.5 meV (right). These beam energies, along with surface temperatures have been selected to find the optimum resolution for the inelastic peaks. Low beam energy and low temperature surface have been employed for peaks corresponding to low energy and momentum transfer, which are associated with the inelastic peaks that appear closer to the specular

peak. Whereas higher energy beam and room temperature surface are needed to achieve a best resolution for the inelastic peaks corresponding to higher energy and moment transfer. The TOF spectra have been converted into an energy transfer scale by means of the corresponding scan curve (see Eq. 1.26). Although the measurements are performed away from the Bragg diffraction angles, the contribution to the TOF spectra due to elastic scattering is generally present. This component is called diffuse elastic or incoherent scattering and is generally used as origin for the energy transfer scale. Furthermore, the width and the intensity of this diffuse elastic peak gives information about the quality of the surface sample. The most interesting aspect of these TOF sequences is the direct evidence of the phonon dispersion modes. These are exemplified by the peaks in the spectra for which the energy transfer changes as a function of the incident angle. Figure 4.6 shows the phonon dispersion curves for Gr on sapphire measured along the $\overline{\Gamma M}$ direction. Phonon dispersion curves for free standing Gr calculated from first principles [49] are also shown as dashed lines. No data points were detected for the in-plane longitudinal acoustic (LA) and transverse acoustic (TA) modes. The TA mode is usually forbidden in HAS measurements for planar scattering in the $\overline{\Gamma M}$ direction due to symmetry as it has been shown for Gr/Cu(111) [67], but this selection rule is not valid in the presence of defects that break the translational symmetry [106]. However, the small energy difference between the LA and TA mode makes it very hard to resolve them in the TOF measurements. We therefore could not obtain any information on these two modes. The out–of–plane acoustic (ZA) mode, on the other hand, is clearly resolved and as expected from the broken symmetry introduced by the sapphire substrate, does not follow a pure acoustic dispersion but has a frequency $\omega_0 = 5.8$ meV at the Γ point. The ZA mode exhibits a parabolic dispersion, softened with respect to the one expected for free standing Gr. This softening is related to the presence of point defects in Gr, as shown below. The ZA dispersion curve can be used to derive more fundamental quantities like the Gr–sapphire coupling strength, g, and the free standing bending rigidity κ [107]. As mentioned above, coupling Gr to a substrate will introduce a gap at a frequency ω_0 at the $\overline{\Gamma}$ point, and the dispersion relation of the flexural mode ZA is given by [77, 108]:

$$\omega_{ZA}^{coupled}(\Delta K) = \sqrt{\frac{\kappa}{\rho_{2D}}\Delta K^4 + {\omega_0}^2}, \tag{4.1}$$

where $\rho = 7.6 \times 10^{-8}$ g/cm^2 is the two–dimensional mass density of Gr, $\omega_0 = \sqrt{g/\rho_{2D}}$ and g is the coupling strength between Gr and substrate [108]. Therefore, from a fit to the experimental data (red curve in Fig. 4.6) using Eq. 4.1 it is possible to determine both g and κ. We obtain $g = (5.8 \pm 0.4) \times 10^{19}$, N/m^3 for the Gr–sapphire interaction. This value

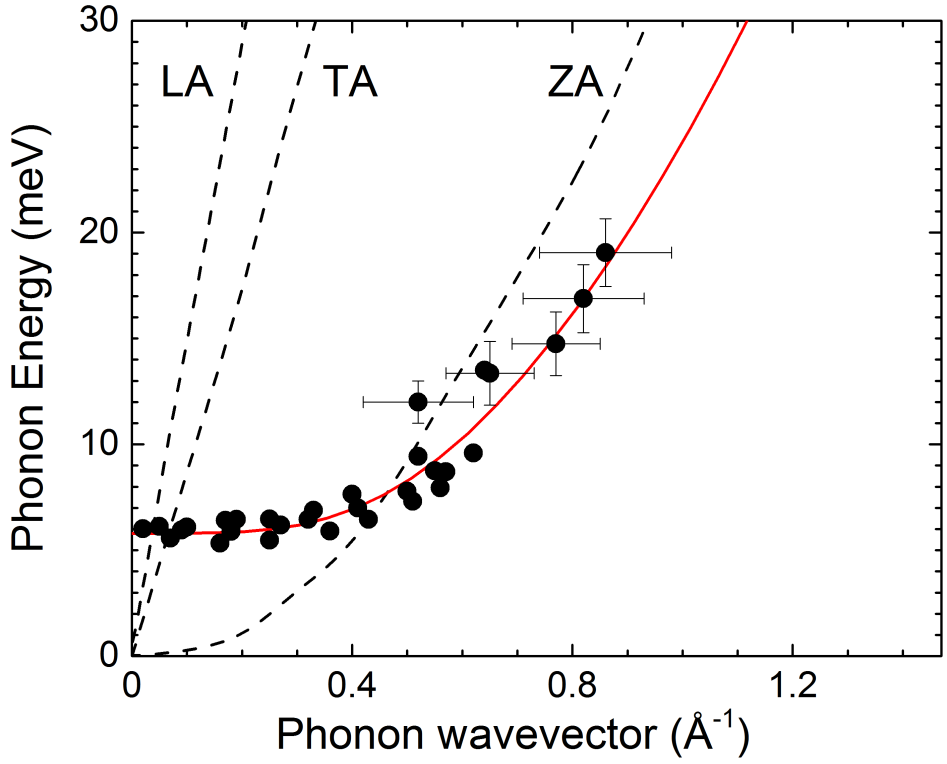

Figure 4.6: Experimentally derived surface phonons for Gr on sapphire measured along the $\overline{\Gamma M}$ direction shown with DFT calculations for free standing Gr [49] (dashed curves). Error bars are shown for some data points. Red curve is a fit to the data – see text.

is almost identical to the one reported for Gr–Cu ($g = (5.7 \pm 0.4) \times 10^{19}$, N/m^3) applying the same procedure [67].

However, we get $\kappa = (0.61 \pm 0.15)$ eV for Gr–sapphire, quite below the value reported for Gr–Cu ($\kappa = (1.30 \pm 0.15)$ eV) and for free standing Gr (κ = 1.20–1.61 eV [107]). This low value of κ reflects the softening of the ZA mode with respect to the one of free standing Gr, and points to a lower Young′s modulus of Gr on sapphire. A recent study has shown that the elastic modulus of Gr decreases with a higher density of vacancies in the Gr lattice [109]. Extrapolation of the data presented in reference [109] shows that a reduction of the Young′s modulus by a factor of 2 can be induced by 2% vacancies. Thus, our results can be interpreted as due to the presence of additional defects in Gr/sapphire (as compared to Gr/Cu), which might arise during the sample preparation through Cu evaporation in vacuum.

4.5 AFM images

Atomic force microscopy (AFM) characterization was carried out at the Instituto de Ciencia de Materiales de Madrid (ICMM) thanks to the assistance of Dr. Félix Jiménez-Villacorta and Prof. Carlos Prieto. Thanks to the proximity (located in the same campus) of this Institute to our laboratory it was possible to characterise the samples as soon as they were removed from the UHV chamber. The AFM images were recorded in the tapping mode using a microscope head and software from Nanotec. Commercial PPP-NCH-w tips, with resonance frequency of about 270 kHz and spring constant around 34 Nm^{-1} (between 10 and 100 Nm^{-1}), adequate for dynamic mode, were utilized to collect topographic images, as well as amplitude and phase mappings. Several areas in different regions were checked for every sample.

Atomic force microscopy confirms the presence of Gr domains over lateral scales of microns in the metal-free regions between Cu microislands formed after Cu evaporation. From a closer examination based on optical and atomic force microscopies the dimensions of these microislands are estimated to be ~0.5-1 μm in height and ~0.5-5 μm in lateral diameter. AFM characterization is focused on the metal-free areas, as shown in Fig. 4.7. AFM topographic images show the presence of large Gr–covered areas. In fact, as illustrated in Fig.4.7a and b, the substrate coverage by Gr layers can reach a value of 80%. A more accurate analysis was completed taking into account several regions of the sample and it can be deduced that the coverage fluctuates between 55% and 80%. Gr flakes reach 1-3 μm size; actually, it seems that some Gr flakes of approximately 3 μm size suspended on the sapphire substrate are apparently torn into smaller flakes. A profile analysis revealed that the Gr layers on the sapphire substrate have a height of 6-8 Å, in agreement with the thickness of monolayer Gr [102], showing randomly oriented wrinkles of 1-4 nm size (see height profiles in Figs. 4.7a and 4.8). Actually, root mean-square (rms) roughness of the Gr layers averaged from randomly selected flakes is 5.3 Å, visibly rougher than the smooth single crystal sapphire substrate, which exhibits an rms roughness of 2.2 Å. An illustration of the rms roughness study is depicted in Fig 4.7c and d. Moreover, residual Cu nanometric grains are observed at the boundaries of the Gr domains, presenting an average size of 2-4 nm, as illustrated in the height profiles (Fig. 4.7a).

The substrate reveals a wavy morphology, attributed to the presence of terraces (see Fig. 4.8) typical from (0001) single crystal sapphire [100]. The height of the steps ranges between 4-5 Å (i.e. around c/3, where c = 12.99 Å is the lattice constant of c–plane

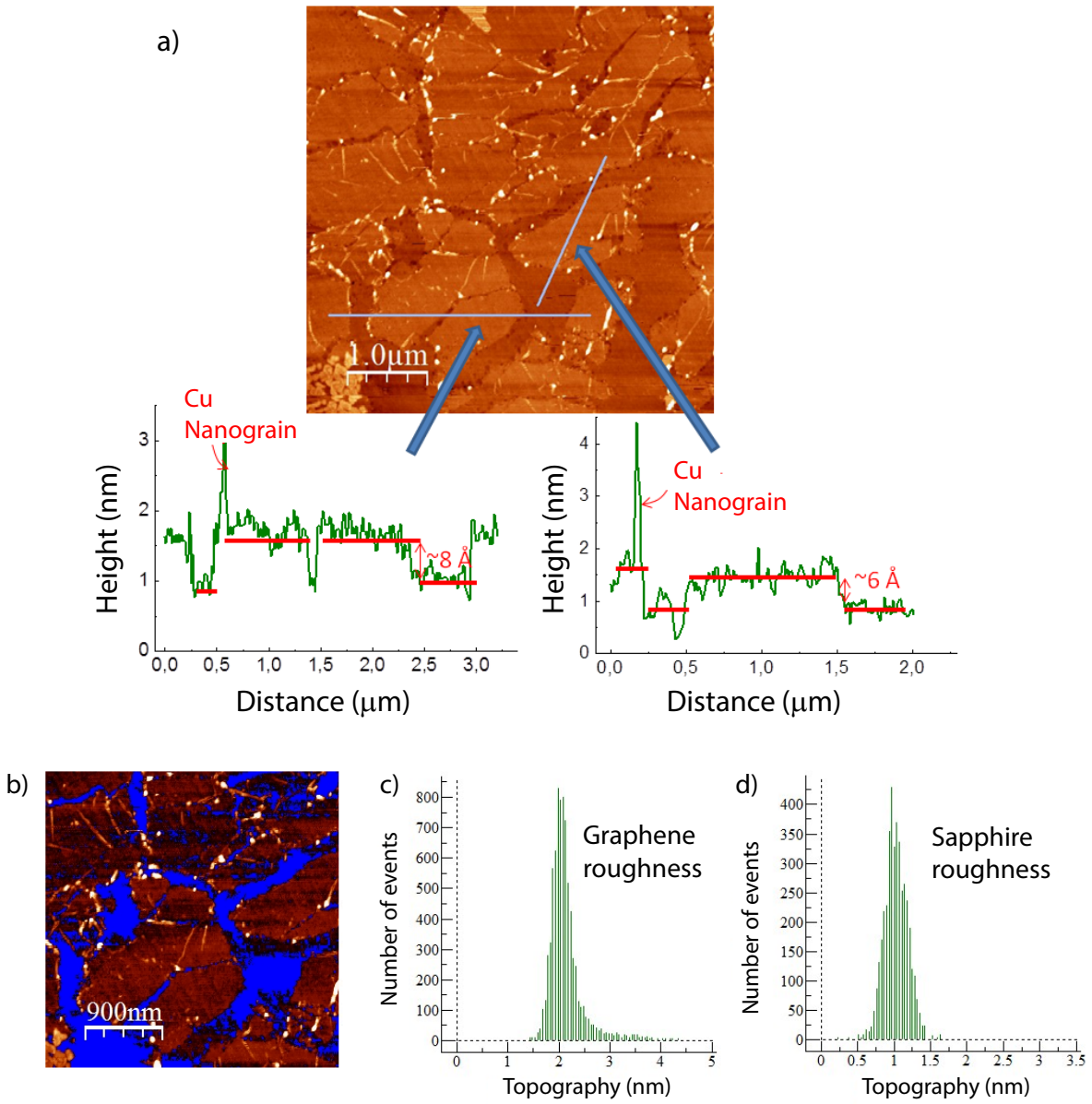

Figure 4.7: (a) AFM topographic image of the Gr/sapphire sample (image: 5 μm × 5 μm, trying to get an appropriate vision of the Gr flake dimensions). AFM image and height profile analysis reveal discontinuous Gr layers of size up to 3 μm, with ∼6-8 Å height. (b) Illustrative example of the estimation of the sapphire coverage by the graphene layers (in this case: 80%), using the flooding analysis (flood height: 1.8 nm). Example describing the estimation of the rms roughness (using height histograms) in the Gr layers (c) and the substrate (d). Several Gr-covered areas and bare substrate areas were selected for the roughness analysis.

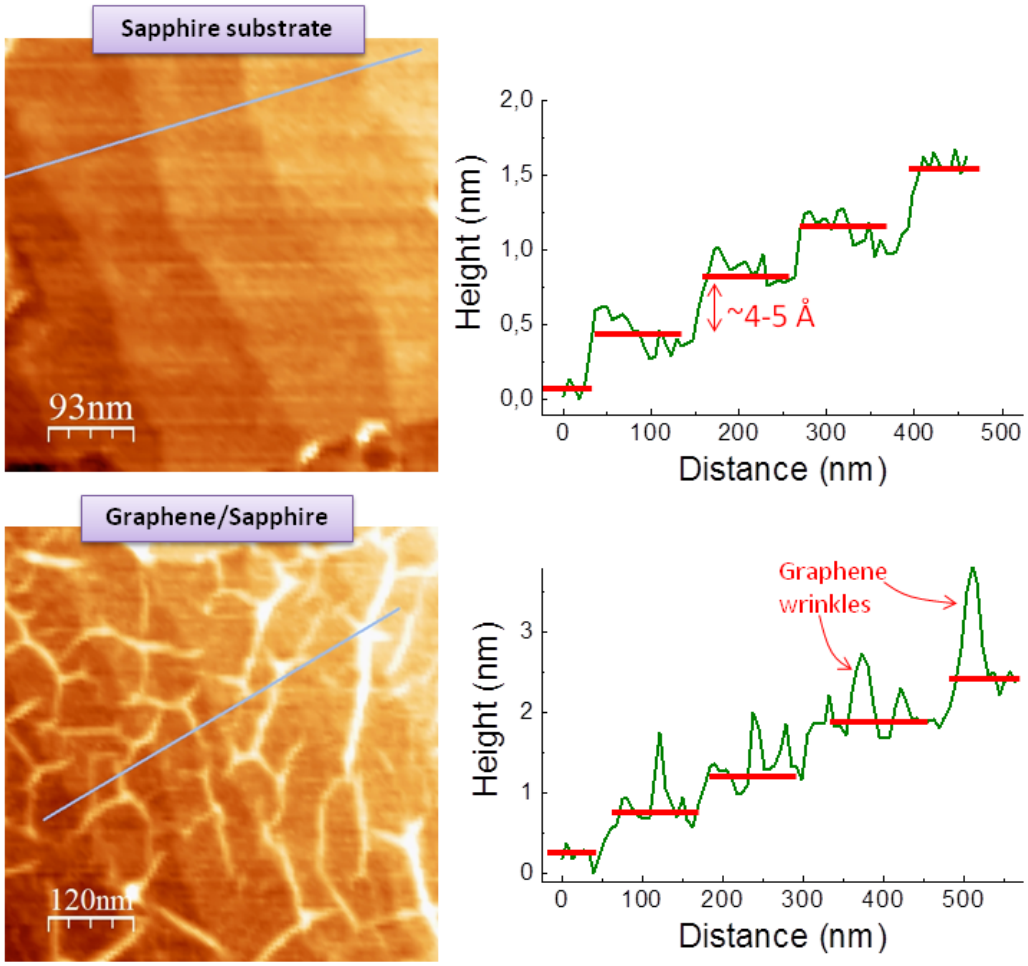

Figure 4.8: AFM images of another region zooming areas representative of the sapphire substrate and Gr/sapphire (with respective height profiles) illustrating the presence of steps corresponding to the substrate and how Gr accommodates to the substrate surface.

sapphire), and its periodicity ranges between 100–150 nm. However, an estimation of the coherence length obtained from the width of the specular HAS peak, that gives an average terraces size [84] of 40 nm, is smaller than the terrace periodicity measured with AFM. This is consistent with the high sensitivity of HAS to low densities of defects, which leads in average to the detection of smaller terraces.

Moreover, the sample exhibits a peculiar morphology of the substrate. From the AFM images in the dynamic mode, the presence of nanometric pits decorating the sapphire substrate is corroborated, predominantly located at the Gr flake boundaries, not present in the bare substrate areas (see Fig. 4.9).

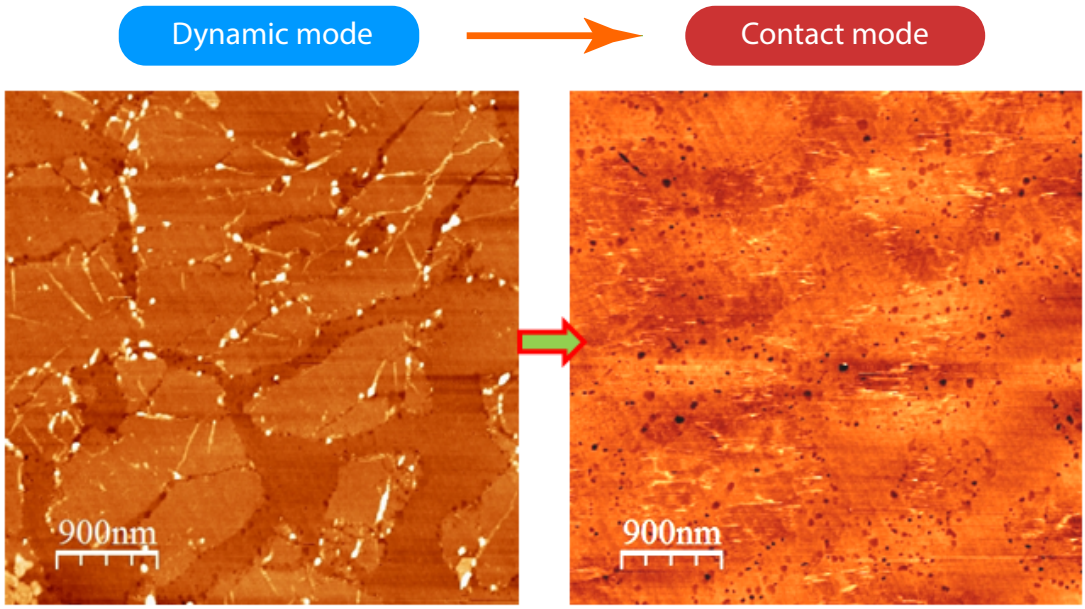

Figure 4.9: Comparison between the topographic images in the dynamic tapping mode and in the contact mode (the normal force mapping of the same area was also represented), revealing that the pit distribution is mainly confined at the Gr domain boundaries.

To gain insight into the possible presence of nanometric pits, we have carried out an additional AFM experiment in the contact mode, which in principle would require a lower spring constant (range 0.1-1 Nm^{-1})[110], using the tip adequate for dynamic mode with a stronger spring constant ($\sim$10-100 Nm^{-1}). Such a strong spring constant of the tip eventually removed the Gr layers, allowing extra topological information and revealing differences between the bare substrate and the substrate underneath the Gr flakes. Contact mode images (Fig. 4.9) confirm the presence of a pit array originally located at the Gr boundary, likely determining the Gr dimensions (depth $\sim$1-2 nm; width variable from 20 to 100 nm). Also, some nanometric pits were observed, to a lesser extent, in the regions where originally Gr settled. The origin of these nanometric pits in the sapphire substrate is likely due to Al_2O_3 carbothermal reduction in vacuum [100, 111]. It is suggested that the tearing process of the Gr layer can be attributed to an effect of such substrate carbothermal reduction combined with the breakthrough of the Gr layer by the evaporated copper.

4.6 UV–VIS transmission spectroscopy

Optical transmission measurements were performed in order to obtain additional information about the transparency and to investigate the effective elimination of the copper between Gr and sapphire substrate. The apparatus for transmission spectroscopy, situated at the ICMM, consists in a double-beam commercial spectrophotometer Varian Cary 4000, with a resolution across UV-Visible spectrum that goes from 180 to 900 nm.

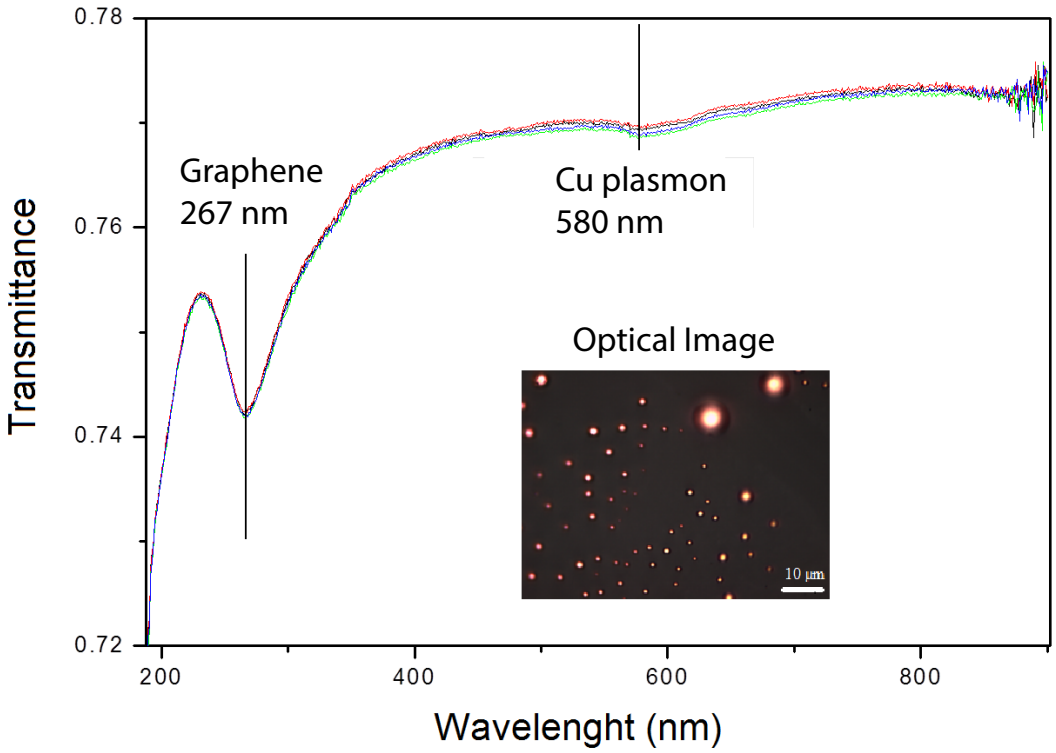

Figure 4.10: Optical transmittance in a 4 mm diameter area. The interband Gr transition and Cu plasmon are detected too. Optical image with Cu residues (scale bar 10 μm) is shown in the inset.

The optical transmission data has been recorded using a window of 4 mm diameter area. Two different areas of the sample have been explored and each area has been normalized with two different clean sapphire substrates. As it is shown in Fig. 4.10, the spectrum is almost the same for all the combinations. The normalization with the substrate is necessary because the intensity of the transmitted beam I depends on the thickness d of the substrate through the relation:

$$I = I_0 e^{-\alpha \mathrm{d}} \tag{4.2}$$

where I_0 is the incident beam intensity and α the absorption coefficient. Thus, a part of the lost intensity is due to the sapphire. The transmittance is defined as the ratio between the outcoming and incoming intensities:

$$T = \frac{I}{I_0} \cdot 100 \tag{4.3}$$

but, in order to evaluate more carefully the transmittance and the features of only the layers above the sapphire, a normalization with clean sapphire substrate is required.

The optical transmittance for Gr/Al_2O_3 after a 30 minutes annealing at 1150 K is around 80%. The characteristic transition at 267 nm reveals the presence of Gr (Fig. 4.10). We ascribe the weak feature around 580 nm to the plasmon of remaining sparse Cu microislands after Cu evaporation, which can also be seen in AFM images (Fig. 4.7a) and in the optical image in Fig. 4.10 shown in the inset.

4.7 Raman spectroscopy

The Raman spectroscopy was carried out at the Instituto de Ciencia de Materiales de Madrid (ICMM) thanks to the assistance of Dr. Esteban Climent-Pascual and Prof. Alicia de Andrés. Raman micro-spectroscopy was also used to characterize the Gr layer before and after the elimination of the copper film for a film thickness of 1000 nm Cu.

The ratio of the intensities of the characteristic Gr G and 2D Raman peaks, I_{2D}/I_G, is related to the quality of the Gr domains, that is, the regularity of the carbon network. For values close to that of pristine Gr, the ratio decrease is related to the presence of strain fields and doping [112, 113]. At high concentration of defects that involve breaking a large fraction of the sp^2 C=C bonds by the formation of vacancies, irregular rings such as Stone Wales defects or O, OH- or other functional groups, the I_{2D}/I_G ratio decreases very significantly and the width of all Raman peaks increases [114]. The so–called defects peak D (TO mode close to the $\overline{K}$ point of the Brillouin Zone) is activated by the presence of defects that supply the required momentum for the Raman process. Therefore, both I_{2D}/I_G and I_D/I_G ratios are used to evaluate the Gr quality. Gr in the as deposited samples is of high quality, with the typical I_{2D}/I_G ratio for Gr on copper and no defects peak D, as shown in Fig. 4.11. After annealing Gr to 1150 K, the I_{2D}/I_G ratio is very similar to the as deposited sample but the defect peak clearly increases, as shown in Fig. 4.11 and Figs. 4.12e-f. This has been observed for Gr on remaining Cu regions and in areas where Cu has been completely eliminated. Raman images of Gr/sapphire have been measured to obtain a statistical analysis of the relevant parameters. The

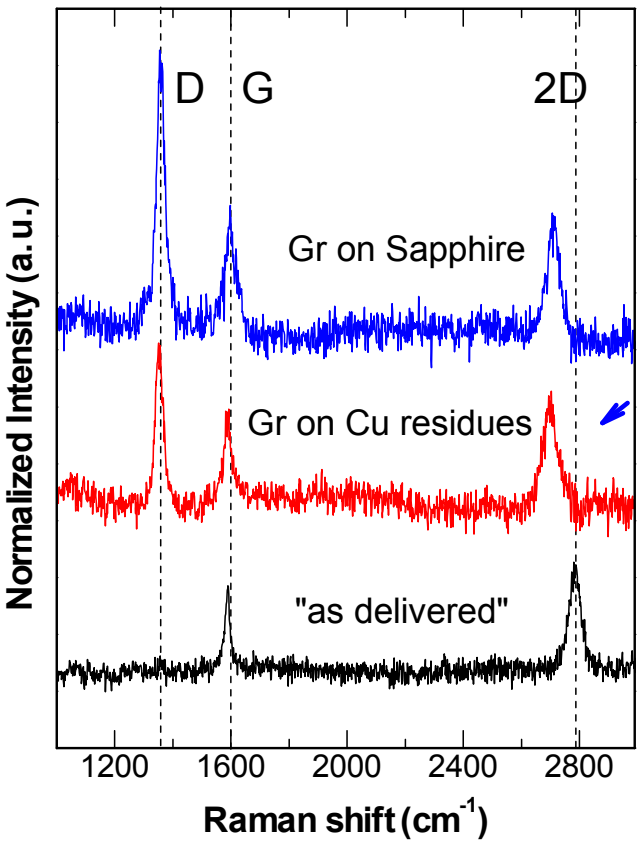

Figure 4.11: Raman spectra of Gr on Cu/Al_2O_3 as deposited (black spectrum), after annealing on remaining Cu microstructures (red spectrum) and on sapphire (blue spectrum). The background due to copper has been eliminated for clarity. D, G and 2D characteristic peaks of Gr are indicated.

optical image of a 10×10 μm^2 area of the sample is replicated by the Raman image of the background (Fig. 4.12 a and b) due to Cu (2000–2500 cm^{-1} region) allowing us to distinguish Gr/Cu and Gr/sapphire regions (Fig. 4.12e-f). This area is representative of the measured Raman images. The image obtained from the I_{2D}/I_G intensity ratio (Fig. 4.12d) evidences the uniformity of Gr over the sample and its quality in terms of the regularity of the carbon network, which is similar to the as–deposited Gr. On the contrary, the I_D/I_G image indicates that the density of defects on sapphire is higher that on the remaining Cu regions (Fig. 4.12c). The intensity of D peak is a compromise between an enhancing factor, the formation of defects that allows the Raman process, and a depleting factor which is the reduction of the density of carbon aromatic rings. D mode corresponds to a vibration of the aromatic rings while G vibration only requires sp^2 hybridization of carbon, therefore G peak intensity is much less sensitive to the presence of defects. The I_D/I_G ratio is used to estimate the density of point defects (0D defects) or the size

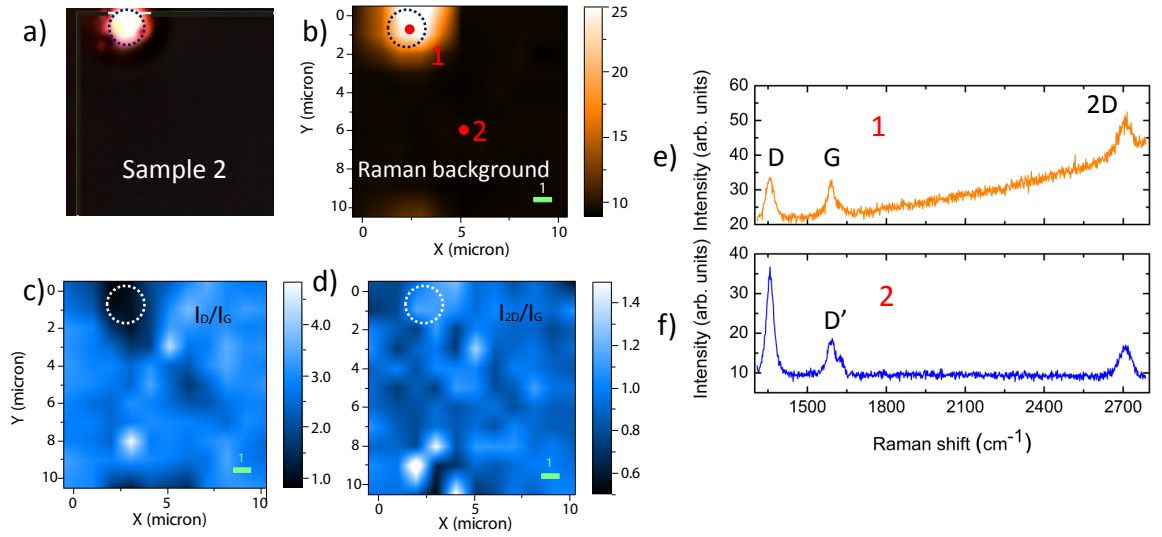

Figure 4.12: a) Optical image, b) Raman image (10 × 10 μm^2) of the background revealing the Cu residues. c) I_D/I_G and d) I_{2D}/I_G Raman images. Raman spectra of Gr on Cu (e) and on sapphire sample (or remaining Cu microstructures) (f). D, G and 2D characteristic peaks of Gr are indicated.

of Gr grains (1D defects) by using different formulas. Both situations present similar behavior upon increasing the defects density or reducing the Gr size: the I_D/I_G ratio first increases up to a maximum value that depends on the excitation wavelength (stage I) and then decreases (stage II). Deciding which kind of defect (0D or 1D) is predominant is not straightforward in most cases. The pioneering work of Tuinstra and Koening (TK) [53] on nanocrystalline graphite established that

$$\frac{I_D}{I_G} = \frac{C}{L_a} \qquad \text{(Stage I)} \tag{4.4}$$

where L_a is the graphite crystallite size and C depends on the laser excitation wavelength. This dependence was established to be $C(\lambda)(\text{nm}) = 2.4 \times 10^{-10}\lambda^4$ (nm) [115] (stage I).

However below around 2-3 nm there is a second regime (stage II) where the ratio decreases as the crystallite size is reduced [54]

$$\frac{I_D}{I_G} = C' L_a^2 \qquad \text{(Stage II)} \tag{4.5}$$

The constant C' is obtained by imposing continuity between both stages resulting in our case $C' \sim 0.438$ for λ_{laser} = 488 nm.

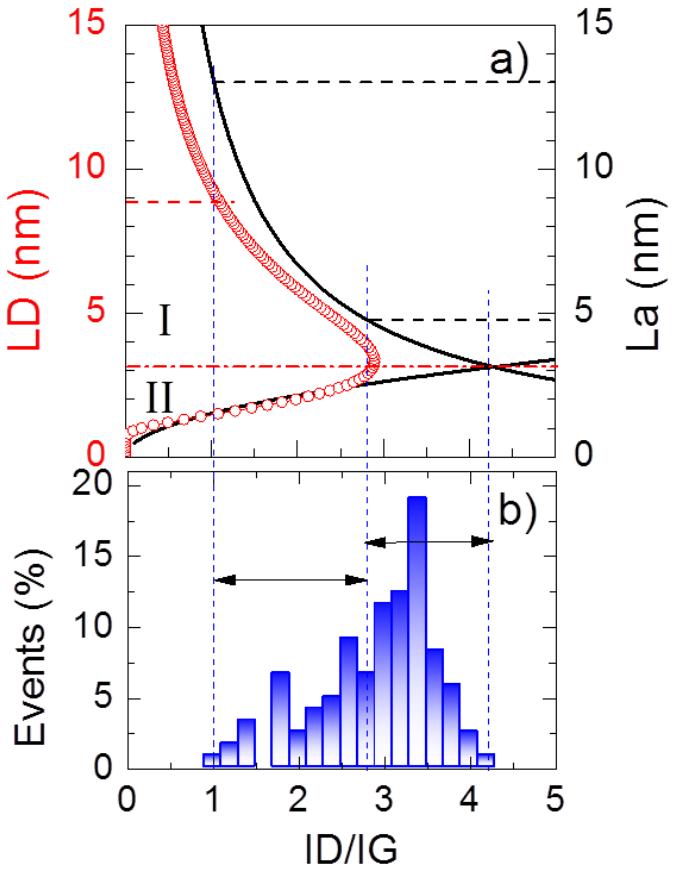

Figure 4.13: a) L_a (black lines) and L_D (red circles) versus I_D/I_G for λ_{laser} = 488 nm; b) statistical distribution of I_D/I_G values in the Raman image of Fig. 4.12e.

On the other hand, the controlled ion bombardment of Gr with different doses to produce carbon vacancies has led to a phenomenological model proposed by Lucchese *et al.* [116] that correlates I_D/I_G and the distance between the defects, L_D . In order to correlate I_D/I_G and the distance between the defects, L_D, the following equation has been used [116] :

$$\frac{I_D}{I_G} = C_A \frac{(r_A^2 - r_S^2)}{(r_A^2 - 2r_S^2)} [e^{-\pi r_S^2/L_D^2} - e^{-\pi(r_A^2 - r_S^2)/L_D^2}] \tag{4.6}$$

with r_a and r_s the length scales that define the region where the D band scattering occurs. r_s is the radius of the structurally disordered area brought on the impact of the ion. r_a is referred as the radius of the area around the point defect in which the D band scattering take place [117]. By taking r_a= 3.1 nm, r_s = 1 nm and C_a = (160 ± 48) E_L^{-4}

deduced from a fit to experimental data [117] the eq. 4.6 can be rewritten as:

$$\frac{I_D}{I_G} = \frac{160}{E_L^4}[e^{-\pi/L_D^2} - e^{-\pi 8.61/L_D^2}] \tag{4.7}$$

The functional dependences of L_a (black lines) and L_D (red circles) versus I_D/I_G are plotted in Fig. 4.11a for λ_{laser} = 488 nm.

Fig. 4.13b shows the number of events of the I_D/I_G values obtained in the Raman image of Fig. 4.12c. The distribution is wide and reaches I_D/I_G ratio up to 4. Since both L_a and L_D are bivaluated, to know whether Gr is in stage I or II we have to look at the widths of the peaks and at the I_{2D}/I_G values. The narrowness of the peaks and the high I_{2D}/I_G ratio ensure that Gr is in stage I in spite of the very high I_D/I_G values. The wide distribution of Fig. 4.13b can be explained to be due to Gr domains with size L_a from 14 to 3 nm (following the black curve in stage I) or to a combination of large regions with point defects with distances L_D = 3 to 9 nm (from the curve with red circles) for the lower I_D/I_G values up to around 2.9 and small Gr domains in the range from 3 to 5 nm for $2.9 < I_D/I_G < 4$. These two scenarios cannot be differentiated by Raman spectroscopy alone; however, the information provided by He diffraction indicates that large coherent domains are present, therefore discarding the first case. The 0D defects density can be then calculated for the $I_D/I_G < 2.9$ using the following relation [52, 116]

$$n_D(cm^{-2}) = \frac{10^{14}}{\pi L_D^2} \tag{4.8}$$

obtaining $n_D = 3 \times 10^{13}$ to 3×10^{12}cm^{-2}. Since the density of carbon atoms in Gr is 3.9×10^{15}cm^{-2}, the estimated defect fractions, from 0.7% to 7%, are below the threshold for the reduction of He diffraction intensity.

4.8 Modified method

4.8.1 He–reflectivity improvements

Several samples have been used in order to improve the preparation method and to obtain a better Gr on sapphire surface with a more reduced number of defects. For this purpose a change in the copper evaporation process has been introduced. During the heating of the Gr/Cu/Al_2O_3 sample, C_2H_4 was introduced in the chamber. In this way, the Gr breaking may be prevented. The He diffraction experiments were carried out in the TEAMS system, which enables the determination of the diffraction reflectivities by

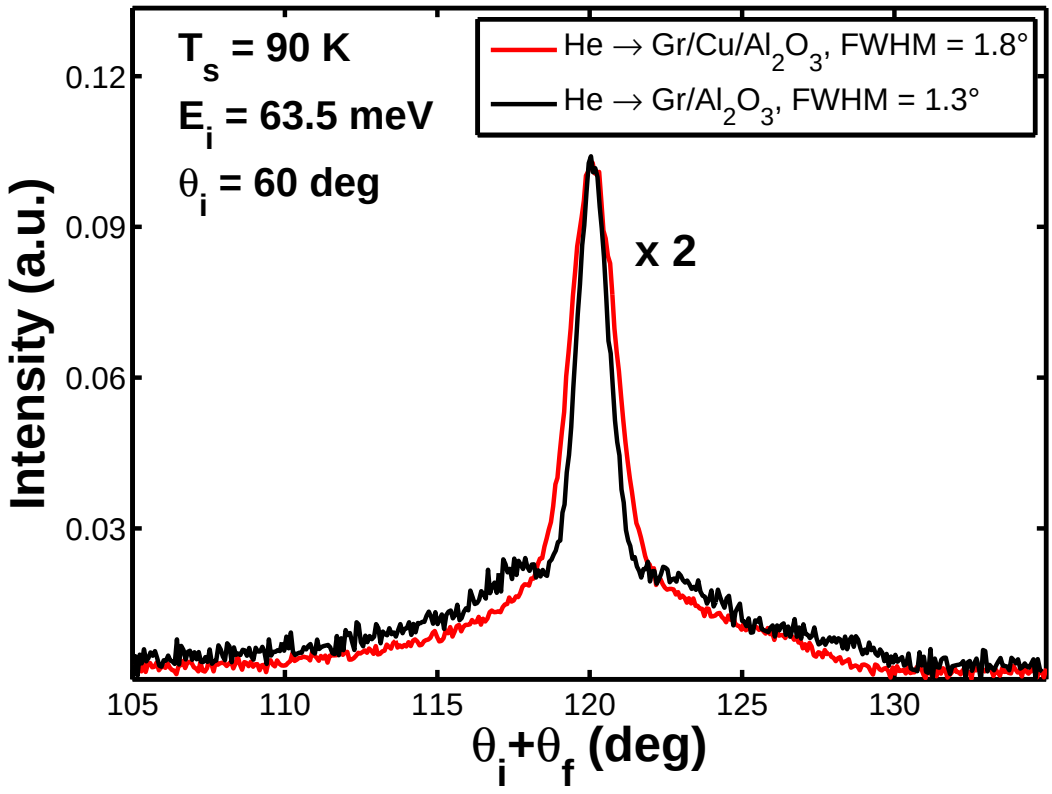

Figure 4.14: Angular distribution of He atoms scattered by $Gr/Cu/Al_2O_3$ (red spectrum) and Gr/Al_2O_3 (black spectrum) along $\overline{\Gamma M}$, measured with TEMAS machine. Diffraction peaks corresponding to the moiré superstructure can be seen in the black spectrum.

measuring directly the incident beam intensity. Angular distributions of He atoms have been recorded before and after the Cu elimination. Fig 4.14 shows a comparison of He scattering by $Gr/Cu/Al_2O_3$ (red spectrum) and Gr/Al_2O_3 (black spectrum) measured along $\overline{\Gamma M}$ direction and under the same conditions: incident beam energy E_i =63.5 meV, surface temperature T_S = 90 K and incident angle θ_i = 60°. Also in this case the narrowing of the specular peak when copper leaves the surface is clear. By performing Gaussian fits to the specular peaks, we obtained the following widths: FWHM = 1.8° for $Gr/Cu/Al_2O_3$ and FWHM = 1.3° for Gr/Al_2O_3. The latter is closer to the angular resolution of the TEAMS instrument, thus revealing the extremely high surface quality of the sample and proving the presence of homogeneous and flat Gr domains. The TEAMS machine does not permit to resolve in detail the diffraction peaks of the Gr/Al_2O_3. However, the convolution of the first order peaks corresponding to the moiré superstructure closest to the specular peak is evident on the black spectrum. The measured absolute reflectivity of He atoms at this

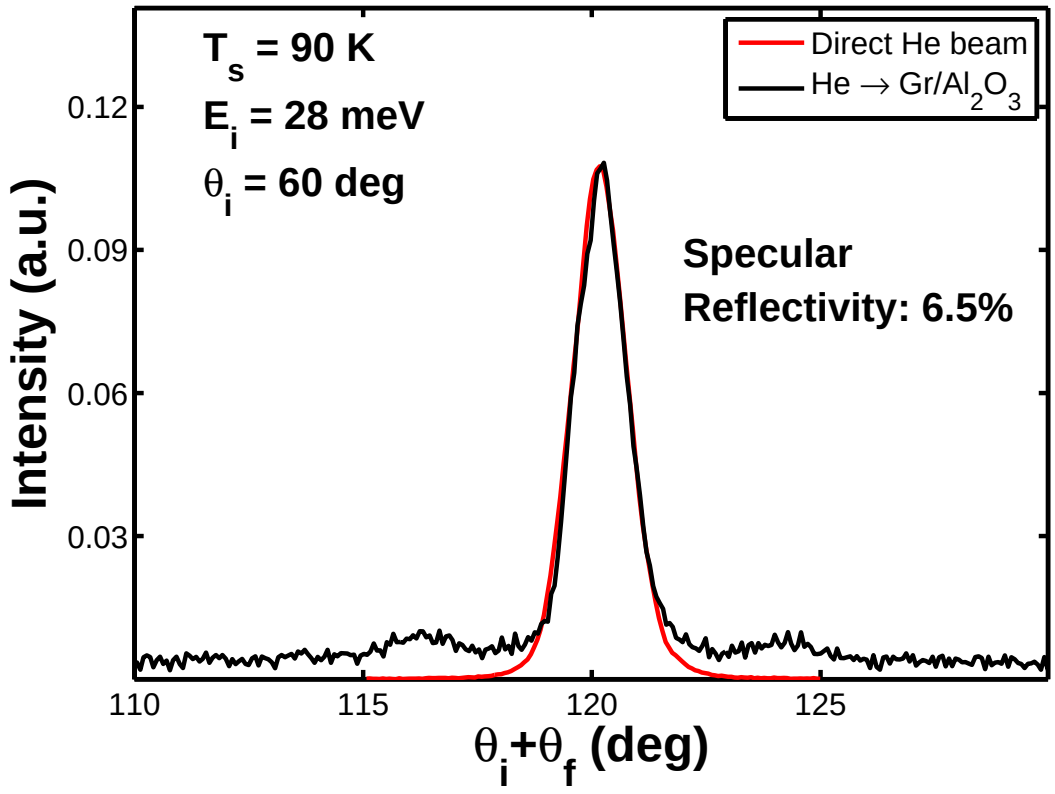

Figure 4.15: Comparison of the incident He beam intensity (red spectrum) with the specular He reflectivity for Gr/Al_2O_3 (black spectrum). The incident energy is 28 meV.

incident energy and angle is a 7.5% for $Gr/Cu/Al_2O_3$ and a 3.5% for Gr/Al_2O_3.

A comparison of the specular Gr/Al_2O_3 peak (black line) to the He direct beam (red line), recorded at E_i = 28 meV, is shown in Fig. 4.15. The specular absolute reflectivity for Gr/Al_2O_3 reaches a maximum of 6.5% when the incident beam is cooled down (E_i = 28 meV). The observation of the sharp specular peak is remarked through Fig. 4.15, where the profile of the Gr/Al_2O_3 peak follows the shape of the direct beam. No difference in the FWHM has been recorded. The value of the FWHM is 1.2° for incident and reflected beam. This remarkable result confirms the extremely high quality of surface ordering and cleanliness for the Gr/Al_2O_3 sample.

4.8.2 AFM

AFM images are recorded under the same experimental conditions that the ones used in the first method. Several images were collected, checking different regions of the sample.

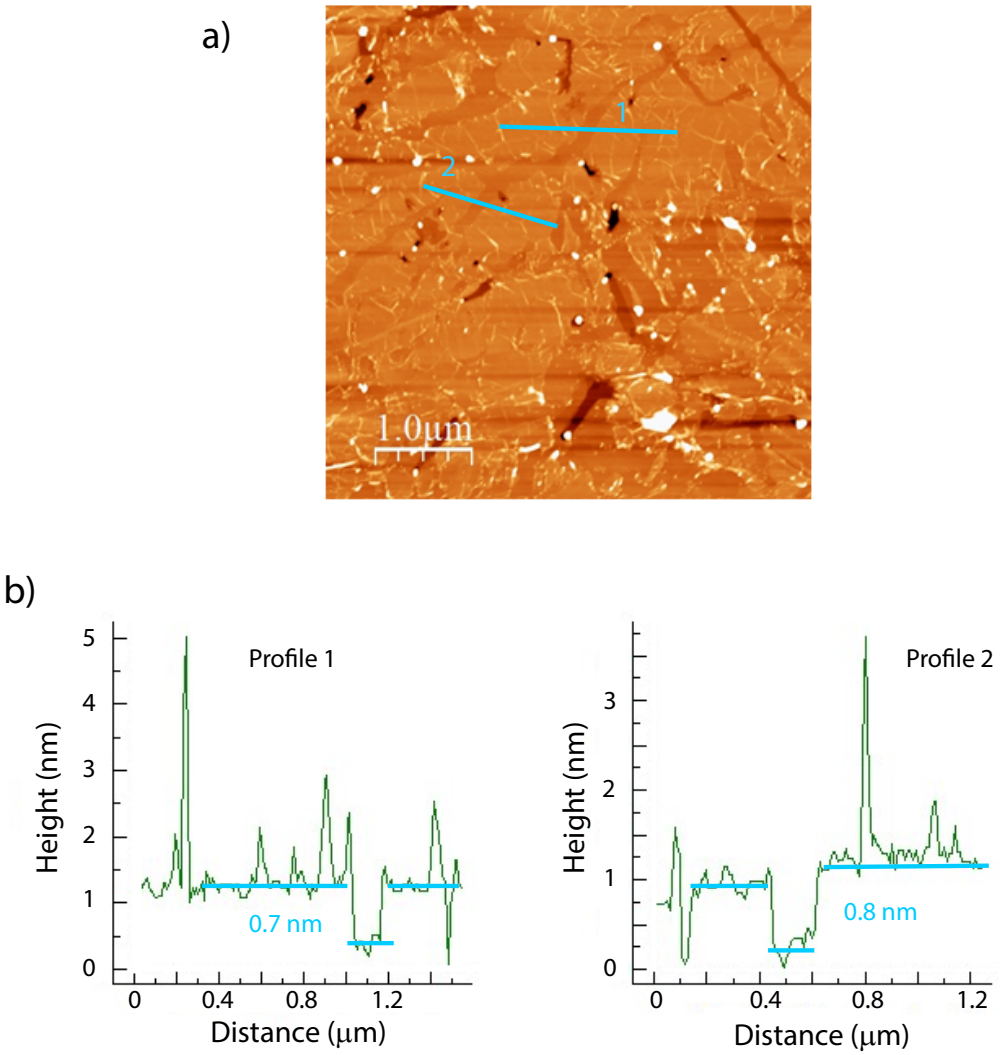

Figure 4.16: (a) AFM topographic image of the Gr/sapphire sample prepared with Ethylene during the Cu evaporation. (b) Height profile analysis scanning two different regions of the surface sample.

Atomic force microscopy images shown in Fig. 4.16a confirm the presence of Gr covering sapphire substrate. As shown in Fig 4.16 b, the hight profile analysis reveals, from the discontinuities of Gr, that the height from the substrate is about 7-8 Å, in agreement with the thickness of Gr monolayer [102]. The morphology of the flakes is similar to the one obtained with the first method. However, a higher Gr coverage and bigger flakes are observed than the one present in the sample prepared without C_2H_4 during the Cu

evaporation. The dimensions of the Gr microislands are estimated to be 1-4 μm. The root mean-square (rms) roughness of the Gr layers averaged from a selected flake is 3 Å smoother than the Gr layer grown with the first method. Also with this sample, Cu microislands are present after Cu evaporation and they have an average height of ~25-50 nm. Finally, big irregular canyon-shaped holes of the substrate (5 nm depth) are observed.

4.8.3 Transmittance improvements

Optical transmission measurements for a 4 mm diameter area have been performed for Gr/Al_2O_3 after annealing at 1150 K in C_2H_4 ambient. Two different areas of the sample have been explored and each area has been normalized with a clean sapphire substrate. The blue and red lines in Fig. 4.17 represents the optical transmittance in these two areas. Highest transmittance can be obtained with the modified method, reaching a 90%.

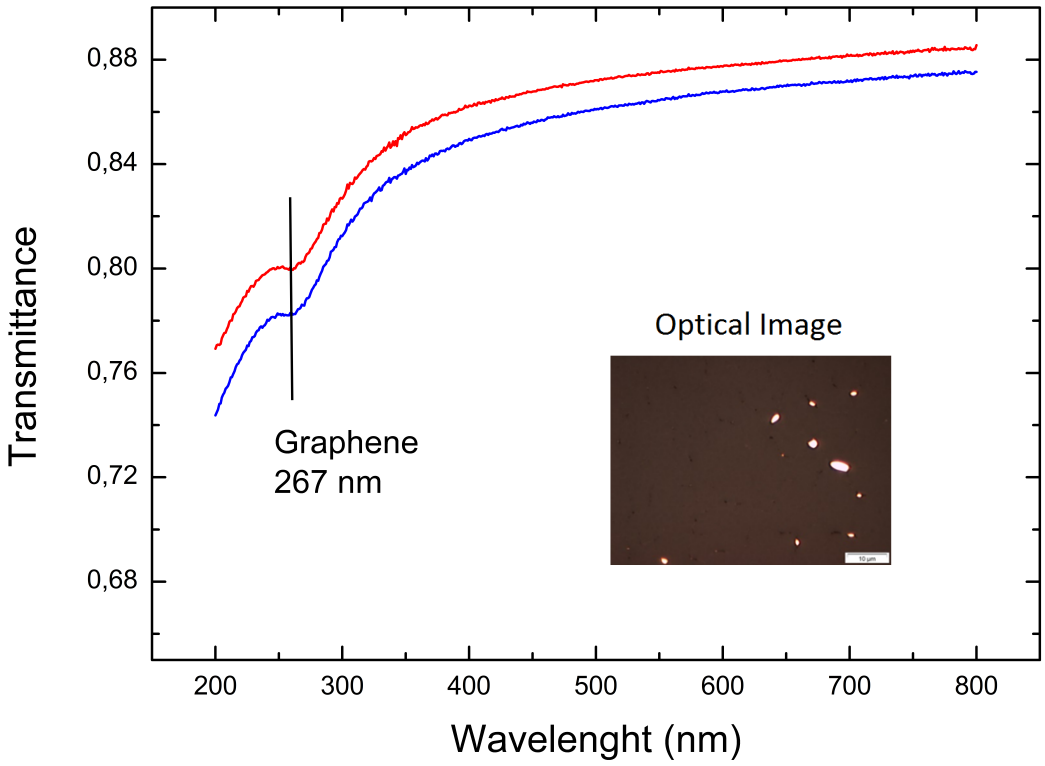

Figure 4.17: Modified method: Optical transmittance in a 4 mm diameter area. The interband Gr transition is detected. Optical image with few Cu residues (scale bar 10 μm) is shown in the inset.

The presence of Gr is testified by the characteristic transition at 267 nm. The optical

image shown in the inset of Fig. 4.17 reveals fewer Cu microislands remained after Cu evaporation than the ones observed with the first method (inset in Fig. 4.10). A better Cu removal is also evidenced by the fact that the Cu plasmon is not detected.

4.8.4 Raman: D mode depleted

As shown in Fig. 4.18 (black spectrum) the Gr in as–deposited sample of 1000 nm Cu film is of high quality (adequate I_{2D}/I_G ratio and no defects peak D). After annealing the sample at 1150K in C_2H_4 ambient, the almost complete elimination of Cu is attained without any significant deterioration of the Gr film. In the areas where copper has been completely eliminated the I_{2D}/I_G ratio decreases only slightly and the defect peak D, although still present, is clearly reduced (Fig. 4.18) in comparison with the sample prepared with the first method (red spectrum). Raman images of the sample have been measured to analyze with higher detail the quality Gr layer and to obtain a statistical analysis of several parameters. The optical image of a 15 × 15 μm^2 area of the sample is replicated by the Raman image of the background due to Cu (1680-2600 cm^{-1} region), Fig. 4.19c, thus allowing to identify when Gr is on Cu and when it is on sapphire.

The mapping of the I_{2D}/I_G intensity ratio shown in Fig. 4.19b reveals the uniformity of Gr over the sapphire surface and that its quality is maintained. The I_{2D}/I_G ratio for Gr/Al_2O_3 has an average of 1.25 (histogram in Fig 4.19d) only slightly lower than the value measured for the as-delivered sample of $Gr/Cu/Al_2O_3$ (~1.4), and higher than the measured for the Gr/Al_2O_3 prepared with the first method (~1). The image obtained from the I_D/I_G intensity ratio, Fig. 4.19a, evidences the presence of defects, although the ratio is considerably reduced in comparison with Gr on sapphire prepared with the first method. From the histogram shown in Fig. 4.19e it can be seen how the ratio oscillates between 0.6 and 1.6, with an average value of 1.1, whereas for the other sample the distribution was very wide and the ratio fluctuated between 1 and 4. From the I_D/I_G ratio it is possible to estimate the distance between defects (L_D) for point defects (0D), the defect density and the size L_a of the pristine Gr areas (1D). As shown in the precedent section, both L_D and L_a experiment two different behaviours depending on the Gr being in a low density defects regime (Stage I) or a high one (stage II). Due to the narrowness of the peaks and the high I_{2D}/I_G ratio it is possible to conclude that the Gr is in the Stage I. Giving that the range of the I_{2D}/I_G ratio is known, it is possible to evaluate L_D and L_a thanks to the eq. 4.7 and eq. 4.4 respectively. For low defect density ($L_D \geq 10$ nm) the eq.

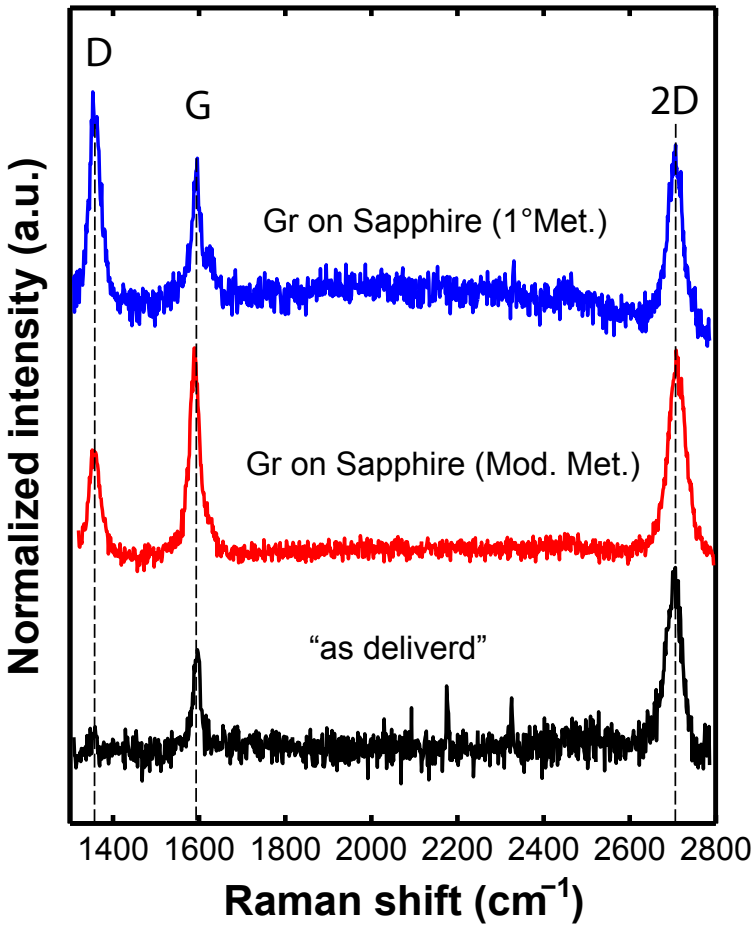

Figure 4.18: Raman spectra of the sample with 1000 nm Cu film as deposited (black curve) and after annealing the sample in C_2H_4 during the copper elimination (blue curve). For comparison the Raman spectra of Gr on sapphire obtained with the first method is shown (red curve). The background due to copper in "as delivered" sample has been eliminated for clarity. D, G and 2D characteristic peaks of Gr are indicated.

4.7 can be approximated giving the following experimental relation [117]

$$L_D^2(nm^2) = \frac{4.3 \times 10^3}{E_L^4(eV^4)} \left[\frac{I_D}{I_G}\right]^{-1} \tag{4.9}$$

Thus, the distribution in Fig. 4.19d can be explained to be due to Gr domain size L_a, from 13 to 8 nm, or to a large region with point defects with distance L_D=11 to 16 nm. Raman spectroscopy cannot distinguish between this two scenarios. However, thanks to the information provided by He–diffraction that points to large coherent domains, the

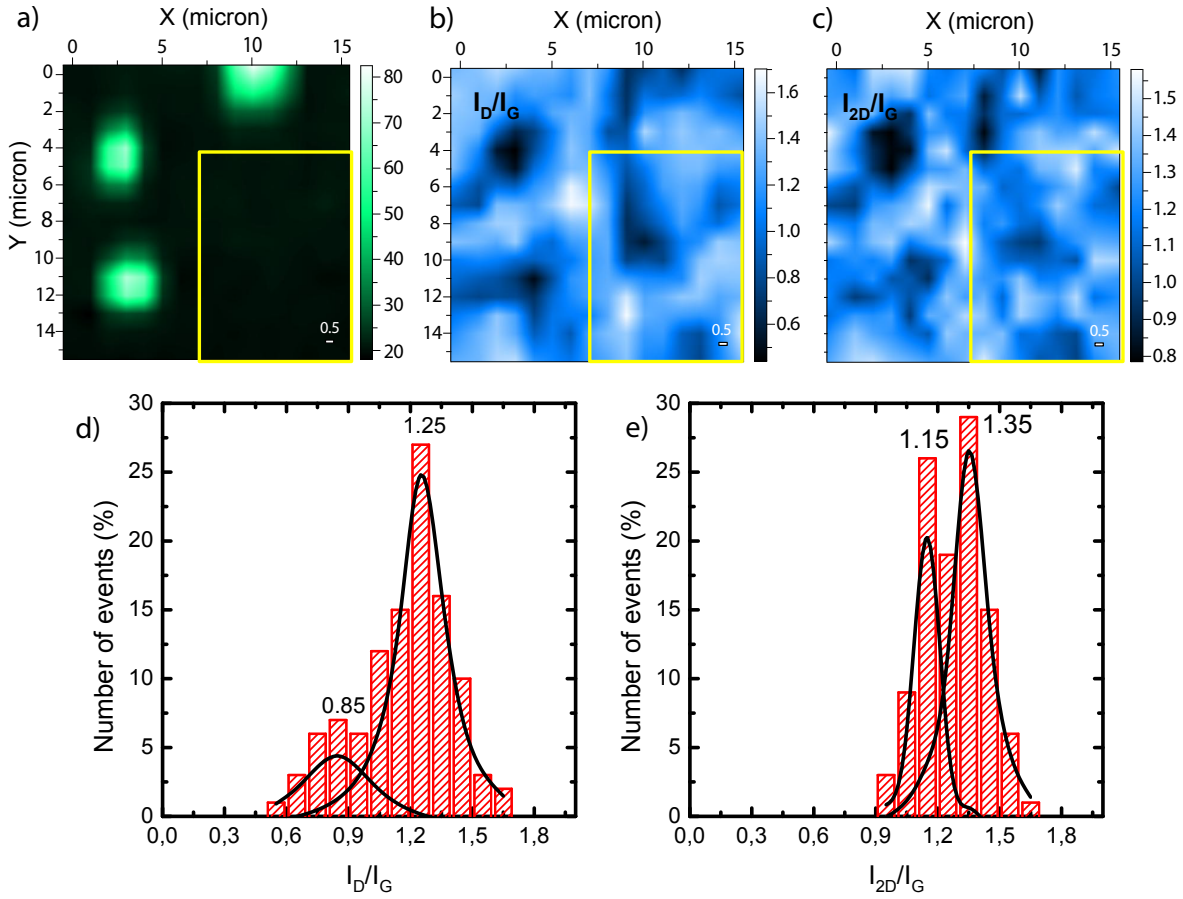

Figure 4.19: Modified method: a) Raman image of the background revealing the Cu residues between 1680 and 2600 cm^{-1}; b) I_D/I_G and (c) I_{2D}/I_G Raman images; statistical distribution of I_D/I_G (d) and I_{2D}/I_G (e) values in the yellow rectangle of the Raman images b) and c) respectively.

presence of 1D defects can be discarded. An estimation of 0D defects is provided from Eq. 4.8, obtaining $n_D = 1.2 \times 10^{11}$ to $3 \times 10^{11} cm^{-2}$, that leads to a defect fraction of 0.003% - 0.007%, noticeable below the defect fraction found with the first method.

4.9 Discussion and remark: long-range order from HAS versus lattice defects from Raman spectroscopy

An important message from our study is that the wrong conclusion might be drawn if both HAS and Raman results were not both available. The observation of clear diffraction

peaks, including a moiré pattern, suggests the existence of a well–ordered Gr overlayer, with little presence of defects, whereas the observation of a pronounced D peak in Raman spectra points to a Gr layer broken into nanometric patches or grains. It should be kept in mind that the two techniques probe different length-scales and are sensitive to different aspects of Gr. While HAS probes macroscopic regions (mm), Raman microscopy averages information from areas $\sim 0.7\mu m$ in diameter. Most importantly, the He–diffraction signal originates from the less defective regions while Raman D peak originates exclusively from the defects of Gr (red areas in Fig. 4.20). Therefore, these techniques reveal quite different aspects of the same samples. Nevertheless, the high intensity of the HAS diffraction peak indicates its origin from a large fraction of the sample and the hundreds of Raman spectra collected across several $10\mu m \times 10\mu m$ areas present small variations. Therefore, the combination of both sets of data proves the existence of large domains of Gr with localized defects as carbon vacancies or arrays of vacancies probably originating during the Cu evaporation at the wrinkles or defects present in the initial Gr layer grown on the Cu film.

The average domain size of Gr/sapphire derived from HAS is 2000 nm, in good agreement with the Gr size obtained from AFM data. For the underlying sapphire substrate, AFM images show terraces (4–5 Å height) with an average domain size of 120 nm, much larger than the 40 nm obtained for the sapphire substrate from the specular width in HAS (which sets a lower limit to the domain size). The different values obtained with AFM and HAS for the average domain size of sapphire are a consequence of the different interaction mechanisms involved in both techniques. Thermal energy He atoms interact with the surface at a very low electron density (ca. 10^{-4} a.u.), 2–3 Å above the surface atoms. This interaction is characterized by a large cross section to single defects. Thus, defects on sapphire reduce the domain size as seen by HAS, leading to detection of smaller terraces in average as compared to AFM. The larger domain size observed for Gr/sapphire is a consequence of a similar mechamism. The Gr layer covers the sapphire substrate like a carpet (see Fig. 4.20), hiding defects and steps, leading to the appearance of larger coherently diffracting domains. This mechanism can be deduced from the strong reduction of the specular FWHM for Gr/sapphire as compared to the sapphire substrate.

The high sensitivity of HAS to point defects, combined with the Debye–Waller attenuation of diffraction intensities, makes it impossible to detect diffraction from surfaces as soon as the density of defects is larger than 15–20 %. This explains for instance the absence of diffraction features from sapphire substrates prepared from scratch, in situ, in our laboratory. Thus, from the observation of high specular reflectivity and

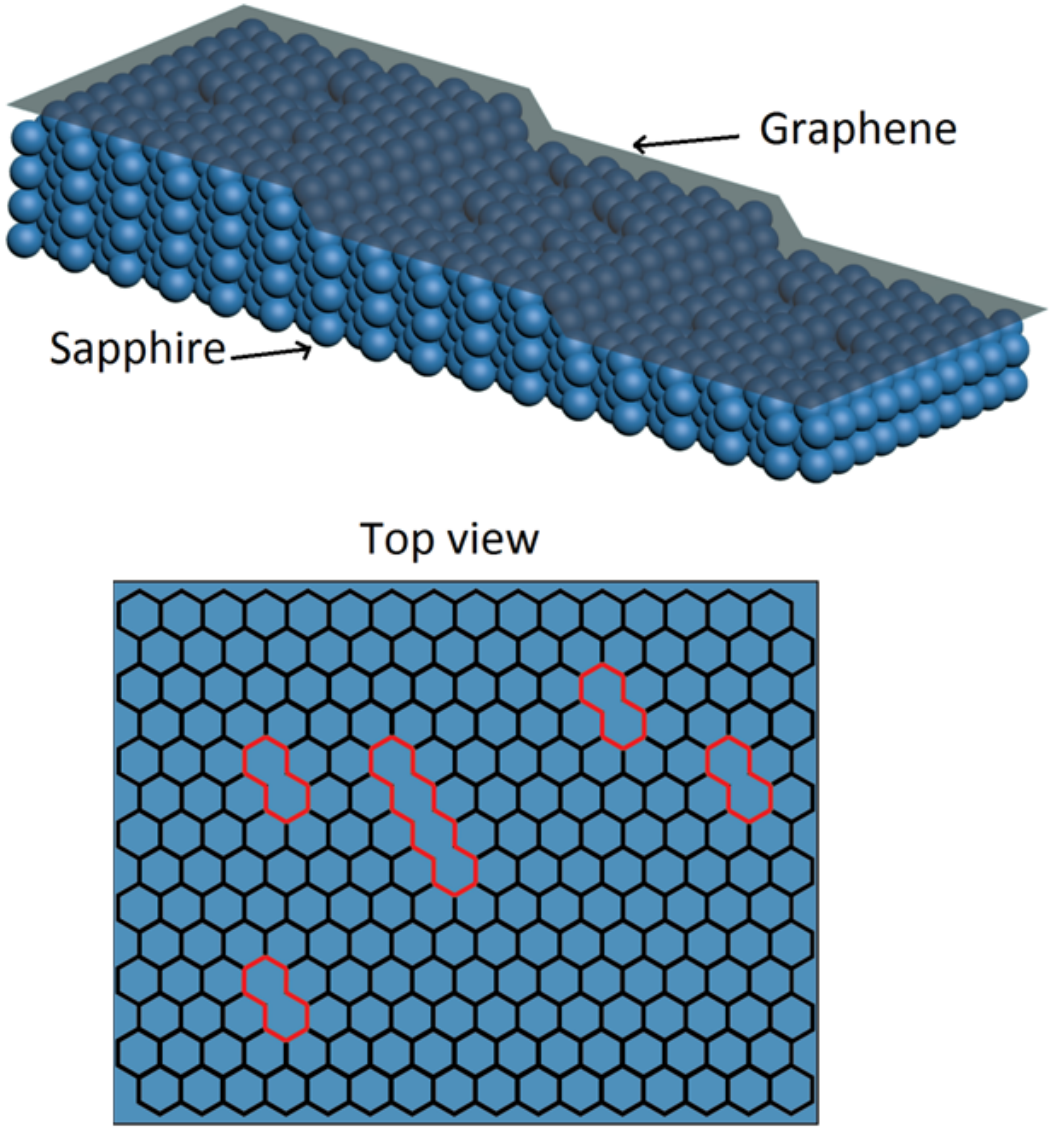

Figure 4.20: Simplified view of the model proposed to explain both HAS and Raman results of Gr on sapphire. The top view shows a surface area leading to He–diffraction. The red areas represent regions leading to the appearance of Raman D signal (Gr defects). See text for details.

diffraction peaks from Gr/sapphire, we can conclude that the density of point defects must be near 5%. This is consistent with the estimation made from the Raman data (0.7 to 7%) and the 2% derived from the determination of the bending rigidity by phonon measurements. Furthermore, this density of point defects is considerably smaller for the modified method, in which a higher reflectivity of the He points out to a minor defect density, estimated around 2%. This value is in agreement with the very low defect

fraction estimated from Raman data (0.003 to 0.007%). The almost complete elimination of Cu is attained without any significant deterioration of the Gr film. This is possible due to the strong planar C–C bond in comparison with the weak Gr-Cu interaction. Presumably, the Cu film leaves the substrate through defects and borders of the Gr patches, as suggested by the detection of ultra–small Cu particles (around 2–3 nm) at theses borders (Fig. 5a). In the case of modified method the deterioration is mitigated by means of ethylene exposure during copper elimination. One possible mechanism for Gr quality improvement could be the partial dissociation of the ethylene, that favours the reconstruction of the Gr itself during Cu evaporation.

4.10 Conclusions

In this chapter it has been shown that a high-quality Gr layer on sapphire can be grown by heating in UHV a Gr layer prepared by CVD on Cu(111)/Al_2O_3. The heating process leads to evaporation of the Cu film, leaving a Gr layer deposited on the sapphire substrate. A second method, named modified method, leads to improve the quality of the Gr layer. The modified method contemplates the use of ethylene during the copper evaporation. Best results have been achieved with this last method.

HAS and AFM data prove the presence of flat and large Gr domains over lateral scales of microns. He–diffraction data reveal that Gr forms an (11×11) moiré pattern, aligned with the (1×1) sapphire unit cell. The lattice constant of Gr on sapphire is $a = (2.44 \pm 0.02)$Å. The bending rigidity $k = (0.61 \pm 0.15)$ eV and the Gr–sapphire coupling strength $g = (5.8 \pm 0.4) \times 10^{19} N/m^3$ have been determined from HAS data of the phonon dispersion of the Gr flexural mode.

Raman mapping shows that the G to 2D peak ratio is comparable for both Gr/Cu/Al_2O_3 and Gr/Al_2O_3 samples, suggesting that the final quality is mainly limited by the quality of the starting Gr layer. Our study shows that the observation of clear He–diffraction features, which points to the existence of large Gr domains over a macroscopic region (of the order of a few microns), may be consistent with the simultaneous observation of large Raman D-peaks arising from regions on the surface not large enough to produce diffraction peaks.

The high specular He reflectivity, reaching 6.5%, the flatness of the surface and a remarkable stability under ambient conditions suggest that Gr/Al_2O_3 represents a significant step in the development of high-reflectivity curved surface mirrors for He-atom microscopy. Sapphire-based Gr layers provide an alternative avenue for the fabrication of

the focusing mirrors in relation to Gr on single crystal metals. For instance, growing Gr on a curved sapphire substrate with the desired focal length should provide a crystalline mirror that incorporates both characteristics of He-reflectivity and those of focusing of a curved mirror.

Finally, we would like to summarize the main advantages of these two method: a short preparation time, from 30 minutes (for the first method) to 2 hours and half (for the modified method), moderate heating temperatures ($\sim 900^{\circ}$C) and high transparency (90%) in the visible range, making these samples suitable for many other applications that require both transparency and electrical conductivity. Moreover, since the method is performed in UHV, it keeps the Gr surface free of contaminants.

CHAPTER 5

FLEXIBLE THIN CRYSTAL MIRRORS

This chapter presents a characterization of flexible thin crystal by means of He scattering. The recent availability of commercial thin crystals led to a renewed interest in curved mirrors as reflective elements for He–microscopy. We have investigated the reflectivity to incoming He atoms of Cu(111), Ni(111) and Ru(0001) crystals of thickness between 50 and 150 μm as well as of Ru(0001) and Ni(111) films deposited on Mica substrate. The results of the thin single crystals have been compared with the ones obtained from bulk crystal surfaces. Our study reveals that a 100 μm thick Cu(111) crystal is the best candidate to be employed as a curved mirror, with an absolute reflectivity of 20% and a long-range crystalline order larger than 200 nm. In contrast, much lower reflectivities (3%-14%) have been measured for thin Ni(111) and Ru(0001) crystals. Remarkable results have been obtained with the Ru(0001)/mica system, that reveals a specular reflectivity of 14%. Finally, we show that a thin (100 μm) Cu(111) crystal can be bent by an electrostatic field to focus an incoming He beam to a spot of 350 μm. Due to the focusing properties of the mirror, a direct beam with less collimation can be used, leading to a larger reflected intensity. The absolute focused intensity is two orders of magnitude larger than previously reported. This represents a big step forward towards achieving the goal of building a high-resolution scanning helium atom microscope.

5.1 Introduction

The design of surface mirrors that are both smooth and curved at nanometer level is a challenging goal. The density of defects on the surface must remain dramatically low, given the high sensitivity of He atoms to them [9]. For the purpose of fulfilling this complex requirement, a new method to design and build these mirrors has been developed in this chapter.

In the past, thin semiconductor crystal, like Si(111), has been bent and used as mirror, since their surfaces can be manufactured with larger terraces and smaller density of defects than metal surfaces. However, the poor flexibility and the large surface corrugation compared to metal crystals causing a limitation to the electrostatically bending and to the intensity of the specular peak. In fact, the absolute specular reflectivity for Si(111) (ca.1%) is considerably smaller than the high reflectivity recorded for metal surfaces (from 15% to 40%) [10, 11].

Not so long ago, the thickness of metal crystals was limited by the technology. However, recent improvements have made available commercial crystals of several metals with about 50 μm in thickness. This feature enables controlled bending of the metal and much more effective manipulation of the samples. Despite this new characteristic, no single study exist about the surface quality and the long-range order of these new thin crystals, which are determinant factors of the intensity of the reflected He beam.

We have studied four different thin crystal surfaces: Cu(111) of 100 μm , Ni(111) of 100 and 50 μm, and Ru(0001) of 150 μm. In order to assess the quality of these surfaces, these results have been compared with data measured from bulk crystals of the same metals. These metals are especially interesting from the point of view of their use as mirrors for He atoms, since a graphene layer can be grown on Ru(0001), Ni(111) and Cu(111). This keeps the surface clean and stable even after exposure to ambient conditions, while the absolute reflectivity remains high: more than 20% for graphene/Ru(0001) [12, 60] and graphene/Ni(111) [11, 118], and 5% for graphene/Cu(111) [67]; in addition, the surfaces maintain their reflectivity in vacuum for periods of weeks or month, a huge advantage for microscopy applications.

Moreover, another flexible crystal has been explored: the muscovite mica. Ru(0001) and Ni(111) thin films have been deposited onto mica substrate by magnetron sputtering. The high reflectivity recorded for Ru(0001) together the flexibility of mica makes also this system a possible candidate to be employed as atomic mirror in He microscopy. Finally, we demonstrate that a thin (100 μm) Cu(111) crystal exhibits the largest ordered

domains, and that its flexibility allows focussing He atoms with a very high reflectivity.

5.2 Flat surfaces: Cu(111), Ni(111) and Ru(0001) thin crystals

In order to select the best thin crystal that can be employed as curved atom mirror a previous investigation of flat surfaces is required. The surfaces are characterized by HAS using the TEAMS system. As described in detail in section 2.2.1,this machine allows the determination of the absolute diffraction reflectivity.

5.2.1 Experimental details

Three different thin metal crystals from MaTecK have been used in this study: Cu(111), Ni(111) and Ru(0001). The crystals are disks with a diameter of 10 mm and with different thicknesses: 100 μm for Cu(111), 100 and 50 μm for Ni(111), and 150 μm for Ru(0001). A comparison has been made with results obtained with Cu(111), Ni(111) and Ru(0001) bulk crystals. These samples are 2 mm thick, and have disk shapes, with a diameter of 8 mm.

The crystals were mounted on a sample holder which can be heated by electronic bombardment and cooled down to 90 K using liquid nitrogen. The surface temperature was measured with a C type thermocouple spot welded to the sample edge. For the thin crystals, the mounting has been modified to prevent a deformation of the thin crystals themselves. For this purpose, the sample has been placed between a molybdenum disk at the bottom and a molybdenum ring with an aperture of 5 mm on top, and tightened so that the sample remains as flat as possible during the preparation procedure.

Clean metal surfaces were prepared in situ in UHV by 15 minutes cycles of ion sputtering (0.6 KeV for Cu(111), 1 KeV for Ni(111) and Ru(0001) with $P_{Ar} \simeq 2 \times 10^{-5}$ mbar) followed by flash-annealing at ca. 850 K for the Cu(111) and 1170 K for Ru(0001) and Ni(111). Few cycles (2-3) were found to be enough to prepare the thin crystal surfaces, in comparison to more than 10 cycles needed for the bulk crystals. Surface cleanliness and order were checked by looking at the angular distribution of the specularly reflected He beam.

5.2.2 He–reflectivity for thin crystals: Cu(111), Ni(111) and Ru(0001)

Figure 5.1a. shows a comparison of angular distributions of He atoms scattered from the four thin different metal surfaces: 100 μm Cu(111), 50 and 100 μm Ni(111) and 150 μm Ru(0001). The intensity (I) of the specular peaks has been normalized with respect to the intensity of the incident beam (I_0). Since the intensity and width of the specular peaks depend on the quality of the surface, it is clear that the best result is obtained for the Cu(111) thin crystal (yellow curve). The specular peak of the Cu(111) surface has a FWHM of 1°, which corresponds roughly to the angular resolution of the HAS machine. An estimation of the domain size w is given by the relationship FWHM $\sim 1/w$, where w is known as transfer width (detailed in section 2.2.1), that corresponds to the largest period of the grating which can be straightforwardly resolved with a given instrument [7]. Thus, the average terrace size of Cu(111) surface is at least 200 nm, i.e. one order of magnitude larger than the transfer width of our system. The specular absolute reflectivity is 20% for an incident energy E_i = 64 meV. The comparison of the spectra in Fig. 5.1b between the thin Cu(111) crystal (yellow spectrum) and the Cu(111) bulk (black spectrum) presents a quite remarkable result: the thin Cu(111) crystal shows a specular peak even sharper than the one from the Cu(111) bulk surface (FWHM = 1.5°), measured under similar scattering conditions (T_S = 90 K, E_i = 64 meV). Furthermore, the absolute specular intensity of the thin crystal is more than twice that of the bulk.

For the other thin crystals investigated the measured FWHM for the specular peak is larger, and an estimation of the corresponding domain size can be obtained from the surface coherence length [84, 119], explained in more detail in section 2.2.1. The specular peak of the 100 μm Ni(111) sample (blue spectra in Fig. 5.1a and c) has a FWHM of 1.7°, which gives an average terrace size of 5 nm, smaller than the one measured for bulk Ni(111) crystal (> 200 nm). A comparison between the specular peak for thin Ni(111) crystal and for the bulk one is shown in Fig. 5.1c . Likewise, the absolute specular intensity is 14% at E_i = 28 meV, whereas the reflectivity measured for the Ni(111) bulk surface is 43% at the same incident energy. If the thickness of the Ni(111) crystal is reduced, the reflectivity gets worse. An FWHM of 2.5° is measured for the thin Ni(111) crystal of 50 μm (green spectra in Fig. in Fig. 5.1a), which yields an average terrace size of 2 nm. Similarly, the reflected specular intensity is reduced to 3% of the incident beam. This effect can be due to two main reasons: the fact that thin metal crystals tend to wrinkle after heating, and the lower quality of thin crystals. The first hypothesis can be

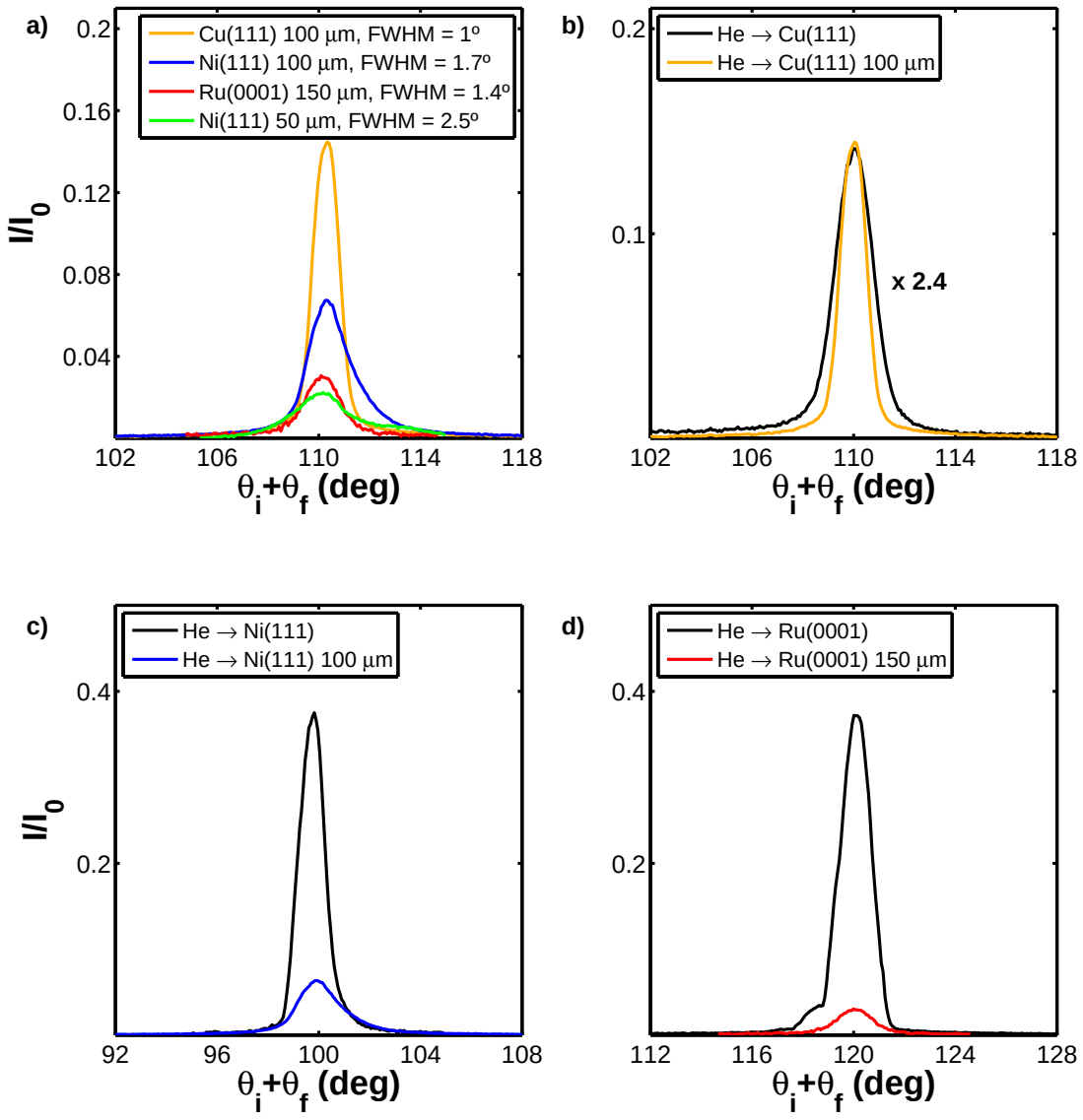

Figure 5.1: a) Angular distributions of He atoms scattered from different thin crystals: 100 μm Cu(111) (yellow), with a beam energy E_i = 64 meV; 50 μm Ni(111) (green) at E_i = 64 meV and 100 μm Ni(111) (blue) at = 28 meV, and 150 μm Ru(0001) (red) at E_i = 28 meV. (b) Comparison of He reflection from 2 mm Cu(111)crystal (black) and 100 μm Cu(111) thin crystal (yellow) at the same experimental conditions (E_i = 64 meV and T_S = 90 K). (c) Comparison of He reflection from 2 mm Ni(111) crystal (black) (measured at E_i = 64 meV) and 100 μm Ni(111) thin crystal (blue) (measured at E_i = 28 meV). (d) Comparison of He reflection from 2 mm Ru(0001) crystal (black) and 150 μm Ru(0001) thin crystal (red) at the same experimental conditions (E_i = 28 meV meV and T_S = 90 K).

Table 5.1: Summary of results obtained for thin and bulk crystals.

Crystal	Thickness	E_i (meV)	Reflectivity	FWHM	terrace size
Cu(111)	100 μm	64	20%	1°	> 200 nm
Ni(111)	100 μm	28	14%	1.7°	49 Å
Ni(111)	50 μm	64	3%	2.5°	20 Å
Ru(0001)	150 μm	28	5%	1.4°	89 Å
Cu(111)	2 mm	64	11%	1.5°	52 Å
Ni(111)	2 mm	64	43%	1°	> 200 nm
Ru(0001)	2 mm	28	53%	1.1°	> 200 nm

excluded since the mounting of the sample forced the crystal to be flat (see experimental section). Therefore, we believe the second reason is more likely, meaning that a worse surface quality is obtained below a given crystal thickness. Finally, the 150 thin μm Ru(0001) crystal has been measured (red curve in Fig. 5.1a and d). Also in this case the quality of the surface is not comparable to the bulk one, as shown in Fig. 5.1d. The FWHM of this thin crystal is 1.4° and the average terrace size is 9 nm. Its specular absolute reflectivity at E_i = 28 meV is 5%, which is a factor of 10 smaller than for the Ru(0001) bulk surface under the same incident conditions. A summary of all the measured surfaces is presented in Table 5.1.

These observations demonstrate that the thin crystal with the highest quality is the thin Cu(111) crystal, in particular for its long range crystalline order. The high specular reflectivity and large crystalline domains, in addition to its flexibility, makes the 100 μm Cu(111) crystal surface a good candidate to build a mirror for neutral atomic beams. For this reason, we have selected this surface to investigate its focusing properties.

5.2.3 He–reflectivity for graphene on thin Ni(111) crystal

With the aim of using these thin crystals as atomic mirrors, a long-term stability under ambient conditions is required. For this reason, we have explored the possibility to grow Gr on thin metal crystals. Ni(111) has been selected for this purpose.

Clean Ni(111) surfaces were prepared in UHV by cycles of ion sputtering (1 KeV $P_{Ar} \simeq 4 \times 10^{-5}$ mbar) and flash-annealing at ca 900 K (prolonged annealing caused S segregation at the surface). After this treatment the sample was exposed to ethylene at T = 850 K and a $P_{C_2H_4} = 2 \times 10^{-6}$ mbar for 5 minutes and a final annealing a 800 K for 10 minutes. The surface order was checked by LEED.

Figure 5.2 presents the results obtained for He scattering from Gr on thin 100 and 50

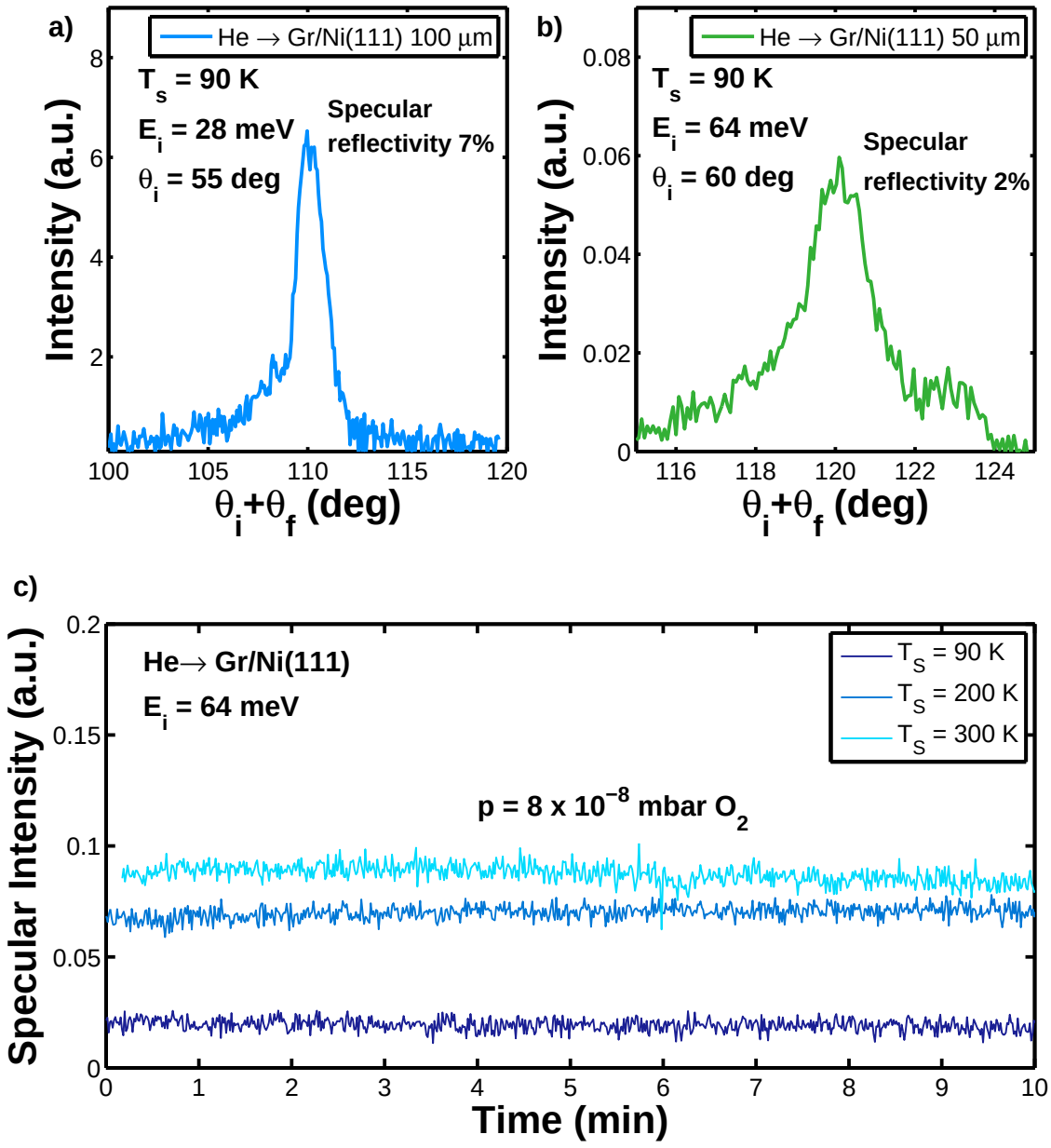

Figure 5.2: He diffraction from Gr on thin Ni(111) crystal of 100 μm. (a) and 50 μm (b). (c) Evolution of Helium specular reflectivity with time exposing the surface to O_2 pressure of 8×10^{-8} mbar.

μm crystals. A higher reflectivity and narrower peak has been measured for the former. This is the same situation than the case of bare Ni(111), as stated in the previous section. As shown in Fig. 5.2a, the absolute specular intensity for the thicker crystal reaches

7% at E_i = 28 meV and θ_i = 55°, whereas an absolute reflectivity of 2% is measured for the 50 μm thin crystal (see Fig. 5.2b) at E_i = 64 meV and θ_i = 60°. The FWHM of thin Ni(111) crystal of 100 μm is 1.5°, which gives an average terrace size of 5 nm. In contrast, the FWHM for the crystal with a thickness of 50 μm reaches a higher value of 1.8° and the average terrace size is 4 nm. In both cases the flatness and the crystallinity of the surface are improved by the Gr layer.

Furthermore, the surface reactivity has been investigated with a higher degree of detail, by monitoring the specular He intensity during O_2 exposure. The results obtained from this analysis are set out in Fig. 5.2c. Three different surface temperatures (90 K, 200 K and 300 K) have been used while exposing the surface to O_2. As demonstrated by the constant He-reflectivity, oxygen adsorption does not occur for all the surface temperature employed. These findings corroborates the inertness of Gr on thin Ni(111) crystals.

5.3 Flat surfaces: Ru(0001) on mica and Ni(111) on mica

Mica is a widely used compound in material science and in surface physics, and it is a good candidate as a mirror material: it is easy to handle, it is flexible, it can be prepared in very thin layers and it exhibits high reflectivity to He atoms (when cleaved in situ) [120, 121]. The latter is a disadvantage from the viewpoint of the He-microscope, since we want to avoid any in situ preparation. For this reason, we have investigated the possibility of preparing a thin metal film on top of mica.

Muscovite mica consists of tethraedral layers composed by oxygen, aluminium and silicon with a thickness of 0.67 nm, held together by potassium ions as shown in Fig. 5.3. The nature of the interaction between potassium ions and the tethraedral layers is electrostatic and it is weak compared to the covalent bond between the atoms of each layer. For this reason, the mica is easily cleaved at the basal (001) surfaces of the tetrahedral layers. [122].

5.3.1 Sample preparation

We started by depositing a thin Ru layer (thickness ~200 nm) by DC sputtering (available at the ICMM) on a thin mica substrate, which was briefly exposed to ambient conditions before being mounted in the HAS-UHV system. The parameters used to grow Ru were:

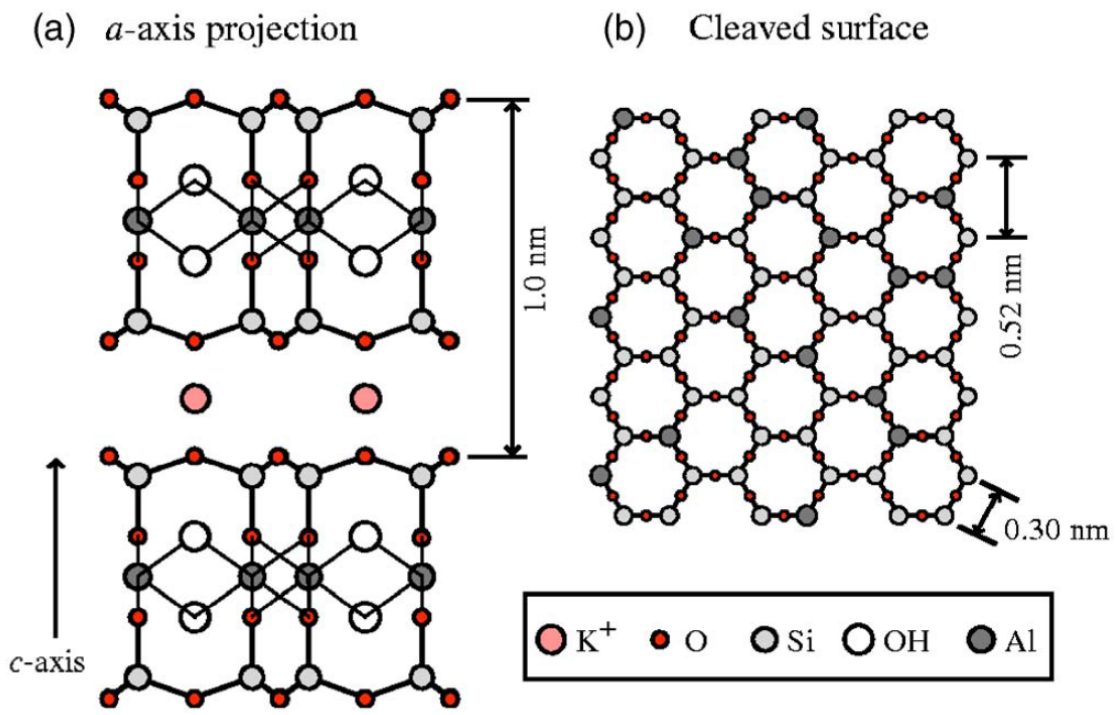

Figure 5.3: Structure of muscovite mica; (a) a-axis projection; (b) cleaved surface (K^+ ions are not shown) [123].

base pressure of the order of 10^{-7} mbar and Ar pressure for sputtering deposition of 5.8×10^{-3} mbar. A sputtering power of 30 W was used and the deposition rate was about 0.06 nm/s. Thickness of the films, measured by profilometer, was 200 nm. We tried different surface temperatures; the best results were achieved at 350 °C. Once in UHV, we performed ion sputtering (1 KeV with $P_{Ar} \simeq 2 \times 10^{-5}$ mbar) to remove the oxide layer, followed by low temperature annealing.

5.3.2 He–reflectivity for Ru(0001) on mica

The He-specular signal detected was quite sensitive to the final annealing temperature, as shown in Fig. 5.4. After 15 minutes of ion sputtering and a low temperature annealing, T_{ann} = 450 K, the He-reflectivity is about 2% of the incident beam. When the annealing temperature rises up to 550 K, a great improvement is observed (see violet spectra in Fig. 5.4). If the temperature rises even more, reaching a value of 650 K (orange spectra), the absolute reflectivity falls slightly. However, the width of the specular peak is noticeably reduced with respect to the one measured after annealing to 550 K. The FWHM of this

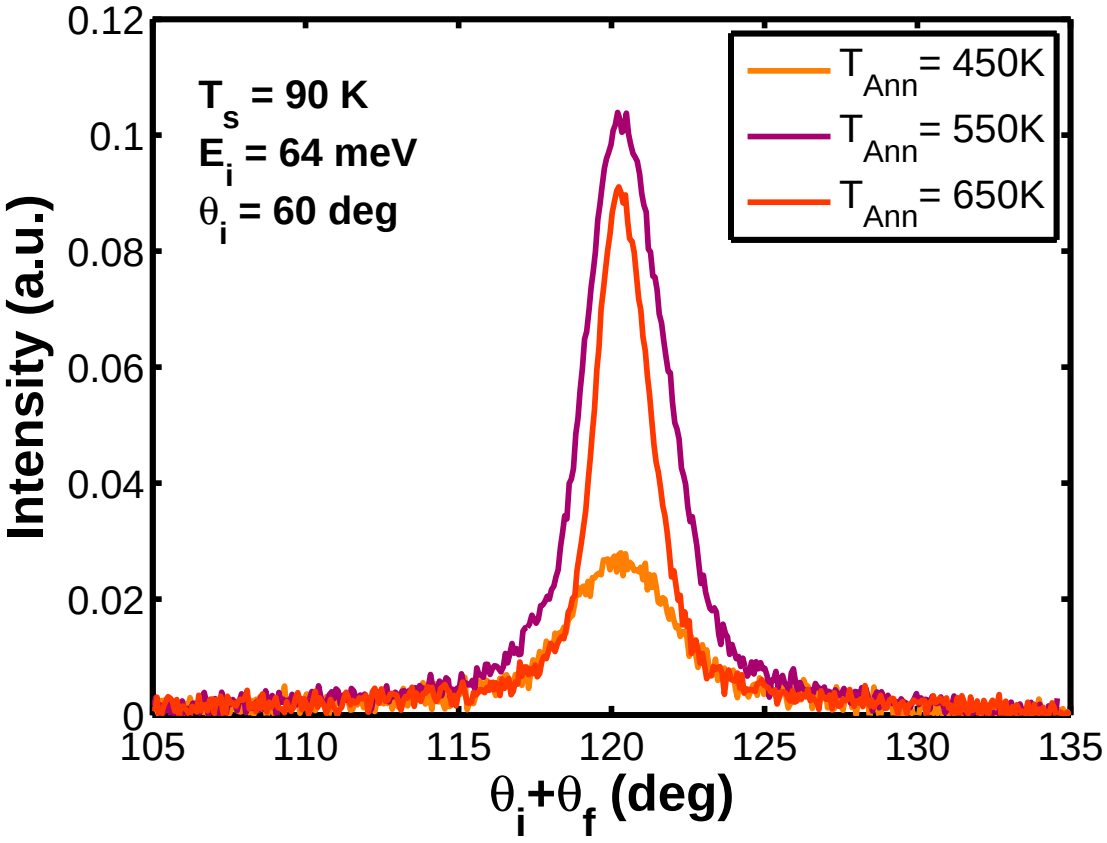

Figure 5.4: Comparison of He-diffraction spectra from Ru(0001)/mica surface after annealing to different final temperatures (indicated in the inset).

system under this preparation conditions is 1.9°, which gives an average terrace size of approximately 4 nm. Usually, more than one cycle of ion sputtering was needed to achieve the best surface quality. However, for Ru(0001)/Mica an inverse trend has been observed. Fig. 5.5, shows three angular distributions taken after one (orange line), two (yellow line) or three (purple line) sputtering cycle, followed by annealing of 650 K. When the number of cycles rises, a worse specular peak is measured. With only three cycles of ion sputtering the intensity falls dramatically. This effect may be explained by the fact that with this system the number of point-like defects increases with further sputtering and that it is non-reversible with surface annealing. HAS is very sensitive to point defects and when the density defects is larger than 15-20% it is impossible to detect diffraction from such surface. It is noteworthy that several samples have been prepared and measured with HAS and all of them showed the same behaviour as function of the number of sputtering cycles.

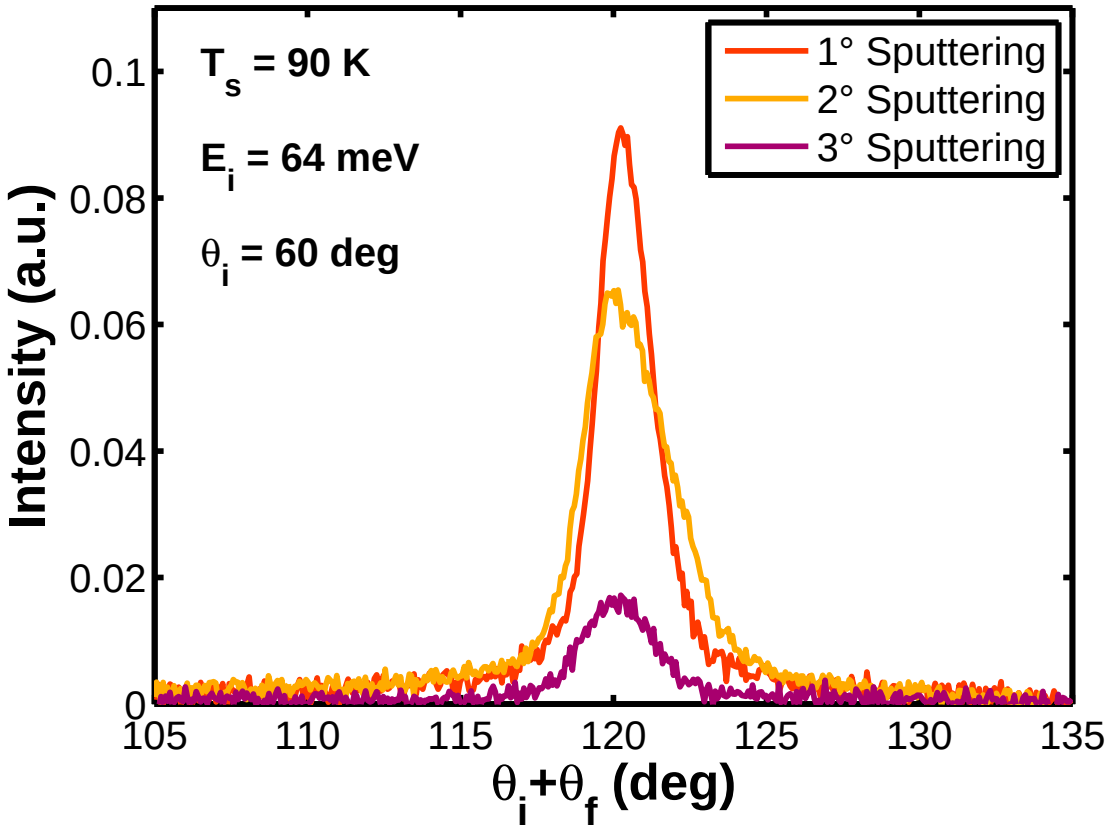

Figure 5.5: Comparison of He atom scattering from Ru(0001)/mica after one, two and three cycles of ion sputtering. The intensity of the specular peak decrease by increasing the number of the sputtering cycles.

The specular reflectivity is 11% for the beam at room temperature and 14% for the beam at 130 K. Unfortunately, graphene cannot be prepared on these samples, since it needs heating to higher temperatures (ca. 1000 K) and mica seems to become unstable when heated above 700 K. To avoid this problem, we tried to grow graphene by sputtering with ethylene in the background (partial pressure of mbar), but no improvement was detected. Regardless of this, Ru/mica samples are good candidates to be used as mirrors for He atoms.

5.3.3 Ni on Mica

Due to lower growth temperature for graphene on Ni, we tried to optimize the growth parameters of Ni on mica by DC magnetron sputtering. Different surface temperatures

have been used during the Ni deposition, in order to find the best conditions. Although the 3D-crystallinity of the samples was checked by XRD, we were not able to see any He diffraction from these samples.

5.4 Curved surfaces

The Cu(111) surface was mounted using the modified sample holder described in the subsection 5.2.1. The electrostatic bending of the sample was achieved by removing the molybdenum disk, allowing the free movement of the thin crystals. The upper electrode had an aperture of 5 mm to allow the He beam in, and it was electrically grounded. The lower electrode was insulated from the sample by a sapphire ring, in order to allow applying a high voltage to the electrode structure.

5.4.1 He–reflectivity for Cu(111): focusing proofs

Figure 5.6. shows the best beam focus achieved by reflection obtained with the thin Cu(111) crystal measured at θ_i = 60° and E_i = 64 meV (black), compared to the incident beam (red). The shape of the beam changes when a high voltage is applied to the electrodes: the direct beam is approximately Gaussian whereas the profile of the reflected beam follows a different distribution. Since the width of the focused beam is smaller than the width of the detector aperture, the measured angular distribution comes out convoluted with the aperture. In order to estimate the size of the focused beam, we have to take into account how the final distribution is generated under the current experimental conditions. A convolution between a Rectangular function (to model the finite aperture of the detector) and a Gaussian (to model the He beam) is used to model the observed angular profile.

For the symmetry of the Rectangular function, one may also want to take just a Heaviside function into account. The Heaviside step function

$$f(x) = \begin{cases} 1 & x \geq 0 \\ \\ 0 & x < 0 \end{cases}$$

is the mathematical description for an ideal edge. The Gaussian distribution in 1-D has

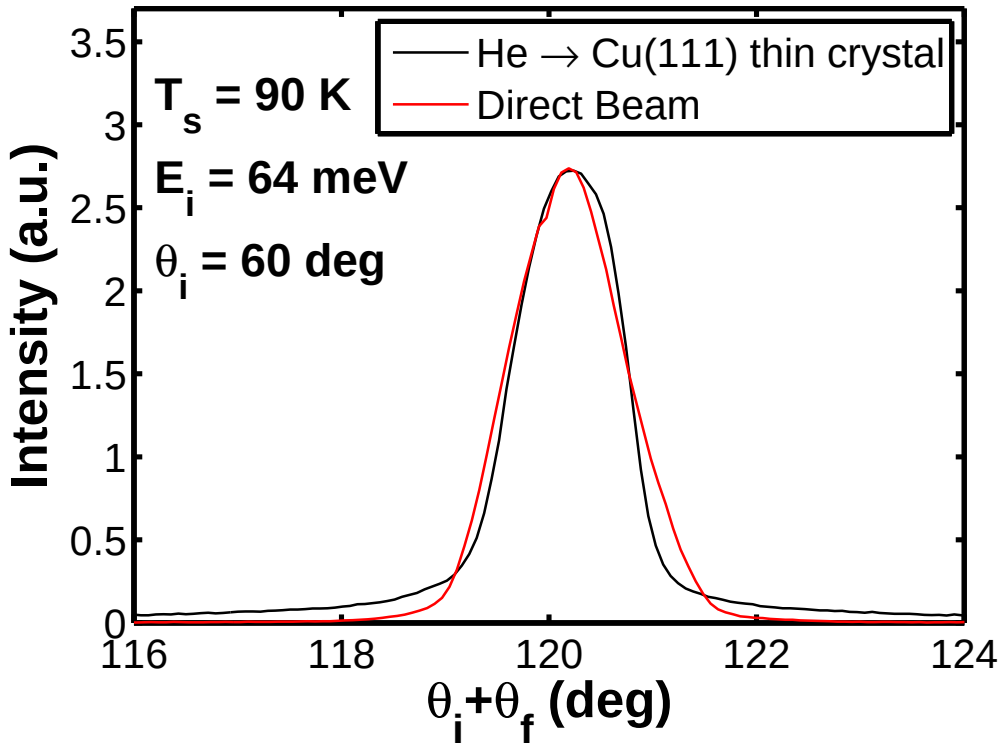

Figure 5.6: He diffraction spectrum from Cu(111) thin crystal (black spectrum) and incident beam spectrum (red spectrum), both measured at an incident beam energy E_i = 64 meV. Differences in the shape are evident: whereas the incident beam is Gaussian, the diffracted beam is not.

the form:

$$h(x) = \frac{1}{\sigma\sqrt{2\pi}} e^{-\frac{1}{2}\left(\frac{x-\mu}{\sigma}\right)^2} \tag{5.1}$$

where σ is the standard deviation of the distribution and μ is the mean of the distribution. The best fit for the slope of the observed data is provided by the convolution of a Gaussian with a Heaviside function. It is defined as:

$$(f * g) = 1 + erf(\frac{x}{\sqrt{2}\sigma}) \tag{5.2}$$

where

$$erf(x) = \frac{2}{\sqrt{\pi}} \int_0^{+\infty} e^{-\frac{1}{2}\left(\frac{x-\mu}{\sigma}\right)^2} \tag{5.3}$$

is the error function.

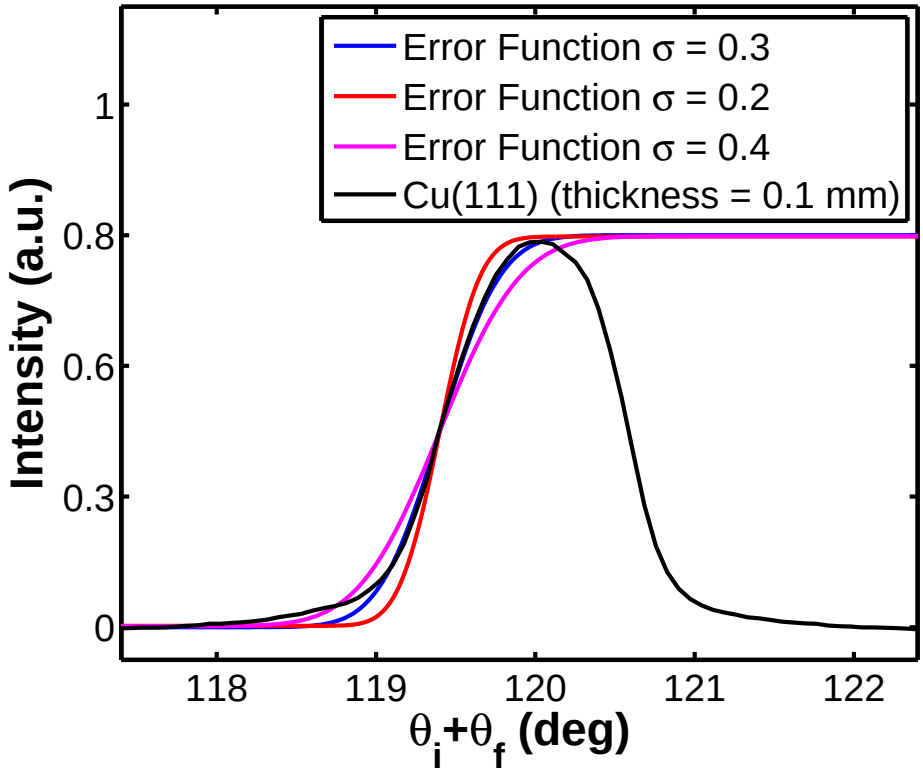

Figure 5.7: Three Gaussian error functions curve are plotted together with the measured beam profile, each one with a different standard deviation (σ). The error function that best fits the specular profile is the corresponding to σ = 0.3. This gives an estimated specular size of 350 μm.

From the best-fit curve shown in Fig. 5.7, we estimate the size of the specular spot to be 350 μm. This is at least a factor 5 better than the values obtained for high-quality flat samples. Unfortunately, due to technical problems with the sample holder, we could not further optimize the focusing conditions, so it is not unlikely that the beam has been focused at a point slightly away from the detector's position. To make sure that the beam has also been focused in the direction perpendicular to the polar scan direction, out-of-plane measurements have been performed, as shown in Fig. 5.8. Also along this direction the width of the specular peak reaches the value of the angular resolution of the HAS machine. However, in this direction the resolution of our equipment it not sufficient to perform an accurate fit along the polar scan direction.

Since we could not change the sample-detector distance, the behaviour of the beam at the detector position has been studied by changing the collimation of the incident

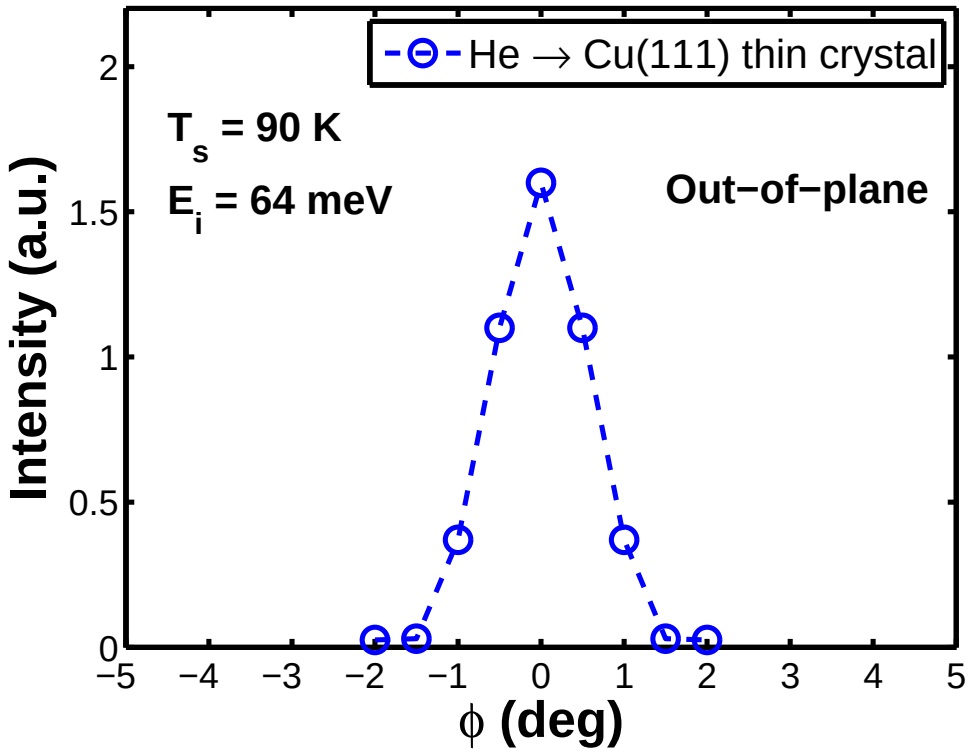

Figure 5.8: Specular He reflectivity out-of-plane: the shape of the specular beam in the perpendicular direction with respect to the in plane specular beam.

beam. Five apertures of different diameters (400, 750, 1200, 2000 and 3000 μm) have been employed to obtain different widths for the direct beam.

Figure 5.9 shows the FWHM and specular intensity plotted as a function of the beam's size at the diaphragm's position. As expected, the intensity of the incident beam increases with increasing illuminated surface area and the same happens with the specular intensity (red line). The FWHM of the specular peak (blue continuous line), in contrast, remains unchanged even after increasing the illuminated area by a factor of ca. 40, whereas the FWHM of the direct beam increases; the same happens for a flat crystal surface (not shown). In fact, due to the finite aperture dimensions of both detector and source, the angular distributions suffer a certain angular broadening, intrinsic to the instrument [7], as shown in section 2.2.1. This leads to an increase of the width of the specular peak when the size of the diaphragm aperture increases. For the HAS machine used in the current work, the angular broadening expected for an aperture of 400 μm is 1.6° (and the one for an aperture of 3000 μm is 9.6°).

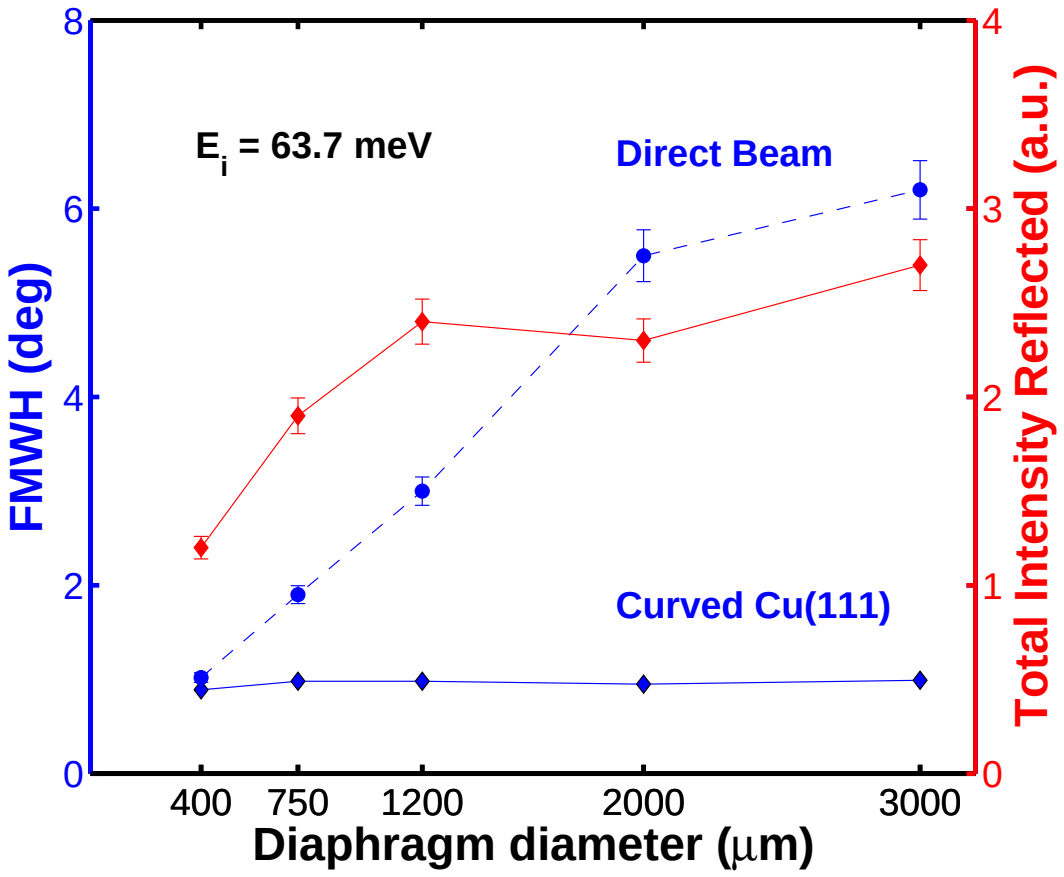

Figure 5.9: Effect of beam collimation on the width and the intensity of reflected beam from curved thin 100 μm Cu(111). Blue: FWHM of reflected and direct beam shown on the left axis. Red: total intensity of the reflected specular peak shown on the right axis.

In contrast, for a curved surface focussing the reflected He beam at the detectors position, the angular broadening is expected to be drastically reduced and should be independent from the incident beams size. Our experiment confirms this expectation. The absolute reflectivity is 65%, with an incident energy of E_i = 28 meV and a surface temperature of 90K, using the smallest aperture of the rotatory diaphragm (400 μm). Furthermore, as shown in Fig. 5.10, at E_i = 28 meV the intensity of the specular peak increases by a factor of 5 when we go from a diaphragm of 400 μm to one of 1200 μm, while the FWHM remains constant. As far as we know, this is the highest value ever measured from a clean metal surface. These results are a clear indication of focusing of neutral He atoms by the thin Cu(111) crystal.

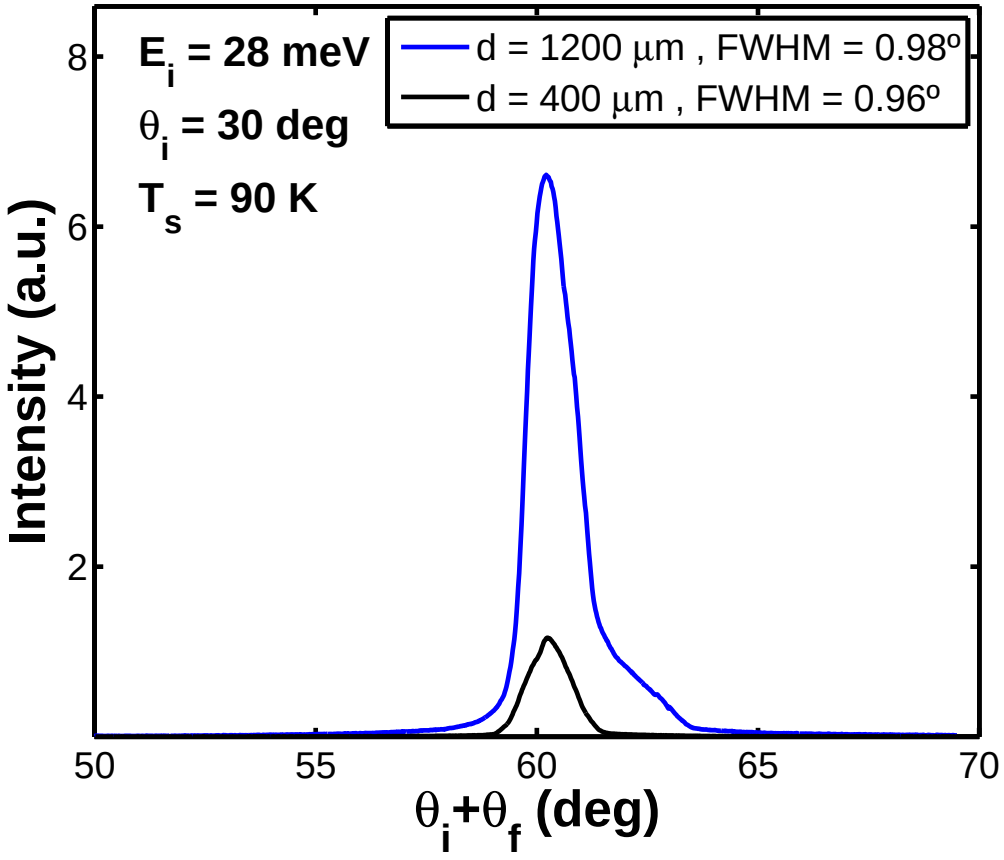

Figure 5.10: Comparison of He atoms scattered from Cu(111) surface by an incident beam with a collimation of 400 μm at diaphragm position (black) and 1200 μm (blue). The incident conditions are E_i = 28 meV and θ_i = 30°. The intensity of the specular peak increases by a factor of 5 while the FWHM remains constant when the diaphragm is changed from 400 to 1200 μm.

5.5 Conclusions

In summary, four different thin crystals have been investigated: 100 μm Cu(111), 50 and 100 μm Ni(111) and 150 μm Ru(0001). In order to select the surface that exhibits the best quality and the highest He-reflectivity, an accurate analysis of their specular peaks has been carried out. The quality of the thin Ni(111) and Ru(0001) crystals was found to be worse than the corresponding bulk ones: the He-reflectivity for the 100 μm Ni(111) surface is 14%, decreasing to 3% for the 50 μm one. Similar results have been obtained for the 150 μm thin Ru(0001) crystal, whose absolute reflectivity is 5%. The corresponding average terrace size lies between 2-9 nm. In contrast, the quality

of the 100 μm Cu(111) crystal exceeds that of a bulk crystal, presenting both a high reflectivity (20%) and long-range crystalline order (>200 nm). High reflectivity (14%) has been recorded also for Ru(0001) on mica substrate with an avarege terrace size of about 4 nm.

A quite significant finding from the current study is that a beam of neutral He atoms has been focused to a spot of 350 μm, with an absolute specular intensity two orders of magnitude larger than any He reflectivity previously reported for a flat or curved crystal. In order to improve the focal spot with this sample, a modification of the present experimental set-up will be required. Finally, owing to their high quality, the thin Cu(111) crystals could be used instead of Cu metal foils when the crystallinity of the substrate is important to achieve best result, like for instance in the growth of large-area monocrystalline graphene [124] or hexagonal boron nitride [125].

CHAPTER 6

MACROSCOPICALLY CURVED MIRRORS

In this chapter it is shown how macroscopically curved atom mirrors have been achieved by coating both sapphire and fused silica plano-concave lenses with graphene-terminated Ru(0001) thin films. Preliminary studies on flat surfaces have been made in order to find the optimum growth parameters for both substrates. We have investigated the reflectivities to incoming He atoms of Gr/Ru(0001)/Al_2O_3 and Gr/Ru/Fused silica samples. The observation of high reflectivity (15%) combined with clear diffraction peaks for Gr/Ru(0001)/Al_2O_3 proves the existence of homogeneous graphene domains. As expected, a lower reflectivity (6%) and a broader specular peak have been measured for Gr/Ru/Fused silica. However, it is a surprising result if we take into account the amorphous nature of fused silica substrates. Then, curved surfaces for both systems have been analysed. Since the reflectivity and the coherence properties of graphene on Ru surfaces are closely related to the quality of the Ru films, long-range order is crucial for the achievement of efficient mirrors. For this purpose, the laser polishing technique has been applied to fused-silica lenses, thus allowing to reduce the surface roughness by roughly one order of magnitude. The improvement of the surface quality of the metal coating grown on top of this substrate is demonstrated by the observation of He diffraction peaks. This is a remarkable result, considering that the starting substrate is an amorphous material. Best results have been obtained with Gr/Ru on curved sapphire. The quality of the surface is comparable with the one measured for flat Gr on Ru(0001) single crystal sample. As far as we know this is the first observation of He diffraction from macroscopically curved surfaces.

6.1 Introduction

Growth of crystalline coatings on curved surfaces is one of the most important challenges in the design of focusing elements. The availability of curved mirrors with few atomic defects would allow to improve optical components for neutral microscopy systems [5, 10], as well as for detection of energetic neutral atoms in space research, X-ray systems [126] and solar cells [127, 128].

Previous work has shown how graphene on Ru(0001) thin films grown epitaxially on α-Al_2O_3(0001) (c-plane sapphire) can be used as a mirror for He atoms [12]. This surface is inert up to 1150 K and provides high reflectivity for thermal He beams. This system, however, is harder to apply to the case of curved substrates, given the difficulties to find commercial curved sapphire. This is why it was decided to open a new research line using different and more easy to find curved substrates. A large number of flat and curved samples (ca, 30) have been investigated with the two UHV-HAS systems, described in section 2.2.1 and 2.2.2, and with Scanning Electron Microscopy (SEM). Besides of Gr/Ru(0001)/Al_2O_3 system, best results have been obtained from Gr/Ru(0001)/Fused silica samples.

Even though the synthesis of graphene on Ru thin films has been achieved on flat amorphous surface, such as SiO_2 [129], and on patterned fused silica surfaces with micrometer-sized concave structure [130], the growth of graphene on macroscopically curved surface and its use as atomic mirror has not been studied yet.

Here, we report a new step towards the realization of the curved mirror to focus beams of He atoms. Specifically, we employed a new focusing element aimed at improving the spot size of the specular beam. For this purpose, the growth of Ru thin films on macroscopically curved surfaces has been achieved, employing both sapphire and fused silica lenses. The mirrors have been made by coating both substrates with Ru films. In the case of fused silica lenses, the surface roughness of commercially available lenses limited the He spot size. This problem was overcome by applying the laser polishing technique, which allows to reduce the surface roughness of the fused silica substrate by roughly one order of magnitude. The subsequently increase of the coating crystallinity leads to the observation of high reflectivity of He beams. This is a remarkable result, and demonstrates that laser polishing enables the preparation of smooth, well-ordered scattering surfaces, even on macroscopically curved and amorphous samples. Finally, Gr/Ru(0001) film has been grown onto a sapphire lens with an exceptional quality demonstrated by the observation of narrow specular peak and clear diffraction peaks.

6.2 Flat surfaces: graphene/Ru(0001) on sapphire

The first step to begin the line of research addressed in this chapter was preparing in a reproducible way high-quality Gr/Ru(0001)/Al_2O_3 samples by ourselves. Previous work had been performed using Gr/Ru/Al_2O_3 samples delivered from Peter Sutter's group, Brookhaven National Laboratory, USA. However, in order to extend the study of Gr terminated Ru(0001) thin film onto different substrates, a prompt production of the samples was essential. Thanks to the collaboration with the group of Prof. Carlos Prieto, located in the Instituto de Ciencia de Materiales de Madrid (ICMM), and the proximity of this Institute to our laboratory, we had the chance to have daily access to their DC/RF magnetron sputtering machine. This facility allowed us to growth Ru(0001) thin film at high temperature of the substrate, ensuring a better quality of the thin film.

6.2.1 Sample preparation

The substrates used to grow Ru(0001) thin films are α-Al_2O_3(0001) (c-plane sapphire). We used Al_2O_3 substrates furnished by three different companies: MaTecK, Shinkosha and MTI. This last company produced a better polished surface thanks to a special Chemical-Mechanical Planarization (CMP) technology.

The sapphire substrates were first sequentially cleaned in ethanol and 2-propanol. Then they were annealed in air at 1000°C for 1 hour. This annealing is needed to smooth the terraces of the surfaces. At this temperature, the obtained ultra-smooth surfaces with atomic step of sapphire subtrates were stable in air for a long period. [131] Thin Ru films were grown on sapphire by DC magnetron sputtering from a Ru target (99.95% purity) at a substrate temperature of 650°C. Base pressure was of the order of 10^{-7} mbar and Ar pressure for sputtering deposition was 5.8×10^{-3} mbar. Sputtering power of 30 W was used and the deposition rate was about 0.06 nm/s. The thickness of the films, measured by profilometer, was 200 nm.

Clean Ru(0001) surfaces were prepared in UHV by cycles of ion sputtering (1 KeV, $P_{Ar} \simeq 2 \times 10^{-5}$ mbar) and flash-annealing at ca 1150 K for Ru on sapphire. The surface cleanliness and order were ensured by the angular distributions of the specularly reflected He, as well as LEED.

In order to obtain the graphene layer onto the clean Ru(0001) surfaces, the samples were heated to 1130 K and maintained at that temperature during exposure to ethylene at pressure $P_{C_2H_4} = 5 \times 10^{-7}$ mbar for 10 minutes and slow cooling in UHV.

6.2.2 He–reflectivity for graphene/Ru(0001) on sapphire

Figure 6.1 shows HAS spectra from three different samples of Gr/Ru(0001)/Al_2O_3. The preparation of the thin film heterostructures is the same for all the samples, but the α-Al_2O_3(0001) (c-plane sapphire) substrate used is different. In the first case, Fig. 6.1a, it was MaTecK substrate, in the second case, Fig. 6.1b, it was Shinkosha substrate, whereas the third sample, shown in Fig. 6.1c, was bought from MTI. The quality of the surface polishing increases from the first to the third sample. As expected, the quality of the epitaxial thin films grown onto the substrates is improved when the order and the flatness of the crystal substrates is better.

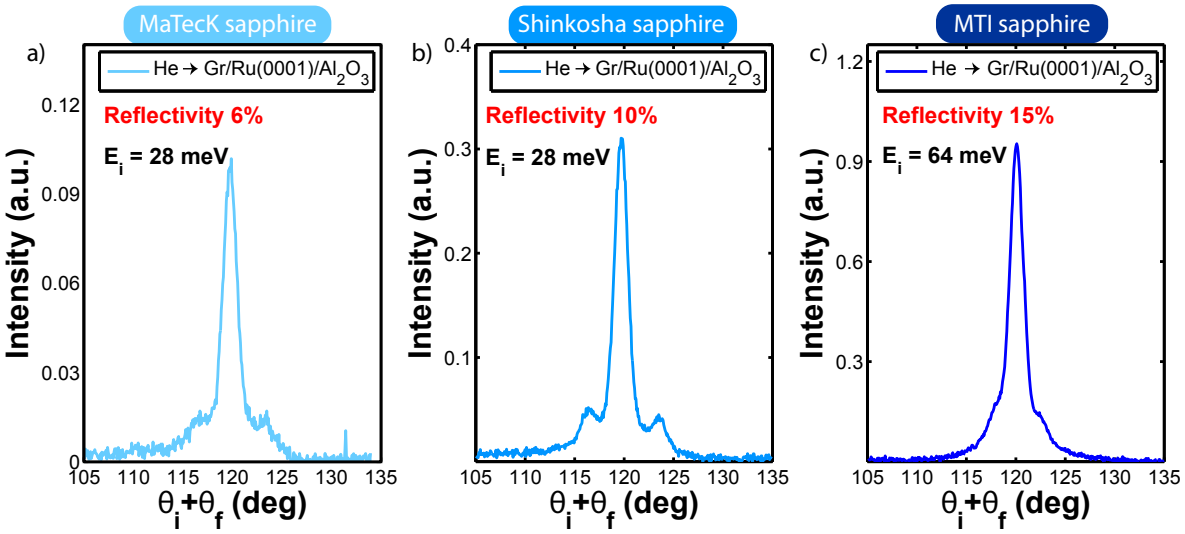

Figure 6.1: He-diffraction from a Gr/Ru(0001) grown on a) MaTeK Al_2O_3, b) Shinkosha Al_2O_3 and c) MTI Al_2O_3. Note the large specular intensity and the presence of the Moiré peaks near the specular one, which demonstrate the presence of a high-quality Gr/Ru(0001) surface.

The characterization of these samples with He atom scattering reflects the features mentioned above. All the samples were aligned in the $\overline{\Gamma M}$ direction. The same incident conditions have been fixed for the three samples measured: an incident angle $\Theta_i = 60°$, a surface temperature of 90 K and an incident energy $E_i = 28$ meV, except for the third sample that was measured at $E_i = 64$ meV. While the overall features seem similar for the three samples, higher specular reflectivity has been recorded for Gr/Ru(0001) grown on MTI substrate. As shown in Fig. 6.1a the specular absolute reflectivity for MaTeK substrate is 6% of the incident beam, whereas a more intense specular peak, which reaches 10%, has been recorded using Shinkosha substrate, shown in Fig. 6.1b. A highest specular reflectivity, 15%, has been measured for Gr/Ru(0001) films grown on

MTI sample. This is approximately three times higher with respect to the first sample if we take into account the Debye-Waller factor [1]. In fact, this factor reveals that by increasing the incident beam energy the intensity of the reflected beam decreases (as explained in more details in section 1.1.4). Also, the width of the specular peak is slightly reduced for the sample prepared with the Shinkosha and MTI substrates. The FWHM ranges from 1.6° for the MaTecK substrate to 1.5° for the Shinkosha and MTI ones. This points out to a smaller density of defects of the Ru(0001) thin film grown on well polished sapphire substrate. In all the samples the angular distributions of the Helium scattering from the Gr/Ru/Al_2O_3 show moiré diffraction peaks close to the specular peak. The moiré peaks in Fig. 6.1c are less evident due to the higher incident energy used (E_i = 64 meV), which causes a shift of the moiré diffraction peaks towards the specular peak. Larger scan measurement, shown in Fig. 6.2, presents diffraction pattern

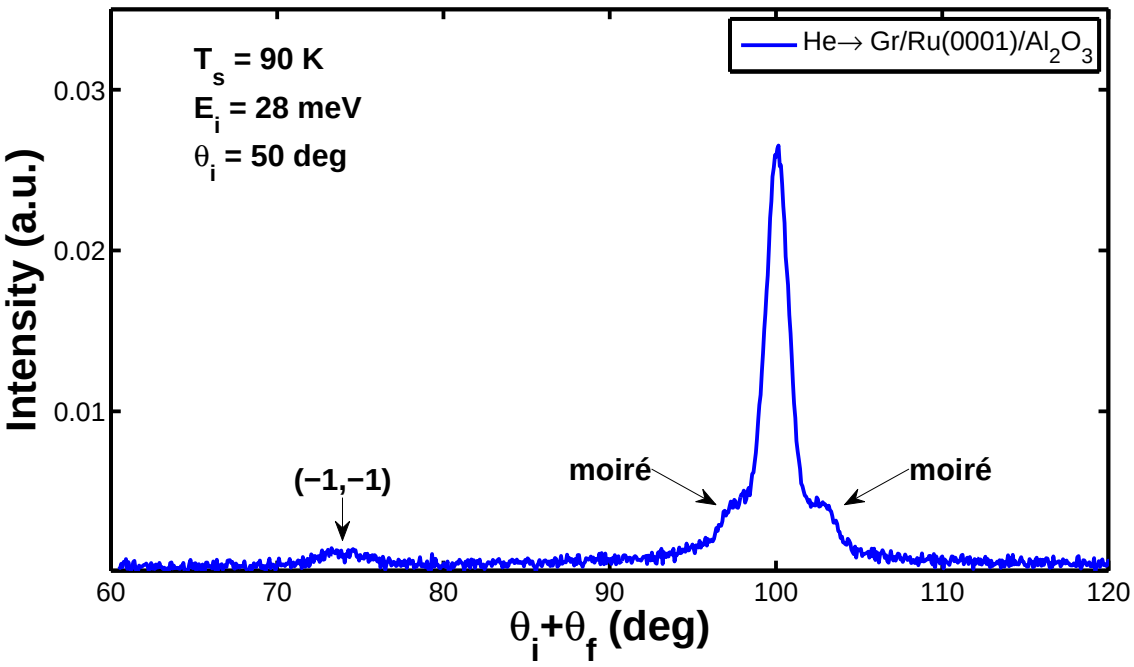

Figure 6.2: Angular distribution of He atoms scattered from Gr/Ru(0001)/Al_2O_3 surface (Shinkosha sapphire). Moiré diffraction peaks close to the specular peak and first-order peck of the Gr lattice.

of Gr/Ru(0001)/Al_2O_3 taken at Θ_i = 50°. Besides moiré peaks close to the specular peak, well resolved first-order peaks (-1,-1) of the Gr lattice was resolved, that confirm the existence of a well-ordered Gr layer. The angular position of the diffracted peak from the Gr layer is in good agreement with expected value for Gr hexagonal structure [57] with

a constant lattice a = (2.46±0.02) Å.

6.3 Flat surfaces: graphene/Ru on fused silica

6.3.1 Sample preparation

The main difference with respect to the preparation of Ru thin film on sapphire substrate described in the previous section was the annealing temperature of the substrates. Thin Ru films (200 nm in thickness) were grown on sapphire by DC magnetron sputtering from a Ru target (99.95% purity) at five different substrate temperatures: 600°C, 630°C, 650°C, 700°C and 725°C. The residual pressure was near 10^{-7} mbar and Ar pressure for sputtering deposition was 5.8×10^{-3} mbar. The deposition rate was about 0.06 nm/s for a DC power of 30 W.

Scanning electron images for all the samples have been recorded with a Philips XL30 Scanning Electron Microscope (SEM) located at the UAM Interdepartmental Investigation Service (SIdI).

After performing the SEM characterization, selected samples have been prepared in UHV chamber and measured with HAS technique. Clean Ru(0001) surfaces were prepared by repeated cycles of ion sputtering (1 keV, $P_{Ar} \simeq 3 \times 10^{-5}$) and flash-annealing at 1150 K. To obtain the Gr layer onto Ru/Fused silica surfaces, the sample was heated to 1130 K and maintained at this temperature during exposure to ethylene at pressure $P_{C_2H_4} = 5 \times 10^{-7}$ mbar for 10 minutes followed by slow cooling in UHV.

6.3.2 Scanning Electron Microscopy (SEM)

Figure 6.3 shows SEM images and grains size distributions of Ru(0001) grown on flat fused silica at five different surface temperatures, that ranges from 600 °C to 725 °C . The surface temperature affects the growth and the morphology of the Ru(0001) thin film. As the temperature rises from 600 °C to 725 °C, the Ru(0001) crystal size increases and the grain size distribution becomes broader, as shown in the sequence of histograms in Fig. 6.3. The mean grains size increases from 120 nm to 250 nm, as the temperature rises from 600°C to 725°C. Besides, the flatness and the homogeneity of the grains is improved when the temperature is increased, as shown by Fig.6.3 sequence. Flatness and grain size are crucial for optimum He-atom mirror, since flatter and larger grains lead to a larger surface coherence, thus improving the width of the specular peak when He is scattered from Ru(0001) thin film.

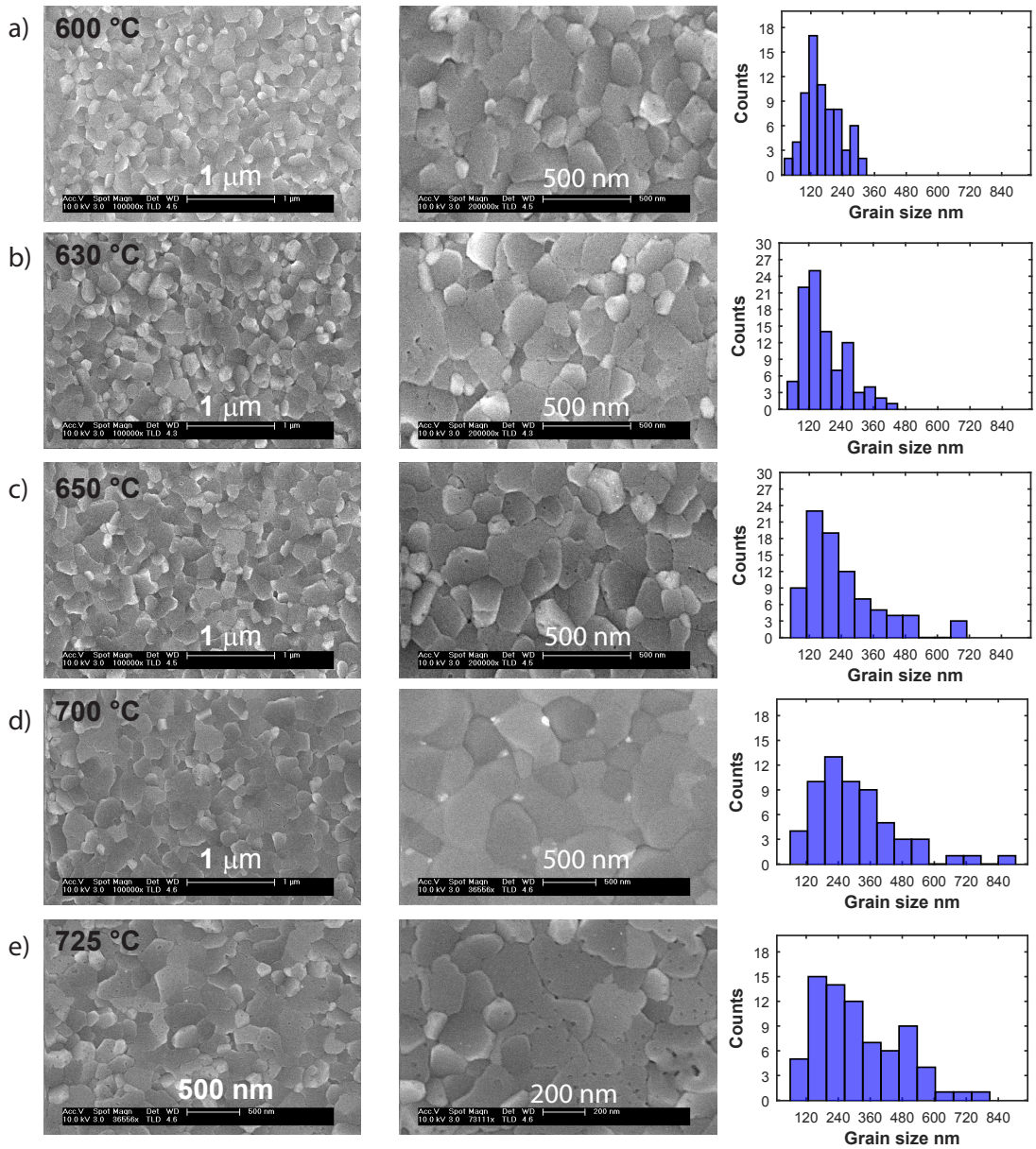

Figure 6.3: SEM images and grain size distributions of the Ru thin films grown at five different substrate temperatures: (a) 600°C, (b) 630°C, (c) 650°C, (d) 700°C, (e) 725°C.

6.3.3 He–reflectivity for graphene/Ru on fused silica

After performing SEM measurements two of the samples have been prepared in UHV chamber and characterized with HAS. Figure 6.4 shows the comparison between the Ru/Fused silica sample prepared at a substrate temperature of 630°C with the one

prepared at 700°C. The angular distributions of the diffracted beam for both Ru/Fused silica samples have been recorded at a surface temperature of 90 K, an incident beam energy of 63.5 meV and an incident angle of 60°. The spectrum presents in Fig. 6.4a corresponds to the sample prepared at 630°C, while the spectra in Fig. 6.4b shows the sample grown at 700°C.

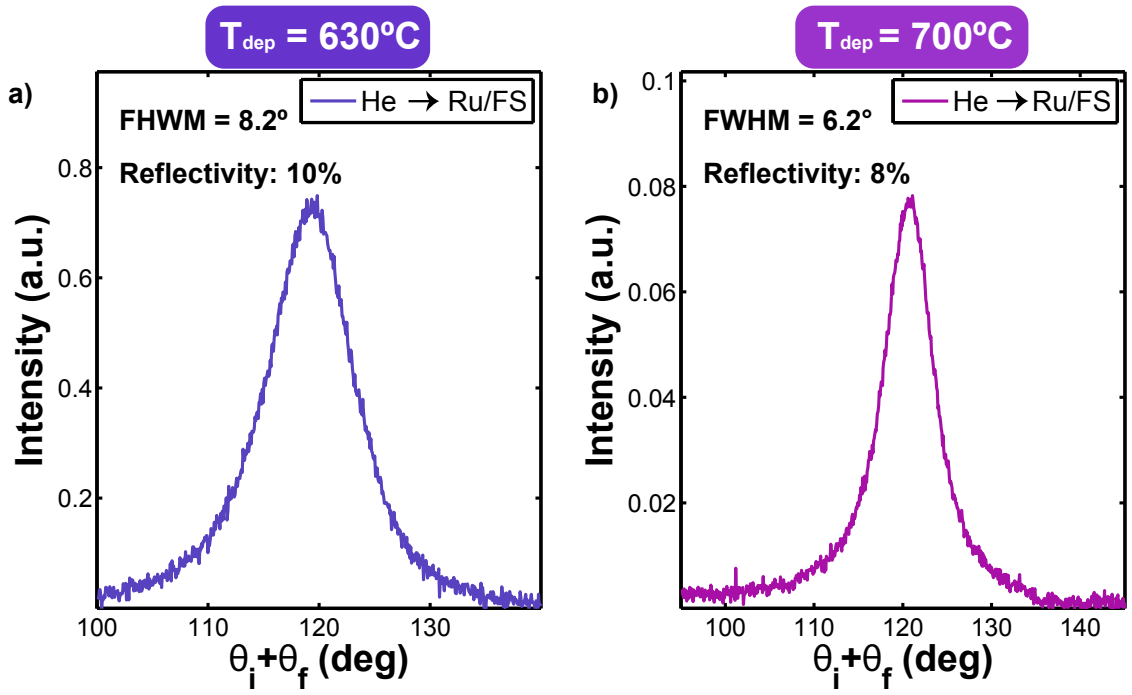

Figure 6.4: Angular distributions for Ru/Fused Silica(FS) samples, taken for E_i = 63.5 meV, θ_i = 60° and T_S = 90 K. Ru film is grown at a substrate temperature of a) 630°C and b) 700°C.

The sample prepared at higher temperature (700°C) presents a narrower peak than the one grown at 630°C. The latter have a FWHM = 8.2°, while the former presents a much smaller FWHM, that reaches only 6.2°. As expected, the sample that shows larger and flatter grains produces a more coherent He scattering, which leads to a narrower specular peak.

Furthermore, we explored the possibility of growing Gr layer onto Ru/Fused silica substrates, in which the Ru film has been grown at a substrate temperature of 650°C. Figure 6.5a shows He angular distribution from Gr/Ru/Fused Silica sample, measured at an incident energy E_i = 28 meV. Broader peak has been recorded, with a FWHM = 9.5°. In contrast, the absolute reflectivity of He atoms at this incident energy reaches 6%. This is a remarkable result if we consider that the starting substrate is amorphous.

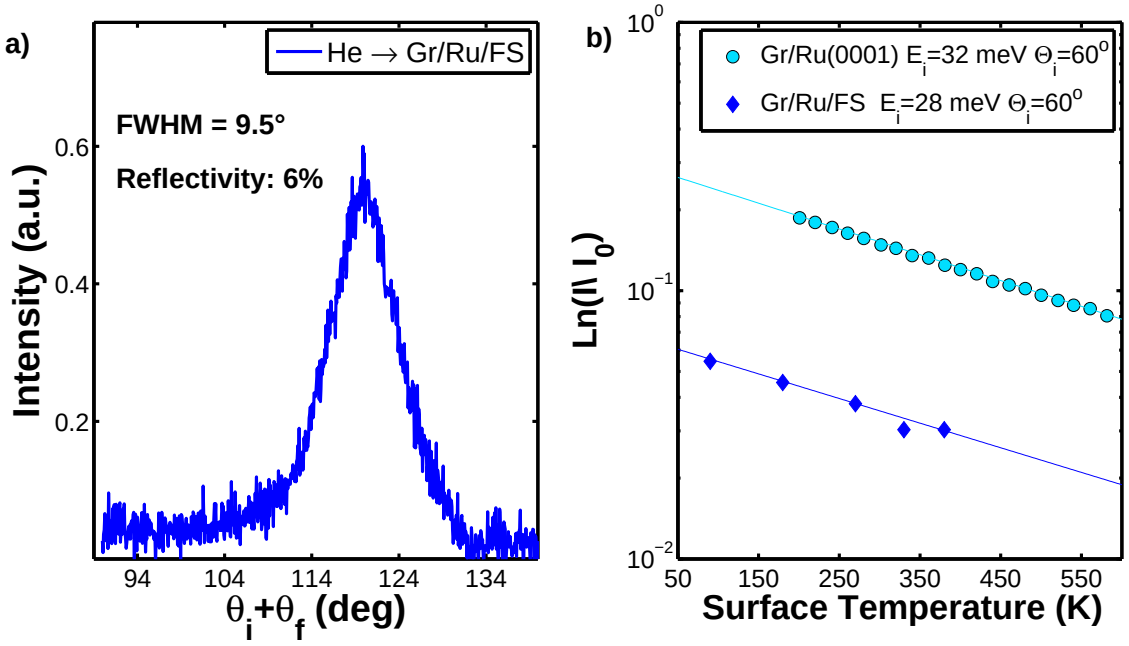

Figure 6.5: a) Angular distribution of He atoms scattered from Gr/Ru/Fused silica sample, taken for E_i = 28 meV, θ_i = 60° and T_S = 90 K. b) He specular intensity dependence as a function of surface temperature. Comparison between Gr on single crystal Ru(0001) [60] (cyan circles) and Gr/Ru on fused silica substrate (blue rhombus).

Due to the large width of the specular peak moiré diffraction peaks are not resolved. However, the stability of the reflecting surfaces is one of the fingerprint of the existence of the Gr layer on the surface. By measuring the surface temperature dependence of the intensity of the specular reflected beam, it is also possible to have information about the effective mass of the surface atoms and thus to ensure the presence of the Gr layer onto the Ru surface. Figure 6.5b shows the comparison of the thermal attenuation of the specular peak for Gr on Ru(0001) single crystal (cyan circles) and on Ru/Fused Silica sample (blue rhombus). The same exponential temperature dependence was recorded for both samples. The best fits to the two set of data, using Eq.1.36 described in section 1.1.4, are represented in Fig. 6.5b as solid lines. The same parameters have been used to fit both data set: an effective mass of 173 amu (corresponding to 1 Ru atom and 6 carbon atoms), a potential well depth of 13 meV [60] and a Debye surface temperature Θ_D = (248 ± 20) K.

6.4 Curved surfaces: graphene/Ru on fused silica with and without laser polishing

6.4.1 Experimental details

Commercial fused silica lenses were laser polished with a novel method recently developed at the Fraunhofer Institute for Laser Technology ILT [132]. The starting point was a commercial fused silica plano-concave uncoated lens, produced by Thorlabs company, with a radius of curvature of -92.0 mm. CO_2 laser radiation was used to heat up the fused silica lens just below evaporation temperature. Thereby, the viscosity was reduced and the initial roughness smoothed due to surface tension. The joint effect of surface melting and surface tension of glass material reduces surface roughness and smooths the surface.

Thin Ru films (200 nm in thickness) were grown on polished and unpolished fused silica lenses by DC magnetron sputtering from a Ru target (99.95% purity) at a surface temperature of 650°C. The base pressure was in the 10^{-7} mbar range and Ar pressure for sputtering deposition was 5.8×10^{-3} mbar. The DC power supplied was 30 W and the corresponding deposition rate was about 0.06 nm/s.

The morphology of the Ru films was investigated *ex situ* by scanning electron microscopy (SEM). SEM analyses were carried out on a FEI Nova NanoSEM 230 microscope, located at the ICMM.

The samples have been prepared in UHV chamber and characterized with HAS technique, using the two apparatus described in section 2.2.1 and 2.2.2. Clean Ru(0001) surfaces were prepared by repeated cycles of ion sputtering (1 keV, $P_{Ar} \simeq 3 \times 10^{-5}$) and flash-annealing at 1150 K in UHV chambers. The Gr overlayer was prepared by annealing the sample to 1150 K and maintaining it at that temperature during C_2H_4 exposure at a pressure $P_{C_2H_4} = 5 \times 10^{-7}$ mbar for 10 minutes, followed by slow cooling in UHV.

6.4.2 Characterization of graphene/Ru on fused silica lenses

The effect of performing laser polishing to a curved fused silica lens prior to depositing the Ru coating is shown in Fig.6.6. The He-diffraction spectrum obtained in the case of laser polished surface (red curve) brings to light a clear sharp specular peak, whereas a low-intensity and broad peak is measured when Ru is grown on the same lens without additional treatments (black curve). Both spectra have been recorded at the same incident

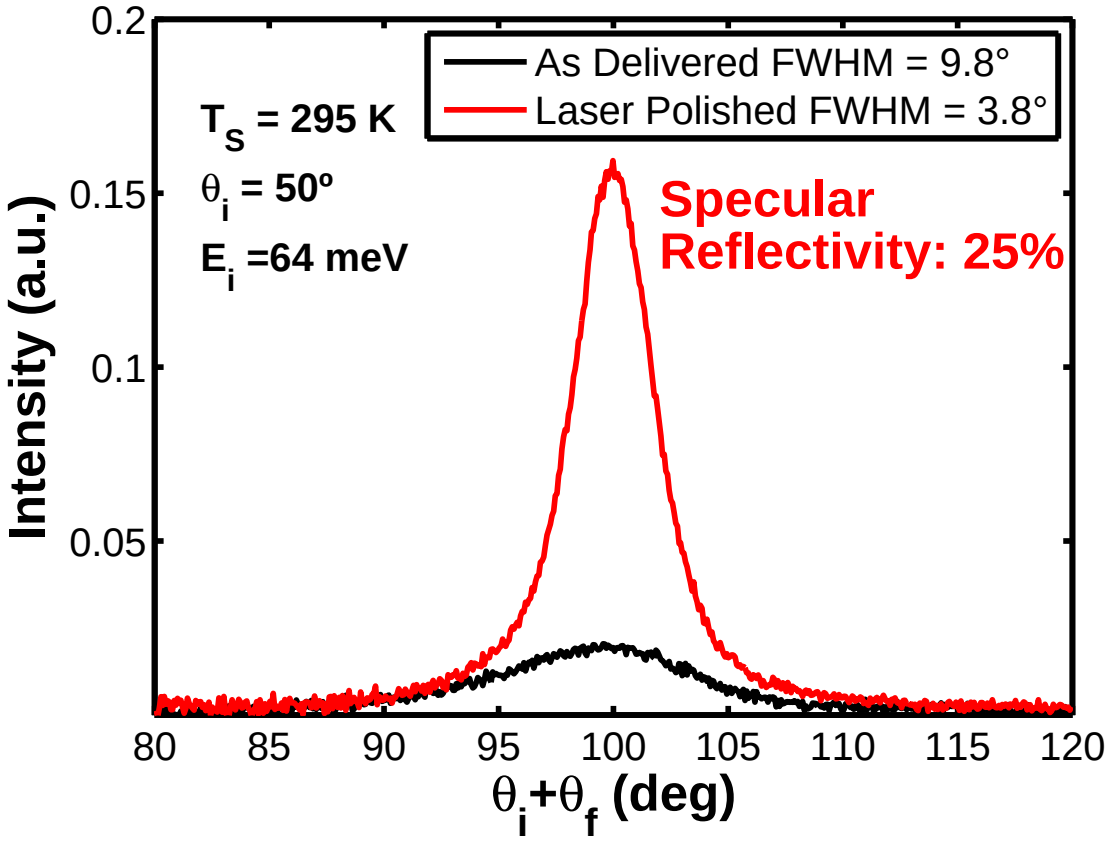

Figure 6.6: Comparison of He-diffraction spectra from two Ru(0001)/fused silica curved samples. The red spectrum corresponds to the laser polished sample, the black one to the sample "as delivered". The quality of the thin Ru film is clearly improved when the fused silica substrate is previously treated by laser polishing.

energy (E_i = 64 meV) and with room-temperature samples. A significant increase in the specular intensity is observed for the last sample. This is a remarkable result, and demonstrates that laser polishing enables the preparation of well-ordered scattering surfaces, even on macroscopically curved samples. The measured absolute reflectivity of He atoms at this incident conditions amounts at 4% for Ru on "as delivered" lens and at 25% for Ru on laser polished lens, which is similar to our best results obtained for clean Ru(0001) surfaces. The corresponding FWHM of the specular peak is 3.8°, much lower than the one for the untreated surface (9.8°). The width of the specular peak depends on the quality of the surface and provides information about the coherence length for the Ru on curved fused silica laser polished surface, as detailed in section 2.2.1. This parameter is of the same order of magnitude that the size [84] of the terraces, that is

~ 13 nm, whereas the coherence length for the Ru on curved lens surface is ~ 5 nm. Therefore, the comparison above clearly shows that Ru surface has larger domains after the substrate has been exposed to the laser polishing treatment.

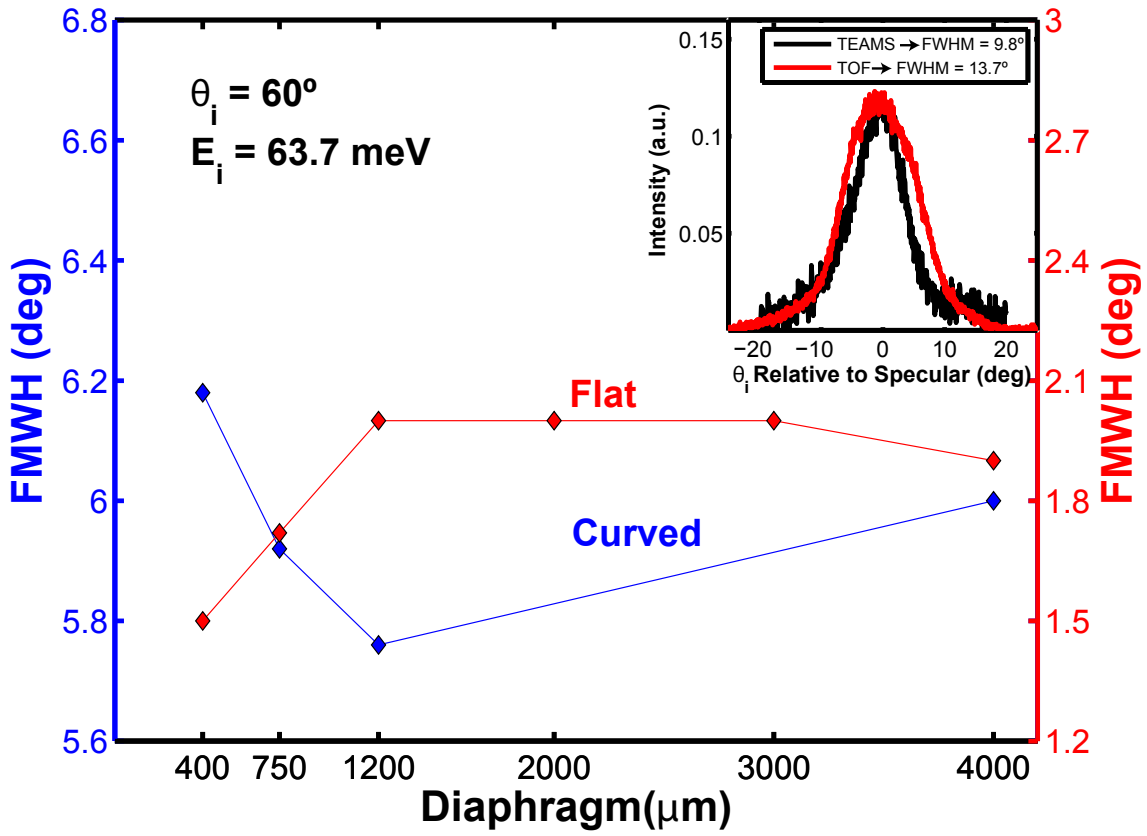

Figure 6.7: Effect of beam collimation on the specular width from Ru on laser polished lens (blue line) and from a flat surface of Cu(111) on sapphire (red line).

The collimation of the incident beam has been controlled through the variation of the aperture of the diaphragm, in order to study the focusing properties of the polished lens. Four different diameters (400, 750, 1200 and 4000 μm) have been used for Ru/Laser polished lens, which lead to four different widths for the direct beam. Figure 6.7 presents the FWHM as a function of the beam size at the diaphragm's position. The FWHM of the specular peak for Ru/Laser polished lens (blue line) decreases from 6.2° to 5.8° when the FWHM of the direct beam increases. On the other hand, the FWHM of the flat surface (red line) increases when the size of the diaphragm apertures is increased, as expected from the theory [7] and shown in the Fig. 2.6 in section 2.2.1. This must be considered as an evidence for the focusing of this mirror. This behaviour can be interpreted as follows:

when the atom beam is narrow enough, the area probed can be reduced to a flat surface; instead, when the beam size increases, the area probed behaves as a curved surface, thus focusing the beam. Nevertheless, when the beam impinges a big surface area, a focusing effect is observed until the area is too big and the irregularity of the surface dominates on the focusing effect.

A further proof of the focusing effect of this mirror is given by the comparison between the angular distribution of Ru on "as delivered" lens taken in TEAMS apparatus and the one taken in ERASMO. As shown in the inset of Fig. 6.7, a broader peak is recorded in ERASMO apparatus than in TEAMS. This is an unexpected result, if we bear in mind that the resolution of ERASMO set-up is much better than the one of TEAMS. Usually, the FWHM of the specular peak for a perfect surface crystal is 0.15° for ERASMO and 1° for TEAMS. An explanation for these measurements is given by the fact that the mirror has a radius of curvature of 92 mm and the detector in ERASMO is located 1698.5 mm away from the sample, whereas for TEAMS distance is just 55 mm. Thus, the mirror has its focus closer to the position of the TEAMS detector, which explains the narrower specular peak measured with this set-up. Defocusing effect is instead observed with ERASMO detector.

In order to use it as a mirror for helium atom beam it is necessary to make the surface inert. This can be achieved by growing a Gr layer onto the Ru surface. Figure 6.8 presents angular distributions, measured in HAS-TOF system, from graphene-terminated Ru on curved laser polished surface recorded for an incident beam energy of E_i = 32.3 meV (black) and E_i = 20.9 meV (red). Diffraction peaks and high specular intensity indicate the presence of a well-ordered surface. First order diffraction peaks ($\bar{1}0$) and (10) are clearly visible. Their appearance at different positions with different incident beam energies confirms that the in-plane Bragg diffraction condition for a hexagonal two-dimensional structure is fulfilled. The angular position of the diffraction peaks corresponds to a lattice constant $a = (2.46 \pm 0.02)$ Å for a Gr/Ru on treated curved fused silica substrate, in agreement with 2.4612 Å, the periodicity of a single carbon layer in graphite [105]. As far as we know, this is the first He-diffraction spectrum reported from a macroscopically curved surface.

In order to study the homogeneity of both samples (Ru on polished and unpolished substrates), interferometry and scanning electron microscopy have been employed. The images in Fig. 6.9a and b correspond to light interferometry measurements performed on the curved fused silica lenses before (a) and after (b) the laser polishing treatment. The morphology of the Ru(0001) thin film grown on curved fused silica is shown in Fig.

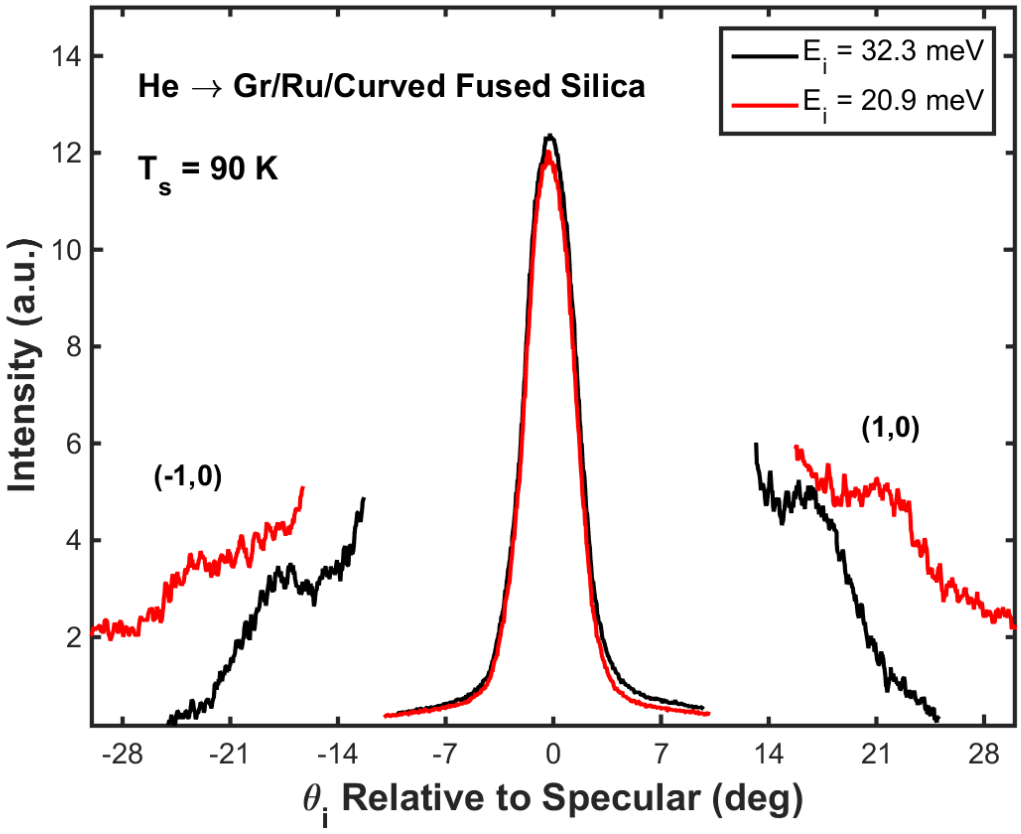

Figure 6.8: He diffraction spectra from the Gr/Ru(0001) on curved fused silica laser polished surface, measured at an incident beam energy E_i = 32.3 meV (black spectrum) and E_i = 20.9 meV (red spectrum). The sample temperature is T_s= 90 K. First order diffraction peaks are labeled with $(\bar{1}0)$ and (10).

6.9c and d, without and with laser polishing, respectively. It can be seen that the grains of the unpolished Ru(0001) surface are non uniform. For the treated surface, in contrast, the coating in the fused silica is compact, smooth and presents a clear homogeneity. A significant decrease in the surface roughness is clearly observed when compared to the unpolished surface shown in Fig. 6.9c. When the fused silica substrate is treated with the laser polishing technique, the Ru crystal size increases and the grains size distribution becomes broader, as shown by the two histograms in Fig.6.9e and f. The maximum grain size detected increases from 200 nm to 1200 nm, and the mean grain size increases from 120 nm to 300 nm when the laser polishing is performed. There is a clear correlation with the interferometry measurements. This suggests that the growing process of 200 nm of Ru is quite sensitive to the small differences observed with light interferometry,

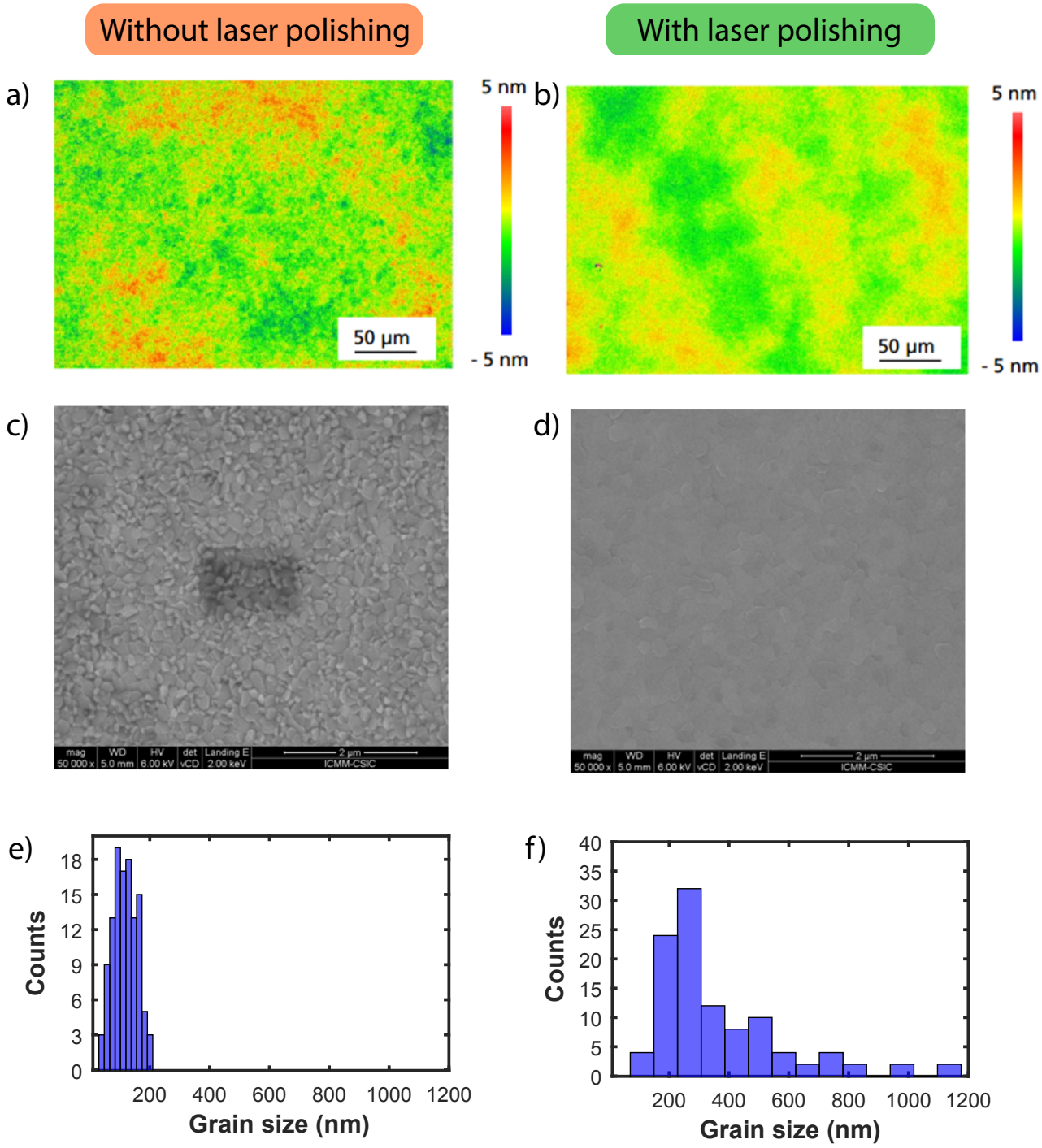

Figure 6.9: Light interferometry images of fused silica curved lenses: (a) Before and (b) after applying the laser polishing treatment. SEM images representative of the morphology of the Ru(0001) thin film grown on curved fused silica before (c) and after (d) laser polishing treatment. Grain size distributions of the Ru thin films grown on unpolished (e) and laser polished (f) fused silica lenses.

leading eventually to the large differences observed with He scattering, highlighted in Fig. 6.6.

6.5 Curved surfaces: graphene/Ru(0001) on curved sapphire

After a long search we have managed to find a company that can produce high quality curved sapphire. The α-Al_2O_3(0001) lenses were produced by SCHOTT GLASS company by specific requirements about curvature, dimension and surface polishing. In fact as mentioned in chapter 3, we had to use a mirror with a radius of curvature of 1666 mm in order to focus 535 mm away from the mirror, where a piezotable is placed. The piezotable has been installed in the TOF arm of ERASMO machine in order to measure micron and submicron spot sizes. The preparation of the Gr/Ru(0001)/Curved Al_2O_3 sample is the same used for flat sapphire, described in the subsection 6.2.1.

6.5.1 He–reflectivity for graphene/Ru(0001) on curved sapphire

Angular distribution of He scattering on Ru(0001)/CurvedAl_2O_3 surface was carried out with TEAMS apparatus in order to verify the quality of the Ru(0001) thin film. To emphasize the very good quality of the surface, a comparison between the He incident beam profile and the reflected one is presented in Fig. 6.10. Both measurements were taken at the same incident energy E_i = 64 meV. The profile of the Ru(0001)/CurvedAl_2O_3 peak follows the shape of the direct beam. Almost the same FWHM were recorded for both spectra, which confirms the high quality of the epitaxial Ru(0001) thin film. To corroborate this feature the morphology of Ru films was investigated by SEM, as shown in the inset in Fig. 6.10. Contrary to the SEM image of Ru/Fused Silica, no grains are observed for Ru(0001)/Curved Al_2O_3 sample. The Ru surface presents a very low roughness and uniform thickness, thus suggesting that the Ru thin film grows epitaxially.

To further explore the property of this system as mirror for neutral particles, the sample was mounted in the ERASMO system, where a piezotable has been mounted. Here, Gr was grown onto Ru(0001)/Curved Al_2O_3 surface. The angular distribution for such a surface is shown in Fig. 6.11. The scan direction of this measurements correspond to the $\overline{\Gamma M}$ direction of the Gr lattice. With this system the specular peak recorded is also very sharp. By performing Gaussian fits of this peak a FWHM of 0.28° is obtained. This value is comparable with the value obtained for Ru(0001) single crystal, that presents

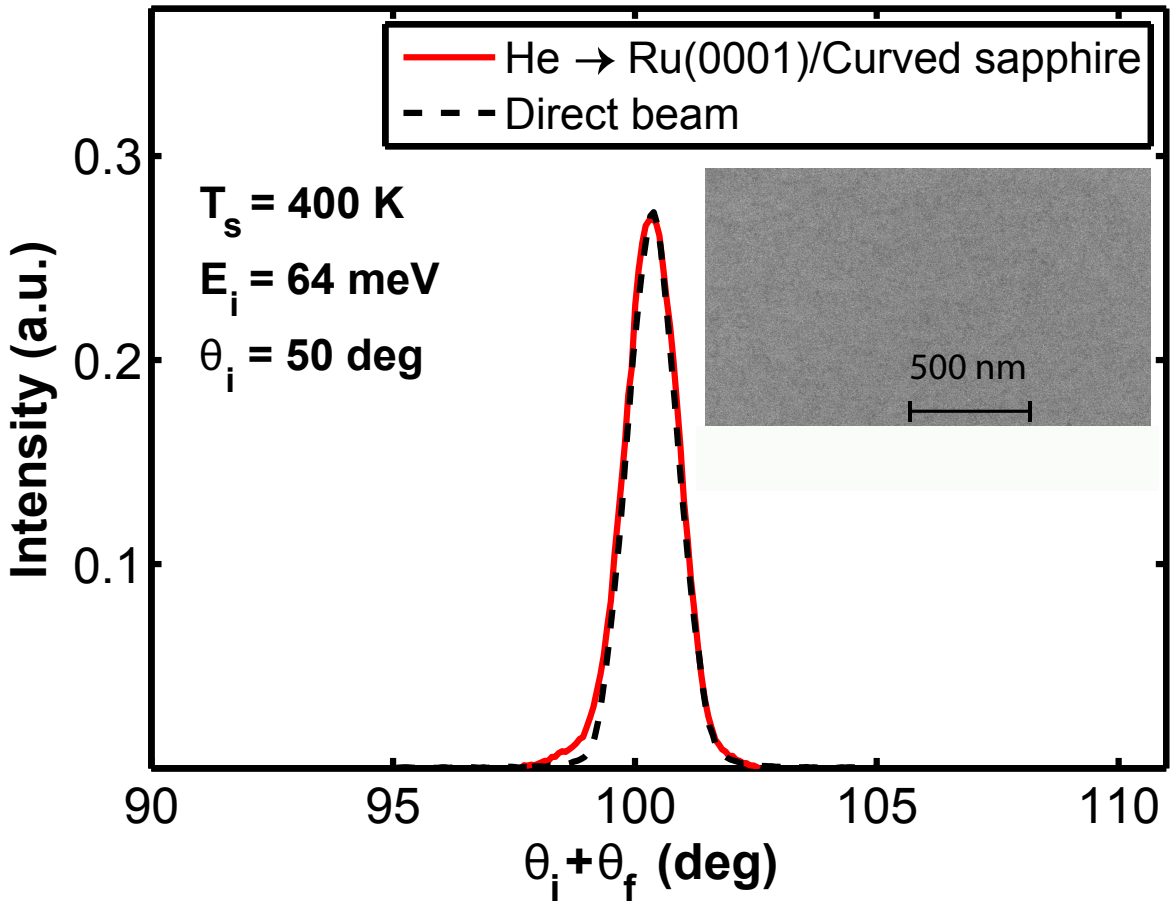

Figure 6.10: Comparison of the incident He beam intensity (black dashed line) with the specular He peak for Ru(0001)/Curved Al_2O_3 (red spectrm). The inset on the right side shows a SEM image of the sample.

a FWHM = 0.15° [133]. Another quite remarkable result from the He scattering from Gr/Ru(0001)/Curved Al_2O_3 is the observation of clear diffraction peaks due to the moiré superstructures resulting from the mismatch of the Gr and Ru(0001) surfaces. The first order diffraction peaks, labelled as G(1,0) and G($\bar{1}$,0), are produced by the Gr lattice. The derived lattice constant using Bragg condition yields a value a = (2.45±0.02) Å, in agreement whit the one obtained for Gr/Ru(0001)/Al_2O_3 in section6.2. The angular position of the diffraction peaks from Gr moiré lattice matches well with an hexagonal structure whit a periodicity of ~ 29.5 Å. The first four orders of the moiré diffraction peaks (indicated as m(1,0), m(2,0), m(3,0), m(4,0) are clearly detected. The high-intensity sharp peak m(12,0) matches exactly the position of the Gr peak G(1,0), and the peak

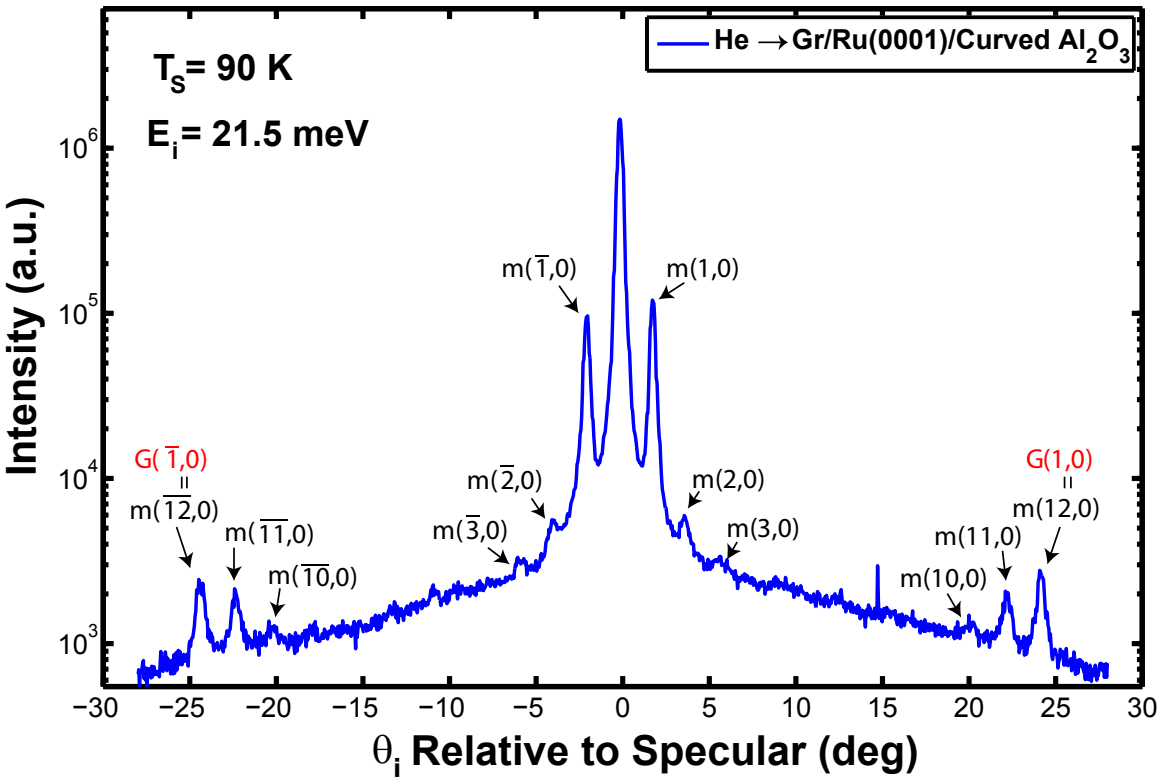

Figure 6.11: Angular distribution of He scattering from Gr/Ru(0001)/Curved Al_2O_3 along $\overline{\Gamma M}$. The sample temperature is 90 K and the incident energy E_i = 21.5 meV. The diffraction peaks of the moiré superstructure are labelled as m(n,0).

m(11,0) matches the position of the first order diffraction of Ru(0001) [134]. Therefore, the proposed model for the moiré (11 × 11) structure of the Gr/Ru(0001)/Al_2O_3 flat surface helds also for this curved surface.

Finally, measurements using the piezoelectric module have been made, in order to evaluate if a focusing effect would be possible with this system. However, no evidence of focusing with He beam was detected. A possible explanation for this is that the polishing of the sapphire lenses generates the required curvature by making concentric circular steps, as shown in Fig. 6.12. The dimension of these steps is such that for the light wavelength the surface appears curved, whereas for He atoms wavelength the sample seems to be composed of flat steps. In fact, experiments with laser beam confirm the focusing effect of this mirror.

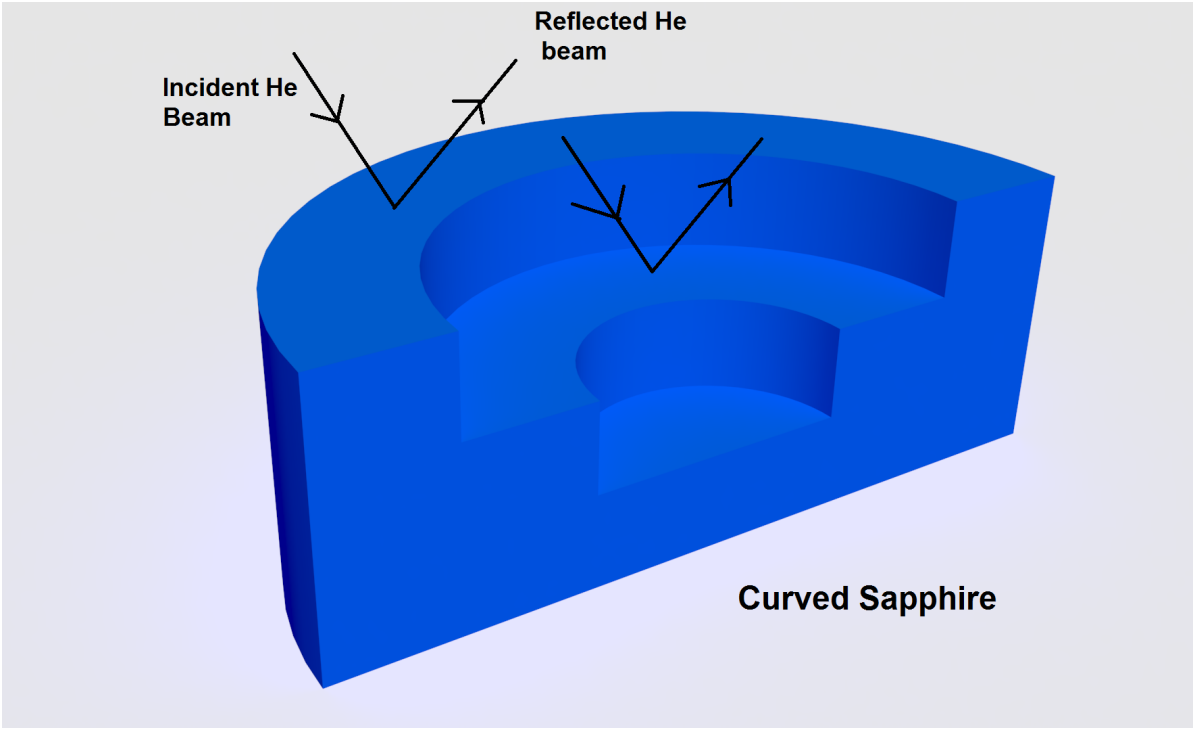

Figure 6.12: Curved sapphire section.

6.6 Conclusions

This chapter shows that the quality of Gr-terminated Ru(0001) thin film presents a strong dependence on the α-Al_2O_3 polishing. Better polishing leads to a better ordered Gr/Ru(0001) film, with a consequently higher He-reflectivity. This reflectivity reaches 15% for a room temperature He-beam.

When the substrate used changes from being crystalline to being amorphous, the quality of the Gr/Ru thin film gets worse. As expected, for amorphous substrates the growth of the Ru film is policrystalline. However, the high He-reflectivity measured for this sample shows the possibility of using amorphous substrate as starting point for building a mirror for He-microscopy. Besides, as far as we know this is the first observation of He-reflectivity from a policrystalline substrate with He scattering technique.

Furthermore, we provide the first clear evidence for the improvement of the surface quality of the metal coatings grown on top of macroscopically curved amorphous substrates. The key element is the use of the laser polishing technique to the fused silica curved substrate prior to deposition of the metallic coating. He atom scattering demonstrates the existence of quasi-epitaxial, long-range ordered domains of Gr/Ru thin

films grown on the curved fused silica laser polished substrates. The observation of both high specular reflectivity, reaching 25% of the incident beam, and first order diffraction peaks are evidences of the coating improvement due to laser polishing treatment. This improvement allows to prepare metal coatings on fused silica with unprecedented low roughness, which may have implications on other research areas, like lenses for solar cells and detection of energetic neutral atoms in space research.

Finally, the possibility to grow high-quality graphene/Ru film on curved sapphire has been confirmed by the observation of clear diffraction peaks due to Gr lattice and moiré superstructure.

CHAPTER 7

QUANTUM DECOHERENCE BEHAVIOUR IN NEON SCATTERING

It is known from previous studies that Ne atoms is more sensitive to surface structural details that He atoms, since anticorrugation effects are not present in Ne diffraction. To evaluate the possibility to employ a Ne beam instead of a He beam in NEMI, we made a systematic study of Ne atom scattering from Ru(0001) and graphene/Ru(0001) surfaces. In both systems, the quantum and classical regimes were observed and analysed. To explore the boundary between the two regimes, a variation of the surface temperature or incident energy is necessary. The classical smooth surface model was used to perform theoretical simulations in order to reproduce the angular distributions and the energy resolved spectra in the classical regime, which allows to determine the effective mass and the Debye temperature. The theoretical calculations, predict sub-specular scattering at low energies that shifts to supra-specular with increasing incident energy, in agreement with experiments. Multiphonon excitations were also observed in the classical regime, where no evidence of quantum features is detected.

7.1 Introduction

The employment of Ne atoms and, more generally, any noble gas scattering is a well established technique to investigate the structural and dynamical properties of surfaces [1, 135]. The use of heavier projectiles is, usually, unfavourable in atom scattering experiments. However, Ne atoms have been shown to be very sensitive to the surface structure when the incident energy and the surface temperature are in the neighbourhood of room temperature or smaller. Furthermore, to explore the possibility of using atomic beams in the classical regime in NEMI, heavier atoms than He have to be employed. Classical scattering conditions are easier to reach using atomic projectiles heavier than He, such as Ne.

The existence of coherent scattering for Ne atoms has been demonstrated for the first time in highly corrugated surfaces, as LiF(110) [136–138] and Cu(117) [139]. First studies on Ne diffraction from dense-packed metal surfaces were carried out from Rieder and Stocker in 1984, from Ni(110) and Pd(110) [140] and by Salanon from Ni(110) [141]. In these studies, the evidence of a higher sensitivity of Ne atoms to the structural details came out. In fact, Ne scattering presented larger corrugation amplitudes than those obtained with He atoms [142–144]. This effect was called anticorrugating effect for He-metal surface interactions and it was systematically studied for the first time by Rieder *et al* in Ni(110)c(2×4)H, and Rh(110)(1×3)H and (1 ×2)H systems [145]. The theoretical explanation of the smoothness observed in He diffraction experiments was given by Annet an Haydock [146]. Regarding Ru surfaces, Ne and Ar diffraction from the clean Ru(0001) surface had already been observed in the past [147]. These early studies showed how a normal corrugation effect is observed with Ne, whereas anticorrugating effects are present in the case of He and Ar.

In this work, systematic experiments of Ne scattered from both bare Ru(0001) and graphene-covered Ru(0001) were performed with two aims. Firstly, study Ne diffraction in the quantum regime. In order to perform this, angular distributions of Ne scattered in quantum regime from both system are reported for a variety of experimental incident conditions. In addition, a comparison between He and Ne diffraction from Gr/Ru(0001) and the different corrugation derived with the two projectiles is discussed. Secondly, study the classical regime of Ne scattering and its quantum boundary i.e. the transition between the coherent quantum regime and the incoherent classical regime for both bare Ru(0001) and Gr/Ru(0001). In this case, the Ne scattering measurements carried out in the classical regime are analyzed with a classical theory of heavy noble gases scattering, called the

smooth surface model (SSM) [148–152]. The comparison between the theoretical and experimental data enables an evaluation of the effective surface mass. By using this effective mass, Debye temperatures for Ru(0001)is obtained from measurements of the thermal attenuation of the specular diffraction peaks in the quantum regime.

Finally, in the classical regime where no evidence of quantum features is detected, energy-resolved scattering spectra exhibit only a single broad multiphonon peak, similar to the situation reported previously for Ne scattering on Ni(111) [153].

7.2 Experimental details

Ne scattering measurements were carried out in both UHV chambers for atoms scattering: TEAMS, described in subsec. 2.2.1 and ERASMO, described in subsec. 2.2.2.

In both systems the Ne beam is generated by introducing the Ne gas from a 60 bar reservoir into a high vacuum chamber (10^{-6} mbar) via a 10 μm platinum nozzle. The incident beam energy can be varied in the TEAMS apparatus between 18 and 151 meV regulating the nozzle temperature, and similarly in the TOF machine up to a maximum of 92 meV.

The sample employed in this study is a Ru(0001) single crystal disk 2 mm thick with a diameter of 10 mm. Clean Ru(0001) surfaces were prepared in UHV by cycles of ion sputtering (1 KeV and $P_{Ar} \simeq 2 \times 10^{-5}$ mbar), followed by oxygen exposures at 1150 K plus final flashes up to 1500 K. In both chambers, surface cleanliness and order were ensured by frequent monitoring of the angular distribution in the neighborhood of a specularly reflected He beam as well as through low energy electron diffraction (LEED) measurements. In order to obtain a graphene surface on the clean Ru(0001) substrate the sample was heated to 1100 K and maintained there during exposure to ethylene at pressure $P_{C_2H_4} = 5 \times 10^{-6}$ mbar for 10 minutes with subsequent slow cooling in UHV [12, 58, 60]. The target temperature was measured with a type-C thermocouple spot-welded to the sample. The angular distributions presented in this work were measured after aligning the sample along the $\overline{\Gamma M}$ direction of Ru(0001), both on clean Ru(0001) and for Gr on Ru(0001).

7.3 Theoretical method

Theoretical calculation were presented thanks to the collaborations with Professor Joseph R. Manson (Clemson University, USA) and Professor Wayne Hayes (Greenville Technical

College, USA).

In the classical regime and for a potential energy surface that if flat except for small thermal vibrations, the smooth surface model (SSM) holds [148–152]. The transition rate $w(\mathbf{p}_f, \mathbf{p}_i)$ for an atom with incident momentum $\mathbf{p}_i$ to be scattered into a final state with momentum $\mathbf{p}_f$ is [148]

$$w(\mathbf{p}_f, \mathbf{p}_i) \propto \frac{1}{(4\pi k_B T \Delta E_0)^{3/2}} |\tau_{fi}|^2 \times exp\Big(-\frac{(E_f - E_i + \Delta E_0)^2 + 2v_R^2 \mathbf{P}^2}{4\pi k_B T \Delta E_0}\Big) \quad (7.1)$$

where $\Delta E_0 = (\mathbf{p}_f - \mathbf{p}_i)^2/2M$ is the recoil energy, M is the effective mass of the surface, T is the surface temperature, E_i and E_f are the initial an final energies of the atom, v_R is a weighted average of phonon velocities parallel to the surface, [154, 155] and $\mathbf{P}$ is the surface-parallel component of the scattering vector $\mathbf{p}_f - \mathbf{p}_i$. The scattering form factor is $|\tau_{fi}|^2$, the mod-squared transition matrix of the interaction potential. As in other studies using the SSM it is approximated by its value for the potential of a hard repulsive wall, $\tau_{fi} \propto p_{fz} p_{iz}$.

The quantity which, in principle, should be compared with the energy resolved inelastic spectra measured here should be the differential reflection coefficient or intensity as a function of final solid angle and final kinetic energy $dR(\mathbf{p}_f, \mathbf{p}_i)/dE_f \Omega_f$ which is obtained from the transition rate upon multiplying by the a Jacobian which is proportional to $|\mathbf{p}_f|$ and dividing by the incident flux which is proportional to p_{iz}. However, there is a correction that must be applied due to the energy dependence of the detectors. The the detector efficiency is proportional to the time that the final scattered particle takes to pass through the ionization chamber, which is inversely proportional to the final momentum. This means that, for comparisons with the present experiments, the theoretical differential coefficient should multiplied by the dettector correction factor of $1/p_f$.

The quantity to be compared with the measured angular distribution intensities is

$$\frac{dR}{d\Omega_f} = \int_0^\infty dE_f \, \frac{dR(\mathbf{p}_f, \mathbf{p}_i)}{dE_f d\Omega_f} \, \frac{p_0}{p_f} \, , \quad (7.2)$$

where the factor $1/p_f$ is the detector correction and p_0 is an arbitrary constant having dimensions of momentum.

7.4 Neon diffraction from clean Ru(0001) and from graphene/Ru(0001)

Figure 7.1 shows measurements of He and Ne atoms scattered form Gr/Ru(0001) in order to emphasize the great difference between He and Ne scattering process for this surface. Both measurements have been taken at an incident energy of 64 meV and a surface temperature of 90 K. Figure 7.1a shows in-plane He scan measured at an incident angle of 60°. Although first and second orders moiré diffraction peaks are clearly detected, their intensity is about one order of magnitude smaller than the specular peak. Likewise, the first order diffraction peak of Gr, Gr($\bar{1}$,0), is observed at a final total angle of 98.5°, but its intensity is two orders of magnitude smaller than the specular peak.

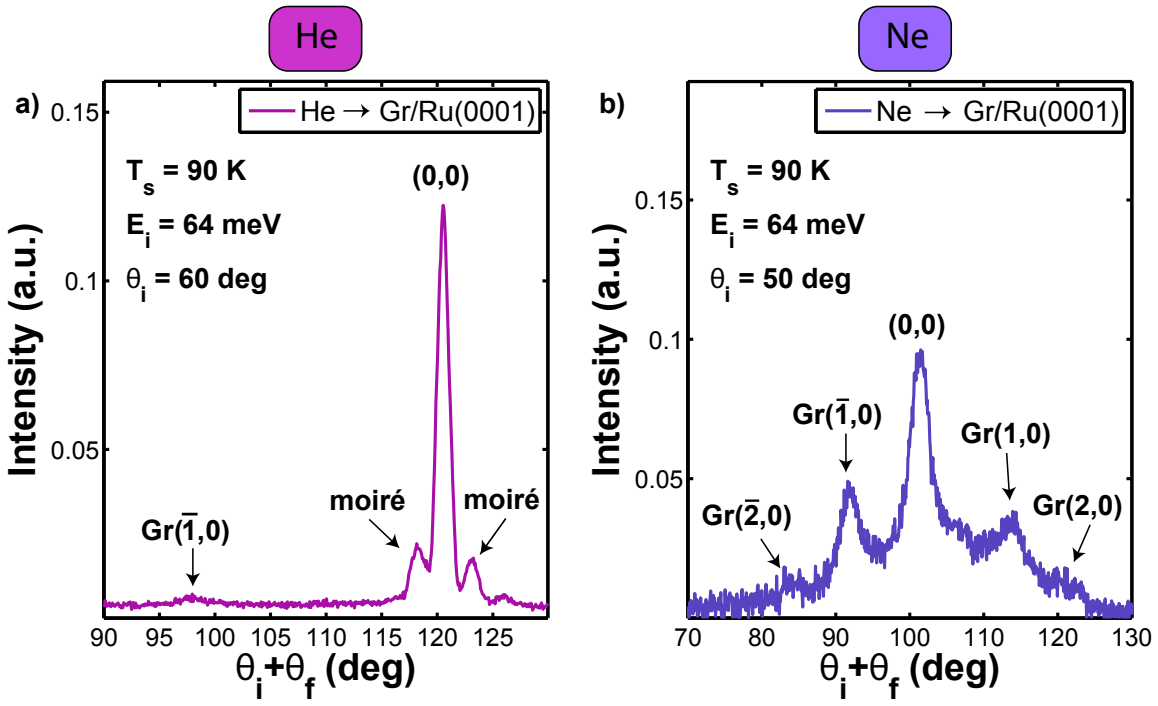

Figure 7.1: In-plane diffraction spectra obtained with (a) He and (b) Ne atomic beams from Gr/Ru(0001) surface. Using Ne atoms the intensity of the specular peak dramatically falls down, whereas the intensity of the diffraction peaks increase up to reach magnitude comparable to the specular peak. This difference indicates a larger corrugation amplitude in the case of Ne.

By contrast, as shown in Fig. 7.1b, diffraction intensities for Ne scattering are of the same order of magnitude than the specular peak. This suggests that the surface corrugation derived from Ne diffraction is higher than the one deduced using He beams. This result seems to be consistent with previous studies, which found systematic differences

in the surface corrugation when probed with He and Ne beams [142–145]. This effect is known as anticorrugating effect in He-metal interaction [145]. The higher corrugation "seen" by Ne atoms is also in better agreement with previous studies about Gr/Ru(0001) corrugation, in which a corrugation of 1.5 Å was reported from x-ray diffraction [156] or low-energy electron diffraction [157]. In addition, density functional theory (DFT) calculations predicted the same corrugation value [158, 159]. In contrast, the structural corrugation obtained by He diffraction is substantially smaller (0.15 Å) [160].

Furthermore, due to the heavier mass of Ne with respect to He, higher diffraction orders are detected with Ne in the same angular scan. In fact, the first two orders of Gr pattern and up to the thirtieth order of the moiré superstructure are detected with Ne scattering. This factor, together with high corrugation of the surface, causes the loss in intensity of the specular peak.

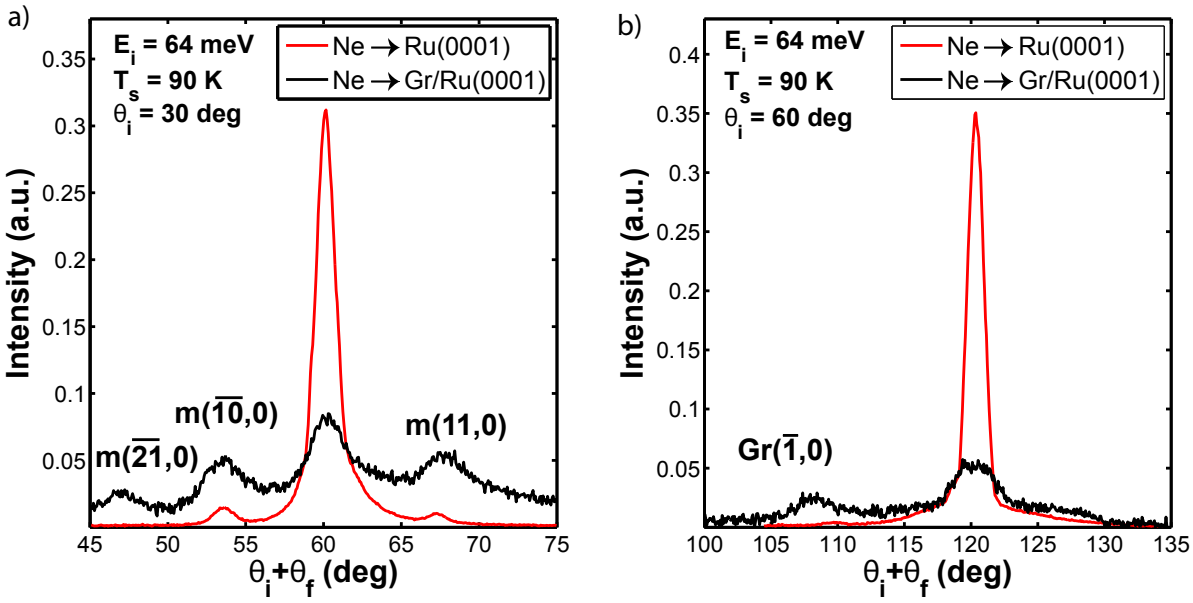

Figure 7.2: Comparison between in-plane Ne diffraction spectra from clean Ru(0001) (red curve) and Gr/Ru(0001) (black curve) surfaces, taken at an incident angle (a) $\theta_i = 30°$ and (b) $\theta_i = 60°$.

In order to compare the enhancement of the surface corrugation due purely to the Gr layer onto Ru(0001) crystal, a comparison of Ne diffraction spectra from bare Ru(0001) and Gr/Ru(0001) surfaces is presented in Fig. 7.2 for two different incident angles. The measurements were recorded along $\overline{\Gamma M}$ direction of the Ru(0001) substrate and under the same conditions: incident beam energy E_i = 64 meV and surface temperature T_s = 90 K. Due to the high-corrugated surface and the many open diffraction channels for

Ne scattering on Gr/Ru(0001) surface, the decrease observed in specular intensity is dramatic.

In the diffraction pattern of Ne scattering from Ru(0001) surface (Fig. 7.2a, red curves) the first order diffraction peaks are clearly visible and their intensity is one order of magnitude lower than the specular peak. When the Gr layer is grown on top of a Ru(0001) crystal, a more complex pattern arises from Ne scattering. The resulting angular distribution is given by the convolution of the Gr diffraction peak with the moiré ones. The angular resolution of TEAMS apparatus is not able to resolve each single peak. However, it is possible to determine the diffraction channel corresponding to the highest peaks.

In Fig. 7.2a the position of the diffraction peaks closest to the specular matches the 10th and the 11th order of the Gr moiré pattern and are indicated with m($\overline{10}$,0) and m(11,0). Also the other visible diffraction peak matches the position of m($\overline{21}$,0). The corresponding periodicity of the moiré superstructure agrees well with a value of a = 29.52 ± 0.02 Å. This result confirms the existence of the moiré underlying superstructure, despite of the lack in resolution for all the diffraction peaks. However, if the incident angle is changed, as shown in Fig. 7.2b, the peaks closest to the specular corresponds now to the first order peak of the Gr pattern, labelled as Gr($\overline{1}$,0). By using the in-plane Bragg diffraction condition for a hexagonal two-dimensional structure, the derived value of the lattice constant of Gr on Ru(0001) is $a = 2.46 \pm 0.02$ Å, identical to the value reported for Gr/Ru(0001) [57]. This result is in good agreement with 2.4612 Å, the periodicity of a single carbon layer in graphite [105].

This difference between distinct incident angles can be interpreted in geometrical corrugation terms. When the Ne atoms impinge the surface with high incident angles, the lower part of the corrugation is not probed. This is the reason why the intensity of the diffraction peaks for higher incident angles is affected, as demonstrated in Fig. 7.2 by the comparison between the Ru(0001) spectra (red curves) taken at θ_i = 30° (a) and θ_i = 60° (b). With small incident angles the Ru(0001) diffraction peaks are clearly resolved, whereas when the incident angle is increased, this features disappear. In the Gr/Ru(0001) case, on the contrary, the peaks do not disappear while increasing the incident angle, but they match with different diffraction positions of the Gr and moiré pattern.

Therefore, if the same interpretation applied to the bare Ru scenario is also followed in this case, it can be concluded that for low incident angles the predominant factor is the moiré corrugation. This is due to the incident beam probing the lowest part of the corrugation. However, when θ_i is increased, moiré corrugation losses importance as Ne

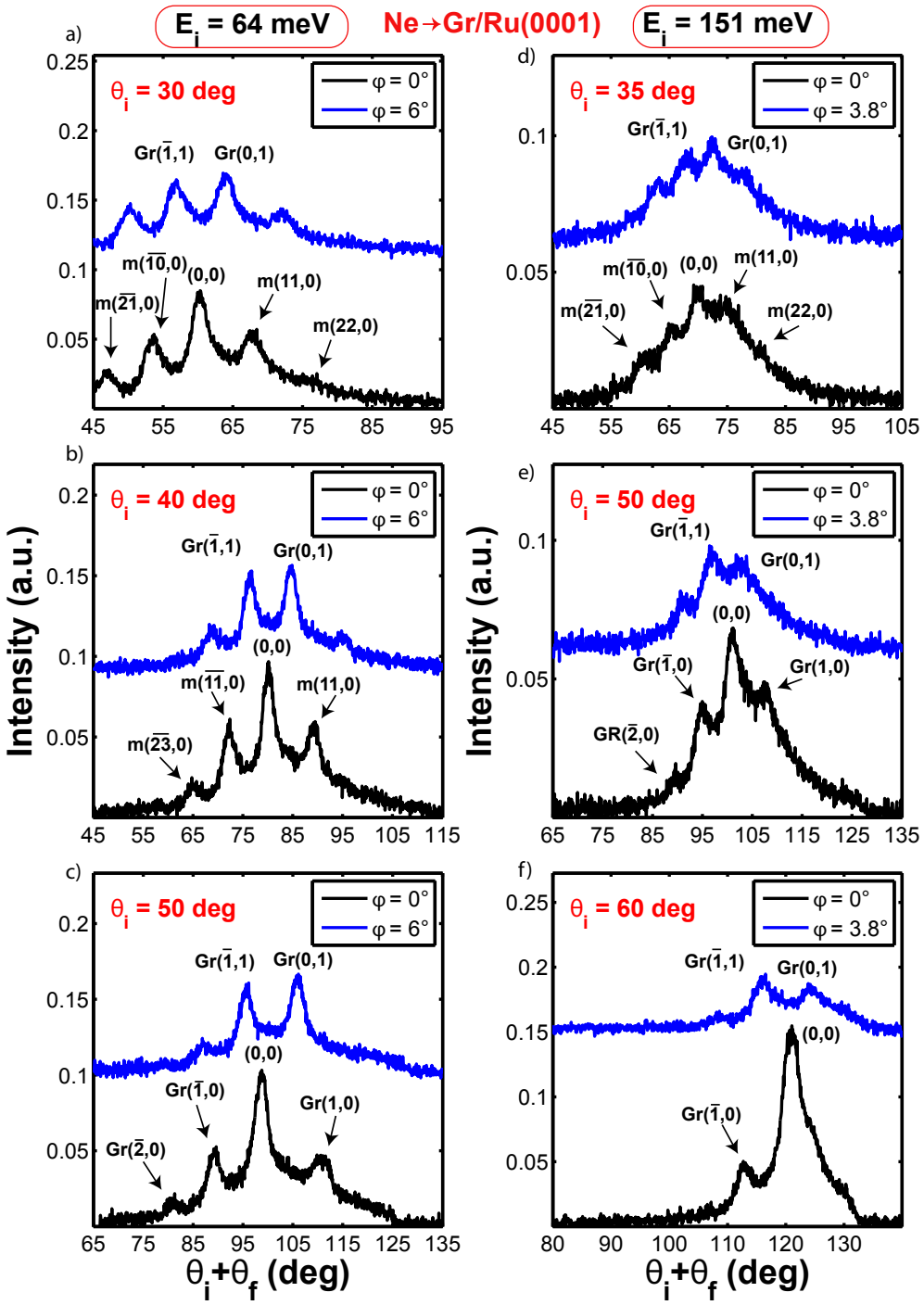

Figure 7.3: In-plane (black curve) and out-of plane (blue curve) angular distributions of Ne scattering on Gr/Ru(0001). Left column ((a)-(c)) shows measurements taken for an incident energy E_i = 64 meV, whereas in the right column ((d)-(f)) are presented measurements for E_i = 151 meV. Different θ_i was used for each incident energy.

behaves as if it were less sensitive to it, so Gr peaks become the dominant factor in the diffraction pattern. It can be then hypothesized, as a result of these analysis, that the underlying moiré superstructure presents a higher degree of corrugation than Gr.

Angular distributions of Ne scattering on Ru(0001) were carried out systematically for different incident energy values, E_i, ranging from 41 to 150 meV and different incident angles, $\theta_i = 30° - 60°$. Both in-plane and out-of-plane diffraction spectra were recorded for all beam energies E_i and incident angles θ_i. Figure 7.3 shows a representative series of Ne diffraction spectra, taken both in-plane and out-of-plane, for Gr/Ru(0001) surface. Out-of-plane diffraction peaks reveals, once again, to be of the same order of magnitude than the specular peak, for both incident energies. However, as discussed before, change in the diffraction peaks appear when the incident angle is varied.

For $\theta_i = 30°$ (Fig. 7.3a), moiré diffraction dominates in the in-plane spectra, as described in Fig. 7.2, whereas the two highest peaks of out-of-plane diffraction correspond to Gr lattice, because the scan has been made for $\phi = 6°$, where the first order out-of-plane diffractions of Gr are expected to appear. In any case, first order of moiré out-of-plane diffraction is relatively close ($\phi = 5°$) to this plane. For this reason the second order diffraction peaks in the out-of-plane scattering are hard to assign at a specific peak. The convolution of the moiré superstructure with the Gr lattice does not enable a clear determination of these peaks. For $\theta_i = 40°$ (Fig. 7.3b), the diffraction peaks match the 11th and the 23rd order of the moiré lattice. The out-of-plane spectra show high intensity for Gr($\bar{1}$,1) and Gr(0,1) peaks, whereas a lower intensity is detected for second order peaks.

However, if the incident angle is raised to 50°, as shown in Fig. 7.3c, the diffraction peaks labelled as Gr($\bar{1}$,0), Gr(1,0) and Gr($\bar{2}$,0) correspond now to the first two order peaks of the Gr pattern. Likewise, the out-of-plane diffraction peaks match the intense Gr($\bar{1}$,1) and Gr(0,1) peaks. When the beam energy is risen up to 151 meV (Fig. 7.3d-f), the interaction structure presents the same order already seen for $E_i = 64$ meV. However, the resolution of the peak is affected by the increase of incident energy.

Gr/Ru(0001) surface does not seem to be suitable as atomic mirror if probed with Ne atoms, due to the high corrugation experimented by the surface in Ne diffraction, that causes low diffraction of the specular peak. However, its use in the classical regime, where all the diffraction features disappear, could be a valid application. For this reason, the following sections explore, the scattering of Ne in the classical regime.

7.5 Quantum decoherence of diffraction

Figure 7.4a shows angular distributions of Ne atoms scattered from a clean Ru(0001) surface for an incident beam energy $E_i = 64$ meV. The attenuation of the specular peak with increasing surface temperature is readily observed. Ne scattering allows a clear visualization of the transition from the quantum to classical regimes. The black spectrum, corresponding to a surface temperature of 90 K, exhibits an evident elastic peak. With increasing surface temperature, the intensity of the specular peak decreases and the background, due to inelastic scattering, begins to dominate (green and cyan spectra).

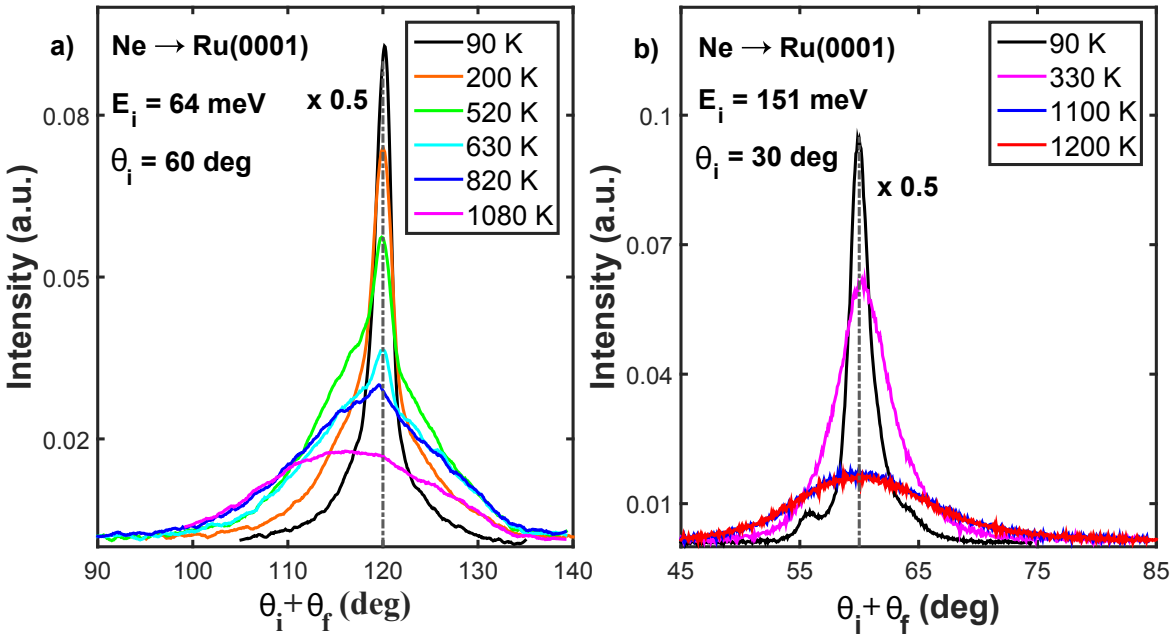

Figure 7.4: Attenuation of the specular peak with increasing surface temperature of the Ru(0001) sample measured at two different incident energies and angles: (a) The incident beam energy is $E_i = 64$ meV and $\theta_i = 60°$, (b) The incident beam energy is $E_i = 151$ meV and $\theta_i = 30°$

At the highest surface temperature, only a broad classical peak is observed (magenta spectrum) and it presents a most probable final angle (peak position) that is shifted sub-specular with respect to the specular diffraction position.

If the incident beam energy is increased, the transition from quantum to classical regime takes place at a lower surface temperature, as shown in Fig. 7.4b. These four spectra have been collected at different surface temperatures, for a fixed nozzle temperature of 700 K corresponding to an incident energy of the Ne beam of 151 meV, and for an incident angle of $\theta_i = 30°$. The existence of a low-intensity, but well resolved $(\bar{1}, 0)$

and (1,0) diffraction peaks can be seen in the lowest temperature (black curve) spectrum. This is the fingerprint of the existence of well–ordered Ru(0001) domains and of the quantum nature of scattering under these conditions. When the surface temperature is slightly above room temperature, the elastic peak almost disappears and the inelastic contribution begins to dominate (magenta spectrum). Note that for E_i = 64 meV, this situation happens at a higher temperature (~ 820K, blue spectrum in Fig.7.4a). Also in this case the asymmetry in the inelastic background for a temperature of 1100 K is observed. However, the shift of the classical peak to the left of the specular peak is less evident.

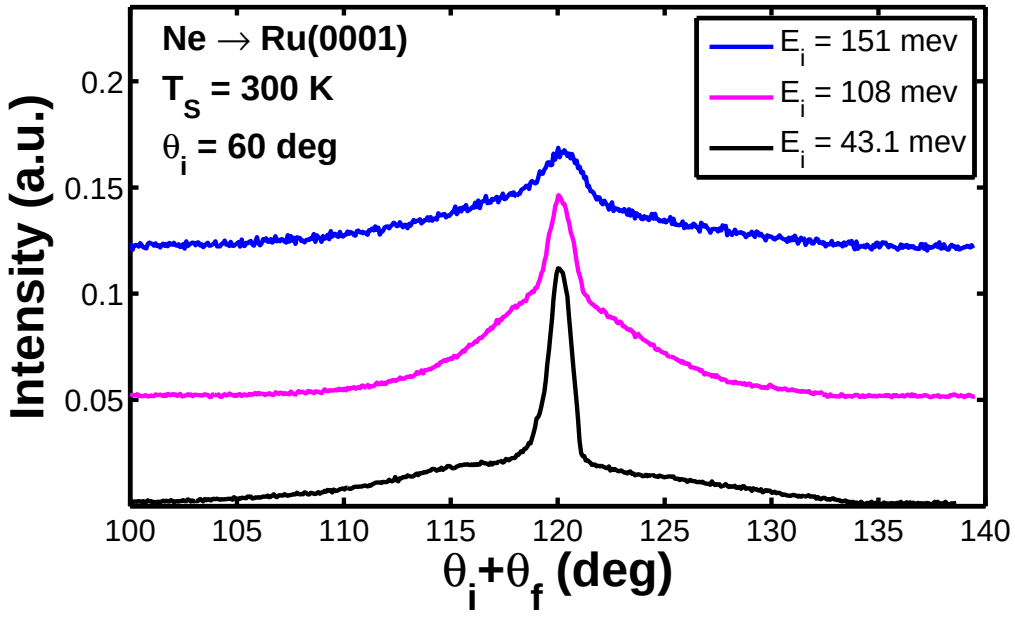

Figure 7.5: In-plane angular distribution of Ne scattering from clean Ru(0001) surface, taken at different incident energies with a fixed surface temperature 300 K.

The transition from quantum regime to the classical one can also be observed by changing the incident energy while the surface temperature is maintained at a fixed value. In Fig. 7.5 the evidence of this phenomena is reported. The incident energy has been changed from 43.1 meV to 151 meV, keeping the surface temperature at 300 K. For E_i = 43.1 meV the quantum peak dominates in Ne scattering. However, the Ne specular peak decreases in intensity when the incident energy is risen, as in the case of E_i = 108 meV, up to disappear when the incident energy reach 151 meV.

Similar results were also obtained for Ne scattering from the Gr/Ru(0001) surface.

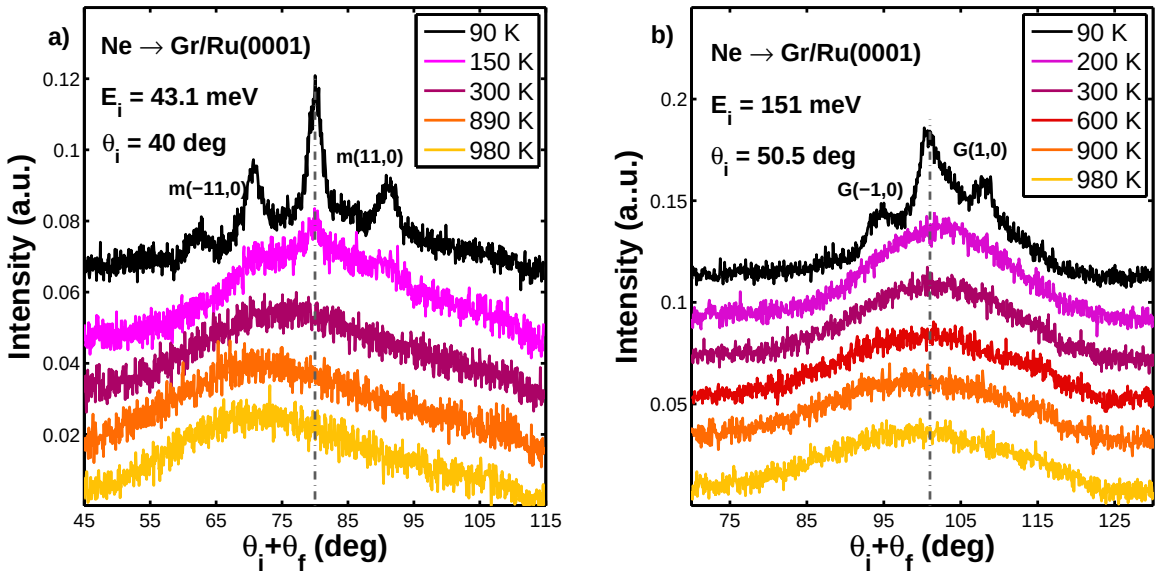

Figure 7.6: Attenuation of the Ne specular peak with increasing surface temperature for Gr/Ru(0001), measured at two different incident energies and angles: (a) $E_i = 43.1$ meV and $\theta_i = 40°$; (b) $E_i = 151$ meV and $\theta_i = 50.5°$. Note how the quantum features are lost when the surface temperature is increased and the maximum of the classical peak is shifted towards sub-specular positions.

Figure 7.6 shows several angular distributions of Ne atoms scattered from Gr/Ru(0001) taken at different surface temperatures from 90 K to 980 K. The data in Fig. 7.6a were recorded for a fixed incident angle $\theta_i = 40°$ and incident energy of 43.1 meV. The existence of well ordered domains can be appreciated in the black spectrum, where diffraction peaks are clearly observed. The positions of the diffraction peaks close to the specular peak correspond to the eleventh order of the Gr moiré pattern and are labelled with m(-11,0) and m(11,0). However, as shown in Fig. 7.6b, when the incident angle is increased the positions of the diffraction peaks match with the first order of the Gr pattern.

The specular and the diffraction peaks of Gr were detected only up to 150 K (magenta spectrum), due to the strong attenuation caused by the Debye-Waller effect and the high corrugation of Gr on Ru(0001). Also for this system broad and asymmetric peaks centered at sub-specular final angles have been detected for temperatures above room temperature. The amount of the peak's shift in this range of temperatures is strongly dependent on the translational energy of the beam. Similarly to the case of clean Ru(0001), the shift of the spectra for Gr/Ru(0001) is more pronounced for the lowest incident energy. If the incident energy is raised to 151 meV, the most probable angle is very near to the specular

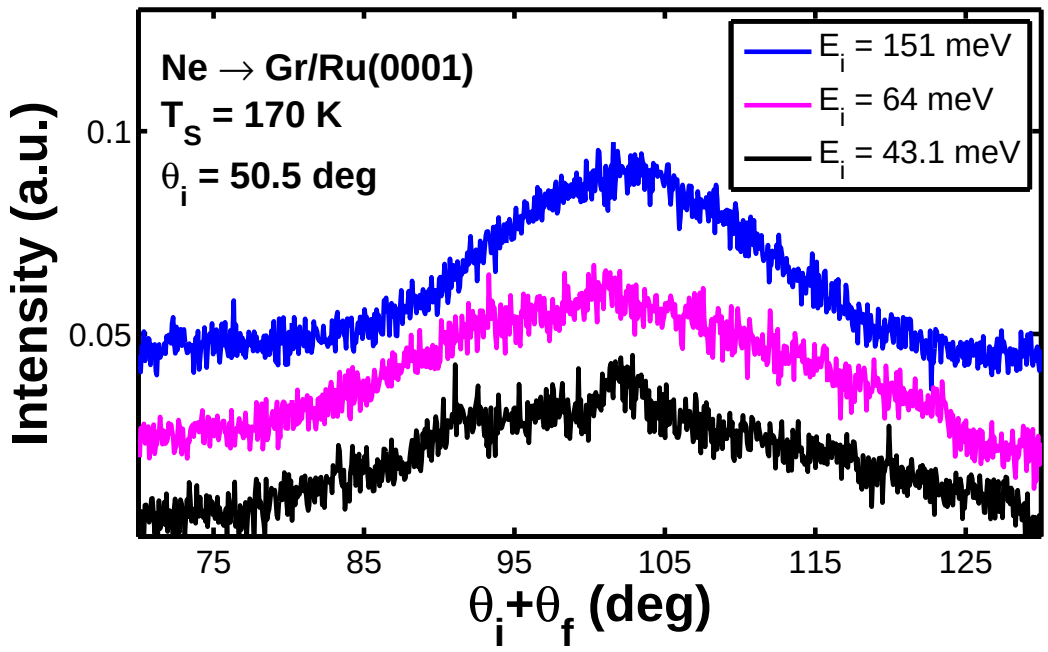

Figure 7.7: In-plane angular distribution of Ne scattering from Gr/Ru(0001) surface, taken at different incident energies with a fixed surface temperature 170 K.

angle (see Fig. 7.6b).

Also for Gr/Ru(0001) system, the attenuation of the Ne specular peak with increasing incident energy can be observed, as shown in Fig. 7.7. The beam energy was varied from 43.1 to 151 meV, while the surface temperature was kept at 170 K. A low surface temperature is used with respect to the Ru(0001) system, due to a faster transition to the classical regime for Gr/Ru(0001) surface. For low incident energy, E_i = 43.1 meV, the specular peak and same diffraction peaks are still visible, although with a very low intensity. Rising the incident beam energy to 64 meV the quantum features of the spectra are almost suppressed, until they disappear completely for E_i = 151 meV.

7.6 Surface Debye temperature

Measurements of the thermal attenuation of the reflected beam provide information on the nature of the scattering, for example whether it is quantum mechanical or classical, and can give an estimate of the surface Debye temperature. The intensity $I(T)$ of a diffraction peak for a surface at a given temperature T is related to its value I_0 that it

would have for a frozen lattice completely at rest by the relation [1]

$$I(T) = I_0 e^{-2W(T)} \tag{7.3}$$

where $\exp\{-2W(T_S)\}$ is the Debye-Waller factor. A standard procedure is to evaluate the Debye-Waller exponent using a Debye model for the phonons at the surface, then for sufficiently large T and for the specular diffraction peak one obtains

$$2W(T) = \frac{24m(E_i \cos^2\theta_i + D)T}{MK_B\Theta_D}\ , \tag{7.4}$$

where m is the mass of the impinging atoms, D is the potential well depth, and Θ_D is the surface Debye temperature. The appearance of the physisorption well depth D added to the energy associated with motion normal to the surface $E_i \cos^2\theta_i$ accounts for the larger energy of the atomic projectile as it moves in the well. [23]

The typical way of evaluating the Debye temperature Θ_D is through evaluation of $2W(T)$ over a range of temperatures. However, this is impractical for the system of Ne scattering from Ru because, as is evident from Fig. 7.4, at high temperatures the specular peak is completely attenuated and disappears while at lower temperatures the surface is rapidly contaminated, most likely with adsorption of residual hydrogen in the vacuum chamber. At lower temperatures, during the time needed to achieve a stable temperature, the reflection will be affected by varying degrees of contamination. For this reason, we choose to obtain similar information from the incident normal energy dependence of the specular beam at fixed temperature as shown in Fig. 7.8 which exhibits logarithmic attenuation plots for both He and Ne scattering from Ru(0001). The Ru(0001) surface temperature was fixed at 90 K in the measurement of Ne scattering and at 200 K in the measurement of He scattering. The values used for D are 13 meV for He and 22 meV for Ne [147]. By taking angular distributions as function of the incident angle, once the incident energy has been set, more accurate and controlled measurements are possible. Before recording each angular distribution, a flash-annealing was made in order to ensure the cleanliness of the surface and when the thermocouple marked a fixed temperature value the measurements started. In this way, the same experimental conditions for each spectra can be ensured.

The logarithmic D-W attenuation of the specular peak for scattering of He (red curve) and Ne (blue curve) atoms from Ru(0001) is shown in Fig. 7.8 as a function of $E_i \cos^2(\theta_i)$. The intensity I represents the area of the Gaussian fit of the specular peak, normalized with respect to the intensity of the direct beam, denoted by I_0. According to Eq. 7.3, the logarithmic plot of the normalized intensity versus $\mathrm{E}_i \cos^2(\theta_i)$ gives rise

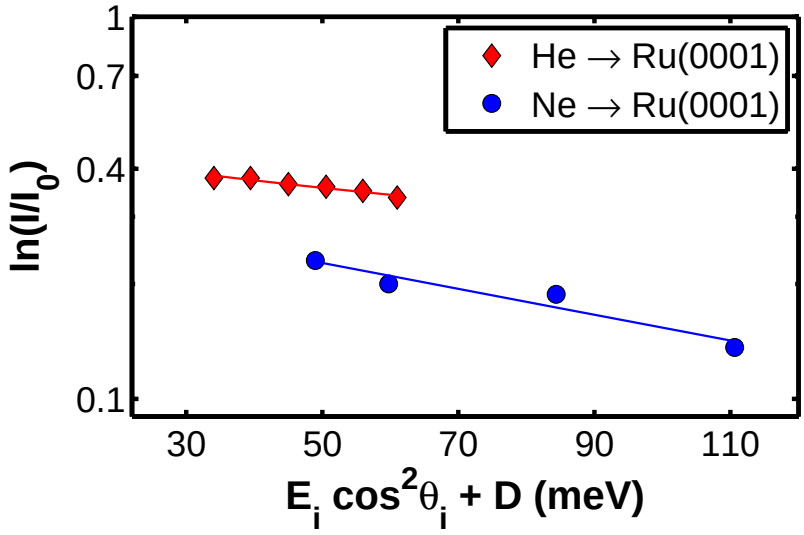

Figure 7.8: Comparison of the thermal attenuation of the specular peak between He (red circles) and Ne blue circles) scattered from Ru(0001). the specular intensity is represented as function of E_i and θ_i. The surface temperature of Ru(0001) is maintained at 200 K for He measurement and at 90 K for Ne measurement.

to a linear decrease in the logarithmic plot, and from the slope one obtains the product $M\Theta_D^2$. Thus, if the effective mass is known an evaluation of the Debye temperature can be made. Previous work on heavier rare gas scattering from Ru(0001) suggests that a large effective mass needs to be considered, approximately 2.5 times the mass of a single Ru atom ($M = 253$ amu) [150]. If such a mass is assumed, the surface Debye temperature is (288 ± 20)K for He/Ru(0001) in agreement with the value measured by E. Ferrari et al. (Θ_D = 295 ± 20)K [161], and this is to be compared with a bulk room temperature value of 415 K [162]. For Ne using this same effective mass the surface Debye temperature would be 505 ± 20 K. This value for Ne is clearly too large, implying that the effective surface mass should be larger for Ne. To have the same Θ_D as found for He, an effective mass of approximately 8 Ru atoms needs to be assumed.

However, the problem of independently measuring the effective mass can be resolved by making measurements in the classical regime at high incident energies and large surface temperatures. As shown by Eq. 7.1, in the classical regime all quantum diffraction is completely attenuated, and what remains is a broader inelastic distribution which is the consequence of large numbers of phonon excitations. This classical intensity of Eq. 7.1 depends on the effective mass M through the recoil energy ΔE_0, but does not

depend on the Debye temperature. The physical reason why the Debye temperature does not appear is because in the classical regime so many phonons are transferred that the nature of the phonon distribution becomes unimportant, i.e., basically any reasonable distribution of phonons at the surface will lead to the same result of Eq. 7.1.

As stated above, the nature of the thermal attenuation can be used to indicate when a particular scattering system is in the classical regime. If the exponent $2W(T)$ is sufficiently large, then the Debye-Waller factor becomes so small that all quantum effects such as diffraction are suppressed and what remains is a classical scattered spectrum. Thus, in order to evaluate the effective mass M in the classical regime what is necessary is to be assured that $2W(T)$ is significantly larger than unity. For Ne scattering, impinging with an incident energy E_i = 64 meV, on clean Ru(0001) surface, the value of $2W(T)$ calculated using Eq. (7.4) at the specular position and at a surface temperature of 1100 K ranges from 4 (corresponding to $\theta_i = 60°$) to 7.5 (corresponding to $\theta_i = 30°$), whereas for the lighter He 2W(T=1100) varies from 2 to 4 when the incident angle goes from 60° to 30°. These values have been evaluated considering the effective mass M_{eff} = 8 M_{Ru}, extrapolated from the the fit in Fig. 7.8. These $2W$ values for Ne are sufficiently large, therefore, measurements in classical regime are possible for Ne scattering on Ru(0001) surface and the classical theory can be applied.

In the next section, we discuss the scattering spectra taken in the classical regime, and from measurements of both angular distributions and energy-resolved spectra, we obtain in independent manner an effective mass for Ne/Ru(0001) equal to the mass of about 8 Ru atoms (M = 814 amu), which implies a surface Debye temperature of approximately 282 K.

7.7 Scattering behaviour in the classical regime

The left hand column of Fig. 7.9 shows a series of angular distributions measured on the TEAMS machine with fixed incident angle as marked, and plotted as a function of total scattering angle $\theta_i + \theta_f$ between the incident beam and detector position. Figure 7.9a shows an angular distribution taken with a high incident energy of 151 meV, an incident angle of 60°, and a surface temperature of 1100 K. This spectrum has been recorded along the $\overline{\Gamma M}$ direction of the Ru(0001) substrate. Ne scattering from Ru(0001) exhibits a broad and symmetric peak centered at the total final scattering angle of approximately 119°. The calculation is shown as a solid line and it was carried out assuming an effective mass of 8 Ru atoms. The value of v_R used in the simulation is 2500 m/s. Under these

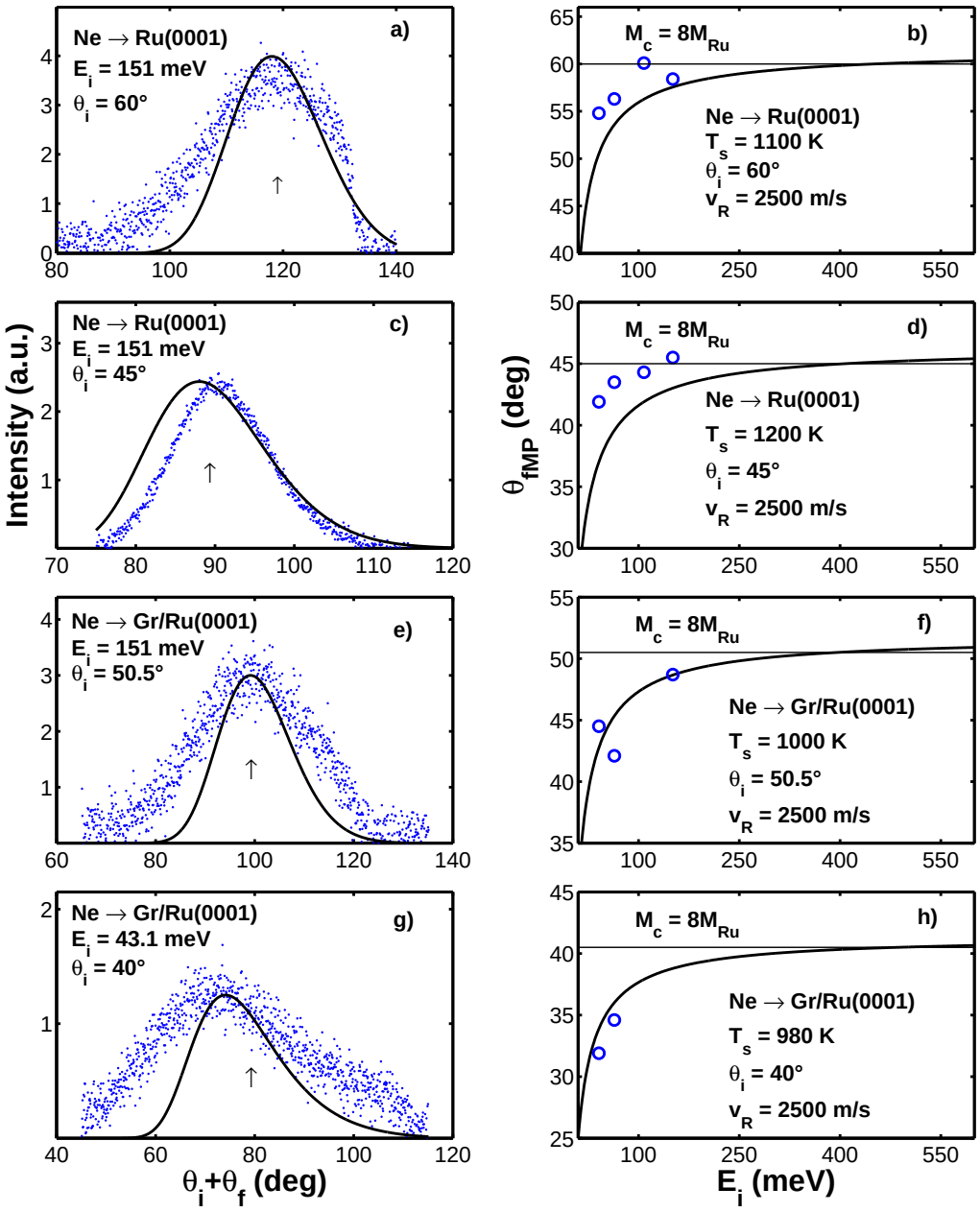

Figure 7.9: Left panels: comparison of the angular distributions for Ne scattering from Ru(0001) (a and d) and Gr/Ru(0001) (e and h) between experimental data (shown as blue points) and calculations (solid curves). Right panels: most probable final angle as a function of incident energy for Ne scattering from Ru(0001) (b and d) and from Gr/Ru(0001) (e and g). Calculations of the most probable final angle for the angular distributions, shown as solid curves (b, d, f and h), predict sub-specular scattering at low energies, shifting to supra-specular scattering at higher energies.

conditions, the experimental spectrum is well reproduced by the SSM.

Figure 7.9b shows the most probable final angle θ_{fMP} as a function of incident energy for Ne scattering from Ru(0001) for the fixed conditions $\theta_i = 60°$ and T_S = 1100 K. The experimental points fall right on the calculated curve with the exception of the single outlying point at E_i = 100 meV. This graph shows that for incident energy less than approximately 500 meV the most probable final angle is predicted to be sub–specular. However, if the incident energy is raised to about 500 meV the most probable angle is very near to the specular angle, and for larger energies it becomes supra–specular. Whether the angular distribution peaks are predicted to be sub-specular or supra-specular depends primarily on incident energy and angle. Calculations indicate it is not strongly dependent on other parameters such as the effective surface mass. For this reason, it is quite interesting to investigate this behaviour for different angles of incidence θ_i. Figure 7.9c presents data recorded at a smaller incident angle, θ_i = 45°, but otherwise with similar experimental conditions, E_i = 151 meV and T_S = 1200 K. The experimental spectrum consists of a somewhat sharper peak than the one measured for θ_i = 60°, at final total angle of approximately 90°. Furthermore the experimental points present a visible asymmetry with respect to the peak maximum. This shoulder is well reproduced by the SSM, as pictured in the solid curve. As shown in Fig. 7.9d the tendency of the most probable final angle as function of the incident energy is also predicted. The behaviour is similar to the one previously observed for θ_i = 60°, but the predicted recovery energy, i.e. the incident energy at which the most probable final angle is at the specular position, decreases to about 400 meV.

Similar results were also obtained for Ne scattering on the Gr/Ru(0001) surface, as shown in Fig.7.9e-h. Figure 7.9e shows angular distribution data for Ne scattering from graphene covered Ru(0001) at an incident energy of 151 meV, a surface temperature of T_S = 1000 K and for an incident angle of θ_i = 50.5°. The calculation using an effective mass M = 8 Ru atoms (M = 814 amu) and the same value of v_R = 2500 m/s taken for the clean Ru(0001) surface is shown as a solid curve. The most probable final angle is well reproduced by the calculation, but the spectral shape of Ne scattering from Gr/Ru(0001) is not as well reproduced by the SSM. The tail of the experimental data appears with a noticeable asymmetry with respect to the peak maximum even to the point of suggesting the presence of two peaks. The same effect has been observed for Ar scattering on Gr/Ru(0001) by H. Shichibe et al. where it was explained with a stronger bond in the valley of the Gr moiré corrugation with respect to that in the region of the hill. This effect could be reproduced with two different effective masses. [163]. Figure 7.9f presents how

the most probable final angle changes as a function of the incident energy in the same experimental conditions for the angular distribution in Fig. 7.9e. From the comparison of the experimental points with the calculations it is evident how the dependence of the most probable final angle is well reproduced by the theory. As pointed out in the previous section, Ne scattering from Gr/Ru(0001) presents a shift to sub-specular angle more pronounced than the one presented in Ne scattering on Ru(0001). This behaviour can also be seen from the spectrum in Fig. 7.9g, taken at a lower incident energy, E_i = 43.1 meV. Also in this case a clear asymmetry in the shape of the peak at supraspecular angles is evident. The SSM calculations shown as a solid curve qualitatively explain the subspecular position, as shown in Fig 7.9h, where the theoretical calculations predict sub-specular scattering at low energies, that shift from sub-specular to supra-specular with increasing incident energy.

7.8 Time–of–flight measurements

Energy-resolved spectra were taken on the HAS-TOF apparatus (ERASMO) with a fixed source-to-detector angle of 105.4° and a series of representative results, converted from time-of-flight to energy transfer ΔE is presented in Fig. 7.10. This series of TOF spectra have been recorded by scattering Ne atoms on Ru(0001) surface for three incident angles $\Delta\theta_i$ = -2, 0 and +2° relative to the specular position. For each incident angle, three different high surface temperatures have been used at 750, 800 and 1000 K . The incident energies range from E_i = 70 to 91.6 meV, as marked in Fig. 7.10. These spectra are characterized by the absence of quantum coherence features such as single-phonon or diffuse elastic peaks, as also observed for Ne scattering from the Ni(111) surface at 420 K [153]. Theoretical calculations using the smooth-surface model are represented in Fig. 7.10 as black dashed lines, using an effective mass $M_{eff} = 8\ M_{Ru}$ atoms and a value of 2500 m/s for v_R as for the angular distributions.

For each energy, the calculations were normalized to the data at the maximum of the corresponding experimental spectrum. The calculations show qualitatively the same general shape and width as exhibited by the data, although the calculations show consistently a shift of about 5 meV towards smaller final energies. The peak position of the calculations is rather insensitive to the effective mass and is essentially unchanged if M is either increased or decreased by the mass of 4 Ru atoms. The discrepancy of roughly 5 meV in peak position between calculations and measurements may be a consequence of the experimental conditions not being fully into the classical regime. As discussed

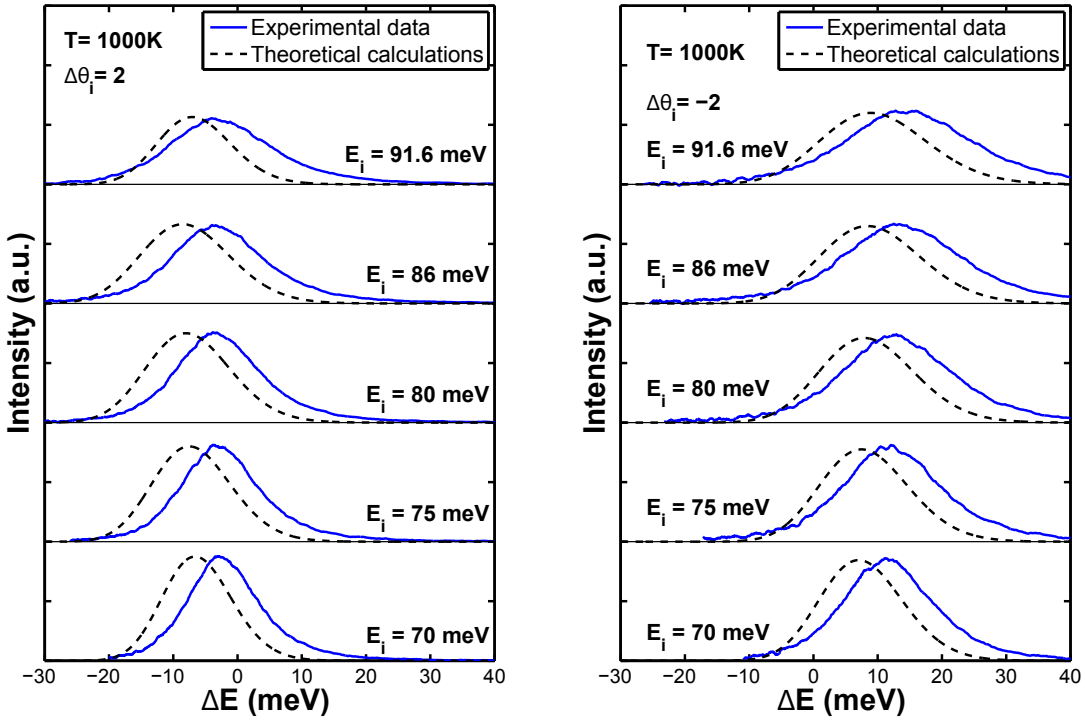

Figure 7.10: Time-of-flight spectra, converted to an energy-transfer scale, for Ne scattered from Ru(0001) at incident energies ranging from 70 meV to 91.6 meV. The incident angle $\Delta\theta_i$ relative to the specular position is -2° and 2°. The theoretical calculations, normalized to the data at each energy, are presented as black dashed curves, using an effective mass $M_{eff} = 8\ M_{Ru}$ and a value of 2500 m/s for v_R.

above, for these conditions the Debye-Waller exponent $2W$ is larger than unity, but not necessarily always much larger, thus the classical theory is not clearly applicable and may give only qualitative behavior.

Although the measured peak positions cannot be made to match the SSM theory, the shapes and widths of the broad peaks are similar. The theory predicts an increase of the widths when the incident energy is increased as shown in Fig. 7.11 where a comparison of the widths (FWHM) between experimental and theoretical spectra is presented. The FWHM are shown as a function of the incident energy for the two incident angle $\Delta\theta_i$ = 2° and -2° measured relative to the specular position, for a surface temperate T_S = 1000 K. For $\Delta\theta_i$ = 2° the spectra present narrower multiphonon peaks than the ones measured at $\Delta\theta_i$ = -2°, taken at the same incident energies. The shape of the calculated peaks match the data reasonably well, however the calculations predict a slightly smaller increase of broadening with energy than that observed.

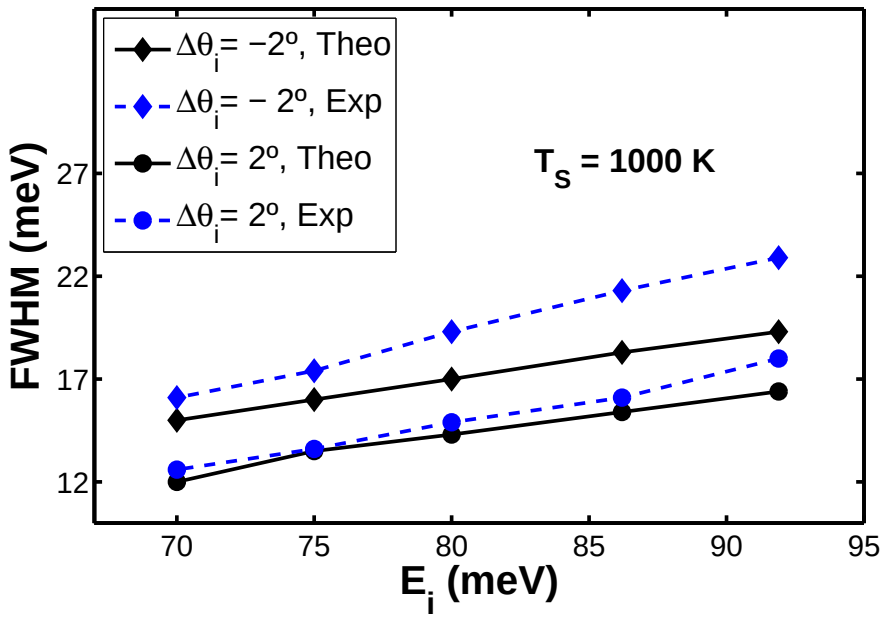

Figure 7.11: Comparison between the experimental and theoretical FWHM of the time-of-flight spectra converted to the energy-exchange domain as function of the incident energy. Two different incident angles $\Delta\theta_i$ = 2° and -2° relative to the specular position are shown. The surface temperature is T_S = 1000 K.

The classical multiphonon peaks such as exhibited in the inelastic spectra of Fig. 7.10 can persist even at low temperatures and incident energies where quantum features such as diffuse elastic peaks or single surface phonon peaks can be observed. It has recently been shown, if care is not taken, that it is possible to misinterpret multiphonon features as being single-phonon peaks [153]. Figure 7.12 shows how the classical multiphonon peaks in Fig. 7.10 can appear as an anomalous single-phonon dispersion curve. Plotted in Fig. 7.12 is energy transfer ΔE as a function of parallel momentum transfer ΔK. In an atom-surface scattering event involving excitation of a single surface phonon of energy $\hbar\omega(\Delta\mathbf{K})$, the conservation law for energy is $E_f - E_i = \hbar\omega(\mathbf{K})$ and conservation of parallel momentum demands that $\mathbf{K}_f - \mathbf{K}_f = \Delta\mathbf{K}$, where $\hbar\mathbf{K}_f$ and $\hbar\mathbf{K}_i$ are the final and initial parallel momentum of the atom, respectively. Combining the two conservation laws results in a quadratic equation for $\Delta E = \hbar\omega(\mathbf{K})$ as a function of $\Delta\mathbf{K}$ gives the so called the scan curve (see section 1.1.3). For a given set of initial conditions, meaning incident energy and angle, only surface phonons with both $\Delta E = \hbar\omega(\Delta\mathbf{K})$ and ΔK lying on the scan curve can be observed. By systematically varying either the incident energy or angle complete dispersion curves for all surface phonons can be mapped onto a graph

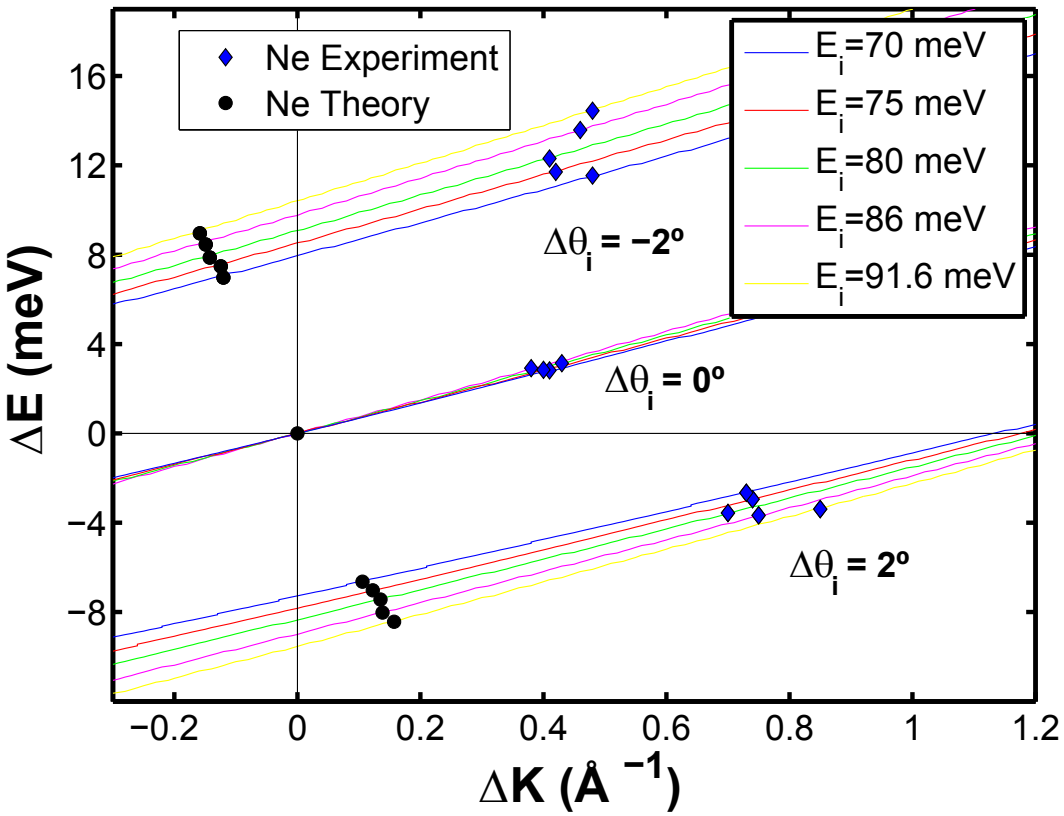

Figure 7.12: Anomalous dispersion curve plot for Ne scattering from clean Ru(0001) showing the energy transfer value of the most probable final energy as a function of parallel momentum transfer of an assumed single-surface-phonon transfer of the same energy. The blue diamonds data points were collected for T = 1000 K, they are the experimental anomalous dispersion points obtained from Fig. 7.10. Black circles are theoretical calculations predicted by SSM model. Single phonon scan curves for incident beam energies used in the experiment are calculated for θ_i = -2° , θ_i = 0° and θ_i = 2° for each incident energy as marked.

such as in Fig. 7.12. For the fixed incident angles of $\Delta\theta_i = -2°$, $0°$ and $+2°$, the solid curves with colors corresponding to different incident energies as indicated are the respective scan curves. The experimental data points, shown as blue diamonds, are positioned on each scan curve at the energy equal to the most probable final energy (peak position) of the corresponding energy-resolved spectrum such as in Fig. 7.10. The predictions of the SSM classical theory are also shown as black filled circles. Although only three different incident angles $\Delta\theta_i$ are shown in Fig. 7.12 it is clear that if a large enough range of $\Delta\theta_I$ values were plotted the most probable final energies would form a curve that resembles a phonon dispersion. A more extensive example for the case of

Ne scattering from Ni(111) is shown in Ref. [153]. However, such a curve is a false, or anomalous dispersion because the energy transfers ΔE extracted from the most probable final energies such as exhibited in Fig. 7.10 are due to multiphonon transfers and are not at all due single phonon features. Such features are less expected for the case of He atom scattering, although they have been observed [164]. On the other hand, for Ne scattering, and by extension for scattering of heavier rare gas projectiles, we have demonstrated here that many experimental conditions are carried out at or near the decoherence boundary between quantum and classical physics. Thus care must be taken to avoid misinterpretation of such anomalous dispersion features which are in fact due to multiphonon transfers.

7.9 Conclusions

In this chapter, we considered the scattering of Ne atoms from clean Ru(0001) and from single layer graphene covered Ru(0001). Ne is an especially useful projectile for this study because its mass is sufficiently small so that for both translational energies and target temperatures in the neighbourhood of room temperature or smaller, its scattering spectra exhibit quantum features such as diffraction, single phonon excitation peaks, or diffuse elastic reflection due to defects and disorder. However, by increasing the target temperatures or incident beam energies to higher values readily obtainable in most experimental configurations all quantum features are attenuated and what remains are scattering spectra that are explained by classical physics.

An experimental diffraction study has been carried out for Ne impinging on clean Ru(0001) and Gr/Ru(0001) surface in quantum regime, achievable with surface temperatures below ambient and energies below 100 meV. Clear specular diffraction as well as off-specular diffraction peaks was observed. Strong evidence was gathered that in the case of Ne diffraction from Gr/Ru(0001) system no anticorrugation effect is observed. Therefore, our study proves that Ne scattering gives a more accurate pictures of the surface structure than the one deduced from He scattering.

As either the temperature or incident Ne translational energy was increased, quantum diffraction was suppressed by the Debye-Waller attenuation. At higher temperatures and larger energies only broad features were observed, and these were well described by the classical theory of the smooth surface model.

Interestingly, the Ne atom scattering characteristics were rather similar for both the clean Ru(0001) and Gr/Ru(0001) targets. In the quantum regime both surfaces exhibited

clear specular diffraction peaks as well as off-specular diffraction. In the classical regime similar broad peaks were observed in both the angular distributions and in the energy resolved spectra. The classical behavior of both Ru(0001) and Gr/Ru(0001) is reasonably well described by the smooth surface theoretical model using the same set of parameters for the effective mass M and v_R.

The combination of successive measurements in either the quantum or classical domain allowed an evaluation of the surface Debye temperature as measured by Ne atom scattering. Measurements of the Debye-Waller attenuation factor in the quantum regime allow for evaluation of the product of the Debye-Temperature Θ_D and the effective surface mass M in the form $M\Theta_D^2$. Measurements in the classical regime depend on the same effective mass, but do not depend on the Debye temperature nor on any other specifics of the phonon distribution. Thus, with an independent measure of M evaluated from fits to the classical scattering features it is possible to make an evaluation of Θ_D for Ru(0001). This value is in agreement with a previous independent measurement using core level photoelectron spectroscopy.

An interesting observation is that for small incident Ne energies the broad classical peaks, observed in the classical regime induced by high surface temperatures, were not centered about the specular angles, but were shifted distinctly in the sub-specular direction. This behaviour occurred for all measured incident angles, and as the incident energy increased, the most probable final angle of the broad classical peak shifted towards the specular position. Calculations with the smooth surface model agree well with this shift, and even predict that at a distinct energy called the recovery energy the most probable final angle would appear precisely at specular. For energies larger than the recovery energy the classical peak would become supraspecular.

It is also noted that at or near the decoherence boundary investigated here, both quantum features and residual classical peaks in the background can appear simultaneously. Because the quasi-classical multiphonon feature appears in the energy resolved spectra as a peak, albeit somewhat broad, it is possible to mistake it as a putative single phonon quantum feature. Complicating this issue is the fact that the classical peak often shifts position as a function of controllable experimental parameters, notably changes of the incident angle, in a way that mimics a single phonon dispersion curve. Thus, care must be taken not to mistake multiphonon peak features as anomalous single phonon dispersion behaviour.

CONCLUSIONS

In this thesis, several original contributions to the NEMI (NEutral MIcroscopy) project have been presented in the context of the design of mirrors able to focus thermal energy He atoms. The atomic mirror is a fundamental element in the development of a scanning neutral helium microscope (NEMI).

Focusing atoms with de Broglie wavelengths of the order of an Ångstrom puts a very high demand on the surface optical elements. In particular, the optimum surface mirror must present high crystallinity and homogeneity over lateral scales of microns, high He reflectivity and stability under ambient conditions. These requirements can be achieved using a surface with the following properties: high quality polishing, low corrugation and inertness to contaminants. Besides, in order to be able to focus on a selected point, all these conditions need to be fulfilled on a curved surface, which makes the target even more difficult to achieve.

With the aim of creating this new mirror, Chapter 4 of this thesis describes in detail two new methods developed to grow a high-quality Gr layer on a sapphire substrate in UHV, using Cu as catalyst. In addition to the novel preparation method, a first experimental characterization of the structure of Gr on sapphire is given, combining HAS measurements, that require UHV conditions, with a set of other techniques, such as AFM and Raman. He–diffraction and Raman provide crucial information on quite different and complementary aspects of the same samples. An important message from our study is that the wrong conclusion might be drawn if HAS and Raman results were not both available. He-diffraction measurements reveal that Gr forms an (11×11) moiré pattern aligned with the (1×1) sapphire unit cell. Furthermore, the inelastic HAS spectra clearly show the phonon dispersion of the Gr flexural mode (ZA). From this dispersion curve the values of the bending rigidity and the Gr–sapphire coupling strength have been determined, thus demonstrating the weak interaction of Gr with the substrate.

The high specular He reflectivity observed, reaching 6.5%, the large Gr domains over lateral scales of microns and a remarkable stability under ambient conditions suggest that Gr/Al_2O_3 is an excellent candidate to be used as atomic mirror. While the

study is limited to flat sapphire, the results can be extrapolated without problems to curved sapphire, which offers better surface quality than fused silica. Moreover, high transparency (90%) was recorded in the visible range, making this system suitable for a large number of applications that require the hybrid properties commonly related with metals (conductivity) and insulators (transparency).

One line of research aimed to the design of He mirrors has been the bending of flexible thin crystals through an electrostatic field. These results are presented in Chapter 5. Metal crystals of thicknesses between 50 and 150 μm have become commercial available in the last years. However, so far no study has been performed about the quality of these samples, or even a comparison with other metal crystals more usually used in surface science studies (bulk samples). The HAS measurements presented in Chapter 5, performed on thin Cu(111), Ni(111) and Ru(0001) crystals, show that the latter two present a much lower surface quality than bulk samples, whereas Cu(111) has a comparable quality and therefore can be used as an atomic mirror. The measurements presented at the end of Chapter 5 show that a He beam can be focused by applying an electrostatic potential to the thin Cu(111) crystal. Furthermore, using a less collimated incident beam, the absolute focused intensity is two orders of magnitude larger than previously reported. In addition a Gr layer can be easily grown on the surface by CVD, making the surface inert under ambient conditions.

In order to get a narrower focal spot with thin Cu(111) crystals, a modification of the present experimental set-up is required. Finally, owing to their higher quality, the thin Cu(111) crystals may replace Cu metal foils in cases in which the crystallinity of the substrate is important to achieve the best result, for instance in the growth of large-area monocrystalline Gr [124] or hexagonal boron nitride [125].

On the other hand, a new line of research in the He focusing elements has been opened since atomic mirror coating on a curved substrate has been demonstrated for the first time, as it is shown in Chapter 6. As a matter of fact, highly promising results have also been recorded during this thesis on macroscopically curved atomic mirror. This mirror has been developed by using Gr–terminated Ru thin films to coat both sapphire and fused silica curved substrates. Chapter 6 summarizes a very important part of this work, which consisted in testing several tens of samples until the best Ru thin film growth conditions have been found. Different sputtering conditions have been tested on different substrates (flat and curved) until He specular peak was clearly detected. Besides, as far as we know, this is the first observation of He-reflectivity from a policrystalline substrate detected with HAS technique.

Furthermore, in order to improve even more the surface quality of the metal coating, laser polishing has been applied to the fused silica substrate prior to the metal deposition. Using both the laser polishing technique and the optimization of the thin film growth process, a specular reflection up to 25% was recorded for Ru thin films on curved fused silica. In addition, the observation of first order diffraction peaks by means of He scattering from Gr/Ru samples shows the existence of quasi-epitaxial, long-range ordered domains of Gr. This is a remarkable result, given that an amorphous commercial piece has been used as substrate in all samples. These results - high reflectivity and Gr order - enable the preparation of metal coatings on fused silica with unprecedented low roughness, which may have implications on other research areas like development of lenses for solar cells and detection of energetic neutral atoms in space research.

The last interesting result presented in Chapter 6 is the growth of high-quality Gr/Ru film on curved sapphire, which has been confirmed by the observation of clear diffraction peaks due to Gr lattice and moiré superstructure.

Finally, in Chapter 7, a systematic study of Ne atom scattering from Ru(0001) and Gr/Ru(0001) has been performed. The high sensitivity of Ne beams to surface details has been verified. No anticorrugation effect is observed for Ne diffraction from Gr/Ru(0001) surface. Therefore, our study proves that Ne scattering gives a more accurate picture of the surface structure than the one deduced from He scattering. However, the higher corrugation of Gr/Ru(0001) "seen" by Ne atoms is unfavourable for an atomic mirror, due to the high loss in intensity of the specular peak. Despite of this, its use in classical regime can be an alternative method to get a focused atomic beam.

Furthermore, the scattering of atoms from surfaces represents an interesting system for examining the decoherence transition from coherent quantum mechanical behaviour at small temperatures and energies to the fully classical regime at high temperatures and energies, with the driving mechanism being excitation of increasingly larger numbers of phonons. The combination of measurements in both quantum and classical domain allowed an unambiguous evaluation of the surface Debye temperature as measured by Ne atom scattering. The angular distribution and TOF measurements recorded for Ne scattering on Ru(0001) and Gr/Ru(0001) in classical regime has been compared compared with theoretical calculations using the smooth surface model. The theory correctly predicts the multi-phonon features recorded, but it does not seem to get the peak at exactly the correct position.

The experimental results presented in this thesis represent a big step forward towards the goal to achieve high-resolution scanning helium microscopy. The three

main requirements that a surface must fulfil to be an optimum atomic mirror (high crystallinity, high reflectivity and stability under ambient conditions) have been achieved for the majority of the flat and curved surface studied in this thesis. Long range order has been recorded for Gr/Al_2O_3, flat and curved thin Cu(111) crystals, Gr/Ru(0001) on flat and curved sapphire and interestingly, for Gr/Ru(0001) on flat and curved amorphous surface (fused silica). High He reflectivity between 6% to 20% has been recorded for Gr terminated substrates. Finally, all surfaces can be passivated with a Gr layer, avoiding the contamination of the surface samples also under ambient conditions. So, we can say that the problems related to the three main requirements have been solved in the course of this thesis for a large family of systems.

For the focusing goal, the comparison between the results obtained for bent mirrors and mascroscopically curved ones shows that currently the first option is more likely to have an immediate use as focusing element in the He microscope. An improvement in focus position through a better control in electrostatic bending could reduce significantly the spot size, which combined with its high reflectivity would allow to create an instrument with higher resolution, which could be useful for fundamental research as well as for industry applications.

However, we have to bear in mind that the second option opened a really new path. In this thesis, for the first time He reflectivity has been demonstrated on a macroscopically curved mirror with a promising high intensity in the reflected beam. Substantial improvements could be achieved along this line by improving the polishing of both sapphire and fused silica curved substrates.

Conclusiones

A lo largo de esta tesis se han realizado varias contribuciones originales al proyecto europeo NEMI en el contexto del diseño de espejos capaces de enfocar átomos de helio de baja energía. Estos nuevos espejos son una parte esencial para el desarrollo de microscopios de helio.

El enfoque de átomos cuyas longitudes de onda de de Broglie se encuentran en el entorno del Angstrom, como el helio, representa una situación de gran exigencia para los elementos ópticos utilizados. En concreto, la superficie óptima para un espejo que vaya a usarse con este fin debe presentar una alta cristalinidad y homogeneidad, una alta reflectividad y una gran estabilidad frente a condiciones ambientales. Todos estos requisitos pueden alcanzarse mediante el uso de una superficie con una alta calidad en su pulido, un bajo nivel de corrugación y baja reactividad frente a posibles contaminantes. Por último, para ser capaz de concentrar los átomos del haz incidente en un único punto y, por tanto, enfocar, debe añadirse la necesidad de usar una superficie curva. Este último factor representa una dificultad añadida importante a la hora de alcanzar el objetivo deseado.

Para crear este nuevo espejo, el capítulo 4 de esta tesis describe en detalle dos métodos novedosos desarrollados con el objetivo de permitir el crecimiento de una capa de grafeno de alta calidad sobre un sustrato de zafiro en UHV, mediante el uso de cobre como catalizador. Adicionalmente a esto, se realizó también la primera caracterización de esta estructura de grafeno a través de mediciones HAS, que requieren UHV, y todo un conjunto de otras técnicas tales como AFM y Raman, que no lo requieren. HAS y Raman proporcionan información crucial en aspectos diferentes, pero complementarios, de las muestras estudiadas. Una conclusión importante de este trabajo es que, dada esta complementariedad, es posible extraer conclusiones equivocadas acerca de la calidad del grafeno si se aplica una sola de las técnicas, en lugar de ambas. Las mediciones de difracción de helio revelan que el grafeno forma un patrón de moiré (11x11) alineado con la celda unidad (1x1) del zafiro. Más aún, los espectros de dispersión inelástica muestran claramente la dispersión fonónica del llamado flexural mode del grafeno (ZA). A partir de

esta curva de dispersión se han determinado los valores de la rigidez frente a flexión y el valor de la ligadura grafeno – zafiro, demostrando así la débil interacción entre ambos.

La alta reflectividad observada para el helio, de hasta un 6,5%; el gran tamaño de los dominios de grafeno (del orden deuna micra) y una notable estabilidad en condiciones ambientales sugieren que el sistema grafeno – zafiro es un candidato excelente para ser usado como espejo atómico. A pesar de que el estudio se ha limitado a muestras planas, los resultados pueden ser extrapolados sin problemas a muestras con zafiro curvo, lo que permitiría obtener mejores calidades de superficie que con sustratos de vidrio. Además, se ha comprobado que el sistema presenta una alta transparencia en el rango visible (90%), lo que indica que el sistema puede ser útil en un gran número de aplicaciones que requieran al mismo tiempo características tradicionalmente asociadas a metales, como la conductividad, y otras asociadas a aislantes, como la transparencia.

En el capítulo 5 se presenta la primera línea de investigación seguida con el objetivo de crear el espejo de helio: la curvatura o flexión de cristales delgados a través de un campo electrostático. Desde hace unos años, existen cristales metálicos de espesores entre 50 y 150 um disponibles comercialmente. Sin embargo, hasta el momento no hay estudios sobrela calidad de estos nuevos cristales, así como tampoco existe una comparación con los cristales metálicos usados habitualmente en los estudios de superficies (bulk samples). Las medidas de scattering de helio recogidas en este capítulo, realizadas con cristales de Cu(111), Ni(111) y Ru(111), muestran que estas dos últimas presentan una superficie de calidad mucho menor que las bulk samples, mientras que la de cobre es comparable y puede ser usado como espejo atómico. Los datos presentados al final del capítulo muestran que es posible enfocar un haz de helio mediante un cristal delgado de Cu(111) sobre el que se ha aplicado un potencial electrostático. De hecho, mediante el empleo de un haz incidente menos colimado la intensidad del haz reflejado es hasta dos órdenes de magnitud mayor que la reportada previamente. Como colofón, una película delgada de grafeno puede crecerse en la muestra mediante CVD, lo que hace que la superficie pase a ser inerte en condiciones ambientales.

Con modificaciones adecuadas del montaje actual, es posible que se pueda conseguir un punto focal más estrecho para espejos de cristales de Cu(111). Por último, debido a la mejor calidad de la superficie de los cristales Cu(111), es posible que estos reemplacen a las láminas de Cu en casos en los que la cristalinidad del sustrato sea importante para alcanzar un resultado óptimo, tal como sucede en el crecimiento de grandes áreas de Gr monocristalino o nitrato de boro hexagonal.

Por otro lado, en el capítulo 6 se ha demostrado por primera vez el recubrimiento con

una capa delgada de un sustrato curvo para espejos atómicos, lo que abre una nueva línea de investigación acerca de elementos para el enfoque de helio. De hecho, se han obtenido resultados muy prometedores a lo largo de esta tesis en espejos atómicos curvados a nivel macroscópico. Este espejo se ha desarrollado mediante el crecimiento de láminas delgadas de rutenio sobre sustratos de zafiro y vidrio, posteriormente pasivadas con una capa de grafeno. El capítulo 6 recoge un parte muy importante de este trabajo, consistente en la prueba de varias decenas de muestras hasta encontrar las condiciones óptimas para el crecimiento por sputtering de películas de Ru y Ni sobre sustratos de vidrio planos y curvos. Además, esta es la primera observación conocida de reflexión de helio sobre películas delgadas depositadas sobre sustratos amorfos detectada mediante HAS.

Con el fin de mejorar aún más la calidad del recubrimiento metálico, se ha aplicado una técnica de pulido láser al sustrato de vidrio previo a la deposición del metal. Con la combinación de ambos métodos, optimización del proceso de crecimiento de la película delgada y pulido láser, se ha obtenido una reflexión especular de hasta el 25% para muestras de películas delgadas de Ru sobre sustrato curvo de vidrio. Además, la observación de los picos de difracción de primer orden a través de scattering de helio sobre muestras de grafeno sobre rutenio revela la existencia de dominios ordenados, extensos y cuasi-epitaxiales en el grafeno. Este es un resultado realmente notable, dado que el sustrato consistía en todos los casos en una pieza amorfa de calidad comercial. Estos resultados – alta reflectividad y existencia de grafeno ordenado – permiten la preparación de recubrimientos metálicos sobre vidrio con un bajo nivel de rugosidad sin precedentes, lo que posiblemente tenga repercusiones importantes en otras áreas de investigación, tal como el desarrollo de lentes para células solares o la detección de átomos de alta energía en investigación espacial.

Por último, en el capítulo 7 se presenta un estudio sistemático del scattering de Ne sobre muestras de Ru(0001) y Gr/Ru(0001). Se ha confirmado la alta sensibilidad del haz de neón a las imperfecciones de la superficie, y no se ha observado ningún efecto de anticorrugación en difracción de Ne sobre muestras de Gr/Ru(0001). Por tanto, se puede concluir que nuestro estudio prueba que el scattering de Ne proporciona una imagen más fiel de la estructura de la superficie que la obtenida a través de scattering de He. Sin embargo, precisamente la mayor corrugación de la superficie de la muestra experimentada por los átomos de neón representa una desventaja para su uso en un espejo atómico, debido a la pérdida de intensidad en el pico especular. A pesar de esto, su uso en el régimen clásico puede considerarse un método alternativo para obtener un haz

atómico enfocado.

El scattering de átomos sobre superficies representa además una herramienta muy interesante para estudiar la transición desde el comportamiento coherente en régimen cuántico, a bajas temperaturas y energías, al comportamiento puramente clásico, a altas temperaturas y energías mediante la excitación de un número más grande de fonones. La combinación de medidas tanto en el dominio clásico como cuántico ha permitido una evaluación inequívoca de la temperatura de Debye de la superficie a través del scattering de Ne. Las medidas realizadas de la distribución angular y el tiempo de vuelo (TOF) se han comparado con las previsiones teóricas calculadas usando el modelo de superficie lisa (smooth surface model). Estos cálculos predicen acertadamente las características multi-fonón detectadas, aunque no parecen tener un buen acuerdo con la posición exacta de los picos.

En conclusión, los resultados experimentales presentados en esta memoria de tesis representan un gran paso hacia la consecución del microscopio de helio de alta resolución. Los tres requisitos principales que la superficie debe cumplir para poder ser un espejo atómico óptimo (alta cristalinidad, alta reflectividad y alta estabilidad en condiciones ambiente normales) se han logrado para la gran mayoría de superficies tanto curvadas como planas estudiadas durante esta tesis. Respecto a la cristalinidad, se han conseguido dominios amplios de grafeno sobre zafiro, cristales delgados de Cu(111) planos y curvos; grafeno sobre rutenio crecido sobre sustrato de zafiro planos y curvos y, además, grafeno sobre rutenio crecido sobre sustratos amorfos de vidrio planos y curvos. Se han conseguido valores altos de reflectividad para el helio, de entre el 6 y el 20%, en muestras recubiertas con una capa de grafeno. Respecto a la estabilidad, todas las superficies pueden pasivarse mediante el añadido de una capa de grafeno, lo que permite evitar la contaminación de la superficie. Se puede concluir, por lo tanto, que cada uno de los problemas asociados a cada una de las tres características principales de las superficies para espejos atómicos se ha resuelto para una gran familia de sistemas durante la elaboración de esta tesis.

Con respecto al objetivo de conseguir el enfoque de un haz atómico, de la comparación entre los resultados obtenidos por espejos doblados y macroscópicamente curvados se puede concluir que la primera opción tiene mayores posibilidades de ser usado como elemento para el enfoque en el microscopio de He. Mejorando la posición del foco a través de un mejor control del doblado electrostático sería posible reducir de manera significativa el tamaño del punto del enfoque, lo que combinado con su alta reflectividad, permitiría crear un instrumento con más alta resolución, algo que podría ser muy útil tanto en la investigación de carácter fundamental como en aplicaciones industriales.

En cualquier caso, hay que tener en mente que la segunda opción abre una línea de investigación completamente nueva. En esta tesis, se ha demostrado por primera vez que un haz de He puede ser reflejado con alta intensidad medianteespejos macroscópicamente curvos. Mejoras sustanciales pueden lograrsemejorando el pulido de los sustratos tanto de zafiro como de vidrio.

PUBLICATIONS

1. G. Anemone, A. Al Taleb, S.D. Eder, B. Holst, D. Farías, *Flexible thin metal crystals as focusing mirrors for neutral atomic beams* **Physical Review B** 95 (20), 205428 (2017)

2. A. Al Taleb, G. Anemone, W. W. Hayes, J. R. Manson, and D. Farías, *Multiphonon excitation and quantum decoherence in neon scattering from solid surfaces*. **Physical Review B** 95(7):75414 (2017)

3. G. Anemone, E. Climent-Pascual, H. K. Yu, A. Al Taleb, F. Jiménez-Villacorta, C. Prieto, A. M. Wodtke, A. De Andrés, and D. Farías, *Quality of graphene on sapphire: long-range order from helium diffraction versus lattice defects from Raman spectroscopy*. **RSC Advances** 6(25):21235 (2016)

4. A. Al Taleb, G. Anemone, D. Farías, and R. Miranda, *Acoustic surface phonons of graphene on Ni(111)*. **Carbon** 99:416 (2016)

5. A. Al Taleb, H. K. Yu, G. Anemone, D. Farías, and A. M. Wodtke, *Helium diffraction and acoustic phonons of graphene grown on copper foil*. **Carbon**, 95:731 (2015)

6. F. Bisti, G. Anemone, M. Donarelli, S. Penna, A. Reale, L. Ottaviano, *Tetrakis erbium quinolinate complexes, electronic structure investigation*. **Organic Electronics**, 14, 8, 1810-1814 (2014)

7. F. Bisti, A. Stroppa, M. Donarelli, G. Anemone, F. Perrozzi, S. Picozzi, L. Ottaviano, *Unravelling the Role of the Central Metal Ion in the Electronic Structure of Tris(8-hydroxyquinoline) Metal Chelates: Photoemission Spectroscopy and Hybrid Functional Calculations*. **The Journal of Physical Chemistry A**, 116, 47,1 1548-11552. (2012)

8. G. Anemone, C. Weingarten, A. Al Taleb, C. Prieto, and D. Farías, *Ultrasmooth Metal Thin Films on Curved Fused Silica by Laser Polishing*. (To be published).

9. G. Anemone, A. Al Taleb, W. W. Hayes, J. R. Manson, and D. Farías, *Quantum decoherence behavior in neon scattering from Ru(0001) and graphene/Ru(0001) surfaces: Experiment and comparison with calculations*. (To be published).

BIBLIOGRAPHY

[1] D. Farías and K.-H. Rieder, "Atomic beam diffraction from solid surfaces," *Reports on Progress in Physics*, vol. 61, no. 12, p. 1575, 1998.

[2] M. Koch, S. Rehbein, G. Schmahl, T. Reisinger, G. Bracco, W. Ernst, and B. Holst, "Imaging with neutral atoms: a new matter-wave microscope," *Journal of Microscopy*, vol. 229, no. 1, pp. 1–5, 2008.

[3] S. Eder, T. Reisinger, M. Greve, G. Bracco, and B. Holst, "Focusing of a neutral helium beam below one micron," *New Journal of Physics*, vol. 14, no. 7, p. 073014, 2012.

[4] S. Eder, X. Guo, T. Kaltenbacher, M. Greve, M. Kalläne, L. Kipp, and B. Holst, "Focusing of a neutral helium beam with a photon-sieve structure," *Physical Review A*, vol. 91, no. 4, p. 043608, 2015.

[5] B. Holst and W. Allison, "An atom-focusing mirror," *Nature*, vol. 390, no. 6657, p. 244, 1997.

[6] K. Fladischer, H. Reingruber, T. Reisinger, V. Mayrhofer, W. E. Ernst, A. E. Ross, D. A. MacLaren, W. Allison, D. Litwin, J. Galas, S. Sitarek, P. Nieto, D. Barredo, D. Farías, R. Miranda, B. Surma, A. Miros, B. Piatkowski, E. S. rd, and B. Holst, "An ellipsoidal mirror for focusing neutral atomic and molecular beams," *New Journal of Physics*, vol. 12, no. 3, p. 033018, 2010.

[7] G. Comsa, "Coherence length and/or transfer width?," *Surface Science*, vol. 81, no. 1, pp. 57 – 68, 1979.

[8] T. Reisinger and B. Holst, "Neutral atom and molecule focusing using a Fresnel zone plate," *Journal of Vacuum Science & Technology B: Microelectronics and Nanometer Structures Processing, Measurement, and Phenomena*, vol. 26, no. 6, pp. 2374–2379, 2008.

[9] B. Poelsema and G. Comsa, *Scattering of thermal energy atoms from discordered surfaces*.
Springer, 1989.

[10] D. Barredo, F. Calleja, P. Nieto, J. J. Hinarejos, G. Laurent, A. L. V. de Parga, D. Farías, and R. Miranda, "A Quantum-Stabilized Mirror for Atoms," *Advanced Materials*, vol. 20, no. 18, pp. 3492–3497, 2008.

[11] A. Al Taleb, G. Anemone, D. Farías, and R. Miranda, "Acoustic surface phonons of graphene on Ni (111)," *Carbon*, vol. 99, pp. 416–422, 2016.

[12] P. Sutter, M. Minniti, P. Albrecht, D. Farías, R. Miranda, and E. Sutter, "A high-reflectivity, ambient-stable graphene mirror for neutral atomic and molecular beams," *Applied Physics Letters*, vol. 99, no. 21, p. 211907, 2011.

[13] R. Doak, "Experimental limitations and opportunities in single-phonon inelastic helium scattering," in *Helium Atom Scattering from Surfaces*, pp. 5–24, Springer, 1992.

[14] M. Barr, K. M. O'Donnell, A. Fahy, W. Allison, and P. C. Dastoor, "A desktop supersonic free-jet beam source for a scanning helium microscope (SHeM)," *Measurement Science and Technology*, vol. 23, no. 10, p. 105901, 2012.

[15] D. Miller, *Atomic and molecular beam methods*, vol. 1.
Oxford University Press, 1988.

[16] G. Scoles *et al.*, *Atomic and molecular beam methods*, vol. 1.
Oxford university press New York, 1988.

[17] J. P. Toennies and K. Winkelmann, "Theoretical studies of highly expanded free jets: Influence of quantum effects and a realistic intermolecular potential," *The Journal of Chemical Physics*, vol. 66, no. 9, pp. 3965–3979, 1977.

[18] H. Hoinkes, "The physical interaction potential of gas atoms with single-crystal surfaces, determined from gas-surface diffraction experiments," *Reviews of Modern Physics*, vol. 52, no. 4, p. 933, 1980.

[19] R. E. Stickney, *The Structure and Chemistry of Solid Surfaces*.
New York:Willey, 1969.

[20] N. Esbjerg and J. Nørskov, "Dependence of the He-scattering potential at surfaces on the surface-electron-density profile," *Physical Review Letters*, vol. 45, no. 10, p. 807, 1980.

[21] D.-M. Smilgies and J. Toennies, "Resolution and intensity considerations of an ideal He atom time-of-flight spectrometer for measurements of surface phonon dispersion curves," *Review of Scientific Instruments*, vol. 59, no. 10, pp. 2185–2194, 1988.

[22] J. Toennies, "Experimental determination of surface phonons by helium atom and electron energy loss spectroscopy," in *Surface Phonons*, pp. 111–166, Springer, 1991.

[23] J. L. Beeby, "The scattering of helium atoms from surfaces," *Journal of Physics C: Solid State Physics*, vol. 4, no. 18, p. L359, 1971.

[24] R. Hooke, *Micrographia: or some physiological descriptions of minute bodies made by magnifying glasses, with observations and inquiries thereupon*.
Royal Society, (1665) 1961.

[25] E. Hecht, *Optics*.
Addison Wesley, New York, 2001.

[26] S. W. Hell and J. Wichmann, "Breaking the diffraction resolution limit by stimulated emission: stimulated-emission-depletion fluorescence microscopy," *Optics letters*, vol. 19, no. 11, pp. 780–782, 1994.

[27] E. Rittweger, K. Y. Han, S. E. Irvine, C. Eggeling, and S. W. Hell, "STED microscopy reveals crystal colour centres with nanometric resolution," *Nature Photonics*, vol. 3, no. 3, pp. 144–147, 2009.

[28] D. Wildanger, R. Medda, L. Kastrup, and S. Hell, "A compact STED microscope providing 3D nanoscale resolution," *Journal of Microscopy*, vol. 236, no. 1, pp. 35–43, 2009.

[29] E. Betzig, G. H. Patterson, R. Sougrat, O. W. Lindwasser, S. Olenych, J. S. Bonifacino, M. W. Davidson, J. Lippincott-Schwartz, and H. F. Hess, "Imaging intracellular fluorescent proteins at nanometer resolution," *Science*, vol. 313, no. 5793, pp. 1642–1645, 2006.

[30] L. Möckl, D. C. Lamb, and C. Bräuchle, "Super-resolved Fluorescence Microscopy: Nobel Prize in Chemistry 2014 for Eric Betzig, Stefan Hell, and William E. Moerner," *Angewandte Chemie International Edition*, vol. 53, no. 51, pp. 13972–13977, 2014.

[31] G. Binnig, H. Rohrer, C. Gerber, and E. Weibel, "Surface studies by scanning tunneling microscopy," *Physical Review Letters*, vol. 49, no. 1, p. 57, 1982.

[32] L. de Broglie, "Nature 112, 1923, 540," *Ann. de Physique (Paris)*, vol. 10, p. 2, 1925.

[33] D. Keith, M. Schattenburg, H. I. Smith, and D. Pritchard, "Diffraction of atoms by a transmission grating," *Physical Review Letters*, vol. 61, no. 14, p. 1580, 1988.

[34] O. Carnal, M. Sigel, T. Sleator, H. Takuma, and J. Mlynek, "Imaging and focusing of atoms by a Fresnel zone plate," *Physical Review Letters*, vol. 67, no. 23, p. 3231, 1991.

[35] R. Doak, R. Grisenti, S. Rehbein, G. Schmahl, J. Toennies, and C. Wöll, "Towards realization of an atomic de Broglie microscope: helium atom focusing using Fresnel zone plates," *Physical Review Letters*, vol. 83, no. 21, p. 4229, 1999.

[36] P. Witham and E. Sánchez, "A simple approach to neutral atom microscopy," *Review of Scientific Instruments*, vol. 82, no. 10, p. 103705, 2011.

[37] P. Witham and E. Sánchez, "Increased resolution in neutral atom microscopy," *Journal of Microscopy*, vol. 248, no. 3, pp. 223–227, 2012.

[38] M. Barr, A. Fahy, J. Martens, A. Jardine, D. Ward, J. Ellis, W. Allison, and P. Dastoor, "Unlocking new contrast in a scanning helium microscope," *Nature Communications*, vol. 7, 2016.

[39] S. D. Eder, *A neutral matter wave microscope (NEMI): Design and setup*. PhD thesis, University of Bergen, 2011.

[40] K. S. Novoselov, A. K. Geim, S. V. Morozov, D. Jiang, Y. Zhang, S. V. Dubonos, I. V. Grigorieva, and A. A. Firsov, "Electric field effect in atomically thin carbon films," *Science*, vol. 306, no. 5696, pp. 666–669, 2004.

[41] K. Novoselov, "Nobel lecture: Graphene: Materials in the flatland," *Reviews of Modern Physics*, vol. 83, no. 3, p. 837, 2011.

[42] A. C. Neto, F. Guinea, N. M. Peres, K. S. Novoselov, and A. K. Geim, "The electronic properties of graphene," *Reviews of Modern Physics*, vol. 81, no. 1, p. 109, 2009.

[43] S. Chen, L. Brown, M. Levendorf, W. Cai, S.-Y. Ju, J. Edgeworth, X. Li, C. W. Magnuson, A. Velamakanni, R. D. Piner, *et al.*, "Oxidation resistance of graphene-coated Cu and Cu/Ni alloy," *ACS Nano*, vol. 5, no. 2, pp. 1321–1327, 2011.

[44] G. Bae, H. Jung, N. Park, J. Park, S. Hong, and W. Park, "Effect of charge-transfer complex on the energy level alignment between graphene and organic molecules," *Applied Physics Letters*, vol. 100, no. 18, p. 183102, 2012.

[45] D. Prasai, J. C. Tuberquia, R. R. Harl, G. K. Jennings, and K. I. Bolotin, "Graphene: corrosion-inhibiting coating," *ACS Nano*, vol. 6, no. 2, pp. 1102–1108, 2012.

[46] M. C. Schabel and J. L. Martins, "Energetics of interplanar binding in graphite," *Physical Review B*, vol. 46, no. 11, p. 7185, 1992.

[47] K. S. Novoselov, A. K. Geim, S. Morozov, D. Jiang, M. Katsnelson, I. Grigorieva, S. Dubonos, and A. Firsov, "Two-dimensional gas of massless Dirac fermions in graphene," *Nature*, vol. 438, no. 7065, pp. 197–200, 2005.

[48] A. K. Geim, "Graphene: status and prospects," *Science*, vol. 324, no. 5934, pp. 1530–1534, 2009.

[49] J.-A. Yan, W. Y. Ruan, and M. Y. Chou, "Phonon dispersions and vibrational properties of monolayer, bilayer, and trilayer graphene: Density-functional perturbation theory," *Physical Review B*, vol. 77, p. 125401, Mar 2008.

[50] L. Malard, M. Pimenta, G. Dresselhaus, and M. Dresselhaus, "Raman spectroscopy in graphene," *Physics Reports*, vol. 473, no. 5, pp. 51–87, 2009.

[51] M. Dresselhaus, A. Jorio, and R. Saito, "Characterizing graphene, graphite, and carbon nanotubes by Raman spectroscopy," *Annual Review of Condensed Matter Physics*, vol. 1, no. 1, pp. 89–108, 2010.

[52] A. C. Ferrari and D. M. Basko, "Raman spectroscopy as a versatile tool for studying the properties of graphene," *Nature Nanotechnology*, vol. 8, no. 4, pp. 235–246, 2013.

[53] F. Tuinstra and J. L. Koenig, "Raman spectrum of graphite," *The Journal of Chemical Physics*, vol. 53, no. 3, pp. 1126–1130, 1970.

[54] A. C. Ferrari and J. Robertson, "Interpretation of Raman spectra of disordered and amorphous carbon," *Physical Review B*, vol. 61, pp. 14095–14107, May 2000.

[55] C. Casiraghi, S. Pisana, K. Novoselov, A. Geim, and A. Ferrari, "Raman fingerprint of charged impurities in graphene," *Applied Physics Letters*, vol. 91, no. 23, p. 233108, 2007.

[56] A. C. Ferrari, J. Meyer, V. Scardaci, C. Casiraghi, M. Lazzeri, F. Mauri, S. Piscanec, D. Jiang, K. Novoselov, S. Roth, *et al.*, "Raman spectrum of graphene and graphene layers," *Physical Review Letters*, vol. 97, no. 18, p. 187401, 2006.

[57] S. Marchini, S. Günther, and J. Wintterlin, "Scanning tunneling microscopy of graphene on Ru (0001)," *Physical Review B*, vol. 76, no. 7, p. 075429, 2007.

[58] A. V. De Parga, F. Calleja, B. Borca, M. Passeggi Jr, J. Hinarejos, F. Guinea, and R. Miranda, "Periodically rippled graphene: growth and spatially resolved electronic structure," *Physical Review Letters*, vol. 100, no. 5, p. 056807, 2008.

[59] P. W. Sutter, J.-I. Flege, and E. A. Sutter, "Epitaxial graphene on ruthenium," *Nature Materials*, vol. 7, no. 5, pp. 406–411, 2008.

[60] A. Politano, B. Borca, M. Minniti, J. J. Hinarejos, A. L. Vázquez de Parga, D. Farías, and R. Miranda, "Helium reflectivity and Debye temperature of graphene grown epitaxially on Ru(0001)," *Physical Review B*, vol. 84, p. 035450, Jul 2011.

[61] D. Martoccia, M. Björck, C. Schlepütz, T. Brugger, S. Pauli, B. Patterson, T. Greber, and P. Willmott, "Graphene on Ru (0001): a corrugated and chiral structure," *New Journal of Physics*, vol. 12, no. 4, p. 043028, 2010.

[62] Z. Sun, Z. Yan, J. Yao, E. Beitler, Y. Zhu, and J. M. Tour, "Growth of graphene from solid carbon sources," *Nature*, vol. 468, no. 7323, pp. 549–552, 2010.

[63] F. Mittendorfer, A. Garhofer, J. Redinger, J. Klimeš, J. Harl, and G. Kresse, "Graphene on Ni (111): Strong interaction and weak adsorption," *Physical Review B*, vol. 84, no. 20, p. 201401, 2011.

[64] X. Li, W. Cai, J. An, S. Kim, J. Nah, D. Yang, R. Piner, A. Velamakanni, I. Jung, E. Tutuc, *et al.*, "Large-area synthesis of high-quality and uniform graphene films on copper foils," *Science*, vol. 324, no. 5932, pp. 1312–1314, 2009.

[65] C. Mattevi, H. Kim, and M. Chhowalla, "A review of chemical vapour deposition of graphene on copper," *Journal of Materials Chemistry*, vol. 21, no. 10, pp. 3324–3334, 2011.

[66] H. K. Yu, K. Balasubramanian, K. Kim, J.-L. Lee, M. Maiti, C. Ropers, J. Krieg, K. Kern, and A. M. Wodtke, "Chemical Vapor Deposition of Graphene on a 'Peeled-Off' Epitaxial Cu(111) Foil: A Simple Approach to Improved Properties," *ACS Nano*, vol. 8, no. 8, pp. 8636–8643, 2014.

[67] A. A. Taleb, H. K. Yu, G. Anemone, D. Farías, and A. M. Wodtke, "Helium diffraction and acoustic phonons of graphene grown on copper foil," *Carbon*, vol. 95, pp. 731 – 737, 2015.

[68] N. Gall', E. Rut'kov, and A. Y. Tontegode, "Interaction of silver atoms with iridium and with a two-dimensional graphite film on iridium: Adsorption, desorption, and dissolution," *Physics of the Solid State*, vol. 46, no. 2, pp. 371–377, 2004.

[69] J. Coraux, A. T. N 'Diaye, C. Busse, and T. Michely, "Structural coherency of graphene on Ir (111)," *Nano Letters*, vol. 8, no. 2, pp. 565–570, 2008.

[70] J. Coraux, M. Engler, C. Busse, D. Wall, N. Buckanie, F.-J. M. Zu Heringdorf, R. Van Gastel, B. Poelsema, T. Michely, *et al.*, "Growth of graphene on Ir (111)," *New Journal of Physics*, vol. 11, no. 2, p. 023006, 2009.

[71] A. Preobrajenski, M. L. Ng, A. Vinogradov, and N. Mårtensson, "Controlling graphene corrugation on lattice-mismatched substrates," *Physical Review B*, vol. 78, no. 7, p. 073401, 2008.

[72] P. Sutter, J. T. Sadowski, and E. Sutter, "Graphene on Pt (111): Growth and substrate interaction," *Physical Review B*, vol. 80, no. 24, p. 245411, 2009.

[73] A. Politano, A. R. Marino, and G. Chiarello, "Phonon dispersion of quasi-freestanding graphene on Pt (111)," *Journal of Physics: Condensed Matter*, vol. 24, no. 10, p. 104025, 2012.

[74] A. Martín-Recio, C. Romero-Muñiz, P. Pou, R. Pérez, and J. M. Gómez-Rodríguez, "Purely substitutional nitrogen on graphene/Pt (111) unveiled by STM and first principles calculations," *Nanoscale*, vol. 8, no. 40, pp. 17686–17693, 2016.

[75] S.-Y. Kwon, C. V. Ciobanu, V. Petrova, V. B. Shenoy, J. Bareno, V. Gambin, I. Petrov, and S. Kodambaka, "Growth of semiconducting graphene on palladium," *Nano Letters*, vol. 9, no. 12, pp. 3985–3990, 2009.

[76] A. Varykhalov and O. Rader, "Graphene grown on Co (0001) films and islands: Electronic structure and its precise magnetization dependence," *Physical Review B*, vol. 80, no. 3, p. 035437, 2009.

[77] A. Al Taleb and D. Farías, "Phonon dynamics of graphene on metals," *Journal of Physics: Condensed Matter*, vol. 28, no. 10, p. 103005, 2016.

[78] J. Wintterlin and M.-L. Bocquet, "Graphene on metal surfaces," *Surface Science*, vol. 603, no. 10, pp. 1841–1852, 2009.

[79] M. Batzill, "The surface science of graphene: Metal interfaces, CVD synthesis, nanoribbons, chemical modifications, and defects," *Surface Science Reports*, vol. 67, no. 3, pp. 83–115, 2012.

[80] A. Dahal and M. Batzill, "Graphene–nickel interfaces: a review," *Nanoscale*, vol. 6, no. 5, pp. 2548–2562, 2014.

[81] E. C. Montoya, *Ferromagnetism in wide band gap materials: Mn-Zno and Mn-Si_3N_4 thin films*.
PhD thesis, Universidad Autónoma de Madrid and Istituto de Ciencia de Materiales de Madrid, 2009.

[82] E. S. Colera, *Estudio por espectroscopía Brillouin de las ondas acusticas de superficie en lamanas delgadas depositadas por sputtering: influencia de la nanoestructura.*
PhD thesis, Universidad Autónoma de Madrid and Istituto de Ciencia de Materiales de Madrid, 2011.

[83] P. N. Ramos, *An experimental study of H_2 diffraction from metal surfaces*.
PhD thesis, Universidad Autónoma de Madrid, 2009.

[84] J. Lapujoulade, Y. Lejay, and G. Armand, "The thermal attenuation of coherent elastic scattering of noble gas from metal surfaces," *Surface Science*, vol. 95, no. 1, pp. 107 – 130, 1980.

[85] D. B. González, *Dinámica de interacción de haces de He, H_2 y D_2 de energía térmica con superícies*.
PhD thesis, Universidad Autónoma de Madrid, 2009.

[86] A. A. Taleb, *Surface structure and dynamics of epitaxial graphene on metals*.
PhD thesis, Universidad Autónoma de Madrid, 2017.

[87] G. Anemone, E. Climent-Pascual, H. K. Yu, A. Al Taleb, F. Jiménez-Villacorta, C. Prieto, A. M. Wodtke, A. De Andrés, and D. Farías, "Quality of graphene on sapphire: long-range order from helium diffraction versus lattice defects from Raman spectroscopy," *RSC Advances*, vol. 6, no. 25, pp. 21235–21245, 2016.

[88] T. Beléndez, C. Neipp, and A. Beléndez, "Large and small deflections of a cantilever beam," *European Journal of Physics*, vol. 23, no. 3, p. 371, 2002.

[89] Y. S. Kim, K. Joo, S.-K. Jerng, J. H. Lee, D. Moon, J. Kim, E. Yoon, and S.-H. Chun, "Direct Integration of Polycrystalline Graphene into Light Emitting Diodes by Plasma-Assisted Metal-Catalyst-Free Synthesis," *ACS Nano*, vol. 8, no. 3, pp. 2230–2236, 2014.

[90] H. Medina, Y.-C. Lin, C. Jin, C.-C. Lu, C.-H. Yeh, K.-P. Huang, K. Suenaga, J. Robertson, and P.-W. Chiu, "Metal-Free Growth of Nanographene on Silicon Oxides for Transparent Conducting Applications," *Advanced Functional Materials*, vol. 22, no. 10, pp. 2123–2128, 2012.

[91] K. Ellmer, "Past achievements and future challenges in the development of optically transparent electrodes," *Nature Photonics*, vol. 6, no. 12, pp. 809–817, 2012.

[92] D. Wei and J. Kivioja, "Graphene for energy solutions and its industrialization," *Nanoscale*, vol. 5, pp. 10108–10126, 2013.

[93] F. Bonaccorso, L. Colombo, G. Yu, M. Stoller, V. Tozzini, A. C. Ferrari, R. S. Ruoff, and V. Pellegrini, "Graphene, related two-dimensional crystals, and hybrid systems for energy conversion and storage," *Science*, vol. 347, no. 6217, p. 1246501, 2015.

[94] D. Lee, H. Lee, Y. Ahn, Y. Jeong, D.-Y. Lee, and Y. Lee, "Highly stable and flexible silver nanowire–graphene hybrid transparent conducting electrodes for

emerging optoelectronic devices," *Nanoscale*, vol. 5, no. 17, pp. 7750–7755, 2013.

[95] J. Sun, Y. Zhang, and Z. Liu, "Direct chemical vapor deposition growth of graphene on insulating substrates," *ChemNanoMat*, vol. 2, no. 1, pp. 9–18, 2016.

[96] Y. Lee, S. Bae, H. Jang, S. Jang, S.-E. Zhu, S. H. Sim, Y. I. Song, B. H. Hong, and J.-H. Ahn, "Wafer-scale synthesis and transfer of graphene films," *Nano Letters*, vol. 10, no. 2, pp. 490–493, 2010.

[97] S. Bhaviripudi, X. Jia, M. S. Dresselhaus, and J. Kong, "Role of kinetic factors in chemical vapor deposition synthesis of uniform large area graphene using copper catalyst," *Nano Letters*, vol. 10, no. 10, pp. 4128–4133, 2010.

[98] S. Bae, H. Kim, Y. Lee, X. Xu, J.-S. Park, Y. Zheng, J. Balakrishnan, T. Lei, H. R. Kim, Y. I. Song, *et al.*, "Roll-to-roll production of 30-inch graphene films for transparent electrodes," *Nature Nanotechnology*, vol. 5, no. 8, pp. 574–578, 2010.

[99] H. Ago, Y. Ogawa, M. Tsuji, S. Mizuno, and H. Hibino, "Catalytic growth of graphene: toward large-area single-crystalline graphene," *The Journal of Physical Chemistry Letters*, vol. 3, no. 16, pp. 2228–2236, 2012.

[100] J. Hwang, M. Kim, D. Campbell, H. A. Alsalman, J. Y. Kwak, S. Shivaraman, A. R. Woll, A. K. Singh, R. G. Hennig, S. Gorantla, M. H. Rümmeli, and M. G. Spencer, "Van der Waals Epitaxial Growth of Graphene on Sapphire by Chemical Vapor Deposition without a Metal Catalyst," *ACS Nano*, vol. 7, no. 1, pp. 385–395, 2013.

[101] M. A. Fanton, J. A. Robinson, C. Puls, Y. Liu, M. J. Hollander, B. E. Weiland, M. LaBella, K. Trumbull, R. Kasarda, C. Howsare, J. Stitt, and D. W. Snyder, "Characterization of Graphene Films and Transistors Grown on Sapphire by Metal-Free Chemical Vapor Deposition," *ACS Nano*, vol. 5, no. 10, pp. 8062–8069, 2011.

[102] A. Ismach, C. Druzgalski, S. Penwell, A. Schwartzberg, M. Zheng, A. Javey, J. Bokor, and Y. Zhang, "Direct Chemical Vapor Deposition of Graphene on Dielectric Surfaces," *Nano Letters*, vol. 10, no. 5, pp. 1542–1548, 2010.

[103] W. A. Schlup and K. H. Rieder, "Determination of surface-defect concentration and distribution with He diffraction," *Physical Review Letters*, vol. 56, pp. 73–76, Jan 1986.

[104] F. Hofmann, J. Toennies, and J. Manson, "A comprehensive experimental study of the dynamical interaction of He atoms with Cu (001) surface phonons," *The Journal of Chemical Physics*, vol. 101, no. 11, pp. 10155–10172, 1994.

[105] J. Nelson and D. Riley, "The thermal expansion of graphite from 15 c. to 800 c.: Part I. Experimental," *Proceedings of the Physical Society*, vol. 57, no. 6, p. 477, 1945.

[106] F. de Juan, A. Politano, G. Chiarello, and H. A. Fertig, "Symmetries and selection rules in the measurement of the phonon spectrum of graphene and related materials," *Carbon*, vol. 85, pp. 225 – 232, 2015.

[107] Y. Wei, B. Wang, J. Wu, R. Yang, and M. L. Dunn, "Bending Rigidity and Gaussian Bending Stiffness of Single-Layered Graphene," *Nano Letters*, vol. 13, no. 1, pp. 26–30, 2013.

[108] B. Amorim and F. Guinea, "Flexural mode of graphene on a substrate," *Physical Review B*, vol. 88, p. 115418, Sep 2013.

[109] G. López-Polín, C. Gómez-Navarro, V. Parente, F. Guinea, M. I. Katsnelson, F. Pérez-Murano, and J. Gómez-Herrero, "Increasing the elastic modulus of graphene by controlled defect creation," *Nature Physics*, vol. 11, no. 1, pp. 26–31, 2015.

[110] A. J. Marsden, M. Phillips, and N. R. Wilson, "**??** Friction force microscopy: a simple technique for identifying graphene on rough substrates and mapping the orientation of graphene grains on copper," *Nanotechnology*, vol. 24, no. 25, p. 255704, 2013.

[111] M. Halmann, A. Steinfeld, M. Epstein, and I. Vishnevetsky, "Vacuum Carbothermic Reduction of Alumina," *Mineral Processing and Extractive Metallurgy Review*, vol. 35, no. 2, pp. 126–135, 2014.

[112] F. Jimenez-Villacorta, E. Climent-Pascual, R. Ramirez-Jimenez, J. Sanchez-Marcos, C. Prieto, and A. de Andrés, "Graphene-ultrasmall silver nanoparticle interacti-

ons and their effect on electronic transport and Raman enhancement," *Carbon*, vol. 101, pp. 305 – 314, 2016.

[113] M. Kalbac, A. Reina-Cecco, H. Farhat, J. Kong, L. Kavan, and M. S. Dresselhaus, "The Influence of Strong Electron and Hole Doping on the Raman Intensity of Chemical Vapor-Deposition Graphene," *ACS Nano*, vol. 4, no. 10, pp. 6055–6063, 2010.

[114] X. Diez-Betriu, S. Alvarez-Garcia, C. Botas, P. Alvarez, J. Sanchez-Marcos, C. Prieto, R. Menendez, and A. de Andrés, "Raman spectroscopy for the study of reduction mechanisms and optimization of conductivity in graphene oxide thin films," *Journal of Materials Chemistry C*, vol. 1, pp. 6905–6912, 2013.

[115] L. G. Cançado, K. Takai, T. Enoki, M. Endo, Y. A. Kim, H. Mizusaki, A. Jorio, L. N. Coelho, R. Magalhães-Paniago, and M. A. Pimenta, "General equation for the determination of the crystallite size La of nanographite by Raman spectroscopy," *Applied Physics Letters*, vol. 88, no. 16, p. 163106, 2006.

[116] M. Lucchese, F. Stavale, E. M. Ferreira, C. Vilani, M. Moutinho, R. B. Capaz, C. Achete, and A. Jorio, "Quantifying ion-induced defects and Raman relaxation length in graphene," *Carbon*, vol. 48, no. 5, pp. 1592 – 1597, 2010.

[117] L. G. Cançado, A. Jorio, E. M. Ferreira, F. Stavale, C. Achete, R. Capaz, M. Moutinho, A. Lombardo, T. Kulmala, and A. Ferrari, "Quantifying defects in graphene via Raman spectroscopy at different excitation energies," *Nano Letters*, vol. 11, no. 8, pp. 3190–3196, 2011.

[118] A. Tamtoögl, E. Bahn, J. Zhu, P. Fouquet, J. Ellis, and W. Allison, "Graphene on Ni (111): Electronic corrugation and dynamics from helium atom scattering," *The Journal of Physical Chemistry C*, vol. 119, no. 46, pp. 25983–25990, 2015.

[119] J. S. Becker, R. D. Brown, E. Johansson, N. S. Lewis, and S. Sibener, "Helium atom diffraction measurements of the surface structure and vibrational dynamics of CH 3–Si (111) and CD 3–Si (111) surfaces," *The Journal of Chemical Physics*, vol. 133, no. 10, p. 104705, 2010.

[120] D. Schmicker, S. Schmidt, J. G. Skofronick, J. P. Toennies, and R. Vollmer, "Epitaxial growth of single-crystal C_{60} on mica by helium-atom scattering," *Physical Review B*, vol. 44, pp. 10995–10997, Nov 1991.

[121] G. Brusdeylins and D. Schmicker, "Elastic and inelastic helium atom scattering at a cleaved mica sheet," *Surface Science*, vol. 331, pp. 237 – 242, 1995.

[122] L. Yang, D. M. Czajkowsky, J. Sun, J. Hu, and Z. Shao, "Anomalous Surface Fatigue in a Nano-Layered Material," *Advanced Materials*, vol. 26, no. 37, pp. 6478–6482, 2014.

[123] T. Fukuma, K. Kobayashi, K. Matsushige, and H. Yamada, "True atomic resolution in liquid by frequency-modulation atomic force microscopy," *Applied Physics Letters*, vol. 87, no. 3, p. 034101, 2005.

[124] V. L. Nguyen, B. G. Shin, D. L. Duong, S. T. Kim, D. Perello, Y. J. Lim, Q. H. Yuan, F. Ding, H. Y. Jeong, H. S. Shin, *et al.*, "Seamless stitching of graphene domains on polished copper (111) foil," *Advanced Materials*, vol. 27, no. 8, pp. 1376–1382, 2015.

[125] H. Wang, X. Zhang, H. Liu, Z. Yin, J. Meng, J. Xia, X.-M. Meng, J. Wu, and J. You, "Synthesis of Large-Sized Single-Crystal Hexagonal Boron Nitride Domains on Nickel Foils by Ion Beam Sputtering Deposition," *Advanced Materials*, vol. 27, no. 48, pp. 8109–8115, 2015.

[126] H. Okuda, K. Nakajima, K. Fujiwara, and S. Ochiai, "Si wafers having one-and two-dimensionally curved (111) planes examined by X-ray diffraction," *Journal of Applied Crystallography*, vol. 39, no. 3, pp. 443–445, 2006.

[127] K. Nakajima, K. Fujiwara, W. Pan, and H. Okuda, "Shaped silicon-crystal wafers obtained by plastic deformation and their application to silicon-crystal lenses," *Nature Materials*, vol. 4, no. 1, pp. 47–50, 2005.

[128] K. Nakajima, K. Ohdaira, K. Fujiwara, and W. Pan, "Solar cell system using a polished concave Si-crystal mirror," *Solar energy materials and solar cells*, vol. 88, no. 3, pp. 323–329, 2005.

[129] E. Sutter, P. Albrecht, and P. Sutter, "Graphene growth on polycrystalline Ru thin films," *Applied Physics Letters*, vol. 95, no. 13, p. 133109, 2009.

[130] E. Sutter, P. Albrecht, F. E. Camino, and P. Sutter, "Monolayer graphene as ultimate chemical passivation layer for arbitrarily shaped metal surfaces," *Carbon*, vol. 48, no. 15, pp. 4414–4420, 2010.

[131] M. Yoshimoto, T. Maeda, T. Ohnishi, H. Koinuma, O. Ishiyama, M. Shinohara, M. Kubo, R. Miura, and A. Miyamoto, "Atomic-scale formation of ultrasmooth surfaces on sapphire substrates for high-quality thin-film fabrication," *Applied Physics Letters*, vol. 67, no. 18, pp. 2615–2617, 1995.

[132] C. Weingarten, S. Heidrich, Y. Wu, and E. Willenborg, "Laser polishing of glass," in *SPIE Optifab*, pp. 963303–963303, International Society for Optics and Photonics, 2015.

[133] D. Maccariello, *Structure and dynamics at graphene interfaces: from metal substrates to adsorbed molecules*.
PhD thesis, Universidad Autónoma de Madrid, 2014.

[134] D. Maccariello, D. Campi, A. Al Taleb, G. Benedek, D. Farías, M. Bernasconi, and R. Miranda, "Low-energy excitations of graphene on Ru (0001)," *Carbon*, vol. 93, pp. 1–10, 2015.

[135] K. Rieder, "Surface structural research with atom beam diffraction: helium versus neon," *Surface Review and Letters*, vol. 1, no. 01, pp. 51–65, 1994.

[136] J. N. Smith Jr, D. O'Keefe, and R. Palmer, "Rare-Gas Scattering from LiF: Correlation with Lattice Properties. II," *The Journal of Chemical Physics*, vol. 52, no. 1, pp. 315–320, 1970.

[137] B. R. Williams, "On the Elastic and Inelastic Scattering of Neon Atoms by a (100) Surface of Lithium Fluoride at 150 K," *The Journal of Chemical Physics*, vol. 55, no. 3, pp. 1315–1322, 1971.

[138] G. Boato, P. Cantini, and L. Mattera, "A study of the (001) LiF surface at 80 K by means of diffractive scattering of He and Ne atoms at thermal energies," *Surface Science*, vol. 55, no. 1, pp. 141–178, 1976.

[139] J. Lapujoulade, Y. Le Cruër, M. Lefort, Y. Lejay, E. Maurel, and N. Papanicolaou, "Diffraction of neon by a (117) copper surface," *Journal de Physique Lettres*, vol. 42, no. 21, pp. 463–464, 1981.

[140] K. Rieder and W. Stocker, "Observation of pronounced neon diffraction from low-index metal surfaces," *Physical Review Letters*, vol. 52, no. 5, p. 352, 1984.

[141] B. Salanon, "Ne diffraction from Cu (110)," *Journal de Physique*, vol. 45, no. 8, pp. 1373–1379, 1984.

[142] G. Parschau, E. Kirsten, A. Bischof, and K. Rieder, "Diffraction of He and Ne and selective adsorption of He on Rh (110)," *Physical Review B*, vol. 40, no. 9, p. 6012, 1989.

[143] K. Rieder, "Diffraction of He and Ne from Ni (113): A comparative study," *Physical Review B*, vol. 39, no. 15, p. 10708, 1989.

[144] R. Apel, D. Farías, H. Tröger, E. Kirsten, and K. Rieder, "Atomic beam diffraction and resonant scattering studies of clean Rh (311) and the c (1× 1) H phase," *Surface Science*, vol. 364, no. 3, pp. 303–311, 1996.

[145] K. Rieder, G. Parschau, and B. Burg, "Experimental evidence for anticorrugating effects in He-metal interactions at surfaces," *Physical Review Letters*, vol. 71, no. 7, p. 1059, 1993.

[146] J. F. Annett and R. Haydock, "Anticorrugating effect of hybridization on the helium diffraction potential for metal surfaces," *Physical Review Letters*, vol. 53, no. 8, p. 838, 1984.

[147] M. Minniti, C. Díaz, J. F. Cuñado, A. Politano, D. Maccariello, F. Martín, D. Farías, and R. Miranda, "Helium, neon and argon diffraction from Ru (0001)," *Journal of Physics: Condensed Matter*, vol. 24, no. 35, p. 354002, 2012.

[148] J. Manson, "Inelastic scattering from surfaces," *Physical Review B*, vol. 43, no. 9, p. 6924, 1991.

[149] J. R. Manson, "Multiphonon atom-surface scattering," *Computer physics communications*, vol. 80, no. 1-3, pp. 145–167, 1994.

[150] W. Hayes and J. Manson, "Rare gas collisions with molten metal surfaces," *The Journal of Chemical Physics*, vol. 127, no. 16, p. 164714, 2007.

[151] W. Hayes and J. Manson, "Determination of the Surface Corrugation Amplitude from Classical Atom Scattering," *Physical Review Letters*, vol. 109, no. 6, p. 063203, 2012.

[152] W. Hayes and J. Manson, "Classical and semiclassical theories of atom scattering from corrugated surfaces," *Physical Review B*, vol. 89, no. 4, p. 045406, 2014.

[153] A. Al Taleb, G. Anemone, W. Hayes, J. Manson, and D. Farías, "Multiphonon excitation and quantum decoherence in neon scattering from solid surfaces," *Physical Review B*, vol. 95, no. 7, p. 075414, 2017.

[154] R. Brako and D. Newns, "Differential cross section for atoms inelastically scattered from surfaces," *Physical Review Letters*, vol. 48, no. 26, p. 1859, 1982.

[155] R. Brako and D. Newns, "Energy and angular distribution of atoms scattered from surfaces," *Surface Science*, vol. 117, no. 1-3, pp. 42–52, 1982.

[156] D. Martoccia, P. Willmott, T. Brugger, M. Björck, S. Günther, C. Schlepütz, A. Cervellino, S. Pauli, B. Patterson, S. Marchini, *et al.*, "Graphene on Ru (0001): a 25× 25 supercell," *Physical Review Letters*, vol. 101, no. 12, p. 126102, 2008.

[157] W. Moritz, B. Wang, M.-L. Bocquet, T. Brugger, T. Greber, J. Wintterlin, and S. Günther, "Structure determination of the coincidence phase of graphene on Ru (0001)," *Physical Review Letters*, vol. 104, no. 13, p. 136102, 2010.

[158] B. Wang, M.-L. Bocquet, S. Marchini, S. Günther, and J. Wintterlin, "Chemical origin of a graphene moiré overlayer on Ru (0001)," *Physical Chemistry Chemical Physics*, vol. 10, no. 24, pp. 3530–3534, 2008.

[159] D.-e. Jiang, M.-H. Du, and S. Dai, "First principles study of the graphene/Ru (0001) interface," *The Journal of Chemical Physics*, vol. 130, no. 7, p. 074705, 2009.

[160] B. Borca, S. Barja, M. Garnica, M. Minniti, A. Politano, J. M. Rodriguez-García, J. J. Hinarejos, D. Farías, A. L. V. de Parga, and R. Miranda, "Electronic and geometric corrugation of periodically rippled, self-nanostructured graphene epitaxially grown on Ru(0001)," *New Journal of Physics*, vol. 12, no. 9, p. 093018, 2010.

[161] E. Ferrari, L. Galli, E. Miniussi, M. Morri, M. Panighel, M. Ricci, P. Lacovig, S. Lizzit, and A. Baraldi, "Layer-dependent Debye temperature and thermal expansion of Ru(0001) by means of high-energy resolution core-level photoelectron spectroscopy," *Physical Review B*, vol. 82, no. 19, p. 195420, 2010.

[162] C. Y. Ho, R. W. Powell, and P. E. Liley, "Thermal conductivity of the elements: a comprehensive review," tech. rep., DTIC Document, 1974.

[163] H. Shichibe, Y. Satake, K. Watanabe, A. Kinjyo, A. Kunihara, Y. Yamada, M. Sasaki, W. W. Hayes, and J. R. Manson, "Probing interlayer interactions between graphene and metal substrates by supersonic rare-gas atom scattering," *Physical Review B*, vol. 91, p. 155403, Apr 2015.

[164] V. Celli, D. Himes, P. Tran, J. Toennies, C. Wöll, and G. Zhang, "Multiphonon processes in atom-surface scattering," *Physical Review Letters*, vol. 66, no. 24, p. 3160, 1991.